

國立交通大學
光電工程學系暨研究所
博士論文

低維度氧化鋅奈米結構：製程、光學性質與染料敏化太陽電池
應用之研究

Low-Dimensional ZnO Nanostructures: Fabrication, Optical
Properties and Applications for Dye-Sensitized Solar Cells

研究生：鄭信民

指導教授：謝文峰 教授

中華民國一百年五月

低維度氧化鋅奈米結構：製程、光學性質與染料敏化太陽電池
應用之研究

Low-Dimensional ZnO Nanostructures: Fabrication, Optical
Properties and Applications for Dye-Sensitized Solar Cells

研究生：鄭信民

Student : Hsin-Ming Cheng

指導教授：謝文峰 教授

Advisor : Prof. Wen-Feng Hsieh



Submitted to Department of Photonics and Institute of Electro-Optical Engineering
College of Electrical Engineering and Computer Science
National Chiao Tung University
In partial Fulfillment of the Requirements
For the Degree of
Doctor of Philosophy
In
Electro-Optical engineering

May 2011

Hsinchu, Taiwan, Republic of China

中華民國一百年五月

誌謝

『不曾長夜嚎哭過，不足以言人生。』我從沒想到，這六年心路歷程，會如斯般辛苦。人生總是充滿驚奇，但也因此，值得細細去品味。回首博士研究的這段時光，幫助及鼓勵我的人很多。首先，要感謝我的指導老師 謝文峰 教授。無論在知識和處世，謝老師皆是我的楷模。每每遇到心情挫折時，與老師談完總是能受到鼓舞，重新出發，從老師身上學到的東西比這本論文要多得太多，我以當謝老師的學生為榮。其次要感謝各位口試委員，除了論文的指正以及建議外，對我選擇踏上學術之路的支持與勉勵，讓我更有勇氣堅持走自己的路。我也要感謝雷射診斷實驗室的夥伴們，在研究及生活上交流，讓我心常保年輕。大學同窗兼室友的摯友旭政，一直以他的經驗建議我最對的路；國峰、俊毅、楊松、小郭及小布丁，在材料合成上的協助與經驗分享；偉豪、易慶在我跨足染敏電池研究時的大力協助；智章學長、博濟在超快光學分析上的不吝指導；輝鴻、新翰、玫丹、明容、穎書等學弟妹們，不嫌棄我老地邀我打羽球及花蓮出遊，均感激在心。

此外，還要感謝工研院材化所的洪健龍組長、劉文亮組長以及林麗娟主任，舉薦我進修。永寬兄、一誠兄以及忠義大哥各位前輩，不嫌煩地引領小弟我執行奈米線計畫；文蒂姐、秀連，教我溶凝膠方法；智仁、世莉協助 TEM 上的分析；宏勝與士欽兄在研究上的心得分享；廖博、松慰、秀芬在氧化鋅相關經驗的交流；瑞雲、湘芸要常容忍我這個失職的 XRD 管理員，均使我銘感五內。太電中心蔡松兩組長、童永樑經理同意讓我使用無塵室；佳樺、坤穆、任安、佳音、文祥在染敏電池上的經驗傳授，都讓我在嶄新領域上，不走過多冤枉路，亦要一併感謝。

最後，更要感謝我偉大的母親，無怨無悔地關懷與支持，幾乎給予我她的全部；還有兩位阿姨，一直覺得我是家族的寶；未來的老婆淑惠，多年來的包容與照顧。在天國的外公與外婆，也謝謝您們辛苦照顧我長大，卻沒能來得及讓您們享受這一刻的喜悅。謹將我完成論文之喜悅與所有曾關心過我的人一同分享。

低維度氧化鋅奈米結構：製程、光學性質與染料敏化太陽電池應用之研究

研究生：鄭信民

指導教授：謝文峰 教授

國立交通大學光電工程學系暨研究所

摘要

利用氣相沉積法搭配預鍍氧化鋅緩衝膜，氧化鋅奈米柱可成功的垂直成長於玻璃、矽、碳化矽以及藍寶石基板上。氧化鋅奈米柱在與基板水平方向的磊晶性質，與預鍍的氧化鋅膜的磊晶性息息相關，均受基板影響。同樣地，在氧化鋅奈米柱的光激發光方面，亦受到選擇不同的基板而有所不同。此外，高密度、垂直成長的氧化鋅奈米陣列亦可成功的磊晶於預鍍氮化鎵緩衝膜的藍寶石基板上。我們發現氧化鋅奈米線成長於氮化鎵緩衝膜上會受到基板影響，而有水平方向 121.9 MPa 的雙軸壓縮應力。在共振拉曼頻譜上，我們發現 n 階 A_1 與 E_1 縱模光學聲子強度比例 ($A_1(nLO)/E_1(nLO)$) 隨階數趨於增加，原因歸咎於聲子在氧化鋅奈米線空間中受到空間侷限所造成的結果。氧化鋅奈米線於常溫及低溫下的光激發光均與能帶附近激子的複合有相關連性。

我們利用溶膠-凝膠法，成功地合成具自組裝的奈米等級氧化鋅二次粒子。藉由穿透式電子顯微鏡的分析，氧化鋅奈米二次粒子是由具相同晶面方向的微小一次粒子所凝結而成。在共振拉曼分析上，我們發現聲子的頻譜有紅移現象，電子與聲子的耦合強度比起經攝氏350以及500度熱處理過後樣品來得小。這種隨著尺寸而變化的電子與聲子耦合，主要是受到 Fröhlich 交互作用所影響；這現象在氧化鋅量子點系統也觀察到。另外，在氧化鋅量子點的吸收光譜與光激發光光

譜研究中，發現譜峰有明顯的藍位移現象，再利用有效質量模型可粗略估計其量子侷限效應在不同氧化鋅奈米晶粒尺寸下的結果。

在染料敏化太陽電池應用上，我們利用水熱法成長氧化鋅奈米線與分歧狀氧化鋅奈米線於導電玻璃上，做為光電極。比起奈米粒子，一維奈米線結構更能減少載子於傳輸過程中的所造成的躍遷損耗。而具分歧狀的氧化鋅奈米線於染料敏化太陽電池的光電流以及效益表現上分別為 4.27 mA/cm^2 以及 1.51% ，均為單純奈米線的兩倍。表面積增加提高了染料吸附是效益提升的主要原因。

我們亦嘗試利用具自組裝性的氧化鋅奈米二次粒子做為染料敏化太陽電池之光電極試驗。我們發現這種具多層級的結構體，除了利用一次粒子維持了染料的吸附效率外，二次粒子的結構並增加了光散射效益，間接提供了更多的光獲取能力。我們也嘗試使用兩種吡啶染料，D149、D205，與氧化鋅光電極搭配，分別達到具高效益的 4.95% 以及 5.34% 染料敏化太陽電池。在使用 D205 染料，我們發現開路電壓以及短路電流提升的原因主要是增加了長鏈的疏水官能基，有效的抑制了電子與電解中液碘離子的再複合。對氧化鋅奈米粒子而言，D205 同時也比 D149 染料具有更優越的電子傳輸率。我們亦利用交流阻抗分析法，比較兩種染料所製備的染料敏化太陽電池，提供電子生命期長短的更直接證據。

Low-Dimensional ZnO Nanostructures: Fabrication, Optical Properties and Applications for Dye-Sensitized Solar Cells

Student: Hsin-Ming Cheng

Advisor: Prof. Wen-Feng Hsieh

Department of Photonics and Institute of Electro-Optical Engineering

National Chiao Tung University

Abstract

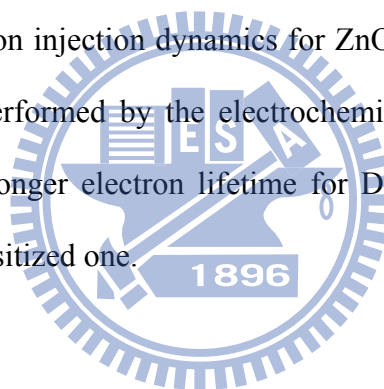
Vertically well-aligned ZnO nanorods were synthesized without employing any metal catalysts on various substrates including glass, Si (111), 6H-SiC (0001) and sapphire (0001), which were pre-coated with *c*-oriented ZnO buffer layers, by simple vapor phase deposition. The in-plane alignments of ZnO nanorods depend on the crystallographic alignment of pre-coated ZnO buffer layer. The photoluminescence of ZnO nanorods are basically related to the type of the substrates. In addition, high-density, vertically oriented arrays of ZnO nanowires were also successfully epitaxial grown on the GaN (0001)-buffered sapphire substrate. We demonstrated that the arrays of ZnO nanowires are well aligned along the *c*-axis and suffer a small biaxial compressive stress of 121.9 MPa. The increasing intensity ratio of *n*th-order longitudinal optical (LO) phonon ($A_I(nLO)/E_I(nLO)$) with increasing scattering order in resonant Raman spectra (RRS) reveals the spatial phonon-confinement as shrinking the diameter of ZnO nanowires. The exciton-related recombinations near the band edge dominate the UV emissions at room temperature as well as at low temperature.

Self-assembled secondary ZnO nanoparticles (NPs), recognized with the

agglomeration of crystalline subcrystals, are successfully synthesized by a simple sol-gel method. TEM images display that one artificial cluster behaves in a single crystal like wurtzite structure owing to the fact that subcrystals coagulate at the same crystal orientation. Moreover, from the RRS measurement, the as-grown sample exhibits phonon redshift; meanwhile, the coupling strength between electron and longitudinal optical phonon, determined by the ratio of the second- to the first-order Raman scattering cross sections, diminishes compared with the samples after post-annealing at 350 °C and 500 °C. The size dependence of electron-phonon coupling is principally as a result of the Fröhlich interaction. ZnO quantum dots (QDs) of controlled sizes have been fabricated by a simple sol-gel method. The blueshift of room-temperature photoluminescence (PL) measurement from free exciton transition are observed decreasing with the QD size that is ascribed to the quantum-confinement effect. From the RRS, the coupling strength between electron and longitudinal optical phonon, deduced from the ratio of the second- to the first-order Raman scattering intensity, diminishes with reducing the ZnO QD diameter. The size dependence of electron-phonon coupling is principally a result of the Fröhlich interaction.

For further dye-sensitized solar cell (DSC) applications, the solvothermal method was utilized to fabricate the ZnO nanowires and branched nanowires on FTO substrates. The one-dimensional branched nanostructures can afford a direct conduction pathway instead of interparticle hopping while using nanoparticles. Furthermore, the short-circuit current density and the energy conversion efficiency of the branched ZnO nanowire DSCs are 4.27 mA/cm² and 1.51 %, which are twice higher than the bare ZnO nanowire ones. The improvement was consequent on the enlargement of internal surface area within the photoelectrode and achieving higher dye adsorption to significantly enhance the performance of the DSCs.

Moreover, self-assembled ZnO secondary NPs have been fabricated as an effective photoelectrode for DSCs. The hierarchical architecture, which manifested the significant light-scattering, can provide more photon harvesting. In addition, dye-molecule adsorption retained sufficient due to enough internal surface area provided by the primary single nanocrystallites. Two indoline dyes, coded D149 and D205, were used as the sensitizers of ZnO DSCs with the optimal energy conversion efficiencies of 4.95% and 5.34%, respectively. The enhancement of V_{oc} and J_{sc} for D205-sensitized ZnO DSCs was ascribed to the effective suppression of electron recombination by extending the alkyl chain on the terminal rhodanine moiety from ethyl to octyl. The higher charge-transfer rate and retardant fluorescence decay reveal that D205 has better electron injection dynamics for ZnO NPs as compared to D149. The further evidence is performed by the electrochemical impedance spectroscopy (EIS) which exhibits the longer electron lifetime for D205-sensitized ZnO DSC in comparison with D149-sensitized one.



Contents

Abstract in Chinese	I
Abstract in English	III
Contents	VI
List of Tables	X
List of Figures	XI

Chapter 1: Introduction

1.1 General properties of ZnO	1
1.1.1 Prelude	1
1.1.2 Crystal Structure	1
1.1.3 Optical Propertie.....	4
1.1.4 Defects in ZnO	6
1.2 Low-Dimensional ZnO Nanostructures.....	9
1.2.1 General of Nanostructures	9
1.2.2 One-Dimensional (1-D) ZnO Nanostructures	11
1.2.3 Zero-Dimensional (0-D) ZnO Nanostructures	12
1.3 Research Motivation	13
1.4 Organization of Dissertation	14
References.....	15

Chapter 2: A Review of Growth and Characterization Techniques

2.1 Growth methods.....	20
2.1.1 Growth of 1-D ZnO Nanowires/ Nanorods.....	20
2.1.2 Growth of 0-D ZnO Nanoparticles/ Quantum dots	35
2.2 Characterization	41

2.2.1 X-Ray Diffraction.....	41
2.2.2 Photoluminescence	43
2.2.3 Raman.....	49
References.....	52

Chapter 3: Experimental Procedures

3.1 Vapor-Solid Synthesis for 1-D ZnO Nanowires/ Nanorods	55
3.2 Hydrothermal Synthesis for 1-D ZnO Nanowires/ Nanorods.....	56
3.3 Sol-Gel Synthesis for 0-D ZnO Nanoparticles/ Quantum dots.....	57
3.4 Materials and Reagents	59
3.5 Characteristic Instruments	60
References.....	62

Chapter 4: Growth and Structural Properties for One-Dimensional ZnO Nanostructures

4.1 ZnO Nanostructures on Buffer Layers.....	63
4.1.1 1-D ZnO Nanorods on ZnO Buffer Layers	63
4.1.2 1-D ZnO Nanowires on GaN Buffer Layers	75
4.2 ZnO Nanostructures from Solvothermal Method	88
4.2.1 ZnO Nanowires on FTO	88
4.2.2 Branched ZnO Nanowires	90
4.3 Summary.....	96
References.....	97

Chapter 5: Growth and Structural Properties for Zero-Dimensional ZnO Nanostructures

5.1 Secondary ZnO Nanoparticles	99
5.1.1 Fabrication and Structural Properties of ZnO Nanoparticles	99

5.1.2 Raman Scattering of ZnO Nanoparticles.....	104
5.1.3 Photoluminescence of ZnO Nanoparticles	110
5.2 Size-controlled ZnO Quantum Dots	112
5.2.1 Fabrication and Structural Properties of ZnO Quantum Dots	112
5.2.2 Band Gap Variation of ZnO Quantum Dots.....	115
5.2.3 Electron-Phonon Coupling of ZnO Quantum Dots.....	119
5.3 Summary	122
References.....	124

Chapter 6: Low-Dimensional ZnO Nanostructures for Dye-Sensitized Solar Cell Applications

6.1 Introduction of Dye-Sensitized Solar Cells (DSCs)	128
6.1.1 A History from Photography	128
6.1.2 Base Principles of DSCs.....	130
6.1.3 ZnO Photoanodes for DSCs.....	134
6.1.4 Research Motivation.....	136
6.2 Experimental Procedures	137
6.2.1 Cell Fabrication	137
6.2.2 Performance Characterization	139
6.2.2.1 The Solar Spectrum and Air Mass.....	139
6.2.2.2 Photocurrent-Voltage (I-V) Characterization	141
6.2.2.3 Incident Photon-to-Current Conversion Efficiency (IPCE).....	146
6.2.2.4 Electrochemical Impedance Spectroscopy (EIS).....	146
6.2.3 Characteristic Instruments	151
6.3 ZnO Nanostructures for DSSC	152
6.3.1 Branched ZnO Nanowires for DSSC	152
6.3.2 Hierarchical ZnO Nanoparticles for DSSC	159

6.4 Summary 178

References 180

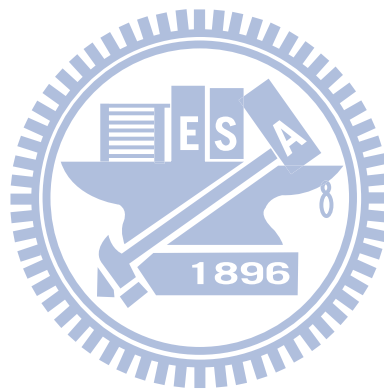
Chapter 7: Conclusions

7.1 Conclusions 187

7.2 Prospective 189

References 191

Curriculum Vitae 192



List of Tables

TABLE 1-1. An appreciation of the potential of ZnO for optoelectronic applications can be obtained by examining this table, which compares the relevant material properties of ZnO with those of other wide band gap semiconductors.....	5
TABLE 1-2. Physical Properties of wurtzite ZnO.....	8
TABLE 2-1. Summarizes some of the studies on solution growth and the resulting structures.....	33
TABLE 2-2. Raman measurement configuration needed to observe the phonon modes in hexagonal ZnO.....	51
TABLE 5-1. Wave number, broadening and the ratio of n-LO phonons found in RRS spectra. The assignments of bulk ZnO are also listed as a reference.....	109
TABLE 6-1. Performances and electron transport properties of the bare ZnO nanowire and the branched ZnO nanowire DSCs determined by photocurrent density-voltage (J-V) characteristics and electrochemical impedance spectroscopy (EIS) analysis.....	156
TABLE 6-2. Kinetic Parameters of the Indoline Dye Emission Decay Analysis....	167
TABLE 6-3. Performances and electron transport properties of the D149- and D205-sensitized DSCs (27 μ m-thick ZnO photoelectrode) determined by J-V characteristics and EIS analysis.....	175

List of Figures

Fig. 1-1. Stick-and-ball representations of ZnO crystal structures.....	2
Fig. 1-2. Primitive cell of the wurtzite-structure and schematic drawing of surfaces cut from a hexagonal single crystal with different surface planes.....	3
Fig. 1-3. Energy levels of native defects in ZnO.	7
Fig. 1-4. Density of states in different dimensional systems.	9
Fig. 2-1. Schematic illustration of vapor-solid growth mechanism.....	21
Fig. 2-2. In situ TEM images recorded during the process of nanowire growth.....	22
Fig. 2-3. A schematic diagram of the horizontal tube furnace for growth of ZnO nanostructures by the solid-vapor phase process.....	23
Fig. 2-4. Scanning electron microscope images of ZnO nanowire arrays grown on sapphire substrates.....	24
Fig. 2-5. Side-view SEM images of ordered ZnO nanorod arrays and hexagonally ordered ZnO nanorod arrays grown by the VLS method on patterned Au-covered GaN/Al ₂ O ₃ substrates.....	24
Fig. 2-6. A collection of nanostructures of ZnO synthesized under controlled conditions by thermal evaporation of solid powders.....	26
Fig. 2-7. SEM images of the 6-fold ZnO nanostructures.....	27
Fig. 2-8. ZnO nanorods grown using low-pressure MOVPE on Al ₂ O ₃ (0001) substrates.....	29
Fig. 2-9. FESEM image of 3-dimensional arrays of ZnO nanorods by using aqueous solution chemical method.....	31
Fig. 2-10. ZnO nanowire array on a four-inch (ca. 10 cm) silicon wafer and ZnO	

nanowire array on a two-inch (ca. 5 cm) PDMS substrate.....	32
Fig. 2-11. Micrograph of an anodic alumina membrane (AAM)	34
Fig. 2-12. Schematic of the routes that one could follow within the scope of sol-gel processing.....	37
Fig. 2-13. FESEM and HRTEM images of hierarchically ordered cone-shaped ZnO nanocrystals.	39
Fig. 2-14. TEM images of OA-stabilized cone-shaped ZnO nanocrystals.	39
Fig. 2-15. TEM images of ZnO nanoparticles obtained in the presence of various surfactants.....	40
Fig. 2-16. X-ray diffraction from 2-dimensional periodic lattices.....	41
Fig. 2-17. Instrumental setup for high-resolution x-ray rocking curve.....	43
Fig. 2-18. Three different concepts of excitons. Excitons (bounded electron-hole pairs) also can be viewed as the excited states of molecules.....	45
Fig. 2-19. A pair excitation in the scheme of valence and conduction band in the exciton picture for a direct gap semiconductor.....	46
Fig. 2-20. Visualization of an exciton bound to an ionized donor (D^+X), a neutral donor (D^0X), and a neutral acceptor (A^0X).....	48
Fig. 2-21. Displacement patterns of the optical phonons of a lattice with wurtzite crystal structure.....	51
Fig. 3-1. A schematic diagram of the experimental apparatus for growth of ZnO nanowires.....	56
Fig. 3-2. Raman detection systems. Light path for triple additive configuration.....	61
Fig. 4-1. Top- and oblique-view SEM photographs of the vertically well-aligned ZnO nanorods fabricated on the various substrates:.....	64

Fig. 4-2. Magnified top-view SEM photographs of the vertically well-aligned ZnO nanorods fabricated on the Si (111), and sapphire (0001) substrates.....	65
Fig. 4-3. The EBSD image taken from two different position of the ZnO nanorods on the Si (111) substrate.....	66
Fig. 4-4. The inverse pole figures of the ZnO nanorods on the Si (111) substrate for the three orthogonal directions.....	66
Fig. 4-5. The EBSD image taken from two different position of the ZnO nanorods on the sapphire (0001) substrate.....	67
Fig. 4-6. The inverse pole figures of the ZnO nanorods on the sapphire (0001) substrate for the three orthogonal directions.....	67
Fig. 4-7. Cross-sectional TEM images and the SAED images of ZnO nanorods grown on ZnO buffer layer.....	68
Fig. 4-8. θ -2 θ XRD profile of ZnO buffer layers on the various substrates.....	70
Fig. 4-9. X-ray Φ -scan profiles of ZnO (2022) plane from ZnO buffer layers on the various substrates.....	71
Fig. 4-10. Typical room-temperature photoluminescence (RTPL) spectra of ZnO nanorods on the various substrates.....	73
Fig. 4-11. SEM images of vertically well-aligned ZnO nanowires grown on GaN-buffered sapphire substrate.....	75
Fig. 4-12. TEM image of wurtzite structure ZnO nanowire and the corresponding electron diffraction pattern.....	77
Fig. 4-13. θ -2 θ XRD profile of ZnO nanowires on epi-GaN(001)/ α -Al ₂ O ₃ (001).....	78
Fig. 4-14. Reciprocal space map of asymmetric (20 $\bar{2}$ 4) diffraction spots of a ZnO nanowires and epi-GaN buffer layer.....	80

Fig. 4-15. Conventional Raman spectrum (using frequency-doubled Yb:YAG laser ($\lambda = 515$ nm)) and resonant Raman scatterings (RRS) (using a He–Cd laser ($\lambda = 325$ nm)) of ZnO nanowires on GaN buffer layer at room temperature.....	82
Fig. 4-16. Fitting profile of RRS spectrum and its decomposition.....	84
Fig. 4-17. Room-temperature and low temperature photoluminescence (PL) spectrum of ZnO nanowires on GaN buffer layer.....	86
Fig. 4-18. Dependence of integrated PL band intensity of 3.343 eV and 3.364 eV on excitation laser intensity at $T = 10$ K.....	87
Fig. 4-19. The SEM images of the ZnO nanowires and nanorods with different growth conditions.....	89
Fig. 4-20. The schematic growth procedure from the original ZnO nanowires to the branched ZnO nanowires and their corresponding FESEM images.....	91
Fig. 4-21. Low- and high-magnification FESEM images of the branched ZnO nanowires after second growth.....	92
Fig. 4-22. The cross section FESEM images of successful branched ZnO nanowires and failed branched ZnO nanowires.....	93
Fig. 4-23. TEM image of a single branched ZnO nanowire.....	94
Fig. 4-24. θ - 2θ XRD profiles and conventional Raman spectra of the branched ZnO nanowires.....	95
Fig. 5-1. Large and local scale of scanning electron micrographs of various aging time products synthesized using 10ml of primary supernatan.....	100
Fig. 5-2. Composition variation analysis by energy dispersive x-ray spectra (EDS) of different aging time products.....	100
Fig. 5-3. TEM images of secondary ZnO NPs recognized of crystalline subcrystals.....	102

Fig. 5-4. SEM micrographs of as-grown secondary ZnO NPs and after 1hour annealing at temperature 350°C and 500°C, respectively.....	103
Fig. 5-5. Normal Raman spectra of as-grown secondary ZnO NPs and after 1hour annealing at temperature 350°C and 500°C, respectively, using a frequency-doubled Yb:YAG laser (= 515 nm).....	105
Fig. 5-6. Resonant Raman scatterings (RRS) of as-grown secondary ZnO NPs and after 1hour annealing at temperature 350°C and 500°C, respectively, using a He–Cd laser (= 325 nm).....	107
Fig. 5-7. Normalized room-temperature PL spectra of the secondary ZnO NPs before and after heat treatment, respectively.....	111
Fig. 5-8. TEM image of the ZnO QDs fabricated using 0.06M precursor with the inset of its corresponding selected area electron diffraction (SAED) pattern...	113
Fig. 5-9. XRD profiles of the ZnO QDs prepared with various concentration of Zn(OAc) ₂	114
Fig. 5-10. Room temperature PL spectra and green emission of ZnO QDs with various sizes; and PL spectra of ZnO QDs (4.2 nm in diameter) as a function of laser power.....	116
Fig. 5-11. The dependence of the band gap enlargement versus the ZnO QDs diameter as calculated from the effective mass model.....	118
Fig. 5-12. Resonant Raman scatterings of ZnO QDs with various particle sizes measured at room temperature using a He–Cd laser ($\lambda = 325$ nm).....	120
Fig. 5-13. Ratio between the second- and the first-order Raman scattering cross section as a function of ZnO diameter.....	121
Fig. 6-1. Energy band diagram of a conventional <i>p-n</i> junction solar cell in the case of short circuit condition and charge separation under illuminations.....	131
Fig. 6-2. Scheme of the operational principle of the DSCs.	132

Fig. 6-3. Dynamics of different electron transfer processes in the conversion of light to electric power by a DSC.....	133
Fig. 6-4. Flow chart of device assembly.....	139
Fig. 6-5. Spectra of Black body 5250°C AM0 and AM1.5, respectively.....	141
Fig. 6-6. A typical $I-V$ curve in the experiment.....	143
Fig. 6-7. A simplified equivalent circuit for DSC.....	145
Fig. 6-8. Equivalent circuit model for DSCs using TiO ₂ photoanode.....	148
Fig. 6-9. Typical curves of impedance spectra for a DSC.....	150
Fig. 6-10. Current density against voltage (J-V) characteristics of the bare ZnO nanowires and the branched ZnO nanowire DSCs.....	153
Fig. 6-11. Nyquist plots and the fitting results of the bare ZnO nanowires and the branched ZnO nanowire DSCs.....	154
Fig. 6-12. The incident monochromatic photon to current conversion efficiency (IPCE) of the bare ZnO nanowire and the branched ZnO nanowire DSCs.....	157
Fig. 6-13. Optical absorption of dye detached from the bare ZnO nanowire and the branched ZnO nanowire substrates.....	158
Fig. 6-14. FESEM and TEM images for the self-assembled ZnO secondary nanoparticles and the schematic multiple scattering of light within the hierarchical ZnO photoelectrode composed by self-assembled ZnO secondary nanoparticles.....	160
Fig. 6-15. Diameter distribution for the ZnO secondary nanoparticles and the corresponding optical absorption spectra of ZnO photoelectrodes with various film thicknesses, from 2 μm to 12 μm.....	161
Fig. 6-16. Molecular structures of indoline D149 and D205 dyes.....	162

Fig. 6-17. Absorption and photoluminescence spectra of D149 and D205 dyes in tert-butyl alcohol/acetonitrile (1/1) solution and D149 and D205 dyes anchored on the 4 μ m-thick ZnO photoelectrodes.....	163
Fig. 6-18.(a) Photoluminescence decay of D149 and D205 dyes in tert-butyl alcohol/acetonitrile (1/1) solution and on ZnO photoelectrodes, respectively. (b) Schematic representation of the charge transfer of photo-excited indoline dyes anchored onto ZnO surfaces.....	166
Fig. 6-19. Photocurrent action spectra of ZnO DSCs constructed using D149 and D205, with different photoelectrode thicknesses.....	169
Fig. 6-20. Relationship between photovoltaic characteristics and photoelectrode thickness of ZnO DSCs. Red circles and blue squares represent D149- and D205-sensitized DSCs, respectively.....	171
Fig. 6-21. Photovoltaic characteristics and Nyquist plots of DSCs with 27 μ m-thick ZnO photoelectrodes and two different indoline dyes (D149 and D205).....	172
Fig. 6-22. The equivalent circuit model of ZnO DSCs composed with hierarchical nanoparticles.....	174
Fig. 6-23. The cell behaviors of D205-sensitized DSCs composed with 23 μ m-thick primary nanoparticles (via girding the secondary ZnO nanoparticles) with 4 μ m-thick commercial ZnO particles (Merck Ltd.) as a scattering layer on the top.....	177

Chapter 1 Introduction

1.1 General Properties of ZnO

1.1.1 Prelude

There has been a great deal of interest in zinc oxide (ZnO) semiconductor materials lately, as seen from a surge of a relevant number of publications. The interest in ZnO is fueled and fanned by its prospects in optoelectronics applications owing to its direct wide band gap ($E_g \sim 3.3$ eV at 300 K). Some optoelectronic applications of ZnO overlap with that of GaN, another wide-gap semiconductor ($E_g \sim 3.4$ eV at 300 K) which is widely used for production of green, blue-ultraviolet, and white light-emitting devices. However, ZnO has some advantages over GaN among which are the availability of fairly high-quality ZnO bulk single crystals and a large exciton binding energy (~ 60 meV, cf. ~ 25 meV for GaN). ZnO also has much simpler crystal-growth technology, resulting in a potentially lower cost for ZnO-based devices.

1.1.2 Crystal Structure

ZnO is an oxide of the group II metal zinc, and belongs to the $P6_3mc$ space group in the Hermann–Mauguin notation [1]. ZnO is on the borderline between a semiconductor and an ionic material. Under most growth conditions, ZnO is an *n*-type semiconductor, though *p*-type conductivity of ZnO has also been reported for growth under certain conditions [2, 3]. The crystal structures shared by ZnO are wurtzite, zinc blende, and rocksalt (or Rochelle salt) as schematically shown in Fig. 1-1. Under ambient conditions, the thermodynamically stable phase is that of wurtzite symmetry. The zinc blende ZnO structure can be stabilized only by growth on cubic substrates,

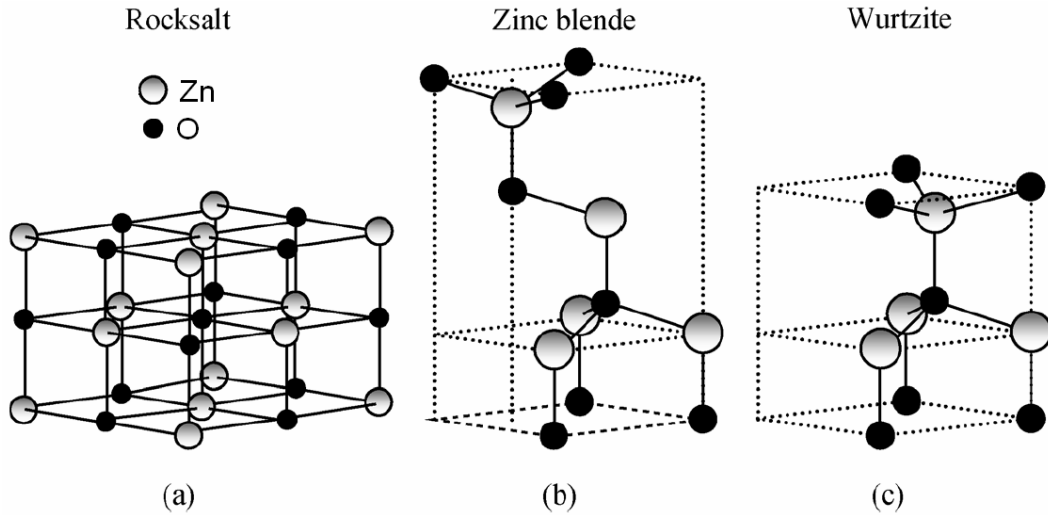


Figure 1-1. Stick-and-ball representations of ZnO crystal structures: (a) cubic rocksalt, (b) cubic zinc blende, and (c) hexagonal wurtzite. Shaded gray and black spheres denote Zn and O atoms, respectively.

and the rocksalt (NaCl) structure may be obtained at relatively high pressures. The wurzite crystal structure is shown in Fig. 1-2a. The lattice parameters of ZnO are $a = 0.32495$ nm and $c = 0.52069$ nm at 300K, with a c/a ratio of 1.602, which is close to the $c/a = \sqrt{8/3} = 1.633$ ratio of an ideal hexagonal close-packed (hcp) structure. In the direction parallel to the c -axis, the Zn-O distance is 0.1992 nm, and it is 0.1973 nm in all other three directions of the tetrahedral arrangement of the nearest neighbors. Even though it is tetrahedrally bonded, the bonds have a partial ionic character.

The lattice is composed of two interpenetrating hexagonal close-packed sublattices, each of which consists of one type of atom displaced with respect to each other along the threefold c -axis by the amount of $u = 0.3825$ ($u = 3/8 = 0.375$ for an ideal wurzite structure) in fractional coordinates. The internal parameter u is defined as the length of the bond parallel to the c -axis (anion-cation bond length or the nearest-neighbor distance) divided by the c lattice parameter. The wurzite-structure lattice is fourfold coordinated. That is, each atom has four nearest neighbor atoms. In a unit cell, zinc occupies the $(0, 0, 0.3825)$ and $(0.6667, 0.3333, 0.88255)$ positions

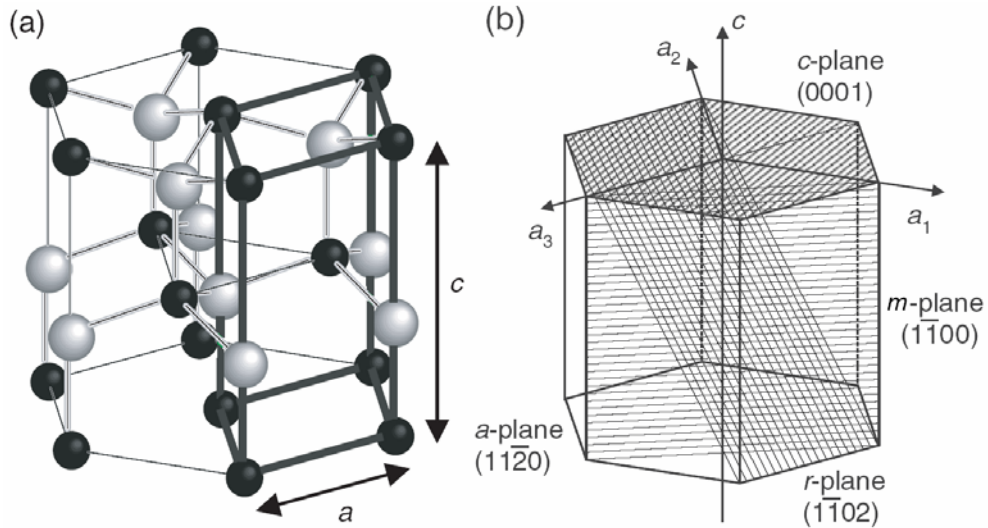


Figure 1-2. (a) Primitive cell (heavy lines) of the wurtzite-structure lattice placed within a hexagonal prism. a and c are the lattice constants. (b) Schematic drawing of surfaces cut from a hexagonal single crystal with different crystallographic orientations (surface planes).

and oxygen occupies the $(0, 0, 0)$ and $(0.6667, 0.3333, 0.5)$ positions [4, 5]. Figure 1-2(b) shows the cuts of different orientations of a hexagonal hcp structure.

The close-packed (0001) planes are made up of two subplanes (A and a), each consisting of either the cationic (Zn) or the anionic (O) species, respectively. The crystal can be considered to have the stacking sequence ...AaBaAaBb... as compared to ...AaBaCcAaBbCc... in diamond cubic silicon and sphalerite (GaAs). The result is a remarkable difference in the properties between (0001) and $(000\bar{1})$ planes of ZnO, the former being Zn terminated and the later being O terminated. This structure does not possess a center of symmetry. The lack of inversion symmetry in ZnO leads to piezoelectricity. The polarity of the c -axis results in the Zn-terminated and O-terminated planes displaying extremely different properties.

The (0001) planes in ZnO are polar and hence, with no reconstructure or passivation, have the maximum surface energy among the low-index planes. This is in fact observed under most conditions during vapor phase growth. Crystals grown via

the vapor phase usually are rod-shaped with hexagonal cross section. The crystals are elongated along [0001] direction and the prismatic sides of these crystals are usually the $\{10\bar{1}0\}$ or $\{11\bar{2}0\}$ planes, implying that the (0001) plane has the highest energy. As a result, the growth rate along the c -axis is the highest.

1.1.3 Optical Properties

Optical properties and processes in ZnO as well as its refractive index were extensively studied many decades ago. Compendiums dealing with optical properties of ZnO and to some extent its alloys from far infrared to vacuum ultraviolet including phonons, plasmons, dielectric constant, and refractive indices are available in the literatures [6, 7]. The renewed interest in ZnO is fuelled and fanned by prospects of its applications in optoelectronics owing to its direct wide band gap ($E_g \sim 3.3$ eV at 300 K), large exciton binding energy (~ 60 meV, Refs [8, 9]), and efficient radiative recombination. The large exciton binding energy paves the way for an intense near band-edge excitonic emission at room and even higher temperature, because this value is 2.4 times the room-temperature (RT) thermal energy ($k_B T = 25$ meV). Therefore, laser operation based on excitonic transitions, as opposed to electron-hole plasma, is expected. In this respect, there have also been a number of reports on laser emission from ZnO-based structures at room temperature and beyond. An appreciation of the potential of ZnO for optoelectronic applications can be obtained by examining Table 1-1, which compares the relevant material properties of ZnO with those of other wide band gap semiconductors.

The optical properties of a semiconductor have their genesis in both intrinsic and extrinsic effects. Intrinsic optical transitions take place between the electrons in the conduction band and the holes in the valence band, including excitonic effects caused

TABLE 1-1. An appreciation of the potential of ZnO for optoelectronic applications can be obtained by examining this table, which compares the relevant material properties of ZnO with those of other wide band gap semiconductors. [10]

Material	Crystal structure	Lattice constants		Band gap energy at RT	Cohesive energy	Melting point	Exciton binding energy	Dielectric constants	
		a (Å)	c (Å)	E_g (eV)	E_{coh} (eV)	T_m (K)	E_b (meV)	$\epsilon(0)$	$\epsilon(\infty)$
ZnO	Wurtzite	3.249	5.207	3.37	1.89	2248	60	8.75	3.75
ZnS	Wurtzite	3.823	6.261	3.8	1.59	2103	39	9.6	5.7
ZnSe	Zinc blende	5.668	...	2.70	1.29	1793	20	9.1	6.3
GaN	Wurtzite	3.189	5.185	3.39	2.24	1973	21	8.9	5.35
6H-SiC	Wurtzite	3.081	15.117	2.86(ind.)	3.17	>2100	...	9.66	6.52

by the Coulomb interaction. Excitons are classified into the free and bound excitons. In high-quality samples with low impurity concentration, the excited states of free excitons can also be observed in addition to their ground-state transitions. Extrinsic properties are related to dopants/impurities or point defects and complexes, which usually create electronic states in the band gap and therefore influence both optical absorption and emission processes. The electronic states of the bound excitons strongly depend on the semiconductor material, in particular the band structure. In theory, excitons could be bound to neutral or charged donors and acceptors. A basic assumption in the description of the principal bound exciton states for neutral donors and acceptors is a dominant coupling of the like particles in the bound exciton states. For a shallow neutral donor-bound exciton, for example, the two electrons in the bound exciton state are assumed to pair off into a two-electron state with zero spin. The additional hole is then weakly bound in the net hole-attractive Coulomb potential set up by this bound two-electron aggregate. Similarly, shallow neutral acceptor bound excitons are expected to have a two-hole state derived from the topmost valence band and one electron interaction. These two classes of bound excitons are by far the most important cases of extrinsic processes. Other extrinsic transitions could

be seen in optical spectra such as free-to-bound (electron-acceptor), bound-to-bound (donor-acceptor), and the so-called yellow/green luminescence. The mostly observed green emission in ZnO luminescence spectra (manifesting itself as a broad peak around 500–530 nm), observed nearly in all samples regardless of growth conditions, is related to singly ionized oxygen vacancies by some and to residual copper impurities by others. A requisite consensus on this issue is still lacking.

1.1.4 Defects in ZnO

Characteristically, defects represent one of the controversial areas of semiconductors, and ZnO is no exception, as the measurement techniques are not able to correlate electrical or optical manifestation of defects to their origin precisely. It is highly appropriate to say that the point defects in ZnO are not so well understood. While numerous assignments of the defect-related luminescence bands can be found in literature, only a few of them are trustworthy [11-13]. Over the years, oxygen vacancies were believed to be the dominant shallow donors in ZnO. Now it is becoming clear that these vacancies are formed in noticeable concentrations only after electron irradiation. As another vital misassignment till now, the green luminescence band in ZnO is commonly attributed to transitions from the oxygen vacancy (V_o) to the valence band. However, it is easy to show that such transition is highly unlikely in n-type ZnO. Problems in the identification of point defects are discussed from theoretical and experimental points of view in this section. It is also important to realize that ZnO is a relatively open structure, with a hexagonal close packed lattice where Zn atoms occupy half of the tetrahedral sites. All the octahedral sites are empty. Hence, there are plenty of sites for ZnO to accommodate intrinsic, namely Zn interstitials (Zn_i) defects and extrinsic dopants.

The electronic energy levels of native imperfections in ZnO are illustrated in Fig. 3. There are a number of intrinsic defects with different ionization energies. The Kröger Vink notation uses: i = interstitial site, Zn = zinc, O = oxygen and V = vacancy. The terms indicate the atomic sites, and superscripted terms indicate charges, where a dot indicates positive charge, a prime indicates negative charge, and a cross indicates zero charge, with the charges in proportion to the number of symbols. Figure 3 shows that there are a number of defect states within the bandgap of ZnO. The donor defects are: $Zn_i^{\bullet\bullet}$, Zn_i^\bullet , Zn_i^\times , $V_o^{\bullet\bullet}$, V_o^\bullet , V_o and the acceptor defects are: V_{Zn}'' , V_{Zn}' . The defect ionization energies vary from ~ 0.05 - 2.8 eV. Zn interstitials and oxygen vacancies are known to be the predominant ionic defect types. However, both defects donate two electrons and so it is difficult to distinguish one from the other using the electrical measurements. As a result which defect dominates in native, undoped ZnO is still a matter of great controversy.

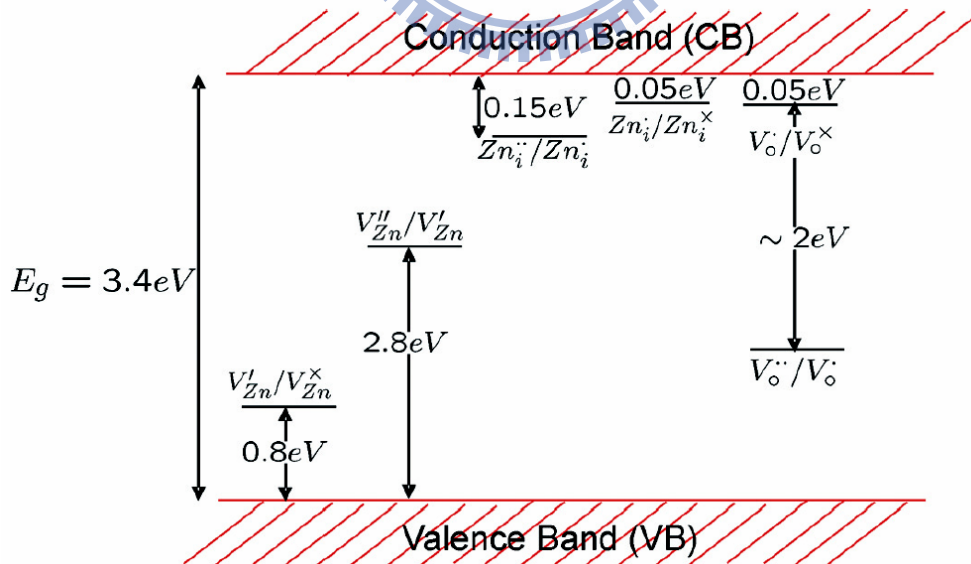


Figure 1-3. Energy levels of native defects in ZnO. [14]

TABLE 1-2. Physical Properties of wurtzite ZnO. [15]

Property	Value
Lattice parameters at 300 K	
a_0	0.32495 nm
c_0	0.52069 nm
a_0/c_0	1.602 (ideal hexagonal structure shows 1.633)
u	0.345
Density	5.606 g/cm ³
Stable phase at 300 K	Wurtzite
Melting point	1975 °C
Thermal conductivity	0.6, 1–1.2
Linear expansion coefficient(/°C)	a_0 : 6.5×10^{-6} c_0 : 3.0×10^{-6}
Static dielectric constant	8.656
Refractive index	2.008, 2.029
Energy gap	3.4 eV, direct
Intrinsic carrier concentration	$< 10^6$ cm ⁻³ (max n-type doping $> 10^{20}$ cm ⁻³ electrons; max p-type doping $< 10^{17}$ cm ⁻³ holes)
Exciton binding energy	60 meV
Electron effective mass	0.24
Electron Hall mobility at 300 K for low n-type conductivity	200 cm ² /V s
Hole effective mass	0.59
Hole Hall mobility at 300 K for low p-type conductivity	5–50 cm ² /V s

Table 1-2 shows a compilation of basic physical parameters for ZnO. It should be noted that there still exists uncertainty in some of these values. For example, there have few reports of *p*-type ZnO and therefore the hole mobility and effective mass are still in debate. Similarly, the values for thermal conductivity show some spread in values and this may be a result of the influence of defects such as dislocations. The values for carrier mobility will undoubtedly increase as more control is gained over compensation and defects in the material.

1.2 Low-Dimensional ZnO Nanostructures

1.2.1 General of Nanostructures

During the last decade, the growth of low-dimensional semiconductor structures has made it possible to reduce the dimension from three (bulk material) to the quasi-zero dimensional semiconductor structures. Generally, the crystal structure of a solid restricts the movement of carriers. In a semiconductor material, the outer electrons of the atoms are delocalized over the entire crystal, with the periodicity of the crystal structure limiting their movement. For certain electron energy, the carrier is allowed to move in one direction, but its motion in a different direction is restricted as a result of destructive interaction from the atomic lattice. This dependence of the electron energy on the momentum of the carrier results in a structure of energy bands where the carrier can exist. The electron energy of low-dimensional semiconductor structures becomes quantized and depends on the structural size. The band gap and density of states (DOS) associated with a quantum-structure differs from that associated with bulk material, determined from the magnitude of the three-dimension wave vector. Figure 1-4 illustrated the density of states in systems of differing dimensionality: bulk, quantum well, quantum wire, and quantum dot.

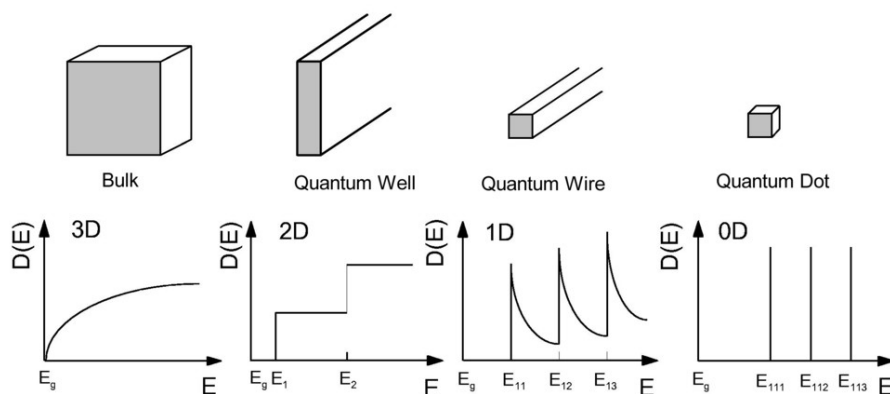


Figure 1-4. Density of states in different dimensional systems.

The degree of quantum confinement is determined by the interaction length over which the bond between an electron and a hole extends in an exciton, compared with the size of the materials. Take quantum dot for example, in weak quantum confinement, the interaction length is shorter than the dimensions of the quantum dot, resulting in very closely spaced quantum-confined energy states. In this case, the quantum dot seems more bulk-like because the electron and hole can separate beyond the exciton interaction length, thus breaking up the exciton and making the transition energy independent of the quantum dot size. In the strong quantum-confinement regime, the quantum dot size is smaller than the electron hole interaction length, resulting in widely spaced energy states. The quantum dot sizes can be so small that the energy spacing between the allowed states in the conduction and valence bands is large enough to cause a so-called phonon bottleneck.

In most semiconductors, excited electrons can relax down to the bottom of the conduction band by losing energy through carrier-carrier and carrier-phonon interactions. However, a phonon bottleneck occurs when the spacing between energy states is much larger than these interelectronic energies (as is the case in strong quantum confinement). In this case, the probability for a carrier in a higher energetic state to lose its energy to a lower energetic state through these interactions becomes very low. As a result, electrons cannot relax to the bottom of the conduction band, and so quantum dots with strong quantum confinement should not be expected to emit light from the normal transition across the band gap. However, this phonon bottleneck has been observed experimentally first in recent years. [16]

According to these above mentions, the quantum confinement effect come from nanostructures become predominant and give rise to many interesting electronic and optical properties.

1.2.2 One-Dimensional (1-D) ZnO Nanostructures

One-dimensional (1-D) nanostructures have attracted intensive attention because of their unique physical, optical and electrical properties resulting from their low dimensionality. The electron-hole interaction will have orders of magnitude enhancement in a nanostructure, due to the dramatically increased electron density of states near the van Hove singularity. ZnO has an effective electron mass of $\sim 0.24 m_e$, and a large exciton binding energy of 60 meV. Tremendous progress has been made to understand the quantum-size behavior and to investigate the size- and morphology-dependent properties. Compared with bulk ZnO, the reported 1-D ZnO nanowires or nanorods have the same lattice constant. However, the significant characteristics of 1-D ZnO nanostructures are their high surface-to-volume ratio and anisotropic carrier transport. With this respect great efforts and contribution from the fruitful group such as Yang's [17] and Wang's group [18] for ZnO nanostructures, have been made persistently to enrich the diversiform morphological world of nanostructures and show their possibilities for versatile utilizations, such as room temperature laser [19], waveguide [20] and piezoelectric nanogenerators [21, 22].

1-D ZnO nanowires and nanorods are also being intensively investigated because they possess a combination of attractively optical, electronic, mechanical, magnetic properties and so on. Extensively potential applications as light-emitting diodes [23, 24], UV photodetectors [25-27], field-effect transistors [28-31], field electron emitters [32-35] gas sensors [36-40], and solar cells [41-47] are continuously be evaluated. Moreover, the observations of quantum confinement [48] and the discrete energy levels [49] are demonstrated in ZnO/ZnMgO nanorod heterostructures. Therefore, the ZnO nanowires and nanorods have become one of the most promising elemental building blocks in nanotechnology applications. Other 1-D ZnO nanostructures such

as nanoneedle, nanopencil, nanobelt, nanotube, nanospiral, nanohelix, nanonail and dendritic nanowire have also been discovered [50, 51], but lack of applications at present merely interesting growth mechanisms have been emphatically demonstrated.

To date, most of the work on 1-D nanostructures ZnO has focused on the synthesis methods. For application of nano-photonics and electronics, it is needed to create ZnO nanowires that are selective area growth, highly aligned and orientation-ordered on substrates. The fundamental optical properties, including the origin of luminescence, carrier-carrier interaction, stimulated emission and lasing are also needed to understand. Furthermore, band-gap engineering, which is the process of controlling or altering the band gap, and fabrication of heterostructure or quantum-structures of ZnO-based nanowires and nanorods are important issues.

1.2.3 Zero-Dimensional (0-D) ZnO Nanostructures

Zero-dimensional (0-D) ZnO nanoparticles (NPs) or quantum dots (QDs) with several nanometers in diameter and large surface to volume ratio are becoming more and more attractive due to their quantum size effect and therefore unique properties different from the bulk ZnO materials. The physical properties in ZnO nanostructures changed dramatically as the diameter closes to the exciton Bohr radius (~ 2.43 nm) of bulk ZnO [52].

Accordingly, a great deal of attention has been paid to nanocrystalline materials for the study of the size-dependent quantum confinement effects. However, the ZnO nanocrystals have not been investigated as much as other semiconductor nanocrystals such as CdSe despite the possibility of UV/blue applications. The greater part of investigations for 0-D ZnO nanostructures focus on the fundamentally physical phenomena, such as band edge emission [53-59], phonon quantum confinement

[60-64], random Laser [65-67] and nonlinear susceptibility [68, 69].

Recently, several applications such as photocatalytic activity [70, 71] and cell labeling [72] have been reported owing to successfully faceted control and surface functionality of ZnO NPs and QDs, respectively. Organization of ZnO NPs and QDs building blocks into premeditated one- (1-D), two- (2-D), and three-dimensional (3-D) architectural systems should be considered as one of the key challenges in today's science and engineering.

1.3 Research Motivation

The synthesis of an array of well-aligned ZnO nanowires and nanorods is of great interest because it is an imperative step to realize nanophotonic devices, which include light-emitting diodes and laser diodes. Various methods have been reported for fabricating arrays of well-aligned 1-D ZnO nanostructures that include vapor transports and condensation methods, template methods, metal-organic source vapor deposition methods, and buffer layer pre-coated methods. The conductive ZnO buffer layer behaves as the active nucleus for growth of ZnO nanorods on different substrate and patterned area for selective growth of ZnO arrays. Accordingly, the buffer layer pre-coated method is a promising candidate for photonic device applications. In order to speed up the practical use of such ZnO nanorod arrays, studies on the growth behavior of vertically well-aligned ZnO nanorods on various substrates for different applications seem more and more imperative. Furthermore, chemical approaches towards such 1-D ZnO nanostructures would also be of interest since they are easy to perform and allow for a facile scale-up procedure. In this respect, a solution-based approach will also be attempted.

ZnO QDs and NPs also are of great interest because of the three-dimensional

confinement of carrier and phonon leads not only continuous tuning of the optoelectronic properties but also improvement in device performance. In this respect, optical properties examined from Raman scattering and photoluminescence (PL) of ZnO NPs with different particle sizes obtained via sol-gel method will be investigated. It is therefore important to realize the size-dependent quantum confinement effect and exciton-phonon interaction within the 0-D ZnO nanostructures from both the fundamental scientific research and photonic application points of view.

1.4 Organization of Dissertation

This dissertation is organized as follow. After Chapter of Introduction, Chapter 2 presents a brief review of growth and characterization techniques. The statement of experimental procedures for all ZnO nanostructures in my present work is illustrated in Chapter 3. The growth of the ZnO nanowires on various substrates via vapor-solid transport with pre-coated buffer layers is then demonstrated in Chapter 4. The structures and optical properties of well-aligned ZnO nanowires/nanorods on different substrate are compared. I also explain the growth mechanism and the epitaxial relationship between the 1-D ZnO nanostructures and the substrates. In Chapter 5, I describe self-assembled secondary ZnO nanoparticles (NPs), and size-controll ZnO quantum dots (QDs) synthesized by a simple sol-gel method. The coupling strength between electron and longitudinal optical phonon is carried out by resonant Raman spectroscopy (RRS). In Chapter 6, the dye-sensitized solar cells (DSC) with hierarchical architecture composed of various low-dimensional ZnO nanostructures are discussed.

Finally, in Chapter 7, I conclude the results and benefits on the low-dimensional ZnO nanostructures. The several issues for further works are also proposed.

References and Notes

- [1] Hadis Morkoç and Ümit Özgür “*Zinc Oxide: Fundamentals, Materials and Device Technology*” (Wiley-VCH Verlag GmbH & Co. KGaA, Weinheim, 2009).
- [2] K. Kim, H. Kim, D-K. Hwang, J-H. Lim and S-J. Park, *Appl. Phys. Lett.* 83, 63 (2003).
- [3] Y. R. Ryu, T. S. Lee and, H. W. White, *Appl. Phys. Lett.*, 83, 87 (2003).
- [4] W. B. Person, “*A handbook of Lattice Spacings and Structures of Metals and Alloys*”, Vol.2, (New York: Pergamon Press, 1967).
- [5] “*International Tables for X-Ray Crystallography*”, (The International Union of Crystallography, 1965).
- [6] C. Bundesmann, R. Schmidt-Grund, And M. Schubert, Far-infrared to vacuum-ultra-violet optical properties of ZnO: phonons, plasmons, dielectric constants, refractive indices, band-to-band transitions, and excitons, in *Transparent Conductive Zinc Oxide*, Springer Series in Materials Science, Vol. 104 (eds K. Ellmer, A. Klein and B. Rech). (Springer, Berlin, 2008).
- [7] C. Bundesmann, “*Phonons and plasmons in ZnO-based alloy and doped ZnO thin films studied by infrared spectroscopic ellipsometry and Raman scattering spectroscopy*”, Ph.D. thesis, Universität Leipzig, 2005 (Shaker, Aachen, 2006)
- [8] D.C. Look, *Mater. Sci. Eng. B*, 80, 381(2001).
- [9] Reynolds, D.C., Look, D.C., Jogai, B., Litton, C.W., Cantwell, G. and Harsch, W.C. *Phy. Rev. B* 60, 2340 (1999).
- [10] Y. F. Chen, D. M. Bagnall, H. J. Koh, K. T. Park, K. Hiraga , Z. Q. Zhu, T. Yao, *J. Appl. Phys.* 84 3912 (1998).
- [11] B. Lin, Z. Fu, Y. Jia, *Appl. Phys. Lett.* 79, 943 (2001).
- [12] K. H. Tam, C. K. Cheung, Y. H. Leung, A. B. Djurišić, C. C. Ling, C. D. Beling,

- S. Fung, W. M. Kwok, W. K. Chan, D. L. Phillips, L. Ding, and W. K. Ge, *J. Phys. Chem. B* 110, 20865 (2006).
- [13] P. Jiang, J. Zhou, H. F. Fang, C. Y. Wang, Z. L. Wang, and S. S. Xie, *Adv. Funct. Mater.* 17, 1303 (2007).
- [14] L. Schmidt-Mende and J. L. MacManus-Driscoll, *Materials Today*, 10 (11), 40 (2007).
- [15] S. J. Pearton, D. P. Norton, K. Ip, Y. W. Heo, and T. Steiner., *Prog. Mater. Sci.* 50, 293 (2005).
- [16] J. Urayama, T. B. Norris, J. Singh and P. Bhattacharya, *Phys. Rev. Lett.* 86, 4930 (2001).
- [17] M. H. Huang, S. Mao, H. Feick, H. Yun, Y. Wu, H. Kind, E. Weber, R. Russo, and P. D. Yang. *Science* 292, 1897 (2001).
- [18] Z. W. Pan, Z. R. Dai, and Z. L. Wang, *Science* 291, 1947 (2001).
- [19] P. Yang, H. Yan, S. Mao, R. Russo, J. Johnson, R. Saykally, N. Morris, J. Pham, R. He, and H.-J Choi, *Adv. Funct. Mater.* 12, 323 (2002).
- [20] J. C. Johnson, H. Yan, P. Yang, and R. J. Saykally, *J. Phys. Chem. B* 107, 8816 (2003).
- [21] Z. L. Wang and J. Song, *Science* 312, 242 (2006).
- [22] Y. Qin, X. Wang and Z. L. Wang, *Nature* 451, 809 (2008).
- [23] Y. C. Kong, D. P. Yu, B. Zhang, W. Fang, and S. Q. Feng, *Appl. Phys. Lett.* 78, 407 (2001).
- [24] C. H. Liu, J. A. Zapien, Y. Yao, X. M. Meng, C. S. Lee, S. S. Fan, Y. Lifshitz, and S. T. Lee, *Adv. Mater.* 15, 838 (2003).
- [25] H. Kind, H. Yan, B. Messer, M. Law, and P. Yang, *Adv. Mater.* 14, 158 (2002).
- [26] C. Soci, A. Zhang, B. Xiang, S. A. Dayeh, D. P. R. Aplin, J. Park, X. Y. Bao, Y. H.

- Lo, and D. Wang, *Nano Lett.* 7, 1003 (2007).
- [27] L. W. Ji, S. M. Peng, Y. K. Su, S. J. Young, C. Z. Wu, and W. B. Cheng, *Appl. Phys. Lett.* 94, 203106 (2009).
- [28] J. Goldberger, D. J. Sirbuly, M. Law, and P. Yang, *J. Phys. Chem. B* 109, 9 (2005).
- [29] Z. Fan and J. G. Lu, *Appl. Phys. Lett.* 86, 032111 (2005).
- [30] J. I. Sohn, S. S. Choi, S. M. Morris, J. S. Bendall, H. J. Coles, W-K. Hong, G. Jo, T. Lee, and M. E. Welland, *Nano Lett.* 10, 4316 (2010).
- [31] H. T. Ng, J. Han, T. Yamada, P. Nguyen, Y. P. Chen, M. Meyyappan, *Nano Lett.* 4, 1247 (2004).
- [32] C. J. Lee, T. J. Lee, S.C. Lyu, Y. Zhang, H. Ruh, H. J. Lee, *Appl. Phys. Lett.* 81, 3648 (2002).
- [33] Y. W. Zhu, H. Z. Zhang, X. C. Sun, S. Q. Feng, J. Xu, Q. Zhao, B. Xiang, R. M. Wang, D. P. Yu, *Appl. Phys. Lett.* 83, 144 (2003).
- [34] Y. K. Tseng, C. J. Huang, H. M. Cheng, I. N. Lin, K. S. Liu, I. C. Chen, *Adv. Fun. Mater.* 13 811 (2003).
- [35] S. Y. Li, P. Lin, C. Y. Lee, T. Y. Tseng, *J. Appl. Phys.* 95, 3711 (2004).
- [36] Z. Fan, D. Wang, P. Chang, W. Tseng, and J. G. Lu, *Appl. Phys. Lett.* 85, 5923 (2004).
- [37] Z. Fan and J. G. Lu, *Appl. Phys. Lett.* 86, 123510 (2005)
- [38] H. T. Wang, B. S. Kang, F. Ren, L. C. Tien, P. W. Sadik, D. P. Norton, S. J. Pearton, and J. Lin, *Appl. Phys. Lett.* 86, 243503 (2005).
- [39] B.S. Kang, Y.W. Heo, C. Tien, D.P. Norton, F. Ren, B.P. Gila, S.J. Pearton, *Appl. Phys. A* 80 1029 (2005).
- [40] C. H. Wang, X.F. Chu, M. M.Wu, , *Sens. Actuators B* 113 320 (2006).

- [41] M. Law, L. E. Greene, J. C. Johnson, R. Saykally, and P. D. Yang, *Nat. Mater.* 4 455 (2005).
- [42] J. B. Baxter and E. S. Aydil, *Appl. Phys. Lett.* 86, 053114 (2005).
- [43] A. D. Pasquier, H. Chen, and Y. Lu, *Appl. Phys. Lett.* 89, 253513 (2006).
- [44] J. J. Wu, G. R. Chen, H. H. Yang, C. H. Ku, and J. Y. Lai, *Appl. Phys. Lett.* 90, 213109 (2007).
- [45] Y. F. Hsu,¹ Y. Y. Xi,¹ A. B. Djurišić,^{1,a} and W. K. Chan, *Appl. Phys. Lett.* 92, 133507 (2008).
- [46] Y. Y. Lin, Y. Y. Lee, L. Chang, J. J. Wu, and C. W. Chen, *Appl. Phys. Lett.* 94, 063308 (2009).
- [47] A. L. Briseno, T. W. Holcombe, A. I. Boukai, E. C. Garnett, S. W. Shelton, J. J. M. Fréchet, and P. Yang, *Nano Lett.* 10, 334 (2010).
- [48] W. I. Park, G. C. Yi, M. Kim, S. J. Pennycook, *Adv. Mater.* 15, 526 (2003).
- [49] T. Yatsui, J. Lim, M. Ohtsu, S. J. An, G. C. Yi, *Appl. Phys. Lett.* 85, 727 (2004).
- [50] Z. L. Wang, *J. Phys.: Condens. Matter* 16 R829 (2004).
- [51] Z. L. Wang, *Materials Today*, 7 (6), 26 (2004).
- [52] R. T. Senger, and K. K. Bajaj, *Phys. Rev. B* 68, 045313 (2003).
- [53] D. W. Bahnemann, C. Kormann, and M. R. Hoffmann, *J. Phys. Chem.* 91 3789 (1987).
- [54] L. Guo, S. Yang, C. Yang, P. Yu, J. Wang, W. Ge, G. K. L. Wong, *Appl. Phys. Lett.* 76 2901 (2000).
- [55] E. A. Meulenkaamp, *J. Phys. Chem. B* 102 5566 (1998).
- [56] E. M. Wong, J. E. Bonevich, P. C. Searson, *J. Phys. Chem. B* 102 7770 (1998).
- [57] S. Sakohara, M. Ishida, M. A. Anderson *J. Phys. Chem. B* 102 10169 (1998).
- [58] S. Mahamuni, K. Borgohain, B. S. Bendre, V. J. Leppert, S. H. Risbud, *J. Appl.*

- Phys.* 85 2861 (1999).
- [59] H. Zhou, H. Alves, D. M. Hofmann, W. Kriegseis, B. K. Meyer, G. Kaczmarczyk, A. Hoffmann, *Appl. Phys. Lett.* 80 210 (2002).
- [60] V. A. Fonoberov, and A. Balandin, *Appl. Phys. Lett.* 85, 5971 (2004).
- [61] V. A. Fonoberov, and A. Balandin, *Phys. Rev. B* 70, 195410 (2004).
- [62] K. A. Alim, V. A. Fonoberov, and A. Balandin, *Appl. Phys. Lett.* 86, 053103 (2005).
- [63] K. A. Alim, V. A. Fonoberov, M. Shamsa, and A. Balandin, *J. Appl. Phys.* 97, 124313 (2005).
- [64] V. A. Fonoberov, K. A. Alim, and A. Balandin, *Phys. Rev. B* 73, 165317 (2006).
- [65] H. Cao, Y.G. Zhao, H. C. Ong, S. T. Ho, J. Y. Dai, J. Y. Wu, and R.P.H. Chang, *Appl. Phys. Lett.* 73, 3656 (1998).
- [66] H. Cao, Y.G. Zhao, S. T. Ho, E. W. Seelig, Q. H. Wang, R. P. H. Chang, *Phys. Rev. Lett.* 82, 2278 (1999).
- [67] X. Wu, A. Yamilov, H. Noh, H. Cao, E. W. Seelig, R. P. H. Chang, *J. Opt. Soc. Am. B* 21, 159 (2004).
- [68] L. Guo, S. Yang, C. Yang, P. Yu, J. Wang, W. Ge, G. K. L. Wong, *Appl. Phys. Lett.* 76 2901 (2000).
- [69] Y. Zhu, H. I. Elim, Y. L. Foo, T. Yu, Y. Liu, W. Ji, J. Y. Lee, Z. Shen, Andrew T. S. Wee, J. T. L. Thong, and C. H. Sow, *Adv. Mater.* 18 587 (2006).
- [70] A. McLaren, T. Valdes-Solis, G. Li, and S. C. Tsang, *J. AM. CHEM. SOC.* 131, 12540 (2009).
- [71] L. Zhang, L. Yin, C. Wang, N. Lun and Y. Qi, *ACS Appl. Mater. Interface* 2 1769 (2010).
- [72] X. Tang, E. Choo, L. Li, J. Ding, and J. Xue, *Chem. Mater.* 22, 3383 (2010).

Chapter 2 A Review of Growth and Characterization Techniques

2.1 Growth Methods

2.1.1 Growth of 1-D ZnO Nanowires/ Nanorods

Vapor-Liquid-Solid (VLS) Method. Among all vapor based methods, the VLS method, which is a growth mechanism based on chemical vapor transport, seems to be the most successful for fabricating nanowires with single crystalline structures and in relatively large quantities. This process was first developed by Wagner et al. to produce Si single crystalline micro-whiskers in 1960s [1], and recently re-examined successfully by Lieber [2] and Yang [3]. The key factor is needed to deposit metal clusters such as Fe, Co, Ni, Cu, Sn and Au as the catalysts. A typical VLS process starts with the dissolution of gaseous reactants into nano-sized liquid droplets of catalyst metal while the liquid droplets are supersaturated with the guest material, followed by nucleation and growth of single crystalline nanorods and then nanowires. The 1D growth is mainly induced and dictated by the liquid droplets, whose size remains essentially unchanged during the entire process of nanowire growth. In the sense, each of liquid droplets serves as a soft template to strictly limit the lateral growth of an individual nanowire. As a major requirement, there should exist a good solvent capable of forming liquid alloy with the target material, ideally they should be able to form eutectic compounds. All of the major steps involved in a VLS process for a Ge nanowire case are schematically illustrated in Fig. 2-1 [3]. In the beginning Ge and Au form liquid alloys when the temperature is raised above the eutectic point. Once the liquid droplet is supersaturated with Ge, growth of nanowire takes place at the solid-liquid interface. The vapor pressure of Ge in the chemical-vapor-deposition

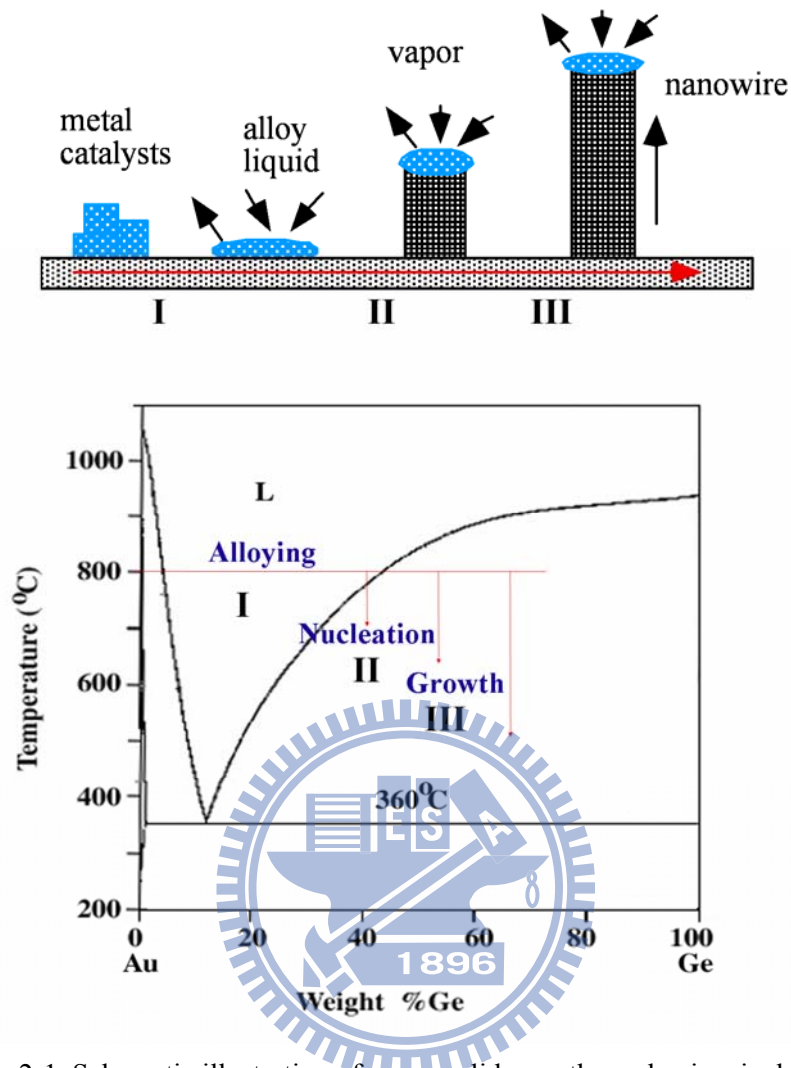


Figure 2-1. Schematic illustration of vapor-solid growth mechanism including three stages (I) alloying, (II) nucleation and (III) axial growth. Three stages are projected onto the conventional Au-Ge phase diagram; (b) shows the compositional and phase evolution during the nanowire growth process. [3]

system has to be kept sufficiently low so that the second ordinary nucleation will be completely suppressed. Figure 2-2 shows a sequence of real-time TEM images during the growth of a Ge nanowire.

Both physical methods (thermal evaporation and laser ablation) and chemical methods (chemical vapor transport and deposition) have been employed to generate the vapor species required for the growth of nanowires, and no significant difference was found in the quality of nanowires produced by these methods.

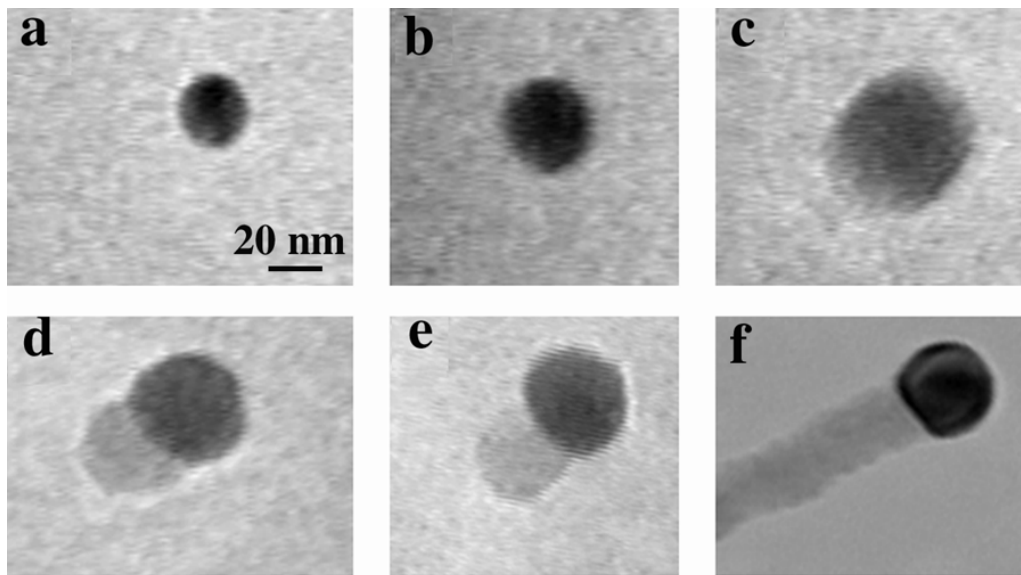


Figure 2-2. In situ TEM images recorded during the process of nanowire growth. (a) Au nanoclusters in solid state at 500 °C; (b) alloying initiated at 800 °C, at this stage Au exists mostly in solid state; (c) liquid Au/Ge alloy; (d) the nucleation of Ge nanocrystal on the alloy surface; (e) Ge nanocrystal elongates with further Ge condensation and eventually forms a wire (f). [3]

The VLS processes are usually carried out in a horizontal tube furnace, as shown in Fig. 2-3. In this schematic, the carrier gas, Ar, is introduced from the left end of the alumina tube and is pumped out from the right end. The source material is loaded on an alumina boat and positioned at the center of the highest temperature zone in the alumina tube. The substrate temperature usually drops with the distance from the position of the source material(s). The local temperature where the substrate is situated (usually 500-700 °C) determines the type of product that will be obtained. To reduce the decomposition temperature, ZnO powder is usually mixed with graphite powder to form the source mixture. At temperatures 800-1100 °C, graphite reacts with ZnO to form Zn, CO, and CO₂ vapors, which then react on the substrate to form ZnO nanostructures.

Self-organized [0001]-oriented ZnO nanowires have been successfully synthesized on sapphire substrates with a Au-catalyzed VLS process by Yang's group

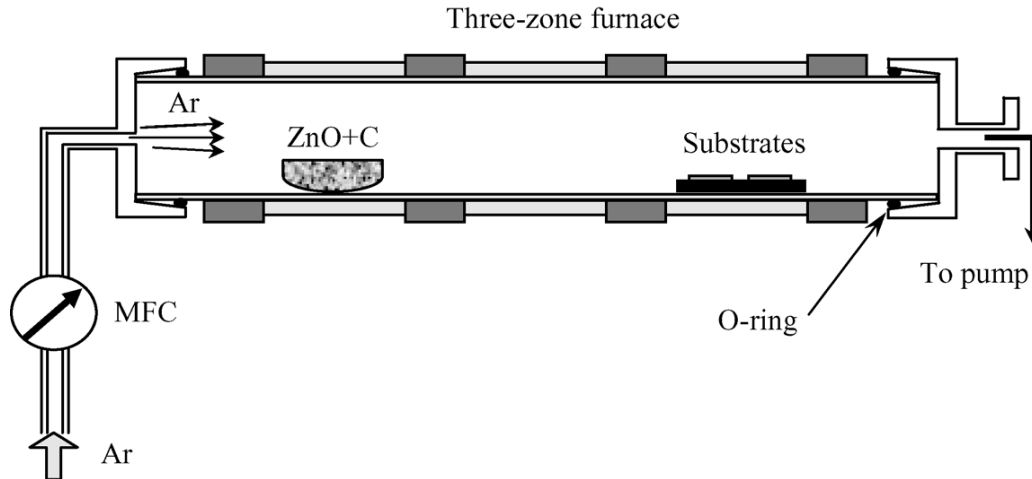


Figure 2-3. A schematic diagram of the horizontal tube furnace for growth of ZnO nanostructures by the solid-vapor phase process.

[4]. As mentioned above, selective nanowire growth could be readily achieved by patterning the Au thin film before growth. Typical scanning electron microscope (SEM) images of nanowire arrays grown on *a*-plane sapphire ($11\bar{2}0$) substrates with patterned Au thin film are presented in Fig. 2-4. By adjusting the growth time, nanowires could be grown up to 10 mm in length. The diameters of these wires range from 20 to 150 nm, although more than 95% of them have diameters between 70 and 100 nm.

Klingshirn's group also identified well-defined lasing modes under optical excitation of ZnO nanorods grown in a similar fashion using catalyst-assisted VLS technique by employing self-organized polystyrene spheres on GaN substrates as a mask during Au evaporation [5]. Ordered arrays of [0001]-oriented ZnO nanorods with 200 nm diameter and 4.7 mm length were obtained with 500 nm rod-to-rod spacing as shown in Fig. 2-5. As alluded earlier, well-aligned ZnO nanorods provide a perfect gain medium as well as act as waveguides and Fabry-Perot resonators with well-defined cavity ends.

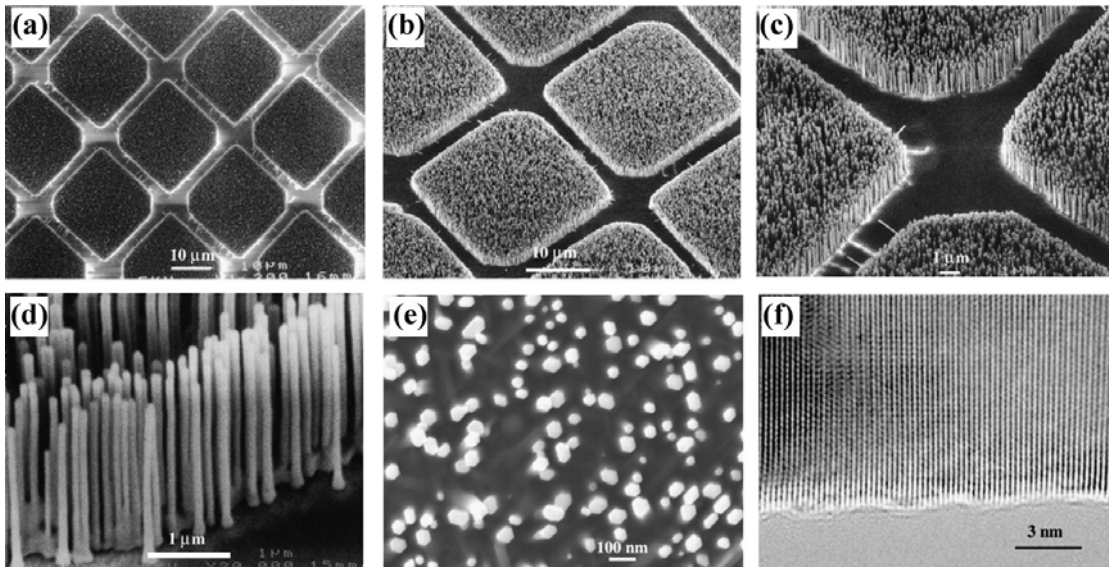


Figure 2-4. Scanning electron microscope images of ZnO nanowire arrays grown on sapphire substrates (a–e). A top view of the well-faceted hexagonal nanowire tips is shown in (e). (f) High-resolution TEM image of an individual ZnO nanowire showing its [0001] growth direction.

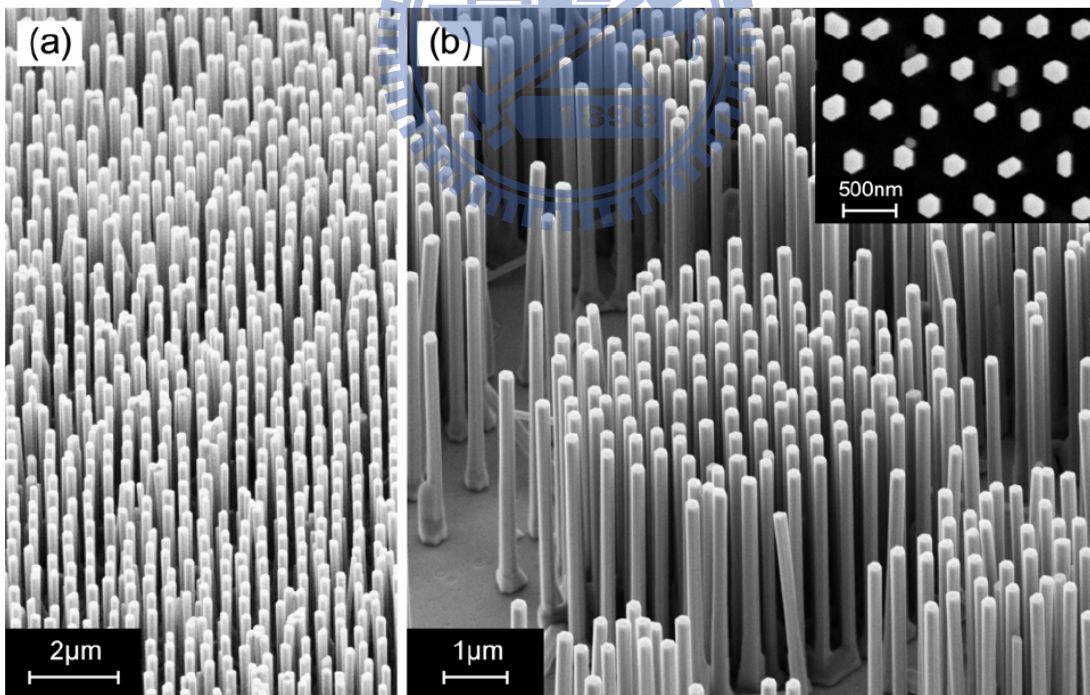


Figure 2-5. (a) 45° side-view SEM images of ordered ZnO nanorod arrays and (b) hexagonally ordered ZnO nanorod arrays grown by the VLS method on patterned Au-covered GaN/Al₂O₃ substrates. The inset is the top view of the nanorod arrays.

Vapor-Solid (VS) Method. The vapor-solid (VS) method is another chemical vapor transport mechanism compared with VLS, depending on the presence of a metal catalyst. VS growth also holds for the growth of 1D ZnO nanomaterials. In this process, evaporation, chemical reduction or gaseous reaction first generates the vapor. The vapor is subsequently transported and condensed onto a substrate. The VS method has been used to prepare whiskers of oxide, therefore, possible to synthesize the 1D nanostructures if one can control the nucleation and the subsequent growth process. According to the difference on nanostructure formation mechanisms, the extensively used vapor transport process can be categorized into the catalyst free VS process and catalyst assisted VLS process. Synthesis utilizing VS process is usually capable of producing a rich variety of nanostructures, including nanowires, nanorods, nanobelts, nanohelix and other complex structures.[6-7]

Using a solid state thermal sublimation process and controlling the growth kinetics (VS growth mechanism), local growth temperature, and the chemical composition of the source materials, a wide range of nanostructures of ZnO have been synthesized by Wang's group, as shown in Fig. 2-6 [7]. The two important characteristics of the wurtzite structure are the noncentral symmetry and polar surfaces. The structure of ZnO, for example, can be described as a number of alternating planes composed of tetrahedrally coordinated O^{2-} and Zn^{2+} ions, stacked alternately along the c -axis. The oppositely charged ions produce positively charged (0001)-Zn and negatively charged (000 $\bar{1}$)-O polar surfaces, resulting in a normal dipole moment and spontaneous polarization along the c -axis, as well as a divergence in surface energy. As a result, the formation of a self-coiled, coaxial, multilooped nanoring structure is spontaneous, which means that the self-coiling along the rim proceeds as the nanobelt grows under the driving force of stacking the polar surfaces.

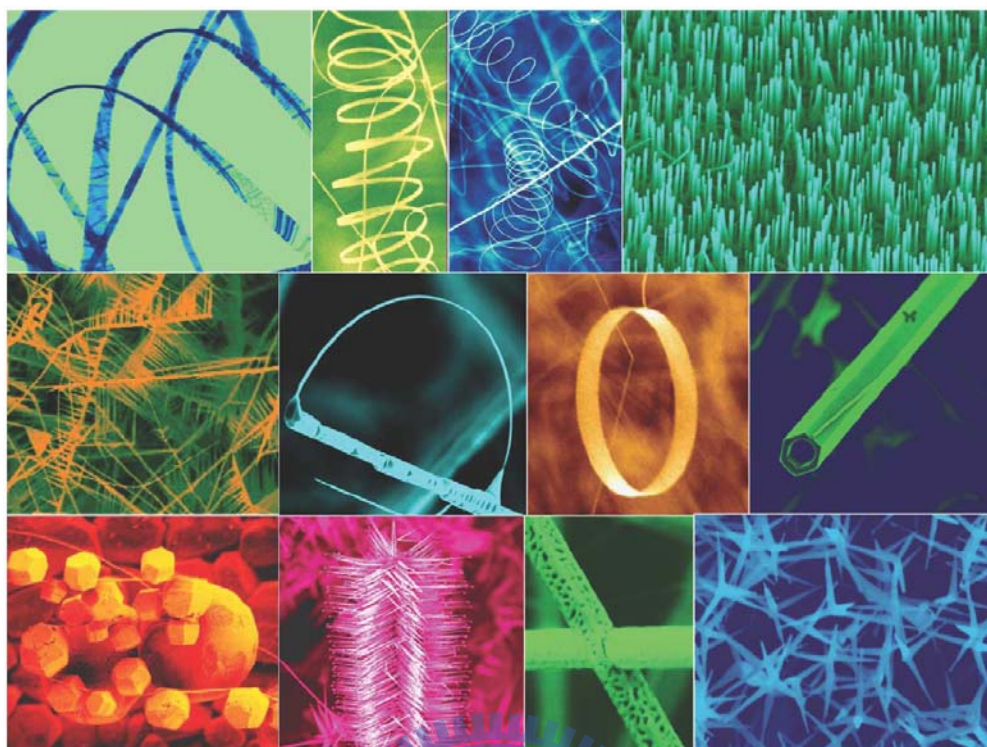


Figure 2-6. A collection of nanostructures of ZnO synthesized under controlled conditions by thermal evaporation of solid powders. [7]

A variety of novel hierarchical nanostructures with 6-, 4-, and 2-fold symmetries have been successfully grown by a vapor transport and condensation technique from Ren's group, as shown in Fig. 2-7 [8]. It was found that the major core nanowires are single-crystal In_2O_3 with 6, 4, and 2 facets, and the secondary nanorods are single-crystal hexagonal ZnO and grow either perpendicular on or slanted to all the facets of the core In_2O_3 nanowires. Because no catalyst is used in the system, the In_2O_3 nanowire growth should be based on the vapor-solid mechanism. On the other hand, it is more difficult to define the ZnO nanorod growth mechanism. Probably ZnO nanorods also grow based on the vapor-solid mechanism because the In_2O_3 core is covered by a ZnO layer that can be the base for further ZnO nanorod growth. Compared to the aligned ZnO grown by the vapor-liquid-solid mechanism [4] with source temperature around 900 °C, the metal and/or metal oxide vapor pressure here

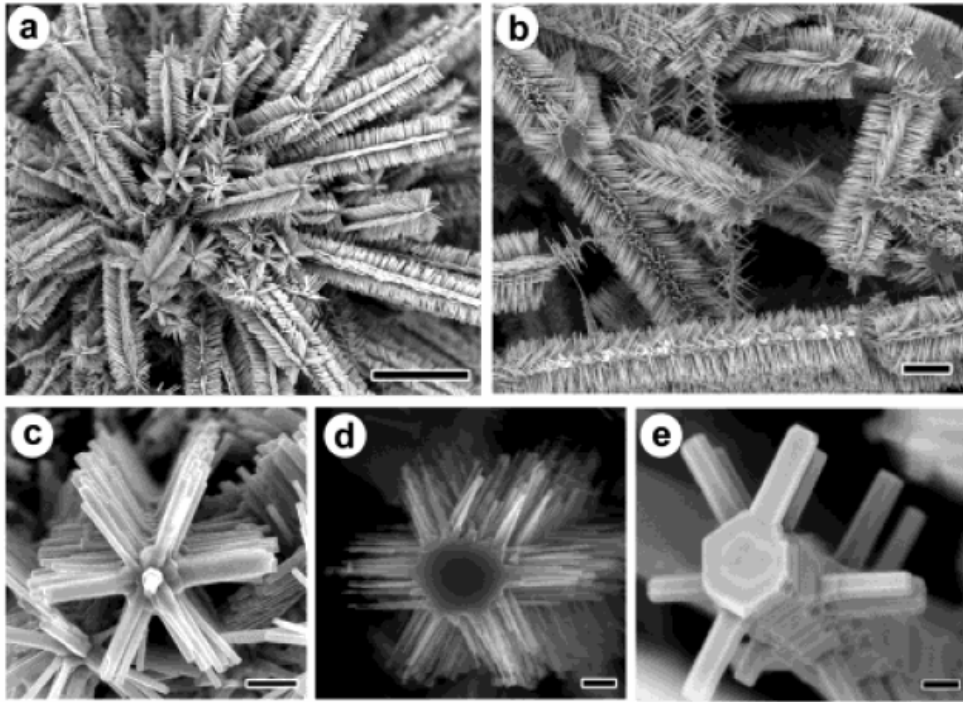


Figure 2-7. SEM images of the 6-fold ZnO nanostructures. (a) SEM image showing the abundance of the 6S-fold symmetry. Scale bar, 10 μm . (b) SEM image showing the 6M-fold symmetry. (c) High magnification SEM image of the 6S-fold symmetry. (d) High magnification SEM image of the 6M-fold symmetry. (e) Head on look at a 6S-fold symmetry to show the hexagonal nature of the major core nanowire. [8]

is much higher. This high vapor pressure is necessary for the growth of the hierarchical structures. The growth conditions such as temperature, pressure, and source component ratios are correlated to affect the supersaturation rate and the structure formed.

Metal-Organic Chemical Vapor Deposition (MOCVD) Method. For device fabrication, heteroepitaxial growth with control over impurities and thickness down to nanometer scale is required. VLS method is limited and cannot completely meet these requirements. Growth of complex structures for device applications can only be accomplished by advanced epitaxial methods such as metal-organic chemical vapor deposition (MOCVD) or metal-organic vapor phase epitaxy (MOVPE) and molecular

beam epitaxy (MBE). Particularly, MOCVD has been proven to be a powerful technique for large-scale production with accurate control over doping and thickness.

For MOCVD growth of ZnO nanorods, usually diethylzinc and oxygen are employed as the reactants and argon as the carrier gas [9]. N₂O as the oxygen source and nitrogen as the carrier gas have also been used [10]. Typical growth temperatures range from 400 to 1050 °C. The growth occurs without a catalyst, and flat terraces and steps are observed at the nanorod tips resulting from the layer-by-layer growth mode, instead of the metallic nanoparticles characteristic to catalyst-assisted VLS processes.

Figure 2-8 shows ZnO nanorods grown by Park et al. [9] using low-pressure MOVPE on Al₂O₃ (0001) substrates at 400 °C without any metal catalysts. Very thin ZnO buffer layers were deposited at a low temperature before the nanorod growth. The mean diameter of nanorods obtained by MOVPE was as small as 25 nm, smaller than the typical diameters of 50-100nm for those prepared by other deposition methods [4]. Furthermore, ZnO nanorods were well aligned vertically, showing uniformity in their diameters, lengths, and densities as revealed from electron microscopy. These ZnO nanorods were epitaxially grown with homogeneous in-plane alignment as well as *c*-axis orientation. The room-temperature PL spectra of the nanorods showed strong and narrow excitonic emission with a dominant peak at 3.29 eV and an extremely weak deep level emission at 2.5 eV, indicating the high optical quality of the nanorods. Free exciton emission lines were still clearly visible at 10 K, and no quantum confinement effect was evident for the nanorods with diameters exceeding 20nm [11].

For ZnO nanorods grown at relatively higher temperatures (700-1050 °C), vertical alignment of the *c*-axis-oriented nanorods was observed only on *a*-plane sapphire substrates, whereas the use of *c*-plane sapphire, Si (111), SrTiO₃ (100), and

SrTiO₃ (111) substrates resulted in rather random alignment [10]. To test the possibility of a catalyst-assisted process, nanorods were also grown on *a*-plane sapphire substrates partially coated with a thin (1-3 nm) gold layer. Close to 100% vertical orientation of ZnO nanorods with a diameter of 50±5nm and a length of several micrometers was observed in areas without gold metallization, while growth with no preferential direction occurred in the areas coated with gold, demonstrating that MOVPE growth of ZnO nanorods is different from the VLS process.

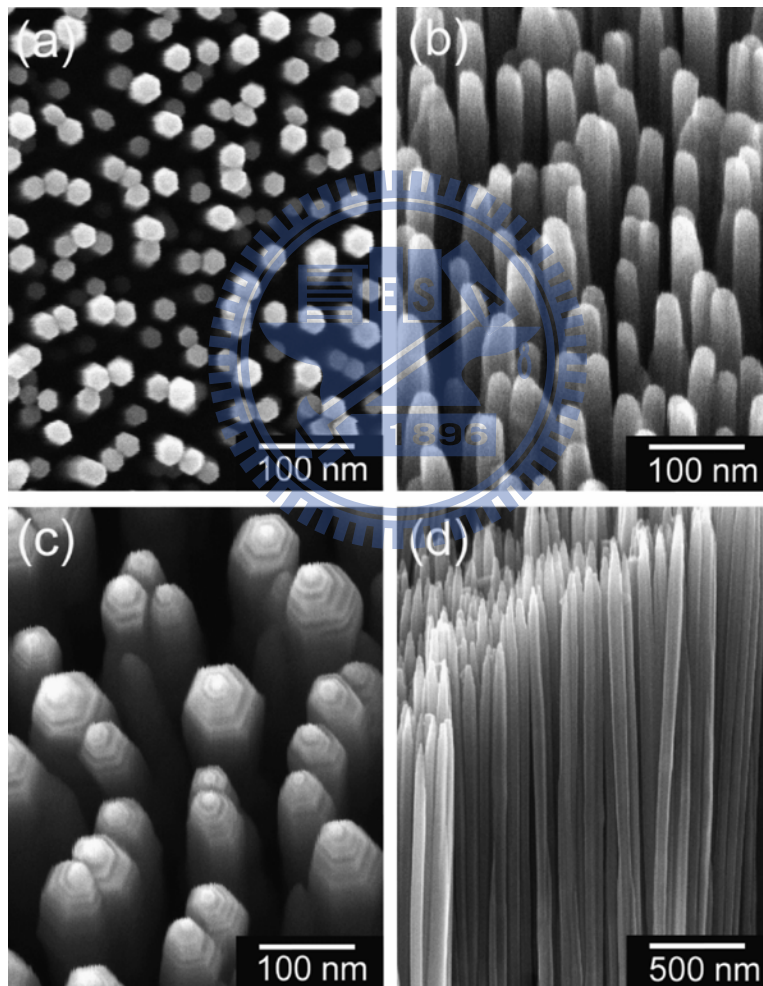
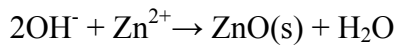
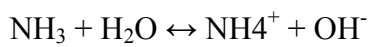
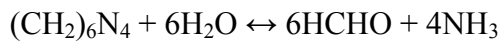


Figure 2-8. (a) plan-view and (b) tilted images of ZnO nanorods with a mean diameter of 25nm and (c) tilted and (d) cross-sectional images of ZnO nanorods with a mean diameter of 70 nm. In (c), hexagon-shaped pyramids with flat terraces and steps are seen at the ends of the nanorods. [9]

Li et al. [12] prepared ZnO nanoneedles on silicon through chemical vapor deposition. The diameters of the needle tips were in the range of 20-50 nm. High-resolution transmission electron microscopy revealed that the nanoneedles were single crystals along the [0001] direction. They exhibited multiple tip surface perturbations, and were just 1-3nm in dimension. Field emission measurements showed fairly low turn-on and threshold fields of 2.5 and 4.0 V mm⁻¹, respectively. The nanosize perturbations on the nanoneedle tips have been assumed to be the cause for such excellent field emission performance. High emission current density, high stability, and low turn-on field make ZnO nanoneedle arrays one of the promising candidates for high brightness field emission electron sources and flat panel displays. Lee [13] and Wu [14] also successfully demonstrated the ZnO nanorods directly on GaAs and fused silica substrates via MOCVD, respectively. Hence, MOCVD is one of the candidates to grown high-density and well-ordered 1-D ZnO nanostructures for practical applications toward manufacturability.

Aqueous Solution-Based Method. For cost-effective growth of ZnO nanostructures, many groups have reported the growth of highly oriented ZnO nanowires and other nanostructures by using aqueous solution methodology. On the other hand, the control of morphology and the positioning of the nanostructures using these techniques are challenging. Solvothermal is extensively employed as a solution route to produce semiconductor nanowires and nanorods. In this process, a solvent is mixed with metal precursors and crystal growth regulating or templating agents, such as amines. This solution mixture is placed in an autoclave maintained at relatively high temperatures and pressures to carry out the crystal growth and the assembly process. The methodology is quite versatile and has enabled the synthesis of

crystalline nanowires of semiconductors and other materials. Andrés-Vergés et al. [15] reported the solvothermal growth method for the first time in 1990. More than 10 years later, Vayssieres et al. [16] used this method to grow nanorods on conducting glass and Si substrates. For this type of growth, a ZnO seed layer is needed to initialize the uniform growth of oriented nanowires. Often, a solution of $\text{ZnO}(\text{NO}_3)_2$ (or other Zinc salt) mixed with hexamethyltetramine (HMT) is used:



Hydroxide ions are formed by the decomposition of HMT and they react with the Zn^{2+} to form ZnO. Figure 2-9 shows some typical nanowire arrays grown using this method. For technical applications, it is important to note that this method operates at low temperature and a homogenous coverage of nanowires can be achieved over large areas.

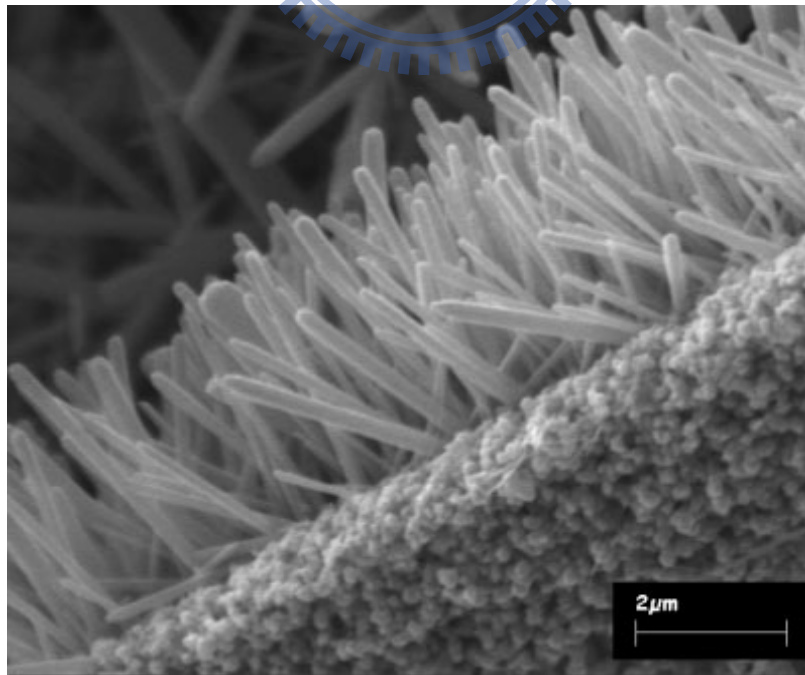


Figure 2-9. FESEM image of 3-dimensional arrays of ZnO nanorods by using aqueous solution chemical method. [16]

For demonstrate the ease of commercial scale-up, a growth of ZnO arrays on four-inch (ca. 10 cm) silicon wafers and two-inch plastic (polydimethylsiloxane, PDMS) substrates was presented by Yang's group, as shown in Fig. 2-10 [17]. In addition, unlike previous reports [15] where crystal growth occurs within enclosed flasks, the current process is carried out in open vessels, which points to the possibility of large-scale reel-to-reel production of such nanowire arrays. This low-temperature hydrothermal method is substrate independent and produces high-quality nanowire arrays on ITO glass, sapphire, titanium foil, and polymer surfaces.

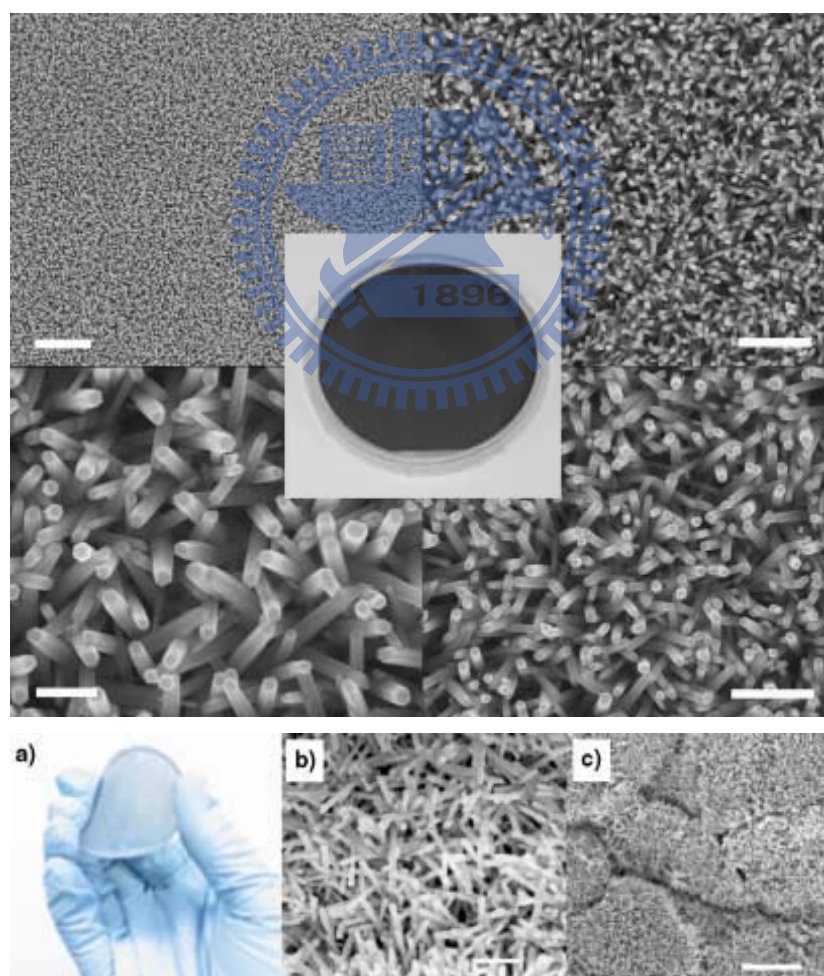


Figure 2-10. (upper) ZnO nanowire array on a four-inch (ca. 10 cm) silicon wafer. (down) ZnO nanowire array on a two-inch (ca. 5 cm) PDMS substrate. [17]

Table 2-1 summarizes some of the studies on solution growth and the resulting structures. [17]

TABLE 2-1.

Growth solution	Resulting morphology	Focus of investigation
Zinc nitrate, HMT	Nanorods, microtubes	On Si and conducting glass substrates
Zinc nitrate, HMT	Nanorods, nanotubes	Influence of substrate and seed layer
Zinc nitrate, HMT	Aligned nanowire arrays	Influence of seed layer
Zinc-nitrate, HMT, citriate	Oriented nanocolumns, nanoplates	Control of aspect ratio: addition of citrate anions decreases aspect ratio
Zinc nitrate, zinc acetate, HMT	Highly aligned nanorods	Influence of substrate and seed layer
Zinc nitrate, triethanolamine, HCl (pH 5)	Ordered nanorods	Influence of substrate and counter ions in growth solution
Zinc nitrate, thiourea, ammonium chloride, ammonia	Nanowires, tower-like, flower-like, tube-like	Influence of reactants, substrate pretreatment, and growth time and temperature
Zinc acetate, sodium hydroxide, citric acid	Disk-like, flower-like, nanorods	Influence of pH on growth solution
Comparison of different growth solutions	Star-like, nanorods	Influence of reaction conditions: ligand, counter-ions, pH, ionic strength, and deposition time Influence of substrate/seed layer
Zn foil, zinc sulfate, ammonium ions, sodium hydroxide	Nanobelt arrays, ordered nanowires	Influence of temperature and concentration of solutions

Template-Assisted Method. Template-directed synthesis represents a convenient and versatile method for generating 1D nanostructures. In this technique, the template serves as a scaffold against which other materials with similar morphologies are synthesized. That is, the in situ generated material is shaped into a nanostructure with a morphology complementary to that of the template. The templates could be nanoscale channels within mesoporous materials, porous alumina and polycarbonate membranes. The nanoscale channels are filled using, the solution, the sol-gel or the electrochemical method. The nanowires so produced are released from the templates by removal of the host matrix. Unlike the polymer membranes fabricated by track etching, anodic alumina membranes (AAMs) containing a hexagonally packed 2D array of cylindrical pores with a uniform size are prepared using anodization of aluminium foils in an acidic medium (Fig. 2-11).

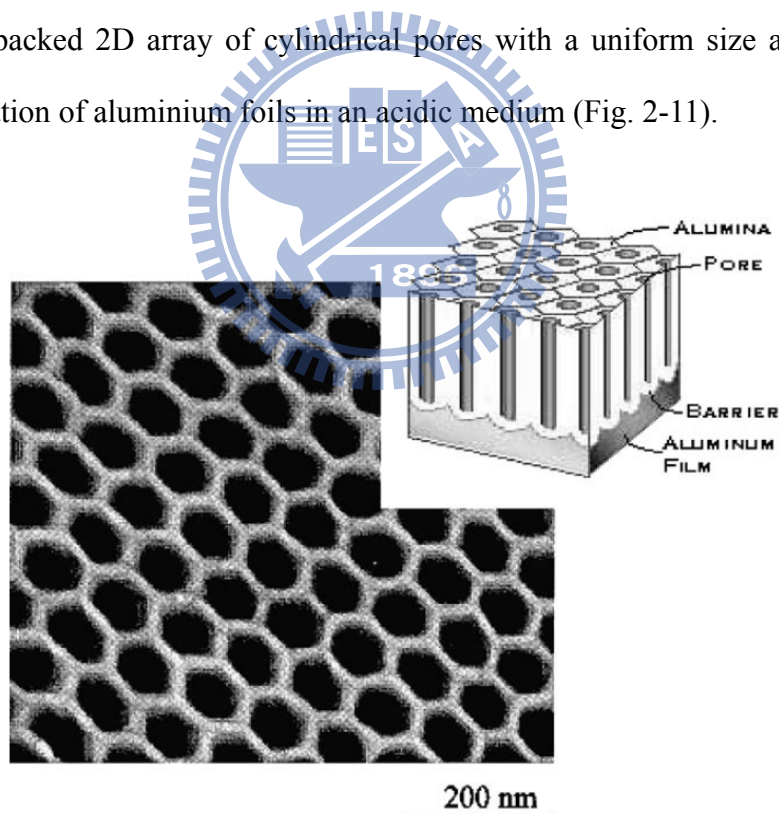


Figure 2-11. Micrograph of an anodic alumina membrane (AAM) (Zheng et al. [18]).

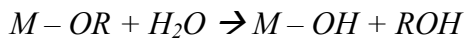
For example, with the help of an electrodeposition method [19-20], AAM with highly ordered nanopores was used as a template, zinc nanowires were fabricated into the nanopores via electrodeposition, forming zinc nanowires array, then the nanowire array was oxidized at 300°C for 2 hours and ZnO nanowire array was obtained. In a sol-gel synthesis method [21], AAM was also used as the template and immersed into a suspension containing zinc acetate for 1 minute, then heated in air at 120 °C for 6 hours. ZnO nanofibers were eventually obtained after removing the AAM template. These methods are complementary to the vapor transport synthesis of ZnO nanostructure, and also employ less rigorous synthesis conditions and provide great potential for device applications.

2.1.2 Growth of 0-D ZnO Nanoparticles/ Quantum dots

It is well known that the factors depend on the synthetic method used and, as a consequence, applications of nanomaterials are differently linked to the successful control of the synthetic process. Various different physical or chemical synthetic approaches have been developed. Several reports on physical ZnO nanoparticles and quantum dot syntheses have been published. They involve, for example, vapor phase transport [22], MOCVD [23, 24], microemulsion [25-27], sol-gel [28-33] and organometallic synthetic method [34-37]. Among these approaches, chemical methods are convenient and may lead to nanomaterials of controlled morphology. However, these syntheses make use of ionic species which may interact with the growth process of the particles and hence modify the final materials.

Sol-Gel Method. A colloid is a suspension in which the dispersed phase is so small (~1-1000 nm) that the gravitational force is negligible and interactions are dominated by the short-range forces, such as Van der Waals attraction and surface

charge. Sol-gel synthesis has two ways to prepare solution. One way is the metal-organic route with metal alkoxides in organic solvent; the other way is the inorganic route with metal salts in aqueous solution. It is much cheaper and easier to handle than metal alkoxides, but their reactions are more difficult to control. The metal-organic route uses metal alkoxides in organic solvent. The inorganic route is a step of polymerization reactions through hydrolysis and condensation of metal alkoxides $M(OR)^Z$, where $M = Si, Ti, Zr, Al, Sn, Ce$, and OR is an alkoxy group and Z is the valence or the oxidation state of the metal. First, hydroxylation upon the hydrolysis of alkoxy groups:



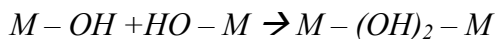
The second step, polycondensation process, leads to the formation of branched oligomers and polymers with a metal oxygenation based skeleton and reactive residual hydroxyl and alkoxy groups. There are 2 competitive mechanisms:

(1) Oxolation: formation of oxygen bridges:



The hydrolysis ratio ($h = H O/M$) decides $X = H$ ($h \gg 2$) or $X = R$ ($h < 2$). 2

(2) Olation: formation of hydroxyl bridges when the coordination of the metallic center is not fully satisfied ($N - Z > 0$):



where $X = H$ or R . The kinetics of olation is usually faster than those of oxolation.

Figure 2-12 presents a schematic of the routes that one could follow within the scope of sol-gel processing [38]. A sol is a colloidal suspension of solid particles in a liquid, whereas, an aerosol is a colloidal suspension of particles in a gas (the suspension may be called a fog if the particles are liquid and a smoke if they are solid) and an emulsion is a suspension of liquid droplets in another liquid. All of these types

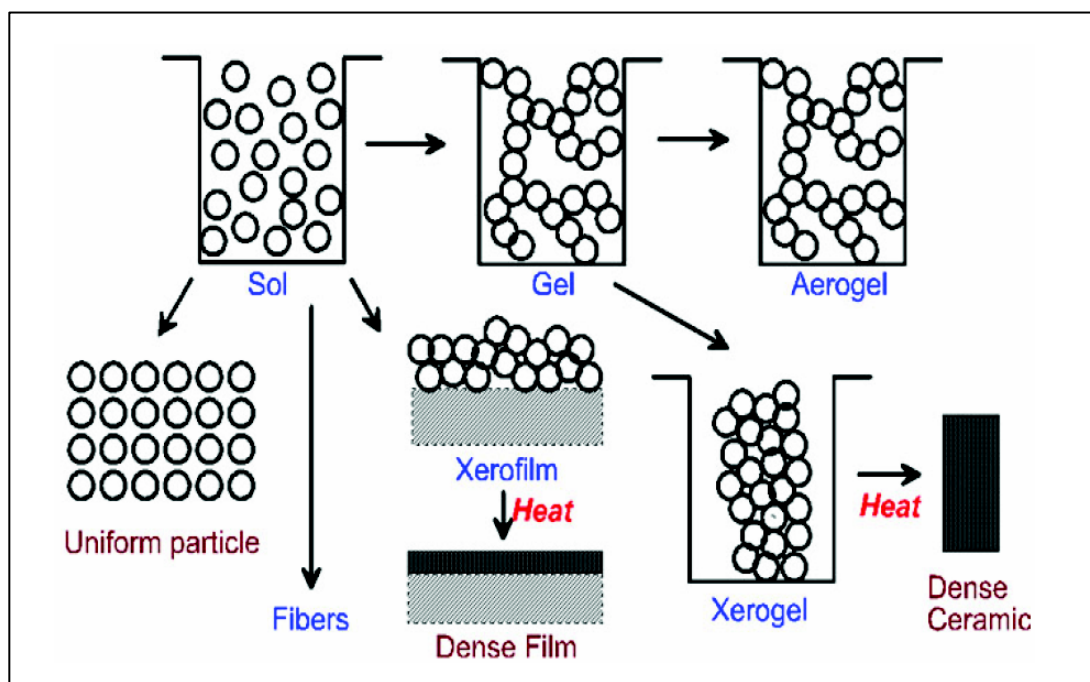


Figure 2-12. Schematic of the routes that one could follow within the scope of sol-gel processing [38].

of colloids can be used to generate polymers or particles from which ceramic materials can be made. In the sol-gel process, the precursors (starting compounds) for preparation of a colloid consist of a metal or metalloid element surrounded by various ligands.

Metal alkoxides are members of the family of metalorganic compounds, which have an organic ligand attracted to a metal or metalloid atom. Metal alkoxides are popular precursors because they react readily with water. The reaction is called hydrolysis, because a hydroxy ion becomes attached to the metal atom. This type of reaction can continue to build larger and larger molecules by the process of polymerization. A polymer is a huge molecule (also called a macromolecule) formed from hundreds or thousands of units called monomers. If one molecule reaches macroscopic dimensions so that it extends throughout the solution, the substance is said to be gel. The gel point is the time (or degree of reaction) at which the last bound is formed that completes this giant molecule. It is generally found that the process

begins with the formation of fractal aggregates that they begin to impinge on one another, then those clusters link together as described by the theory of percolation. The gel point corresponds to the percolation threshold, when a single cluster (call the spanning cluster) appears that extends throughout the sol; the spanning cluster coexists with a sol phase containing many smaller clusters, which gradually become attached to the network. Gelation can occur after a sol is cast into a mold, in which it is possible to make objects of a desired shape.

Joo et al. demonstrated ZnO nanocrystals with various shapes synthesized by non-hydrolytic ester elimination sol-gel react using zinc acetate precursor with a variety of surfactant, including trioctylphosphine oxide (TOPO), oleic acid (OA), 1-hexadecylamine (1-HDA), and tetradecylphosphonic acid (TDPA), respectively [33]. 1, 12-Dodecanediol was selected as the alcoholic reagent because of its high boiling point and reasonable reaction rate with zinc acetate ($\text{Zn}(\text{OAc})_2$). ZnO nanostructures with the shape of hierarchically self-assembled spherical, cone-shaped, hexagonal cone-shaped, and rod-like were obtained incorporated the stabilizer TOPO, OA, HDA and TDPA, respectively. As shown in Fig. 2-13 and 2-14.

Organometallic Synthetic Method. As a chemical method, the nature of the ion present in solution can influence processes such as coarsening and aggregation, which can compete with nucleation and growth leading to a modification of the particles size distribution. Organometallic have been used to overcome this problem. For example, $\text{Zn}(\text{C}_2\text{H}_5)_2$ has been reported to be a good precursor for ZnO after its transformation into an alkoxide prior to hydrolysis and heat treatment [34]. This approach has allowed the preparation of ZnO nanoparticles from the dialkylzinc precursor $\text{Zn}(\text{c-C}_6\text{H}_{11})_2$ by Chaudret's group [35-37].

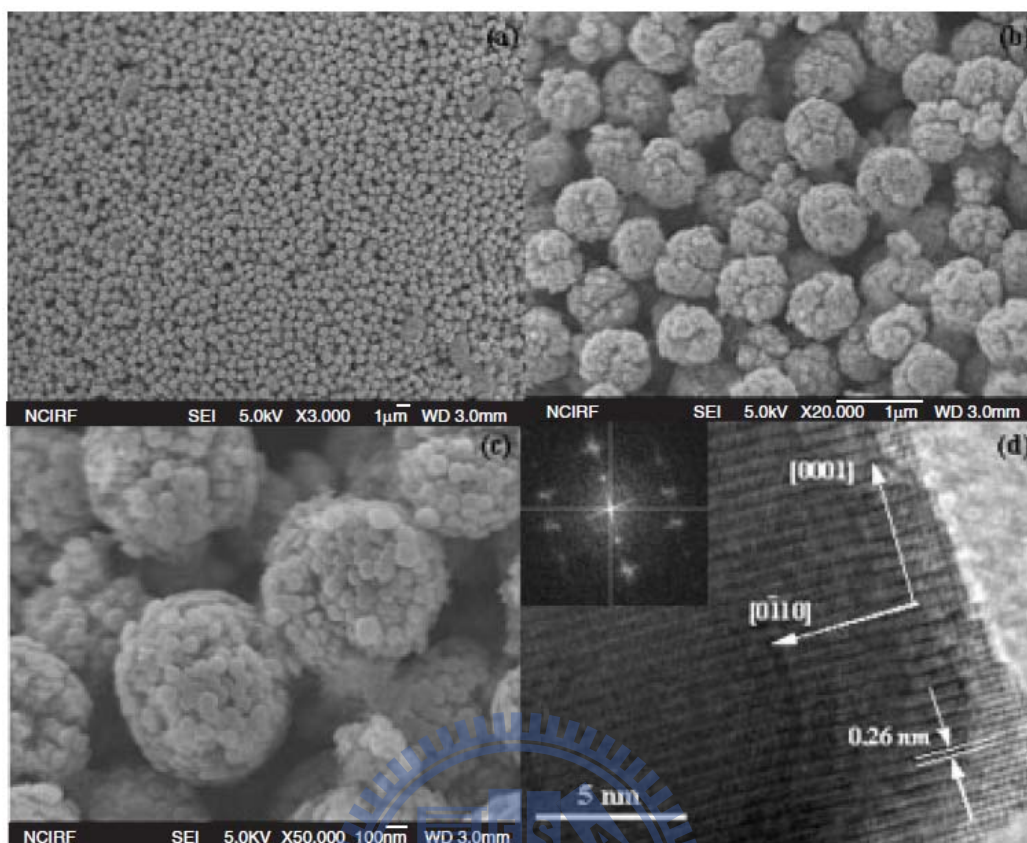


Figure 2-13. (a)-(c) FESEM and (d) HRTEM images of hierarchically ordered cone-shaped ZnO nanocrystals. The inset in (d) shows the fast Fourier transform (FFT) pattern of the HRTEM image. [33].

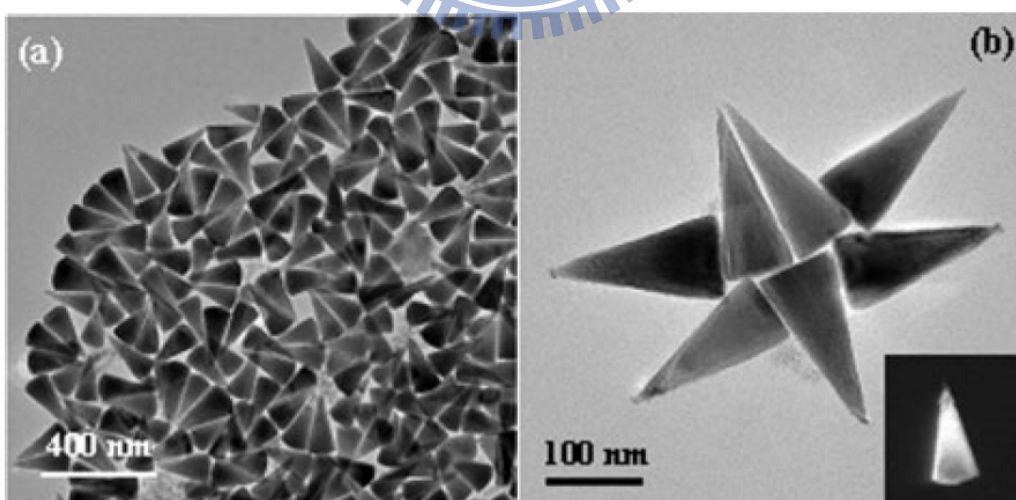


Figure 2-14. (a), (b) TEM of images OA-stabilized cone-shaped ZnO nanocrystals. The inset in (b) shows a dark-field image of a single cone-shaped ZnO nanocrystal. [33].

Most organometallic complexes are air-sensitive and decompose exothermically in air. Chaudret supposed that the kinetics of this decomposition may control the formation of nanomaterial. Therefore a controlled oxidation of the precursor in solution could lead, in one step, to oxide nanoparticles, the shape and size of which could be controlled by the different parameters of the system (such as the nature of the organometallic precursor, the ligands or surfactants present, the solvent used, and so on.)

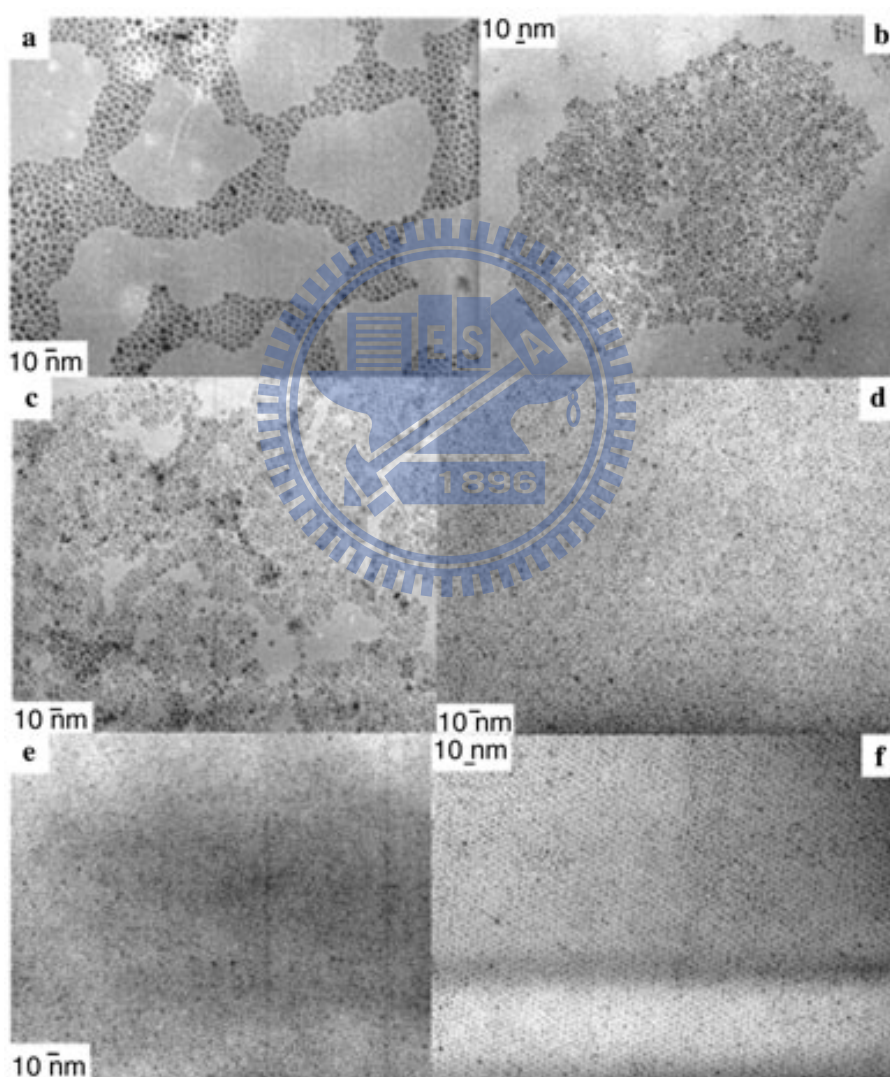


Figure 2-15. TEM images ZnO nanoparticles obtained in the presence of : (a) OA and OIA (1:1) without other solvent; (b) OA and OIA (2:1) without other solvent; (c) OA and OIA (10:1) without other solvent; (d) OA and LcA (1:1) in THF; (e) DDA and OcA (1:1) in THF; (f) HDA and OIA (1:1) in THF [37].

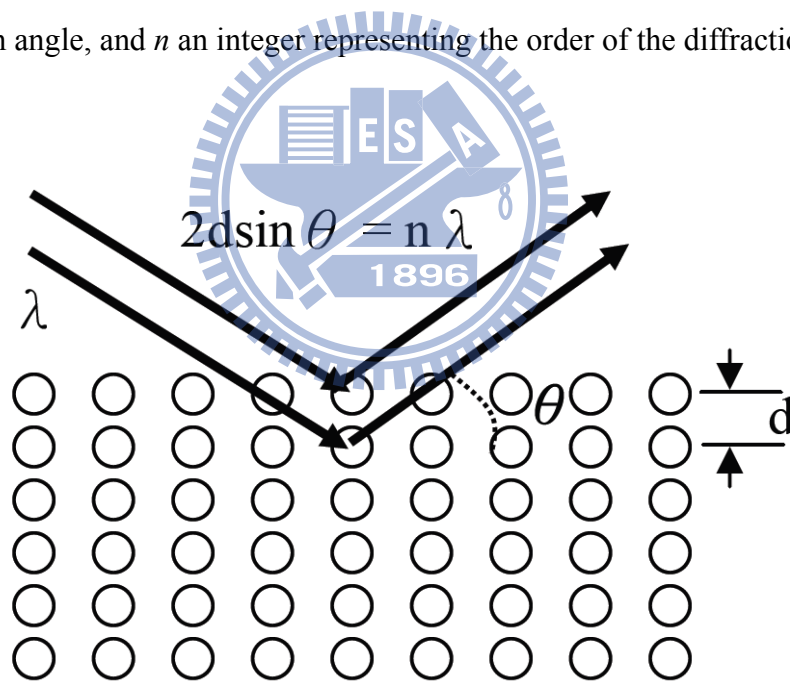
2.2 Characterization Techniques

2.2.1 X-Ray Diffraction [39]

The peaks of an x-ray diffraction (XRD) pattern are directly related to the atomic distances. Consider an incident monochromatic x-ray beam interacting with the atoms arranged in a periodic manner as shown in 2-dimension in Fig. 2-16. The atoms, represented as circles in the graph forming different sets of planes in the crystal. For a given set of lattice planes with an inter-plane distance of d , the condition for a diffraction (peak) to occur can be simply written as

$$2d \sin\theta = n\lambda \quad (2.1)$$

which is known as the Bragg's law. In this equation, λ is the wavelength of the x-ray, θ the diffraction angle, and n an integer representing the order of the diffraction peak.



Bragg's Law

Figure 2-16. X-ray diffraction from 2-dimensional periodic lattices.

Let's consider a hexagonal unit cell (such as wurtzite ZnO) which is characterized by the lattice parameters a and c , the equation representing the spacing of the plane for the hexagonal structure is

$$\frac{1}{d^2} = \frac{4}{3} \left(\frac{h^2 + hk + k^2}{a^2} \right) + \frac{l^2}{c^2} \quad (2.2)$$

Combining Eq. (2.1) with (2.2), (2.3) can be obtained as:

$$\frac{1}{d^2} = \frac{4}{3} \left(\frac{h^2 + hk + k^2}{a^2} \right) + \frac{l^2}{c^2} = \left(\frac{2 \sin \theta}{\lambda} \right)^2 \quad (2.3)$$

after a proper arrangement:

$$\sin^2 \theta = \frac{\lambda^2}{4} \left[\frac{4}{3} \left(\frac{h^2 + hk + k^2}{a^2} \right) + \frac{l^2}{c^2} \right] \quad (2.4)$$

Thus, the lattice parameters can be estimated from XRD spectrum via (2.4).

The sizes of the nanocrystallites can also be determined by XRD using the measurement of the full width at half maximum (FWHM) of the XRD lines. The

Debye-Scherrer equation represent as:

$$D = \frac{0.89\lambda}{B \cos \theta} \quad (2.5)$$

where D is the average diameter of the nanocrystallite, λ is the wavelength of the x-ray source (usually $\text{CuK}\alpha$, $\lambda = 1.5405\text{\AA}$), and B is the deconvoluted FWHM (that means broadened effect comes from the nanocrystalline size only) of XRD peak at the diffraction angle θ .

Furthermore, for the epitaxy systems, such as well-aligned 1-D ZnO nanorods and nanowires on specific substrates, a high-resolution x-ray rocking curve with

precious optics (~ 26 arcsec., 1 arcsec. = $1/3600$ deg.) would be performed for investigate the structural quality and orientation. The high-resolution optics can be obtained after the incident x-ray beam pass through the choice monochromator or channel-cut crystal. Different from the conventional ω - 2θ scans geometry, the spectrum of x-ray rocking curves are collected from count the intensity around the diffraction peak with rocking the sample only.

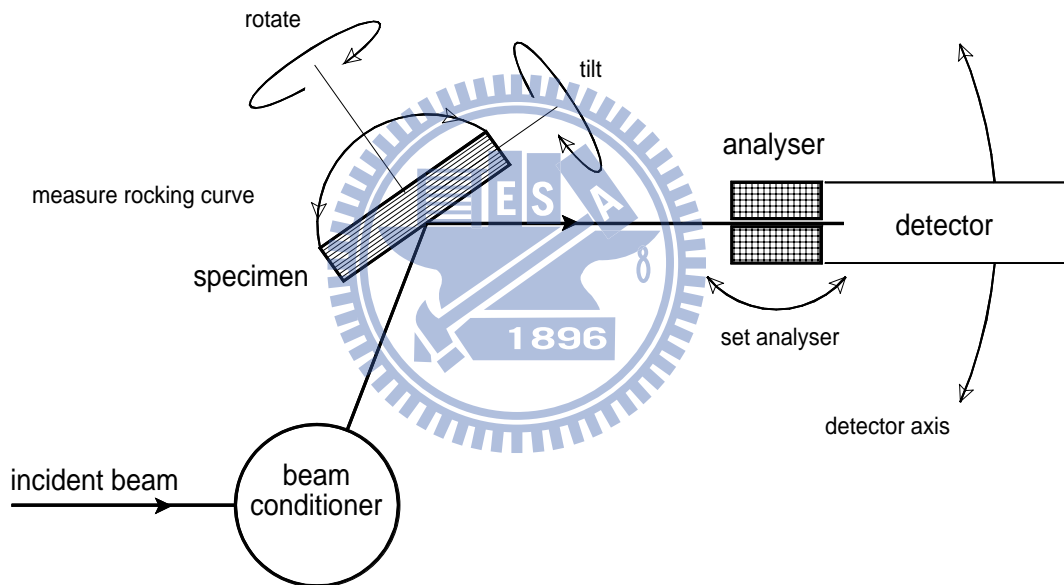


Figure 2-17. Instrumental setup for high-resolution x-ray rocking curve.

2.2.2 Photoluminescence [40]

Photoluminescence (PL) is one of the most useful optical methods for the semiconductor industry, with its powerful and sensitive ability to characterize impurities and defects in semiconductors, which affect material quality and device

performance. To control crystal purity is crucial in many optical applications, such as laser action, optical gain, and active optical devices. A given impurity produces a set of characteristic spectral features. The fingerprint identifies the impurity type, and often several different impurities can be seen in a single PL spectrum. And the linewidth of PL peak is an indication of sample quality and crystallinity, although such analysis has not yet become highly quantitative.

Since the PL emission requires that the system be in a nonequilibrium condition, and some means of excitation is needed to act on the semiconductor to produce hole-electron pairs. We consider the fundamental transitions, those occurring at or near the band edges. The ground state of the electronic system of a perfect semiconductor is a completely filled valance band and a completely empty conduction band. We can define this state as the “zero” energy or “vacuum” state. If we start from the above-defined ground state and excite one electron to the conduction band, we simultaneously create a hole in the valance band. In this sense an optical excitation is a two-particle transition. The same is true for the recombination process. An electron in the conduction band can return radiatively or nonradiatively into the valance band only if there is a free space, i.e., a hole. Two quasi-particles are annihilated in the recombination process. What we need for the understanding of the optical properties of the electronic system of a semiconductor is therefore a description of the excited states of N-particle problem. The quanta of these excitations are called “excitons” which have been classified as Wannier exciton and Frenkel exciton. It should be mentioned that in insulators like NaCl, or in organic crystals like anthracene, excitons also exist with electron-hole pair wavefunctions confined to one unit cell. Frenkel excitons cannot be described in the effective mass approximation. In Wannier excitons, the Bohr radius (i.e. the mean distance between electron and hole) is larger in

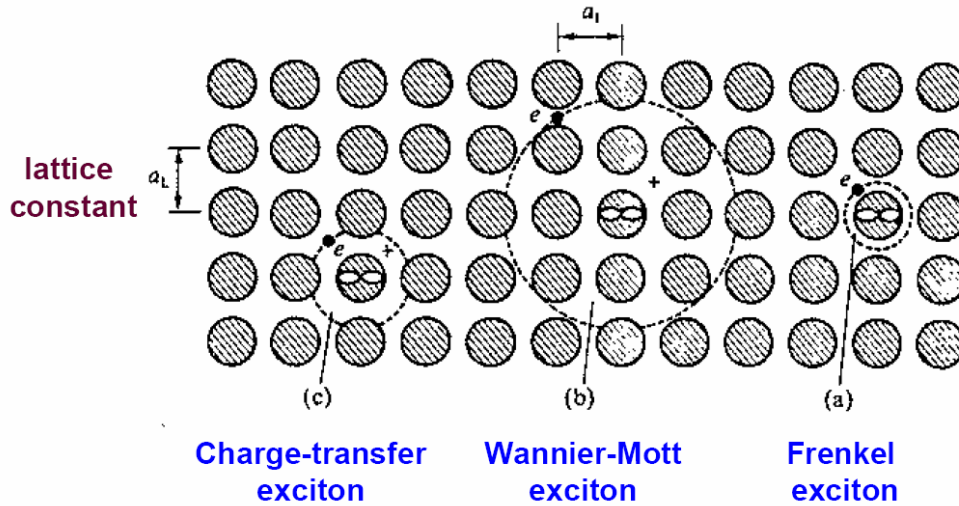


Figure 2-18. Three different concepts of excitons. Excitons (bounded electron-hole pairs) also can be viewed as the excited states of molecules.

comparison with the length of the lattice unit cell. This situation is well realized in narrow-gap semiconductors (most II-VI, III-V, and column IV semiconductors) which usually have large dielectric constant ($\epsilon \gg 1$) and small reduced exciton mass ($\mu \ll m_0$). Therefore, we always deal with Wannier excitons in all semiconductors, inclusive of ZnO certainly. Here we will consider the Wannier excitons more specifically.

Using the effective mass approximation, it is suggested that the Coulomb interaction between electron and hole leads to a hydrogen-like problem with a Coulomb potential term

$$\frac{-e^2}{4\pi\epsilon_0\epsilon|r_e - r_h|}$$

Excitons in semiconductors form, to a good approximation, a hydrogen or positronium like series of states below the gap. For a simple parabolic band in a direct-gap semiconductor one can separate the relative motion of electron and hole and the motion of the center of mass. This leads to the dispersion relation of exciton as shown in Fig. 2-19.

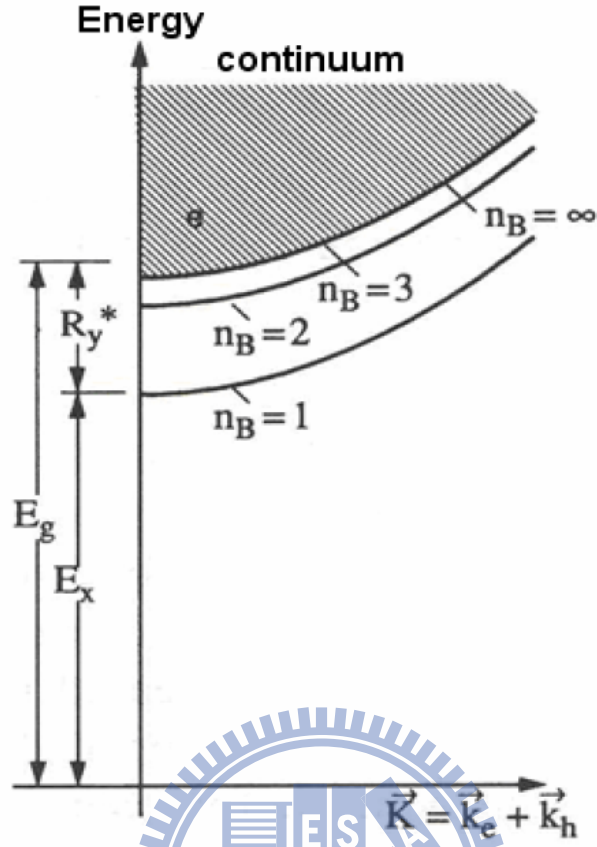


Figure 2-19. A pair excitation in the scheme of valence and conduction band in the exciton picture for a direct gap semiconductor. [40]

$$E_{ex}(n_B, K) = E_g - Ry^* \frac{1}{n_B^2} + \frac{\hbar^2 K^2}{2M} \quad (2.6)$$

where $n_B = 1, 2, 3 \dots$ is the principal quantum number, $Ry^* = 13.6(\mu/m_0\epsilon^2)$ is the exciton Rydberg energy, $M = m_e + m_h$, and $K = k_e + k_h$ are the translational mass and wave vector of the exciton, respectively. The series of exciton states in eq. 2.6 has an effective Rydberg energy Ry^* modified by the reduced mass of electron and hole and the dielectric constant of the medium in which these particles move. The radius of the exciton equals the Bohr radius of the H atom again modified by ϵ and μ . Using the material parameters for typical semiconductors one finds that the orbits of electron and hole around their common center of mass average over many unit cells and this in turn justifies the effective mass approximation in a self-consistent way. These excitons

are called Wannier excitons. The exciton Bohr radius of bulk ZnO is defined 2.34 nm by Senger [41] who demonstrated exciton radius in ZnO quantum dots changed dramatically as the crystal size closes to 2.34 nm.

A real crystal is never perfect. Imperfections such as ion vacancies, interstitials, or substitutional atoms (either native or intentionally introduced) exist in densities ranging from $n_i < 10^{12} \text{ cm}^{-3}$ in ultrapure crystals. The imperfections can attract excitons that become localized at the defect sites to form bound exciton complex (BEC). The binding energy of the exciton to the defect is often quite small, typically a few meV. Therefore, the bound excitons are best observed at very low temperatures. An exciton may be bound to a donor, which is a substitutional atom with a higher number of valance electrons compared with the host atom, or to an acceptor, a substitutional atom with a lower number of valance electrons. Donors contribute excess electrons to the crystal, while acceptors tend to capture electrons or equivalently donate holes. Donor or acceptor atoms may be electrically charged or neutrals. When the donor atom has given away its initial extra valance electrons, it becomes positively charged and it referred to as an ionized donor. Similarly, when an acceptor atom has captured an electron (or equivalently released a hole), it has a negative charge and is called an ionized acceptor. In contrast, a neutral donor or acceptor has no charge, since it has kept its original number of valance electrons. Excitons may get bound to either an ionized donor or acceptor, or a neutral donor or acceptor by forming complexes represented schematically in Fig. 2-20. An ionized acceptor does not usually bind an exciton since a neutral acceptor and a free electron are energetically more favorable. The binding energy E^b of exciton to the complex usually increases according to $E_{D^+X}^b < E_{D^0X}^b < E_{A^0X}^b$.

In many crystals, the binding energy of the exciton to a neutral donor or acceptor

of single crystal ZnO consists mainly of two bands. The one in UV region corresponds to near-band-edge (NBE) emission is attributed to exciton states; the other one in visible region is due to structural defects and impurities.

2.2.3 Raman Scattering

When light is scattered from the surface of sample, the mainly scattered light is found to contain the same wavelengths that were incident on the sample (Rayleigh scattering) but also different wavelengths at very low intensities (few parts per million) which represent an interaction of the incident light with material. The energy shifts of the scattering photons are small, but can be measured by interferometric techniques. Usually, the phonon wave vectors are very small compared to the size of the Brillouin zone so that the interactions are only with zone center phonon. Thus, one can have interaction with either the zone center acoustic phonons or the optical phonons. The interaction with acoustic phonons is called Brillouin scattering while the interaction with optical phonons is called Raman scattering. All of the Raman mode frequencies, intensities, line-shapes, and line-widths, as well as polarizations can be used to characterize the lattices and impurities. The intensity gives information on crystallinity. The line-width increases when a material is damaged or disordered, because damage or disorder occurs in a material will increase phonon damping rate or relax the rules for momentum conservation in Raman process.

The different long-wavelength phonon branches in a given crystal correspond to different symmetries of vibration of the atoms in the unit cell and are characterized by irreducible representations of the space group of the crystal lattice. If the wavelengths of the Raman phonons are assumed to be effectively infinite, then the crystal point group can be used in classifying the phonon symmetries. This infinite wavelength

assumption is not valid for Raman-active phonons which are also infrared active.

The selection rules for Raman-active phonons can be determined by standard group-theoretical methods and the calculation is described in some detail by Heine [42], who based his work on the polarizability derivative theory of Born and Bradburn [43]. The result is that a phonon can participate in a first-order Raman transition if and only if its irreducible representation is the same as one of the irreducible representations which occur in the reduction of the representation of the polarizability tensor. The irreducible representations by which the components of the polarizability tensor transform are conveniently listed by Herzberg and Wilson *et al.* [44, 45] for the set of molecular point groups, which includes the 32 crystal point groups.

The intensity of the Raman-scattered radiation depends in general on the directions of observation and illumination relative to the principal axes of the crystal. The angular variation of the scattering gives information about the symmetry of the lattice vibration responsible. The anisotropy of the scattering can be predicted for a vibration of any given symmetry by standard group-theoretical methods.

GaN-, AlN- and InN-based materials are highly stable in the hexagonal wurtzite structure although they can be grown in the zinc blende phase and unintentional phase separation and coexistence may occur. The wurtzite crystal structure belongs to the space group $C_{6v}^4(P6_3mc)$ and group theory predicts zone-center (Γ point of the Brillouin zone) optical modes are A_1 , $2B_1$, E_1 and $2E_2$ [46]. The A_1 and E_1 modes are both Raman and infrared active; and $B_1(\text{low})$ and $B_1(\text{high})$ modes are silent. The A_1 and E_1 modes are polar, resulting in a splitting of the longitudinal (LO) and the transverse (TO) modes. However, the nonpolar E_2 modes are Raman active and have two frequencies: $E_2(\text{high})$ is related to the vibration of oxygen atoms and $E_2(\text{low})$ is associated with the Zn sublattice. The displacement vectors of the phonon normal

TABLE 2-2. Raman measurement configuration needed to observe the phonon modes in hexagonal ZnO. [46]

Mode	Configuration
$A_1(\text{TO}), E_2$	$X(Y, Y) \bar{X}$
$A_1(\text{TO})$	$X(Z, Z) \bar{X}$
$E_1(\text{TO})$	$X(Z, Y) \bar{X}$
$E_1(\text{TO}), E_1(\text{LO})$	$X(Y, Z) Y$
E_2	$X(Y, Y) Z$
E_2	$Z(Y, X) \bar{Z}$
$A_1(\text{LO}), E_2$	$Z(Y, Y) \bar{Z}$

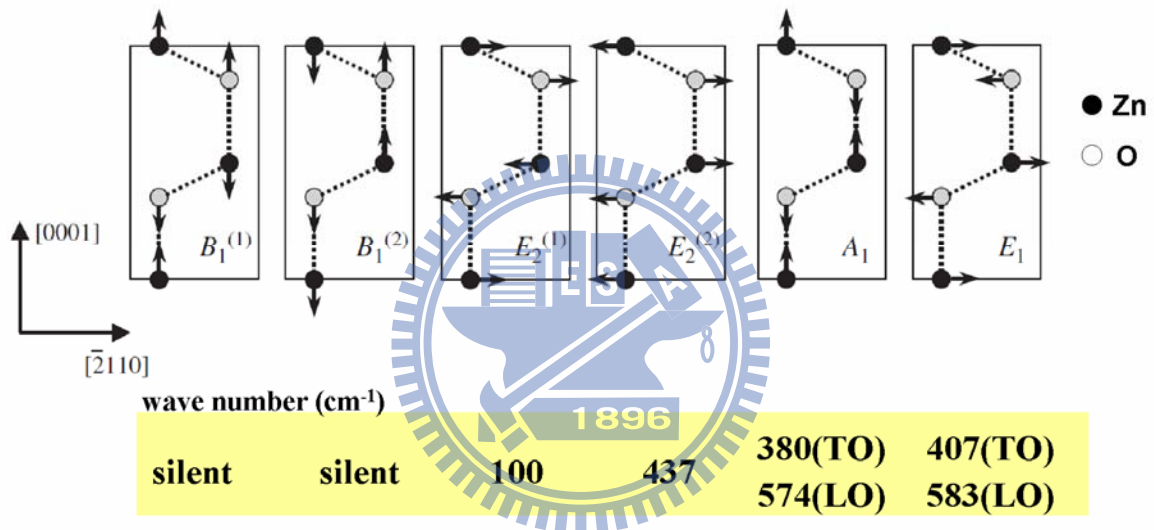


Figure 2-21. Displacement patterns of the optical phonons of a lattice with wurtzite crystal structure. [47]

modes are illustrated in Fig. 2-21. For the lattice vibrations with A_1 and E_1 symmetry, the atoms move parallel and perpendicular to the c -axis, respectively. The details of the mode–Raman configuration relationship are also provided in Table 2-2.

References and Notes

- [1] R. S. Wagner, and W.C. Ellis, *Appl. Phys. Lett.* 4, 89(1964).
- [2] A. M. Morales and C. M. Lieber, *Science* 279,208 (1998).
- [3] Y. Wu and P. Yang. *J. Am. Chem. Soc.* 123, 3165 (2001).
- [4] M. H. Huang, S. Mao, H. Feick, H. Yun, Y. Wu, H. Kind, E. Weber, R. Russo, and P. D. Yang. *Science* 292, 1897 (2001).
- [5] H. Zhou, M. Wissinger, J. Fallert, R. Hauschild, F. Stelzl, C. Klingshirn, and H. Kalt, *Appl. Phys. Lett.* 91, 181112 (2007).
- [6] Z. W. Pan, Z. R. Dai, and Z. L. Wang, *Science* 291, 1947 (2001).
- [7] Z. L. Wang, *Materials Today*, 7 (6), 26 (2004).
- [8] J. Y. Lao, J. G. Wen, and Z. F. Ren, *Nano Lett.* 2, 1287 (2002).
- [9] W.I. Park, D.H. Kim, S. W. Jung, and G. C. Yi, *Appl. Phys. Lett.* 80, 4232 (2002).
- [10] R. Kling, , C. Kirchner, T. Gruber, F. Reuss, and A. Waag, *Nanotechnology*, 15, 1043 (2004).
- [11] W. I. Park, Y. H. Jun, S.W. Jung, and G. C. Yi, *Appl. Phys. Lett.* 82, 964 (2003).
- [12] Y. B. Li, Y. Bando, and D. Golberg, *Appl. Phys. Lett.* 84, 3603 (2004).
- [13] W. Lee, M. C. Jeong and J. M. Myoung, *Nanotechnology* 15, 254 (2003).
- [14] J. J. Wu and S. C. Liu, *Adv. Mater.* 14, 215 (2002).
- [15] M. Andrés. Vergés, *J. Chem. Soc., Fraday Trans.* 86, 959 (1990)
- [16] L. Vayssieres, *Adv. Mater.* 15, 464 (2003).
- [17] L. Schmidt-Mende and J. L. MacManus-Driscoll, *Materials Today*, 10 (5), 40 (2007).
- [18] M. Zheng, L. Zhang, X. Zhang, J. Zhang, G. Li, *Chem. Phys. Lett.* 334, 298 (2001).
- [19] Y. Li, G. S. Cheng, and L. D. Zhang, *J. Mater. Res.* 15, 2305 (2000).

- [20] Z. Wang and H.L. Li, *Appl. Phys. A* 74, 201 (2002).
- [21] B. B. Lakshmi, P. K. Dorhout, and C. R. Martin, *Chem. Mater.* 9, 857 (1997).
- [22] J. G. Lu, Z. Z. Ye, J. Y. Huang, L. P. Zhu, B. H. Zhao, Z. L. Wang, and S. Fujita, *Appl. Phys. Lett.* 88, 063110 (2006).
- [23] L. M. Yang, Z. Z. Ye, Y. J. Zeng, W. Z. Xu, L. P. Zhu and B. H. Zhao, *Solid State Commun.* 138, 577 (2006).
- [24] S. T. Tan, X. W. Sun, X. H. Zhang, B. J. Chen, S. J. Chua, A. Yong, Z. L. Dong and X. Hu, *J. Crystal Growth* 290, 518 (2006).
- [25] L. Guo, Y. L. Ji, H. Xu, P. Simon, and Z. Wu, *J. Am. Chem. SOC.* 124, 14864 (2002).
- [26] L. Guo and S. Yang, *Chem. Mater.* 12, 2268 (2000).
- [27] L. Guo, S. Yang, C. Yang, P. Yu, J. Wang, W. Ge, G. K. L. Wong, *Appl. Phys. Lett.* 76 2901 (2000).
- [28] L. Spanhel and M. A. Anderson, *J. Am. Chem. SOC.* 113, 2826 (1991). (SG)
- [29] P. Hoyer, H. Weller, *J. Phys. Chem.* 99, 14096 (1995).
- [30] S. Bandyopadhyay, G. K. Paul, R. Roy, S. K. Sen, S. Sen, *Mater. Chem. Phys.* 174, 83 (2002).
- [31] G. K. Paul, S. Bandyopadhyay, S. K. Sen, S. Sen, *Mater. Chem. Phys.* 79, 71 (2003).
- [32] T. Andelman, Y. Gong, M. Polking, M. Yin, I. Kuskovsky, G. Neumark, and S. O'Brien, *J. Phys. Chem. B* 109, 14314 (2005).
- [33] J. Joo, S. G. Kwon, J. H. Yu, and T. Hyeon, *Adv. Mater.* 17, 1873 (2005).
- [34] M. Shim, P. Guyot-Sionnest, *J. Am. Chem. SOC.* 123, 11651 (2001).
- [35] M. Monge, M. L. Kahn, A. Maisonnat, and B. Chaudret, *Angew. Chem. Int. Ed.* 42, 5321 (2003).

- [36] M. L. Kahn, M. Monge, V. Collière, F. Senocq, A. Maisonnat, B. Chaudret, *Adv. Funt. Mater.* 15, 458 (2005).
- [37] M. L. Kahn, M. Monge, E. Snoeck, A. Maisonnat, and B. Chaudret, *Small* 1, 221 (2005).
- [38] C. J. Brinker and G. W. Scherer, "Sol-Gel Science", pp. 303.
- [39] B. D. Cullity, "Elements of X-ray diffraction", 2nd ed, (Addison Wesley, Canada, 1978).
- [40] C. F. Klingshirn, "Semiconductor Optics" 2nd edition (Springer, Berlin, 2005).
- [41] R. T. Senger, and K. K. Bajaj, *Phys. Rev. B* 68, 045313 (2003).
- [42] V. Heine, "Group Theory in Quantum Mechanics" (Oxford: Pergamon Press, 1960).
- [43] M. Born, and M. Bradburn, *Proc. roy. Soc. A*, 188, 161 (1947).
- [44] G. Herzberg, "Infra-red and Raman Spectra of Polyatomic Molecules" (New York: D. Van Nostrand, 1945).
- [45] E. B. Wilson, J. C. Deuius, and P. C. Cross, "Molecular Vibrations" (New York : McGraw-Hill Book Co. 1955).
- [46] Hadis Morkoç and Ümit Özgür "Zinc Oxide: Fundamentals, Materials and Device Technology" (Wiley-VCH Verlag GmbH & Co. KGaA, Weinheim, 2009).
- [47] E. Ruiz, S. Alvarez, P. Alemany, *Phys. Rev. B* 49, 7115 (1994).

Chapter 3 Experimental Procedures

3.1 Vapor-Solid Synthesis for 1-D ZnO Nanowires/ rods

Growth on ZnO Buffer Layer. The vertical arrays of well-aligned ZnO nanorods were synthesized on various substrates, which were pre-coated with *c*-oriented ZnO buffer layers. The pre-coated substrates and ZnO nanorods were fabricated by the following procedure. First, the ZnO buffer layers were grown on various substrates including glass, Si (111), 6H-SiC (0001) and *c*-plane sapphire, by pulsed laser deposition (PLD) technique using a KrF excimer laser (wavelength of 248 nm and pulse duration of 25 ns) to ablate a ceramic ZnO target (99.999%) at 600°C for 2 hours and *in-situ* annealing for 1 hour at 700°C under the pressure of 10^{-8} Torr. The thicknesses of the ZnO buffer layers were around 900nm under roughly control. Then the substrates were loaded 2 cm above an alumina boat containing 1g metal zinc balls. The boat was put in the middle of the tube furnace. The furnace temperature was increased to 550°C and maintained for 30 min. High-purity argon gas was simultaneously introduced at a flow rate of 500 sccm. While the growth process was complete, the tube furnace was cooled to room temperature in Ar-gas ambience and a gray-white colored product was found over the substrates. The typical schematic of the equipment for synthesis is shown in Fig. 3-1.

Growth on GaN Buffer Layer. The vertically well-aligned ZnO nano arrays were epitaxially fabricated on the GaN-buffered sapphire substrate by employing catalyst-free metal vapor deposition. Synthesis of the ZnO nanowire arrays was carried out in low-pressure vapor phase deposition system which includes a horizontal alumina tube in a conventional furnace. Zinc vapor source is 99.9% Zn metal powder

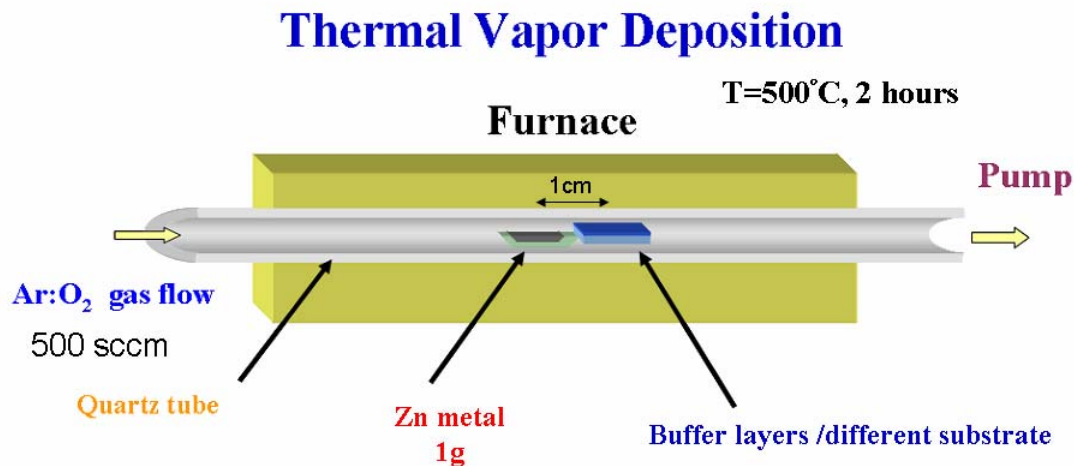


Figure 3-1. A schematic diagram of the experimental apparatus for growth of ZnO nanowires.

from Strem Chemicals. High-quality epitaxial GaN(0001) buffer layers of up to 2 μm thick were grown on (0001) sapphire substrates by the metal-organic vapor phase epitaxy (MOVPE). The GaN/sapphire substrates and zinc vapor source in an alumina boat were inserted into the quartz tube and put closely in the middle of the furnace. Afterwards, the chamber was heated up to 550 $^{\circ}\text{C}$ at a rate of 20 $^{\circ}\text{C}/\text{min}$ under a constant of 55 sccm Ar and 1 sccm oxygen flows and kept for 1h. After cooling to the ambient temperature, a white deposition layer was found over the substrate. More detailed growth condition and the description of reaction chamber were described elsewhere which was a little modified from Fig. 3-1 [1].

3.2 Hydrothermal Synthesis for 1-D ZnO Nanowires/ rods

The ZnO nanowires were fabricated from a modified aqueous solution method similar to Law et al. [2]. The sequence of chemical reactions for ZnO fabrication is following:

1. $C_6H_{12}N_4 + 6H_2O \leftrightarrow 6CH_2O + 4NH_3$
2. $C_6H_{12}N_4 + Zn^{2+} \rightarrow [Zn(C_6H_{12}N_4)]^{2+}$
3. $NH_3 + H_2O \leftrightarrow NH_4^+ + OH^-$
4. $Zn^{2+} + 4NH_3 \rightarrow Zn(NH_3)_4^{2+}$
5. $Zn^{2+} + 4OH^- \rightarrow Zn(OH)_4^{2-}$
6. $Zn(NH_3)_4^{2+} + 2OH^- \rightarrow ZnO + 4NH_3 + H_2O$
7. $Zn(OH)_4^{2-} \rightarrow ZnO + H_2O + 2OH^-$
8. $[Zn(C_6H_{12}N_4)]^{2+} + 2OH^- \rightarrow ZnO + H_2O + 2OH^- + C_6H_{12}N_4$

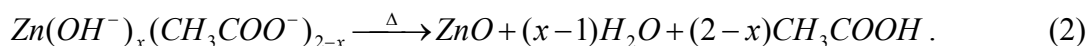
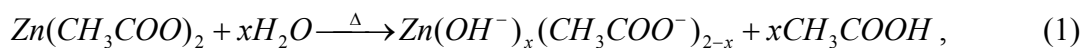
Arrays of ZnO nanowires were synthesized on FTO substrates (10 Ω per square, Nippon Sheet Glass.) that were first cleaned thoroughly by acetone/ethanol sonication and then coated with a thin film of ZnO quantum dots, 3-4 nm in diameter, by dip-coating in a Zn(OAc)₂ concentrated ethanol solution. The arrays of ZnO nanowires were synthesized on seeded fluorine doped tin oxide (FTO) substrates by immersing the seeded substrates in aqueous solutions containing 0.08 M zinc nitrate hydrate (98%, Riedel-deHaën), 0.08 M hexamethylenetetramine (HMTA, 99%, Showa), and 12 mM polyethylenimine (PEI, branched, low molecular weight, Aldrich) at 95 °C for 10 hours.

Because nanowire growth slowed after this period, substrates were repeatedly introduced to fresh solution baths in order to obtain long wire arrays. The arrays were then rinsed with deionized water and baked in air at 450 °C for 30 minutes to remove any residual organics.

3.3 Sol-Gel Synthesis for 0-D ZnO NPs/ QDs

ZnO Nanoparticles. The sol-gel method was chosen to produce monodisperse

ZnO colloidal spheres due to its simple handling and narrow size distribution. The ZnO colloidal spheres were produced by a two-stage reaction process similar to that described by Seelig et al [3], and reactions were ascribed as the following equations:



The Eq. (1) is the hydrolysis reaction for Zn (OAc)₂ to form metal complexes. We increased the temperature of reflux from RT to 160°C and maintained for aging. The zinc complexes will dehydrate and remove acetic acid to form pure ZnO as Eq. (2) during the aging time. Actually, the two reactions described above proceed simultaneously while the temperature is over 110°C. All chemicals used in this study were reagent grade and employed without further purification. In a typical reaction, 0.01 mol zinc acetate dihydrate (99.5% Zn(OAc)₂, Riedel-deHaen) was added to 100 ml diethylene glycol (99.5% DEG, EDTA). Then the temperature of reaction solution was increased to 160°C and maintained for aging at least 1 hour. White colloidal ZnO was formed in the solution that was employed as the primary solution. The secondary solutions were composed of Zn(OAc)₂ (0.01mole) and various amount of primary supernatant (5ml to 20ml) in 100ml DEG and the reaction began in the same way as the primary reaction. The white gelatinous production of ZnO particles ranging in diameter from 50 to 300 nm (depend on the amount of primary supernatant) were successfully synthesized under the well-controlled concentration with stable heating rate. From our observations, the particle with a diameter of nearly 185 nm is the optimized condition that can be used to fabricate self-assembled periodic array. The spherical shape of the ZnO colloid is recognized with agglomeration of many primary single crystallites ranging from 6 to 12 nm,

hence, here we usually named these ZnO colloids as secondary ZnO nanoparticles. Powder samples were prepared by placing a drop of colloidal suspension on preheated Si(100) substrates (for optical measurements) and carbon-coated copper grids (for TEM measurements). The excess solvent was then removed and the specimens were allowed to dry in air. The dry powders were then inserted to a furnace and heated at 350°C and 500°C for 1 hour in air ambient.

ZnO Quantum Dots. The ZnO quantum dots were produced from zinc acetate dihydrate (99.5% Zn(OAc)₂, Riedel-deHaen) in diethylene glycol (99.5% DEG, EDTA), the same to what we presented above. The slight difference is that we placed the final product in a centrifuge operating 3000 rpm for 30 minutes. A high speed centrifuge was used to separate the final colloids into the upper suspension and the white bottom layer. After this procedure, the solution was separated into two gradations. The white bottom layer included the secondary ZnO clusters and the upper suspension was more transparent and included the dispersive single crystalline ZnO QDs. Unlike the secondary clusters, the single crystalline ZnO QDs were almost monodispersive because of the stable surface during the chemical reaction. The average size of ZnO QDs can be tailored under well-controlled concentration of precursor, Zn(OAc)₂, including 0.04, 0.06, 0.08, 0.1, 0.16 and 0.32 M.

3.4 Materials and Reagents

- (1) Zn metal powder (99.9% , Strem Chemicals).
- (2) Zinc acetate dihydrate (Zn(OAc)₂ ·2H₂O, 99.5%, Riedel-deHaen).
- (3) Zinc nitrate hydrate (Zn(NO₃)₂, 98%, Riedel-deHaen).
- (4) Hexamethylenetetramine (HMTA) ((CH₂)₆N₄, 99%, Showa).

- (5) Polyethylenimine (PEI) ($(C_2H_5N)_n$, branched, low molecular weight, Aldrich).
- (6) Diethylene glycol (DEG) (99.5%, ethylenediamine-tetra-acetic acid (EDTA)).

3.5 Characteristic Instruments

Powder XRD. Philips PW1700 X-ray diffractometer (XRD) with Cu $K\alpha$ radiation.

High Resolution X-ray Diffraction (HRXRD). Bede D1 diffractometer equipped with a asymmetrically cut Si(220) monochromator and horizontal divergence slits with a width of 100 μm and a height of 2 mm to select the Cu $K_{\alpha 1}$ radiation.

Field Emission Scanning Electron Microscopy (FESEM). (1) LEO 1530, equipped with an EDAX energy-dispersive X-ray (EDX). (2) JOEL-6500, equipped with an energy dispersive spectroscopy (EDS) [Oxford] and electron beam scattering diffraction (EBSD) facilities.

Transmission Electron Microscope (TEM). JEOL JEM-2000FX transmission electron microscope (TEM) operated at 200 KeV. JEOL JEM-2100F field emission transmission electron microscope (FETEM) operated at 200 KeV.

Raman Spectroscopy. Conventional and resonance Raman spectroscopy were carried out by a frequency-doubled Yb:YAG laser ($\lambda = 515 \text{ nm}$) and a He–Cd laser ($\lambda = 325 \text{ nm}$), respectively, and a Jobin-Yvon T64000 micro spectrometer with a 1800 grooves/mm grating in the backscattering configuration was employed. The whole Raman spectra were taken with an accumulation time of 120s from the focused incident laser light about $\sim 1\mu\text{m}$. Figure 3-2 demonstrates triple additive configuration of Jobin-Yvon T64000 micro spectrometer systems. For the purpose of high spectral resolution ($< 0.15 \text{ cm}^{-1}$).

Photoluminescence (PL). The photoluminescence measurement was made also using a 20mW He-Cd laser at wavelength of 325nm and the emitted light was dispersed by a TRIAX-320 spectrometer and detected by a UV-sensitive photomultiplier tube. A closed cycle refrigerator was used to maintain the measured temperature at 10 K while low-temperature measurements.

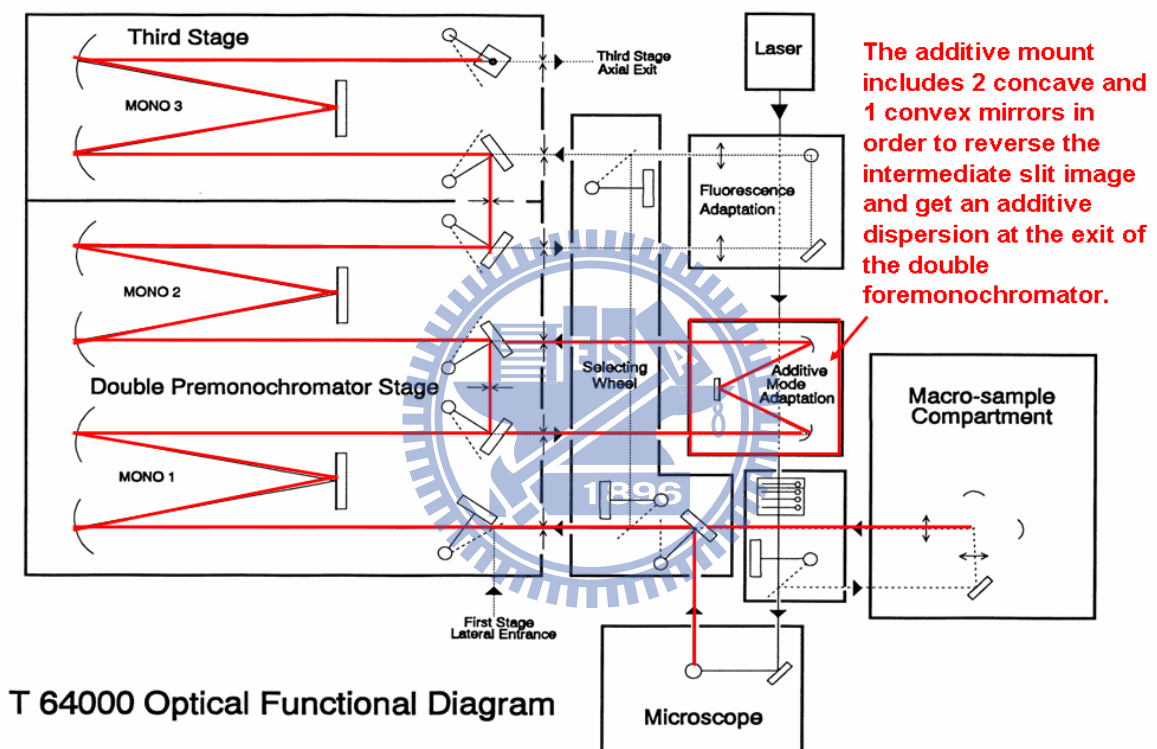


Figure 3-2. Raman detection systems. Light pass for triple additive configuration :
for a very high spectral resolution ($< 0.15 \text{ cm}^{-1}$)

References and Notes

- [1] Tseng, Y. K.; Chia, C. T.; Tsay, C. Y.; Lin, L. J.; Cheng, H. M.; Kwo, C. Y.; Chen, I. C. *J. Electrochem. Soc.* **2005**, 152, G95.
- [2] Law, M.; Greene, L. E.; Johnson, J. C.; Saykally, R.; Yang, P. *Nat. Mater.* **2005**, 4, 455.
- [3] Seelig, E. W. Tang, B. Yamilov, A. Cao, H. and Chang, R. P. H. *Mater. Chem. Phys.* **2003**, 80, 257.



Chapter 4 Growth and Structural Properties for 1-D ZnO Nanostructures

4.1 ZnO Nanostructures on Buffer Layers

4.1.1 ZnO Nanorods on ZnO Buffer Layers

In this section, we report that vertical arrays of well-aligned ZnO nanorods were synthesized on various substrates including glass, Si(111), 6H-SiC(0001) and sapphire(0001), which were pre-coated with *c*-oriented ZnO buffer layers. We will discuss the relationship of in-plane orientation between ZnO nanorods and buffer layers below. Then photoluminescence (PL) properties of the nanorods were also comparatively investigated.

Parts a-h of Figure 4-1 show typical top- and oblique-view SEM photographs of the vertically well-aligned ZnO nanorods, with the lengths of several micrometers, fabricated on the various substrates. As shown, non-uniform, less-aligned ZnO nanorods grow on both glass (Fig. 4-1(a) and (b)), Si (111) (Fig. 4-1(c) and (d)) and 6H-SiC (0001) (Fig. 4-1(e) and (f)). In the case of sapphire (0001) (Fig. 4-1(g) and (h)) substrates, vertically well-aligned ZnO nanorods of a uniform diameter and length were formed. A special interesting part of the ZnO nanorods is the relationship of in-plane orientation which discovered from top-view SEM photographs by the fast Fourier transform (FFT), as shown in the insets. The insets in Fig. 4-1(a) and (c) display the blurred spots. It depicts that the ZnO nanorods on glass and Si (111) are randomly oriented in the in-plane direction. On the contrary, the vertically aligned ZnO nanorods on 6H-SiC(0001) and sapphire(0001) show an in-plane alignment with six-fold symmetry confirmed from the hexagonal starlike spots, as shown in the insets in Fig. 4-1(e) and (g). Moreover, Fig. 4-2(a) and (b) show the magnified top-view

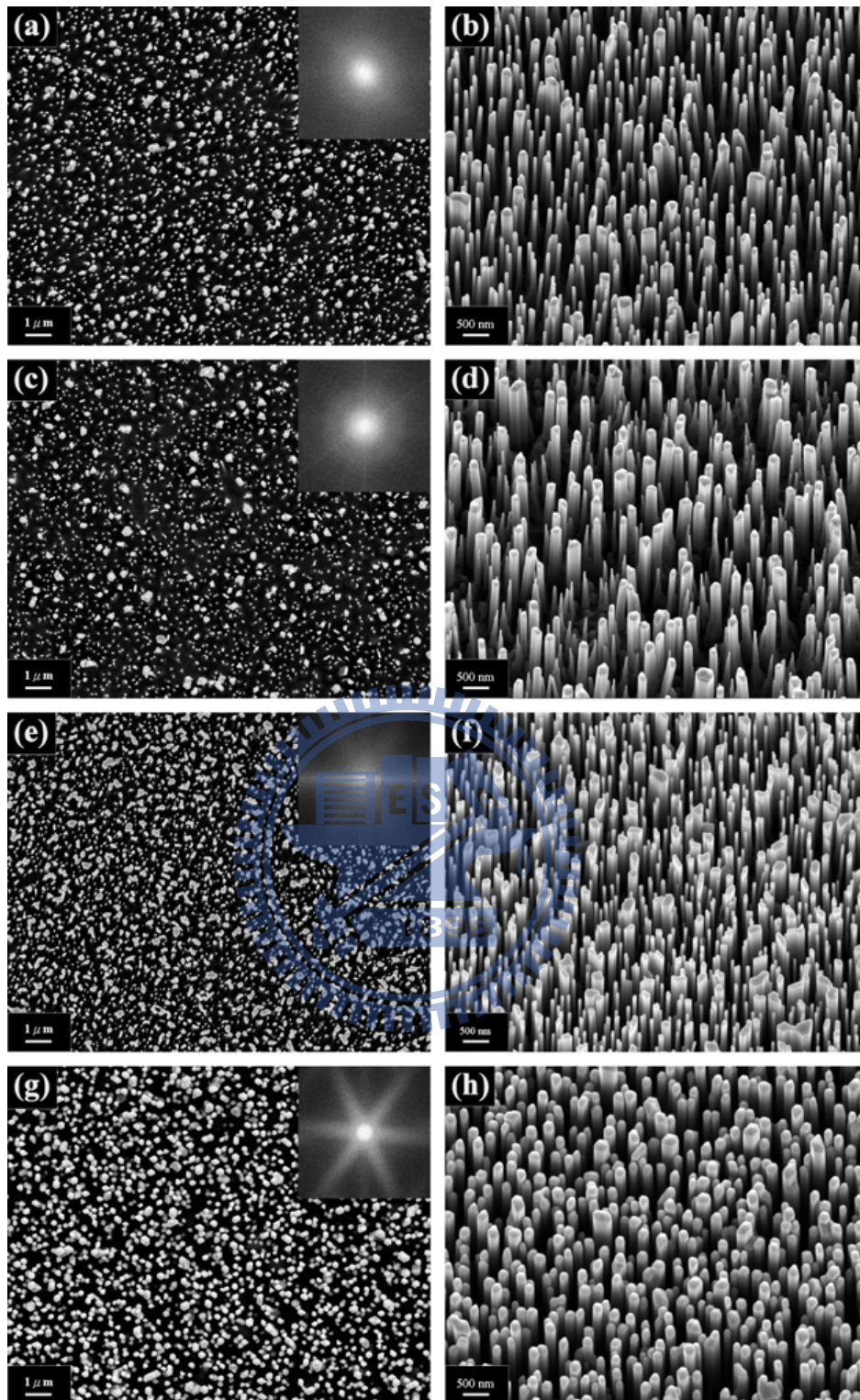


Figure 4-1. Top- and oblique-view SEM photographs of the vertically well-aligned ZnO nanorods fabricated on the various substrates: (a and b) glass, (c and d) Si (111), (e and f) SiC (0001), (g and h) sapphire (0001). The insets of (a), (c), (e) and (g), display the corresponding FFT images from top-view photographs.

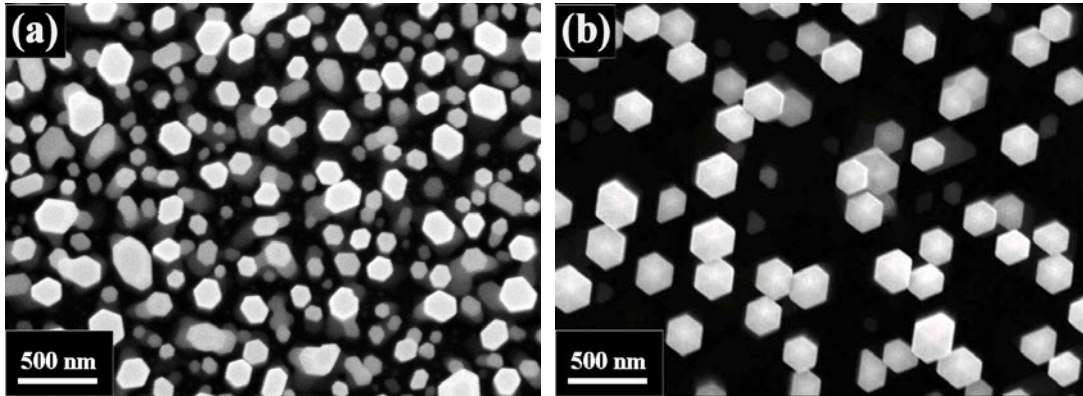


Figure 4-2. Magnified top-view SEM photographs of the vertically well-aligned ZnO nanorods fabricated on the (a) Si (111), and (b) sapphire (0001) substrates.

SEM images of the ZnO nanorods on the Si (111), and sapphire (0001) substrates, respectively. The photographs reveal more evidences that the nanorods have different in-plane orientation when grow on different substrates. The same direction of six-fold facets of individual ZnO nanorods exhibits the better epitaxial relationship for the rods on sapphire (0001) than on Si (111) and other substrates we used. Since the ZnO nanorods were grown continuously above the pre-coated ZnO buffer layers, we firmly believe the differences of relationship of in-plane orientation come from the influences of the pre-coating layers.

The electron beam scattering diffraction (EBSD) also provides crystallographic information of the micro-structures. Figure 4-3 shows the EBSD patterns of two different positions from the ZnO nanorods on the Si (111) substrate. The EBSD patterns constitute a number of Kikuchi lines but are not identical. To specify an orientation, it is necessary to define a reference frame consisting of at least two axes, which is known as a coordinate system. Important surfaces or directions associated with the shape of the specimen are commonly used to define the axes. The direction normal to the specimen surface is called ‘normal surface’, in-plane directions are the

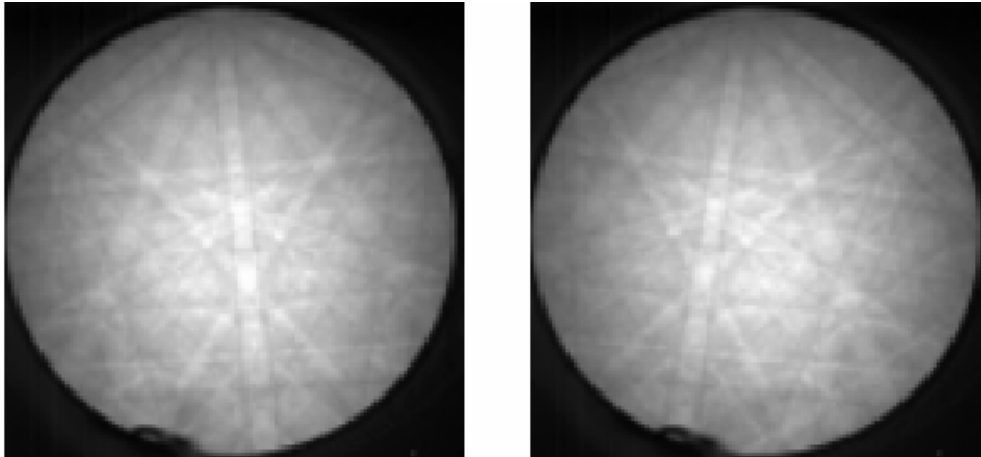


Figure 4-3. The EBSD image taken from two different positions of the ZnO nanorods on the Si (111) substrate.

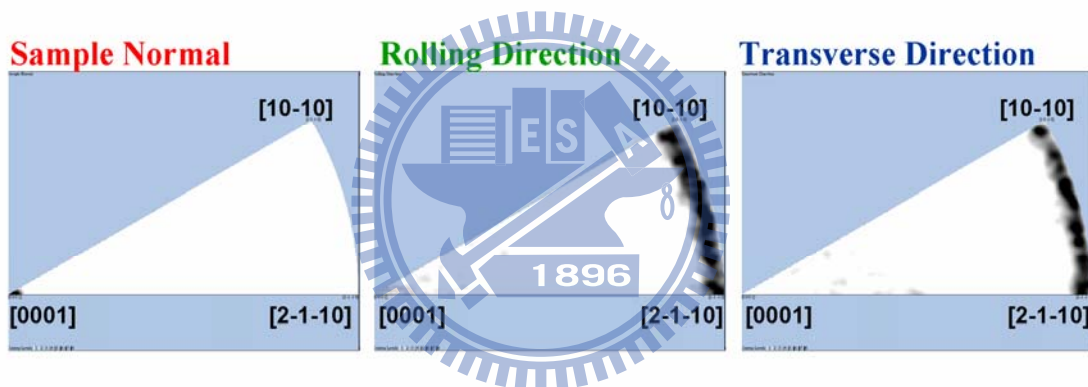


Figure 4-4. The inverse pole figures of the ZnO nanorods on the Si (111) substrate for the three orthogonal directions.

‘rolling direction’ and ‘transverse direction’. Figure 4-4 shows the inverse pole figures. In the normal surface direction, a single spot was observed as a result of the vertically aligned of the nanorods. However, both in the rolling and transverse directions, a continuous curve appeared. It indicates that the in-plane orientation of nanorods is disordered.

On the contrary, the EBSD patterns of two different positions from the ZnO nanorods on the sapphire (0001) substrate are identical as shown in Fig. 4-5. The

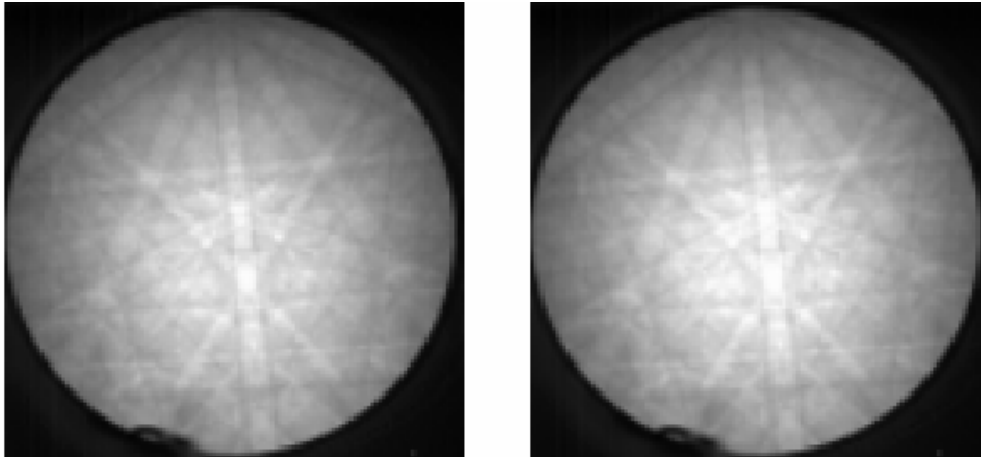


Figure 4-5. The EBSD image taken from two different positions of the ZnO nanorods on the sapphire (0001) substrate.

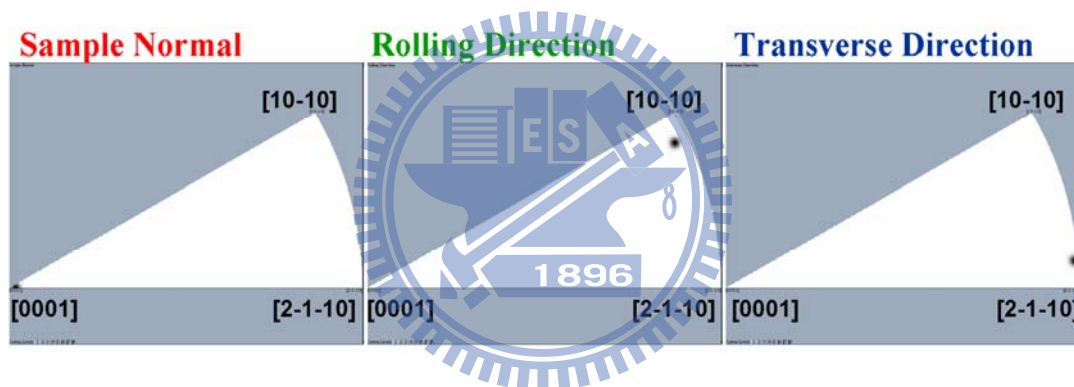


Figure 4-6. The inverse pole figures of the ZnO nanorods on the sapphire (0001) substrate for the three orthogonal directions.

inverse pole figure maps are shown in Fig. 4-6. A discrete peak was observed both at the rolling and transverse directions. It clearly indicates that the nanorods with not only the out of plane order but also in-plane order.

Figure 4-7(a) shows the cross-sectional TEM image of ZnO nanorods on Si(111). The difference on brightness of the image is due to the diffraction from varied crystallographic planes. Therefore, the ZnO film has a grainy and columnar structure. Furthermore, the ZnO nanorods were grown along the columnar grains of ZnO film.

ZnO buffer layer behaves as the active nucleus for growth of ZnO nanorods. In addition, the selected-area electron diffraction (SAED) patterns, as shown in Fig. 4-7(b) and (c) indicate the columnar grains of the ZnO film were grown along the [0001] direction and hence ZnO nanorods were also epitaxially grown along the same direction. Figure 4-7(e) shows a high resolution TEM (HRTEM) image confirmed that the nanorods is a single crystal and the lattice spacing of approximately 5.2Å along the *c*-axis, indicating again [0001] as the preferred growth direction for ZnO nanorods.

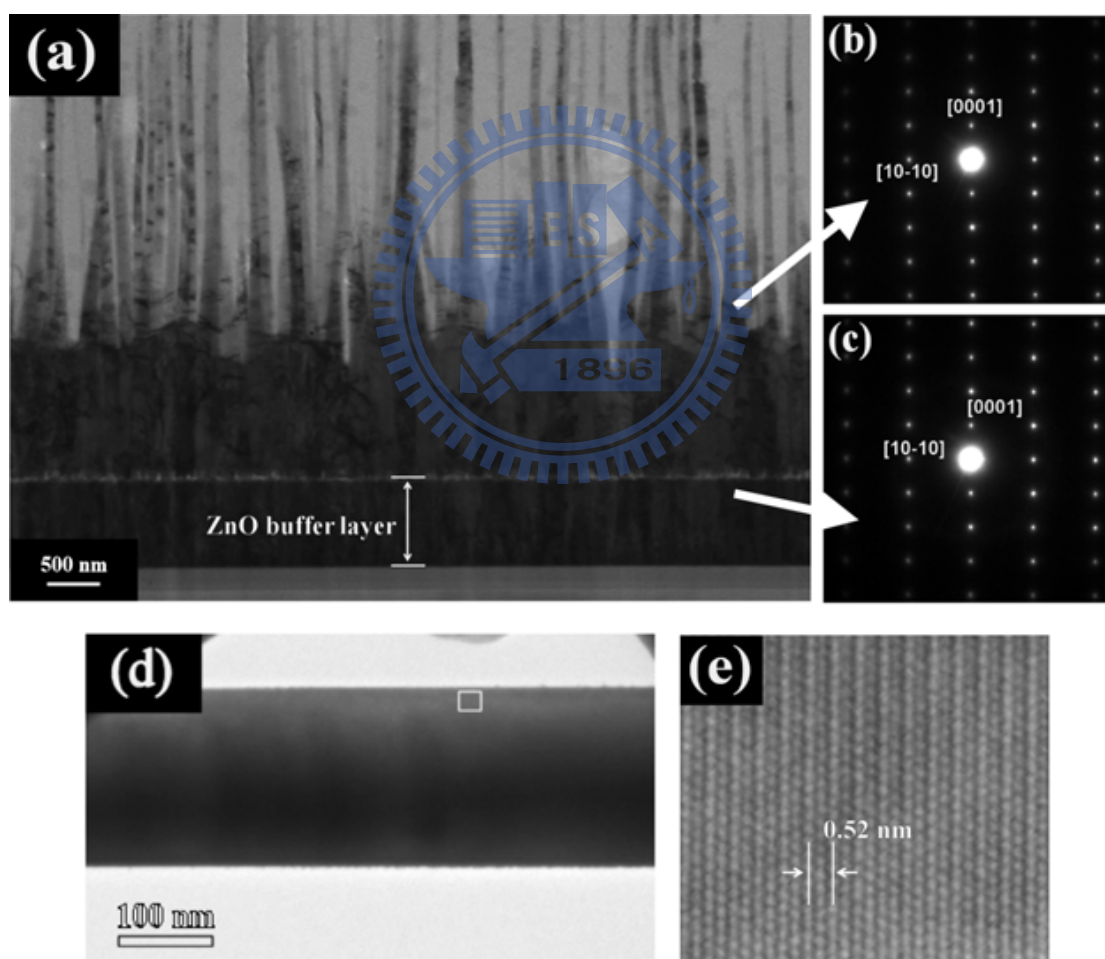


Figure 4-7. (a) Cross-sectional TEM image of ZnO nanorods grown on ZnO buffer layer. (b) and (c) The SAED images of ZnO nanorods and buffer layer, respectively. (d) Single nanorods image, no catalyst particle at the end. (e) HRTEM image shows the [0001] direction and the lattice spacing 0.52 nm.

Whereas the ZnO buffer layer below governs the in-plane orientation of ZnO nanorods above. Investigating the growth orientation and crystal alignment of the ZnO buffer layers grown on the substrates seems more significant. Various XRD techniques were performed. Figure 4-8 shows the θ - 2θ x-ray diffraction patterns. Only the {0001} reflection family of ZnO and surface paralleled plane of substrate appear in the wide angle XRD profile, indicating all the ZnO films have a single ZnO phase as well as a complete c -axis preferential growth. Meanwhile, the corresponding ZnO(0002) θ -rocking curve was also performed to investigate the degree of alignment to the normal of the surface, as depicted in the inset of Fig. 4-8. The ZnO buffer layer, which was grown on the glass, shows very broad vertical mosaic distribution of 2.56° , as shown in the inset of Fig. 4-8(a). The broad mosaic distribution causes some ZnO nanorods grown slightly along the inclined angle, due to the mosaic grains behave as the nucleus for growth of ZnO nanorods. These can be easily expected since the glass substrate has amorphous phase. Comparison with the glass substrate, the mosaic distributions become narrower as 0.73° and 0.85° for ZnO films grown on Si (111) and SiC (0001) substrates, respectively. The slightly tilt ZnO nanorods can also be found on those two substrates. It should be noted here that the mosaic distributions of the ZnO buffer layer on sapphire(0001) shows extremely narrow FWHM values of 0.056° as shown in the inset of Fig. 4-8(d), meaning that the buffer layer on the sapphire substrates were almost perfectly grown along the c -axial direction. Therefore, the ZnO nanorods reflect more uniformity and vertical alignment on sapphire (0001) being comparable to other substrates.

To explaining the in-plane growth relationship of ZnO nanorods, the XRD Φ -scan analysis of ZnO($20\bar{2}2$) plane was using to investigate the ZnO buffer layers on different substrates. Figure 4-9(a) and (b) demonstrate that the ZnO buffer layers

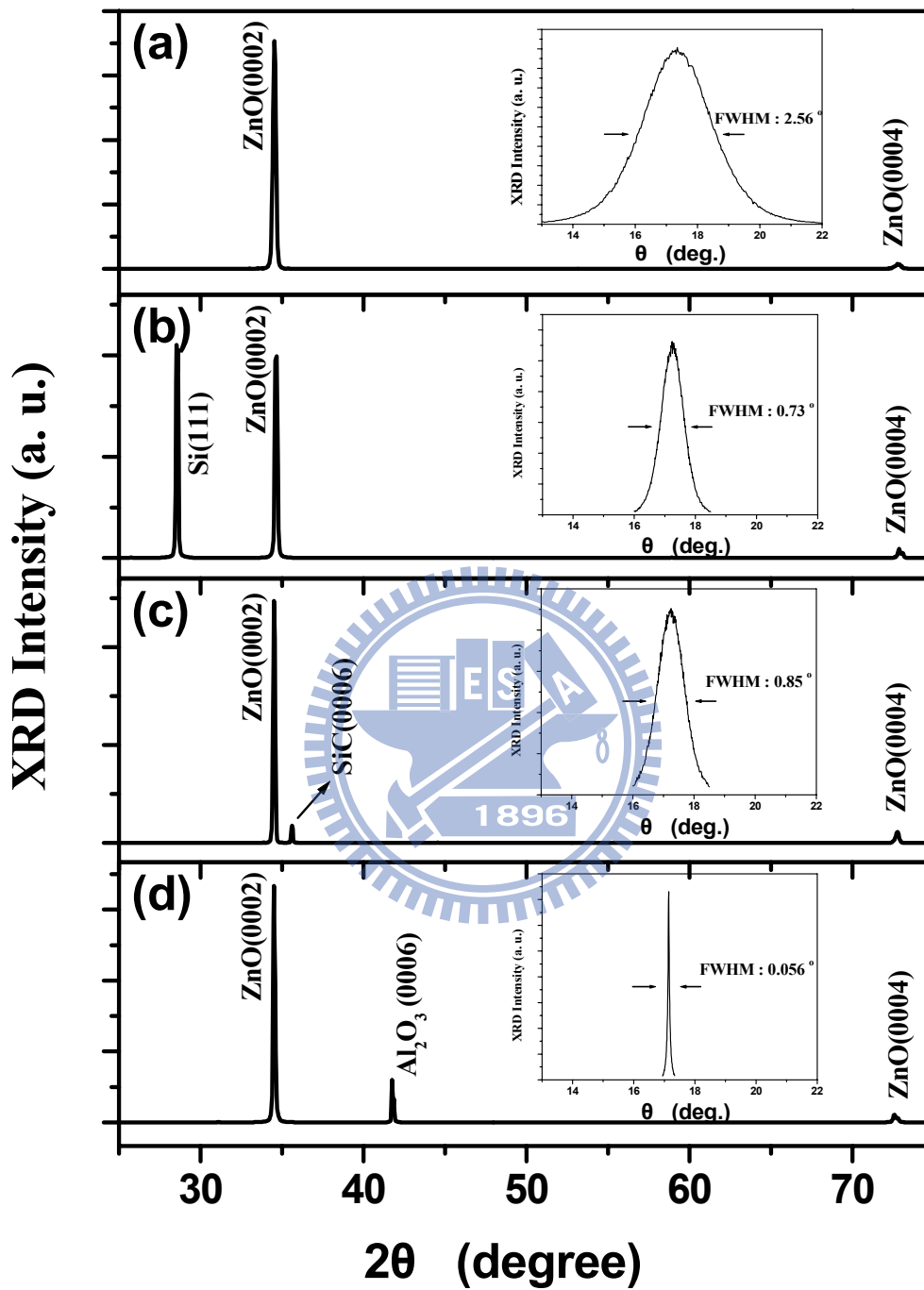


Figure 4-8. θ - 2θ XRD profile of ZnO buffer layers on the various substrates: (a) glass, (b) Si (111), (c) SiC (0001), (d) sapphire (0001), and corresponding ZnO(0002) θ -rocking curve show as the insets.

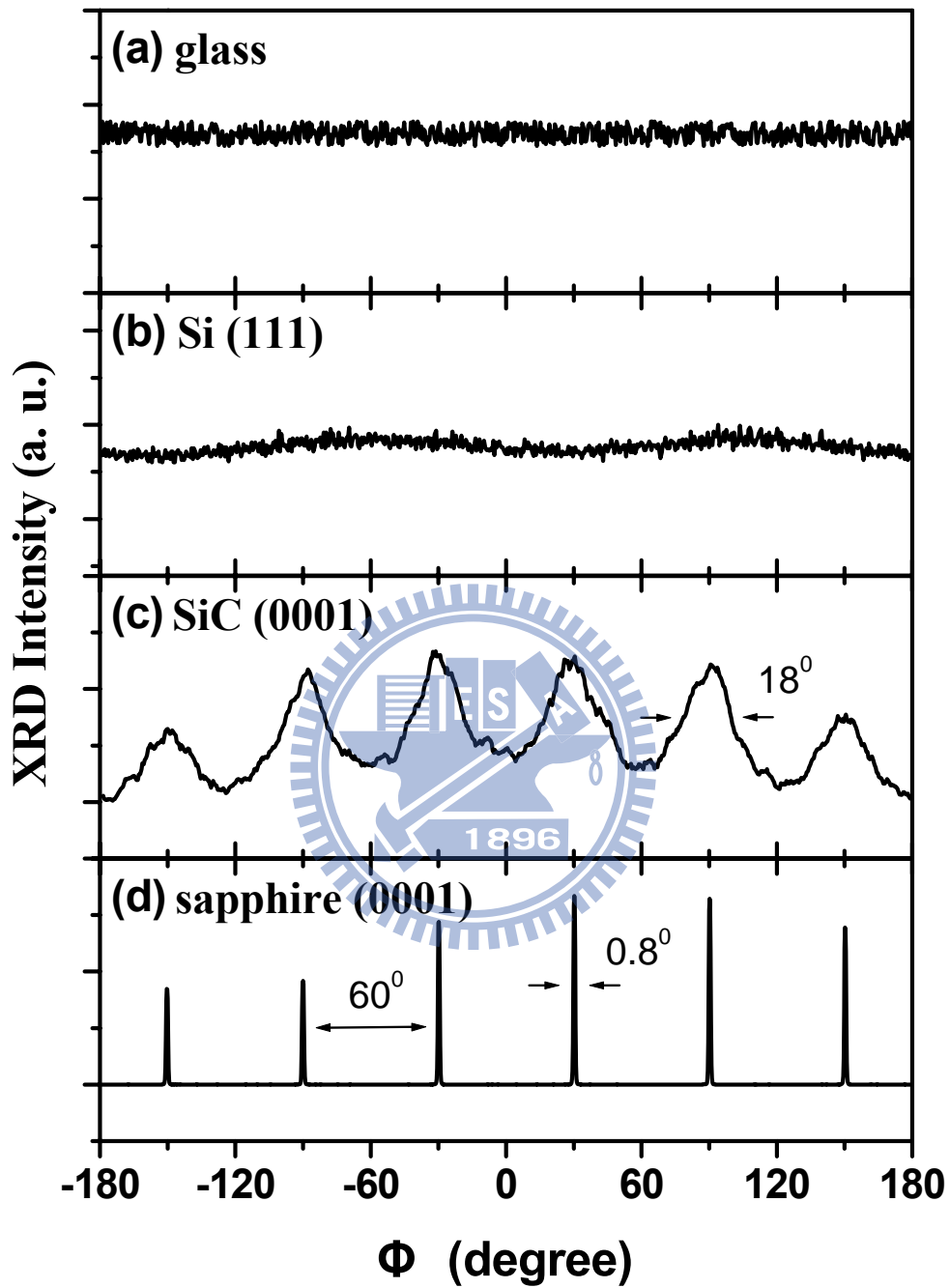


Figure 4-9. X-ray ϕ -scan profiles of ZnO (20 $\bar{2}$ 2) plane from ZnO buffer layers on the various substrates: (a) glass, (b) Si (111), (c) SiC (0001) and (d) sapphire (0001).

on glass and Si(111) have random alignment along the in-plane direction. The reasons are explained in terms of amorphous phase for glass and the possible formation of an amorphous silica layer between ZnO and Si substrate. Although the lattice mismatch between ZnO and Si (111) is $\sim 3.5\%$, but the difficulty basically stems from the fact that Si surface gets easily oxidized during the nucleation stage of a ZnO growth process [1]. In contrast, the ZnO buffer layers on 6H-SiC(0001) and sapphire(0001) exhibit an in-plane alignment with six-fold azimuthal symmetry, as shown in Fig. 4-9(c) and (d). Integrated evidence indicates that the epitaxial relationship between ZnO buffer layer and 6H-SiC (0001) substrate would be $[0001]_{\text{ZnO}} // [0001]_{\text{SiC}}$ along the normal of the substrate, and $[10\bar{1}0]_{\text{ZnO}} // [10\bar{1}0]_{\text{SiC}}$ along the in-plane direction. For sapphire substrate the epitaxial relationship would be $[0001]_{\text{ZnO}} // [0001]_{\alpha\text{-Al}_2\text{O}_3}$ and $[10\bar{1}0]_{\text{ZnO}} // [11\bar{2}0]_{\alpha\text{-Al}_2\text{O}_3}$. In addition, the sharp peaks of XRD ϕ -scan for ZnO buffer layer on sapphire (0001) indicate well aligned in the in-plane direction with comparison of the buffer layer on SiC(0001). This result also consist with the FFT SEM image as shown the sharp star-like spots when ZnO nanorods grown on sapphire (0001). Consequently, we consider the excellent normal and in-plane alignment for ZnO buffer layer on sapphire (0001), therefore improving the growth of ZnO nanorods.

The PL spectra of the ZnO nanorods on different substrates are shown in Fig. 4-10. For all spectra, sharp ultraviolet (UV) peaks observed in the range of 3.0–3.4 eV were attributed to the exciton-related recombination. The weak green emissions in the range of 2.1-2.7 eV, attributed to the oxygen vacancies (V_o), are investigated when using glass and Si (111) substrate, as shown in Fig. 4-10(a) and (b). The weak yellow emission in the range of 1.9-2.4 eV, attributed to the oxygen interstitials (O_i), is appeared when using SiC (0001) substrate, as shown in Fig. 4-10(c).

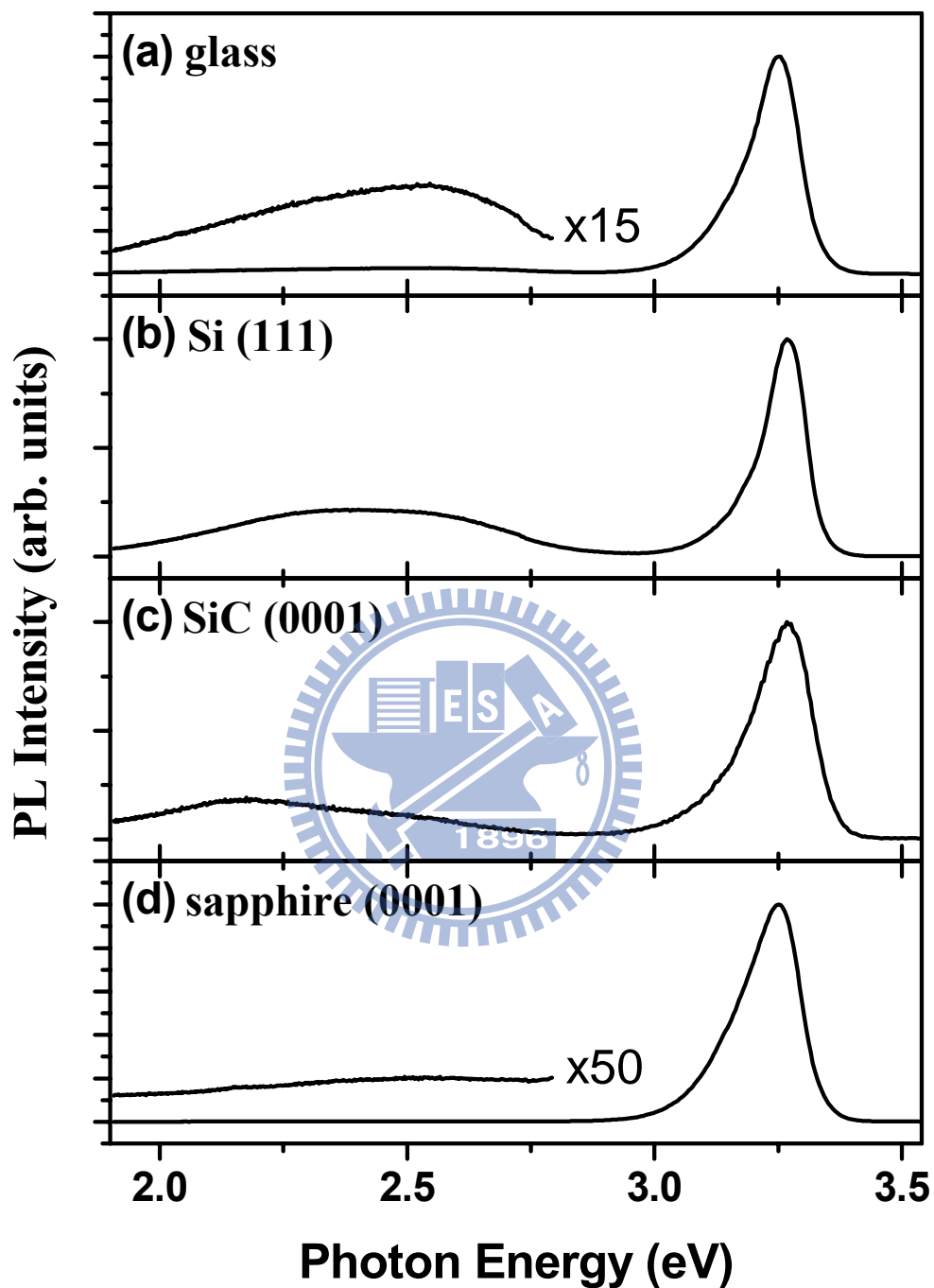


Figure 4-10. Typical room-temperature photoluminescence (RTPL) spectra of ZnO nanorods on the various substrates: (a) glass, (b) Si(111), (c) SiC(0001), and (d) sapphire(0001). All the ZnO nanorods exhibit a strong UV emission, and the distinct visible emissions, as shown in enlarged in the inset (a), (b) and (c), were attributed to nonstoichiometric defects.

The strong UV emission with no visible band in the PL spectra indicates that the ZnO nanorods grown on sapphire (0001) have a good crystal quality with few nonstoichiometric defects, as shown in Fig. 6(d). The various defect-related emissions were also reported in ZnO nanostructures fabricated by different method [2]. In our work, we suppose the visible emissions come from the interface between pre-coated buffer layers and nanorods, because of strain and squeeze from discontinuous ZnO grain. Other analytical techniques such as cathodoluminescence will be used to confirm this controversy in our further investigation.

In summary, well-aligned ZnO nanorods were synthesized without employing any metal catalysts on glass, Si (111), 6H-SiC (0001) and sapphire (0001), but were pre-coated with *c*-oriented ZnO buffer layers. The alignments of ZnO nanorods on the different substrates depend on the crystallographic alignment of pre-coed ZnO buffer layer. Similarly, the photoluminescence measurements show the distinct appearance of ZnO nanorods on different substrates. Among various substrates, ZnO nanorods grown on the sapphire (0001) substrate exhibit only UV peak without noticeable visible emission confirm epitaxial growth and good crystalline quality. Consequently, crystal structure and characterization of ZnO nanorods are basically related to the type of the substrates used.

4.1.2 ZnO Nanowires on GaN Buffer Layers

In this section, we report that vertical arrays of well-aligned ZnO nanowires were epitaxially fabricated on the GaN-buffered sapphire substrate by employing catalyst-free metal vapor deposition. We will discuss the interesting optical features of phonon quantum confinement and efficient UV emission in the use of Raman and photoluminescence (PL) spectroscopy. We also confirm a very small strain in the arrays of single crystal ZnO nanowires by transmission electron microscopy (TEM) and high resolution X-ray diffraction (HRXRD).

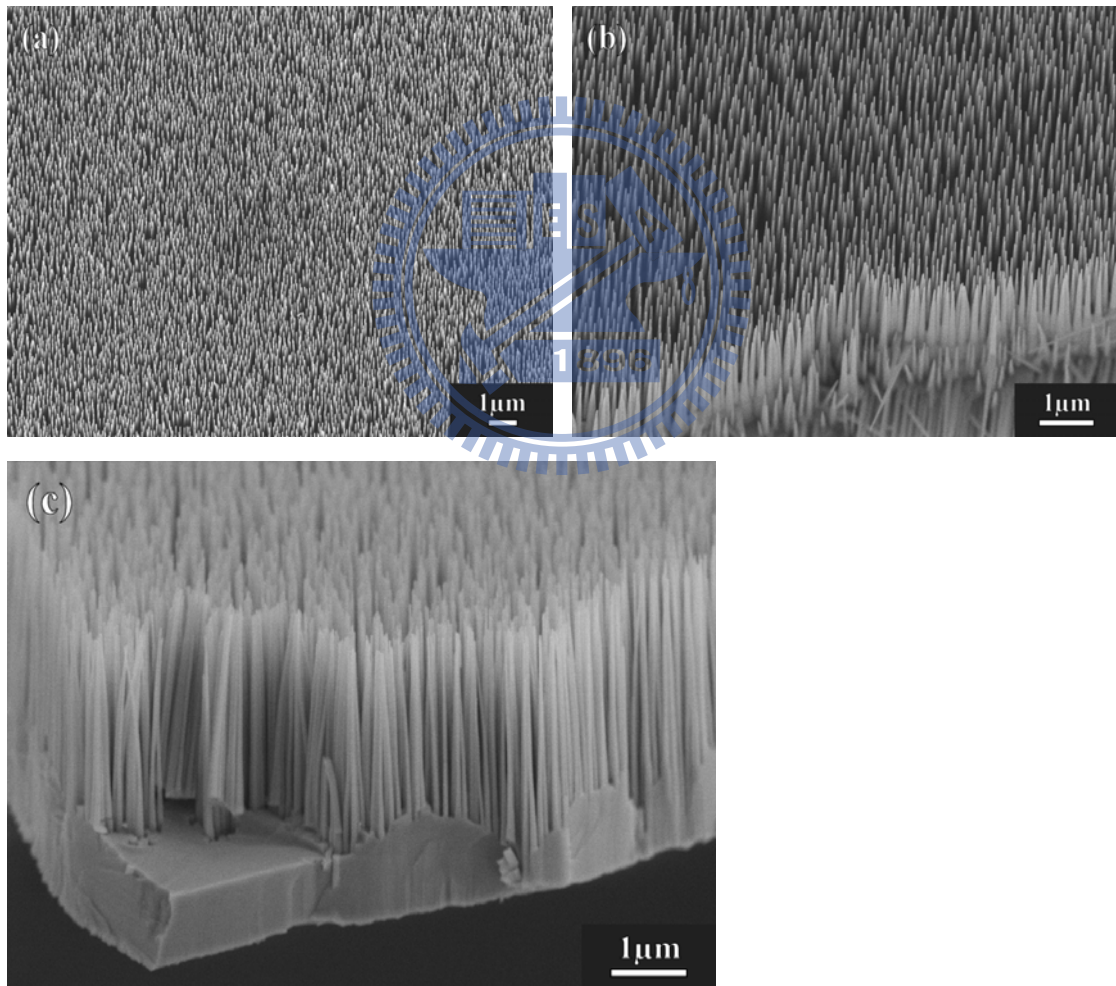


Figure 4-11. SEM images of vertically well-aligned ZnO nanowires grown on GaN-buffered sapphire substrate. (a, b) Large-scale and magnified SEM micrographs shows the uniformly 80–100 nm in diameter of ZnO nanowires and (c) cross-sectional image shows the length about 3.0 μm.

The general morphology of ZnO nanowires was obtained using field emission scanning electron microscopy (FESEM). As shown in Figure 4-11, vertically well-aligned arrays of ZnO nanowires with high density ($\sim 10^{10} \text{ cm}^{-2}$) were uniformly grown over the entire substrate. The length and diameter of the nanowires were controlled in the range between (2.8-3.0) μm and (80–100) nm, respectively. The EDS analyses showed that the nanowires are composed of Zn and O, while the element of Ga was also detected on the substrate. Further structural characterization of the ZnO nanowires was performed with TEM. Figure 4-12(a) displays the TEM image of a nanowire scratched from the substrate, and its selected area electron diffraction (SAED) pattern reveals the single-crystal wurtzite structure of the ZnO nanowire. From the high-resolution TEM (HRTEM) image, we determined the lattice spacing to be 0.52 nm that corresponds to the d -spacing of (0002) crystal planes. The inset in Figure 4-12(b) displays the fast Fourier transform of the HRTEM image that confirms the ZnO nanowires are preferentially oriented in the c -axis direction.

Figure 4-13 shows the θ - 2θ X-ray diffraction patterns. Only the {0001} reflection family of ZnO, GaN, and the sapphire substrate appear in the wide-angle XRD profile of Figure 4-13(a). Statistical evidence indicates that the epitaxial relationship between ZnO and GaN with the sapphire substrate would be $[0001]_{\text{ZnO}} // [0001]_{\text{GaN}} // [0001]_{\alpha\text{-Al}_2\text{O}_3}$ along the normal of the substrate, and $[10\bar{1}0]_{\text{ZnO}} // [10\bar{1}0]_{\text{GaN}} // [11\bar{2}0]_{\alpha\text{-Al}_2\text{O}_3}$ along the in-plane direction. More evidence of epitaxial growth was confirmed using the XRD phi-scan analysis, described in the previous report [3]. Meanwhile, the measurement of XRD θ -rocking curve was also performed to investigate the degree of alignment to the normal of the surface, as indicated in the inset of Figure 4-13(a). It depicts that the θ -rocking curve of ZnO(0004) has a full

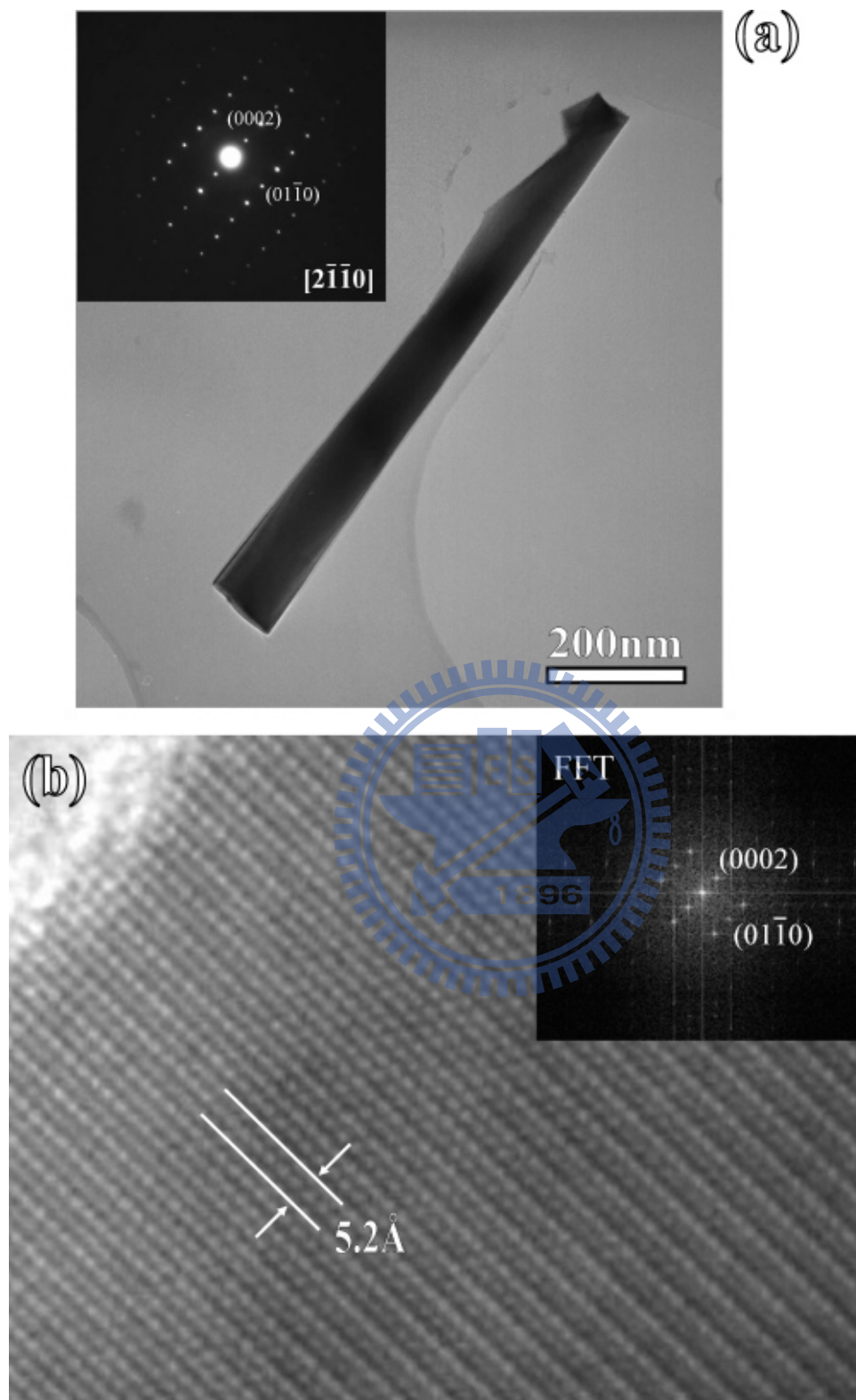


Figure 4-12. (a) TEM image of wurtzite structure ZnO nanowire and the corresponding electron diffraction pattern (inset). (b) HRTEM image with inset of its corresponding FFT pattern.

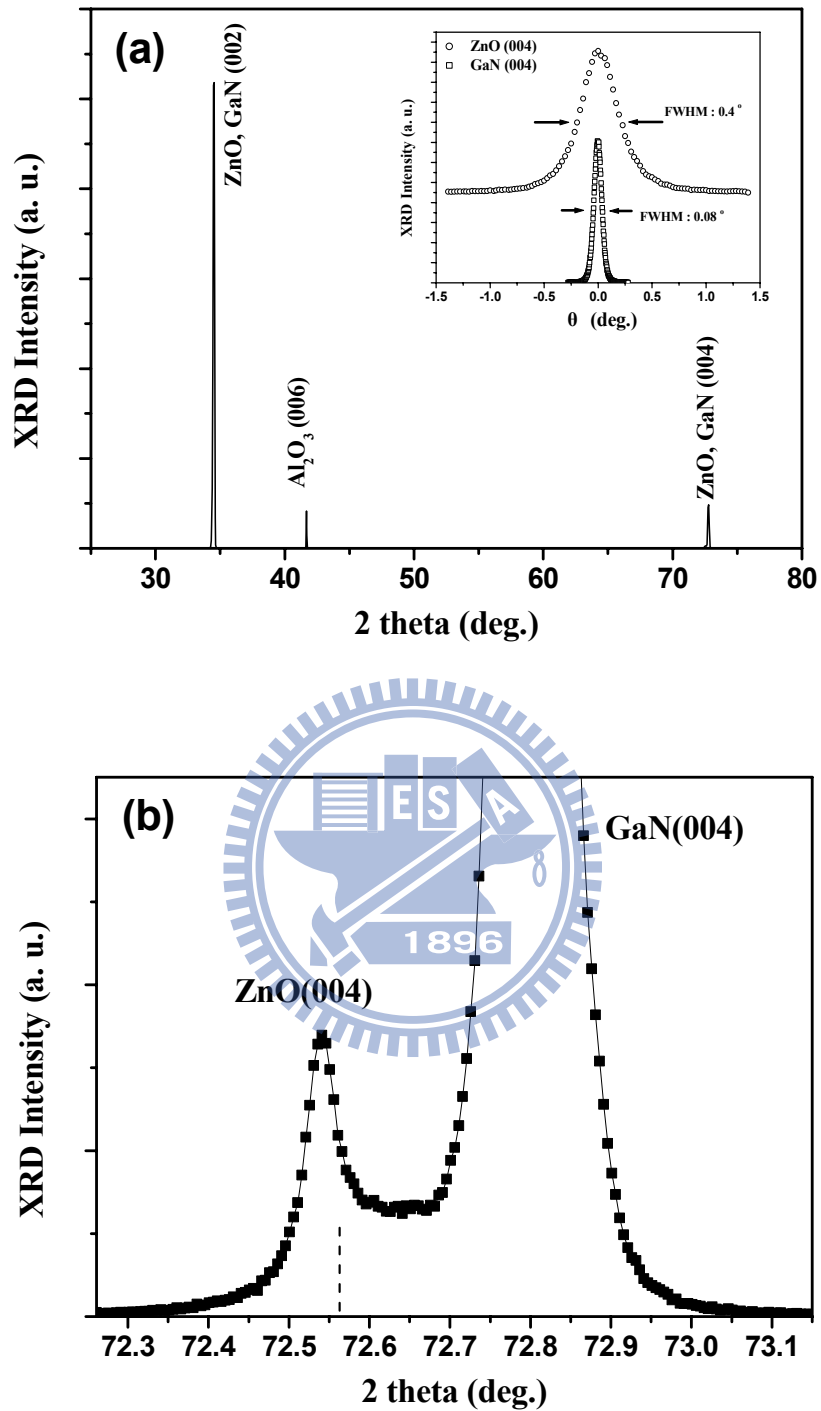


Figure 4-13. (a) θ - 2θ XRD profile of ZnO nanowires on epi-GaN(001)/ α -Al₂O₃(001). The inset depicts the θ -rocking curves of ZnO(004) and GaN(004), respectively. (b) HRXRD shows the (004) reflection of ZnO nanowires slightly shift from that of the strain-free ZnO powder (dash line).

width at half-maximum (fwhm) of 0.4° . The fwhm of ZnO nanowires grown on GaN-buffered *c*-plane sapphire was smaller than those directly grown on the *c*-plane sapphire without the buffer layer [4]. The narrow fwhm of the ZnO(0004) diffraction peak implies that the *c*-axes of nanowires are well oriented along the normal of the substrate surface but it is still 5 times larger than the (0004) peak of GaN buffer layer because of the tilt mosaic effects on ZnO nanowires. Since the similar mosaic structure can be easily observed for the epi-GaN layers [5], the quality of the ZnO nanowires grown on epi-GaN is basically limited by the quality of epi-GaN used as the buffer layer or even worse. The HRXRD pattern shown in Figure 4-13(b) demonstrates the strongly reflected GaN(0004) diffraction peak and the relatively weak ZnO(0004) peak, separately. However, it should be mentioned that the position of ZnO(0004) peak at 72.541° corresponds to $c = 5.208\text{\AA}$, which slightly differs from that of the strain-free ZnO powder [6] with $c = 5.206\text{\AA}$. The wurzite ZnO crystal would be elongated along the *c*-axis under a tensile strain in *c*-plane.

To further explore the strain in ZnO nanowires, reciprocal space mapping (RSM) was carried out to determine *a* and *c* lattice parameters of ZnO nanowires. Figure 4-14 shows the RSM of the asymmetric $(20\bar{2}4)$ reflection of the arrays of ZnO nanowires and the epi-GaN buffer layer. The reflection of the underlying GaN template has always been used as a reference and therefore the points in reciprocal space are given by *l* and *k* in units of the reciprocal vectors of GaN, $[0001]_{\text{GaN}}$, and $[10\bar{1}0]_{\text{GaN}}$, respectively. For the wurzite materials such as GaN and ZnO, the magnitudes of these vectors are $|[0001]| = (2\pi/c)$ and $|[10\bar{1}0]| = (4\pi/\sqrt{3}a)$, which unambiguously determine the correlation between the values of *l* and *k* and the lattice constants *c* and *a* in real space, respectively. Because the GaN buffer layer has $c_{\text{GaN}} = 5.192\text{\AA}$ and $a_{\text{GaN}} = 3.188\text{\AA}$, which is also strained by the sapphire substrate, the

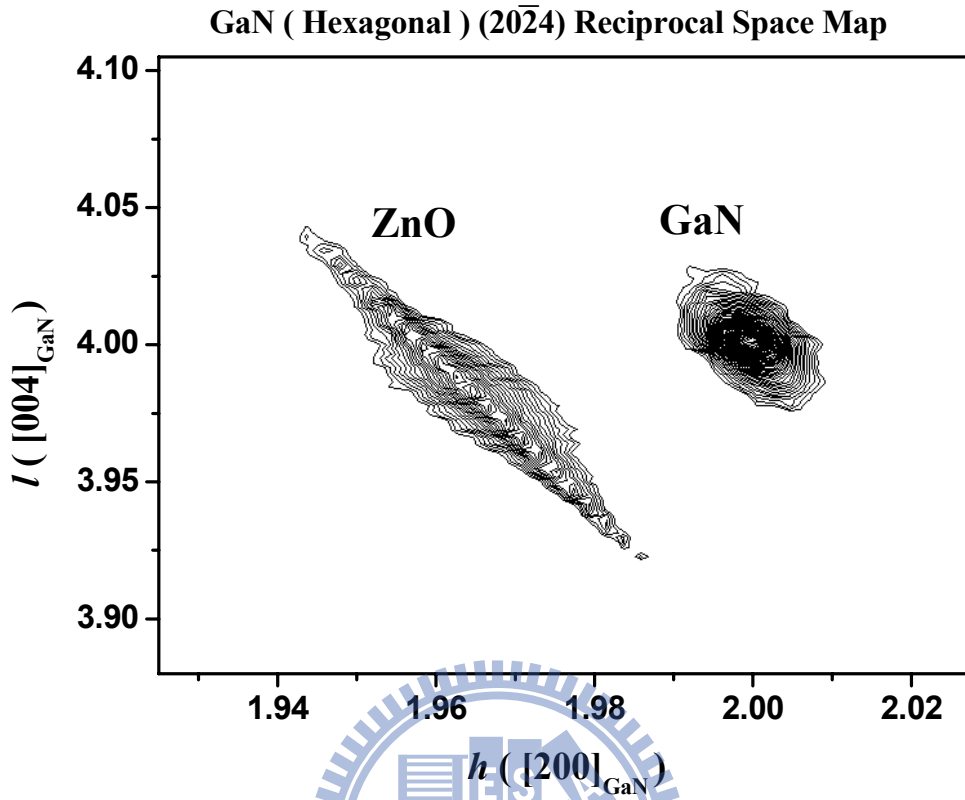


Figure 4-14. Reciprocal space map of asymmetric ($20\bar{2}4$) diffraction spots of a ZnO nanowires and epi-GaN buffer layer. The intensities are plotted logarithmically.

lattice constants of ZnO nanowires in the arrays can be estimated to be $c_{\text{ZnO}} = 5.208 \text{ \AA}$ and $a_{\text{ZnO}} = 3.248 \text{ \AA}$ by use of the relationships: $l^*|[0001]_{\text{GaN}}| = (2\pi)/(c_{\text{ZnO}}/4)$ and $h^*|[10\bar{1}0]_{\text{GaN}}| = (4\pi)/(\sqrt{3} a_{\text{ZnO}}/2)$. The lattice constants slightly differ from those of the strain-free ZnO powder, which has $c_o = 5.2066 \text{ \AA}$ and $a_o = 3.2498 \text{ \AA}$; thus, the strains: $\varepsilon_{zz} = \varepsilon_{cc} = (c - c_o)/c_o > 0$ and $\varepsilon_{xx} = \varepsilon_{aa} = (a - a_o)/a_o < 0$, indicate a biaxial compressive strain in the a -plane, and an uniaxial tensile strain along the c -axis. Since the thermal expansion coefficient of ZnO ($6.51 \times 10^{-6}/\text{K}$) is a little distinct from that of GaN ($5.59 \times 10^{-6}/\text{K}$) [7] and the reaction occurs at the low temperature of $550 \text{ }^\circ\text{C}$, it is expected that the strain comes from the nature lattice misfit between ZnO and GaN.

The residual in-plane biaxial stress can be obtained via the equation [8]

$$\sigma = -453.6 \times 10^9 \varepsilon_{zz} . \quad (1)$$

It can thus be calculated that the arrays of ZnO nanowires have a compressive stress of -121.9 MPa when using the strain value $\varepsilon_{zz} = 0.0269 \%$, which is quite smaller than that of ZnO nanowires grown on other substrates [9].

The UV Raman scattering was performed to investigate the vibrational properties of the ZnO arrays of ZnO nanowires at room temperature. Since the wurtzite structure of ZnO and GaN belongs to the space group $C_{6v}^4 (P6_3mc)$, one primitive cell includes two formula units, with all of the atoms occupying $2b$ sites of symmetry C_{3v} . Group theory predicts the existence of the following optic modes: $A_1 + 2B_1 + E_1 + 2E_2$ at the Γ point of the Brillouin zone; B_1 (low) and B_1 (high) modes are normally silent; A_1 , E_1 , and E_2 modes are Raman active, and A_1 and E_1 are also infrared active. Thus, A_1 and E_1 are split into longitudinal (LO) and transverse (TO) optical components. Figure 4-15(a) shows a normal Raman spectrum of the ZnO nanowires which was taken with an accumulation time of 300 s from a $1 \mu\text{m}^2$ spot size excited by a frequency-doubled Yb:YAG laser ($\lambda = 515 \text{ nm}$). As we can see, the remarkable E_2 (high) mode of ZnO is located at 437 cm^{-1} ; the weak and almost invisible signal around 580 cm^{-1} is contributed to the A_1 (LO) and E_1 (LO); and the E_1 (TO), E_2 (high), and A_1 (LO) modes that belong to the epi-GaN buffer layer were also observed at 559 cm^{-1} , 569 cm^{-1} and 737 cm^{-1} , respectively, because of the penetration of 515-nm laser light. In the backscattering geometry, the E_1 (LO) mode is theoretically forbidden according to the Raman selection rules, however, it can be still visible if the incident direction of the excited light beam with respect to the crystal axes is not well-defined in the use of the focusing lens for micro-Raman measurement, and thus mixed modes may be observed. Furthermore, the bending and the tilting of ZnO nanowires may probably cause the

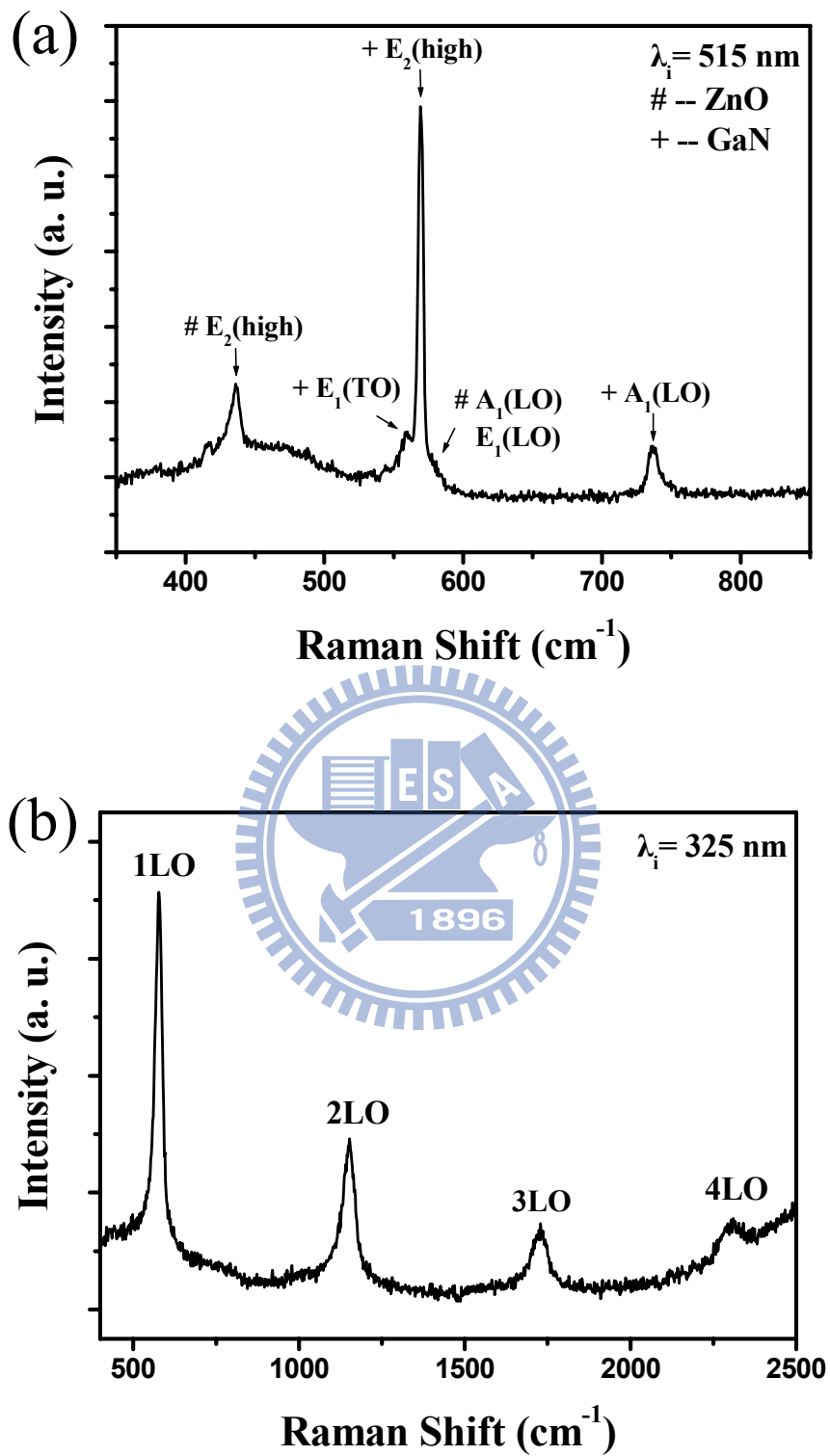


Figure 4-15. (a) Conventional Raman spectrum of ZnO nanowires on GaN buffer layer at room temperature using a frequency-doubled Yb:YAG laser ($\lambda = 515 \text{ nm}$). (b) Resonant Raman scatterings (RRS) of ZnO nanowires on GaN buffer layer using a He-Cd laser ($\lambda = 325 \text{ nm}$). The $n\text{LO}$ refers to the n th longitudinal optical phonon.

appearance of the $E_I(\text{LO})$ mode.

For the advanced study, we used a He–Cd laser ($\lambda = 325 \text{ nm}$) as the excitation source. In resonant Raman scattering (RRS), the exciting photon energy is resonant with the electronic interband transition energy of the wurtzite ZnO. The polar symmetry makes the $A_I(\text{LO})$ and $E_I(\text{LO})$ modes the dominant modes and it may exhibit different frequencies from the transverse-optic (TO) modes. An intense multi-phonon scattering was observed in the resonant Raman spectrum of Figure 4-15(b), where four major bands were observed, centered at 577, 1154, 1729, and 2300 cm^{-1} , with bandwidths of 28 cm^{-1} , 49, 58, and 62 cm^{-1} , respectively, which mainly result from the polar symmetry modes $A_I(\text{LO})$ and $E_I(\text{LO})$ and their overtones. The first order Raman mode at 577 cm^{-1} is a superposition of the $A_I(\text{LO})$ mode at 574 cm^{-1} and the $E_I(\text{LO})$ mode at 583 cm^{-1} in which Zn atoms and O atoms have the same vibration direction, respectively to the neighbor lattices of the wurtzite ZnO [10]. The weak peak, around 437 cm^{-1} , which is contributed to the $E_2(\text{high})$ mode around 437 cm^{-1} , is almost imperceptible as a result of other (overlapping/stronger) RRS peaks. The absence of the TO modes could be attributed to the special angle between the wave vector of photons and the c -axis of the wurzite ZnO crystals in the near backscattering geometry employed in our measurement.

Multiphonon scattering processes have also been previously reported for single crystalline bulk ZnO [11], and recently for ZnO films [12], ZnO-opal structures [13] and ZnO nanowires grown on m -sapphire [14]. The line widths of multiphonon scatterings cannot be explained by the equation [10] $\sigma(n\text{LO}) = 9n \text{ (cm}^{-1}\text{)}$. The observed broadening of phonon line width is attributed to the phonon quantum confinement in ZnO nanowires. A similar broadening effect has also been observed in ZnO nanoparticles [15] and in ZnO nanowires [14], which were grown on an

m-sapphire substrate. Careful analysis of the resonant Raman spectrum was performed by the peak fitting, as shown in Figure 4-16. The luminescence baseline was first removed and double Lorentzian profiles were chosen to fit the individual peaks of $A_1(nLO)$ and $E_1(nLO)$. The results of curve fitting give the multiphonon scattering of $A_1(nLO)$ located at 571, 1139, 1713, and 2282 cm^{-1} , with the multiphonon scattering of $E_1(nLO)$ located at 581, 1156, 1737, and 2313 cm^{-1} . The intensity ratio of $A_1(nLO)/E_1(nLO)$ was obviously increased for the higher order phonon scattering. Because the atoms in the E_1 mode displace along the a -axis, they could be easily restrained with the degrees of freedom defined by the cross section of ZnO nanowires. On the contrary, the A_1 mode is less affected by shrinking the diameter of ZnO wires because of its vibration along the c -axis. Accordingly, the intensity ratio of A_1/E_1 increases as the order of phonon scattering is increased. It is again further evidence of the phonon quantum confinement in ZnO nanowires.

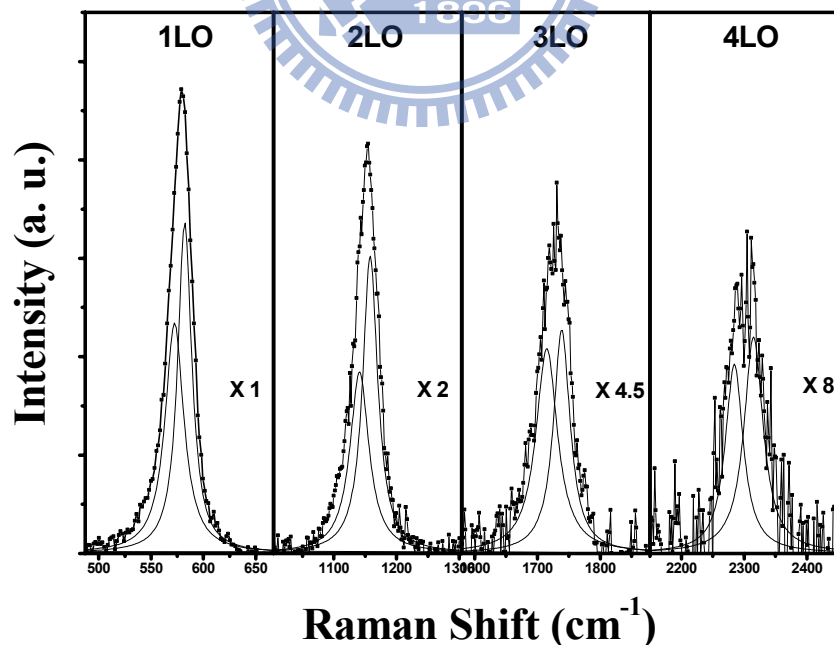


Figure 4-16. Fitting profile of RRS spectrum and its decomposition. The scatter lines represents the recorded nLO RRS, and the solid lines are its decomposition which indicate $A_1(nLO)$ and $E_1(nLO)$, respectively.

Figure 4-17(a) shows a typical PL spectrum taken at room temperature, which consists of a strong UV peak at 3.26 eV and relatively no other visible emission. The UV band was attributed to the exciton-related emission near the band-edge, usually be reported as the recombination of free excitons. The strong UV emission with no visible band in the PL spectra indicates that the ZnO nanowires grown on GaN have a good crystal quality with few nonstoichiometric defects. To investigate the UV emission in more detail, Figure 4-17(b) shows the low-temperature photoluminescence (LTPL) spectra measured at $T = 10$ K under various laser intensities. The excitation intensities were set from 0.05 Wcm^{-2} to 12 Wcm^{-2} . The bound exciton peak situated at 3.343 eV is predominant with its longitudinal (LO) phonon replicas at the lower energy side. In the inset of Figure 4-17(b), other than this dominant peak that has been previously reported as the recombination of excitons bound to neutral donors or acceptors [16, 17], there is an additional weak feature situated on the high-energy shoulder around 3.364 eV. This higher energy emission is attributed to the donor-bound exciton (D^0X) which is usually observed in ZnO single crystals [18], epitaxial layers [19] and other reports of 1-D ZnO rods and wires [20, 21].

With an increase in excitation intensity we observed a remarkable increase in the PL intensity, with neither a blue nor a red shift. The variation of the integrated emission intensity versus the excitation laser intensity can be fitted to the simple power law: $I \propto L^\gamma$, as shown in Figure 4-18, where I is the PL intensity, L is the excitation laser intensity, and γ is a dimensionless exponent. The integrated intensity of the PL band increases super linearly with the excitation intensity, with $\gamma = 1.039$ and 1.015 for the 3.343 and 3.364 eV peaks, respectively. The exponent γ generally lies between 1 and 2 for the free- and bound-exciton emission, and is less than or

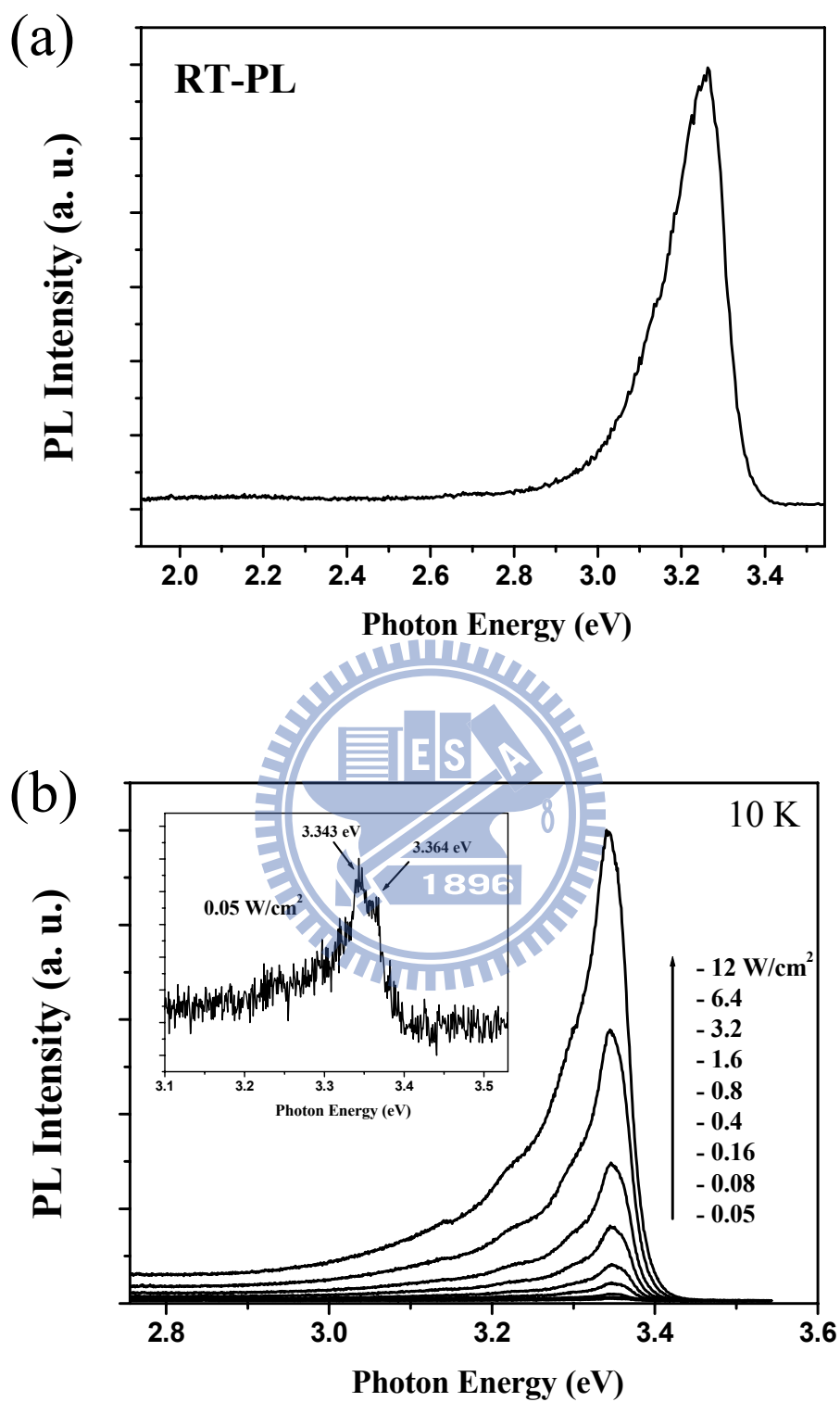


Figure 4-17. (a) Room-temperature photoluminescence (PL) spectrum of ZnO nanowires on GaN buffer layer. (b) PL spectra of ZnO nanowires as a function of excitation laser intensity (from 0.05 Wcm^{-2} to 12 Wcm^{-2}) at low temperature $T = 10\text{K}$.

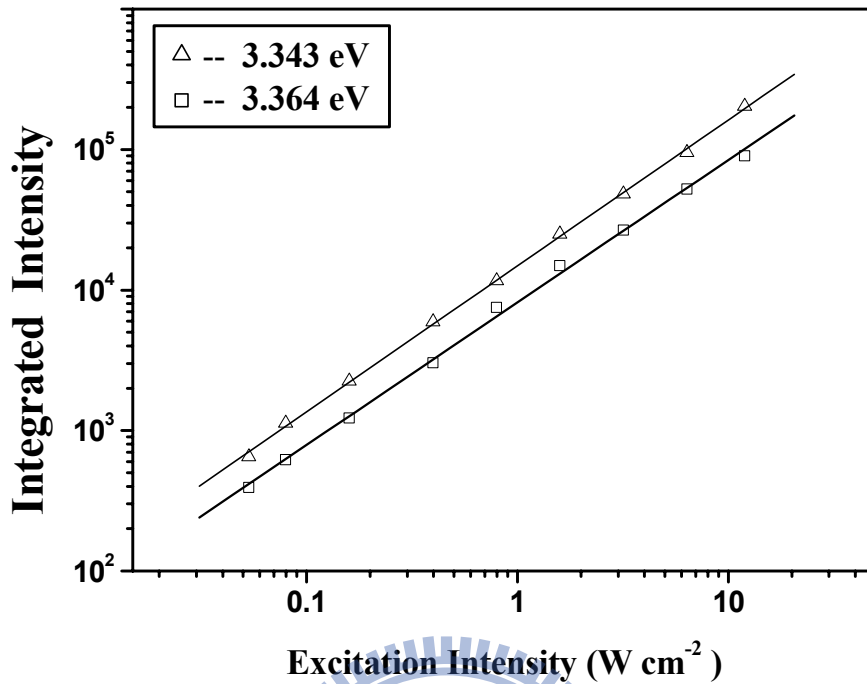


Figure 4-18. Dependence of integrated PL band intensity of 3.343 eV and 3.364 eV on excitation laser intensity at $T = 10\text{K}$.

equal to 1 for free-to-bound and donor-acceptor pair recombinations [22]. The obtained values of $\gamma = 1.039$ and 1.015 confirm our assignment that the observed UV emission bands of ZnO nanowires are due to excitonic emissions.

In summary, high-density, vertically oriented arrays of ZnO nanowires were successfully epitaxially grown on the GaN(0001)-buffered sapphire substrate without any catalyst. FESEM micrographs demonstrate that the ZnO nanowires possess a good crystalline structure with diameters of 80 nm to 100 nm and lengths of several micrometers. TEM micrograph and HRXRD spectra demonstrate that the arrays of ZnO nanowires are well aligned along the c -axis and suffer a small biaxial compressive stress of 121.9 MPa. The resonant Raman spectra show good crystal quality and reveal phonon modes that are affected by the size confinement of the ZnO

nanowire. Room-temperature and low-temperature photoluminescence exhibit almost no nonstoichiometric defects in the crystallite. The exciton-related recombinations near the band edge dominate the UV emissions at room temperature as well as at low temperature ($T = 10$ K).

4.2 ZnO Nanostructures from Solvothermal Method

4.2.1 ZnO Nanowires on FTO

The process of the growth of the ZnO nanowires is similar to Law et al. [23] as described in chapter 3.3. Arrays of ZnO nanowires were synthesized on FTO substrates, that were first cleaned thoroughly by acetone/ethanol sonication and then coated with a thin film of ZnO quantum dots, 3-4 nm in diameter, by dip-coating in a 0.005M Zn(OAc)₂ concentrated ethanol solution. The arrays of ZnO nanowires were synthesized on seeded fluorine doped tin oxide (FTO) substrates by immersing the seeded substrates in aqueous solutions containing 0.06 M zinc nitrate hydrate, 0.06 M hexamethylenetetramine (HMTA), and 7.5 mM polyethylenimine (PEI) at 95 °C for 2.5 hours to 7.5 hours. Figure 4-19 shows the tilted-view SEM images of the ZnO nanowires on FTO layers and AZO layers (alumina doped ZnO, 50~200 Ω per square, preliminary sample from MCL/ ITRI), respectively. It seems that the aspect ratio (length against diameter) of nanowires can be increased when using PEI. The lengths of nanowires are also prolonged while increase the growth times. Furthermore, the ZnO nanostructures with different morphology can be observed while using various substrates. The density and diameter of ZnO nanowires seems to be influenced while using AZO substrates. By sputtering technique, we presumed that the grain size of thick AZO films (200~300 nm) is bigger than dip-coating method, which caused the increase the nanowires diameter and the good orientation as well. However, the

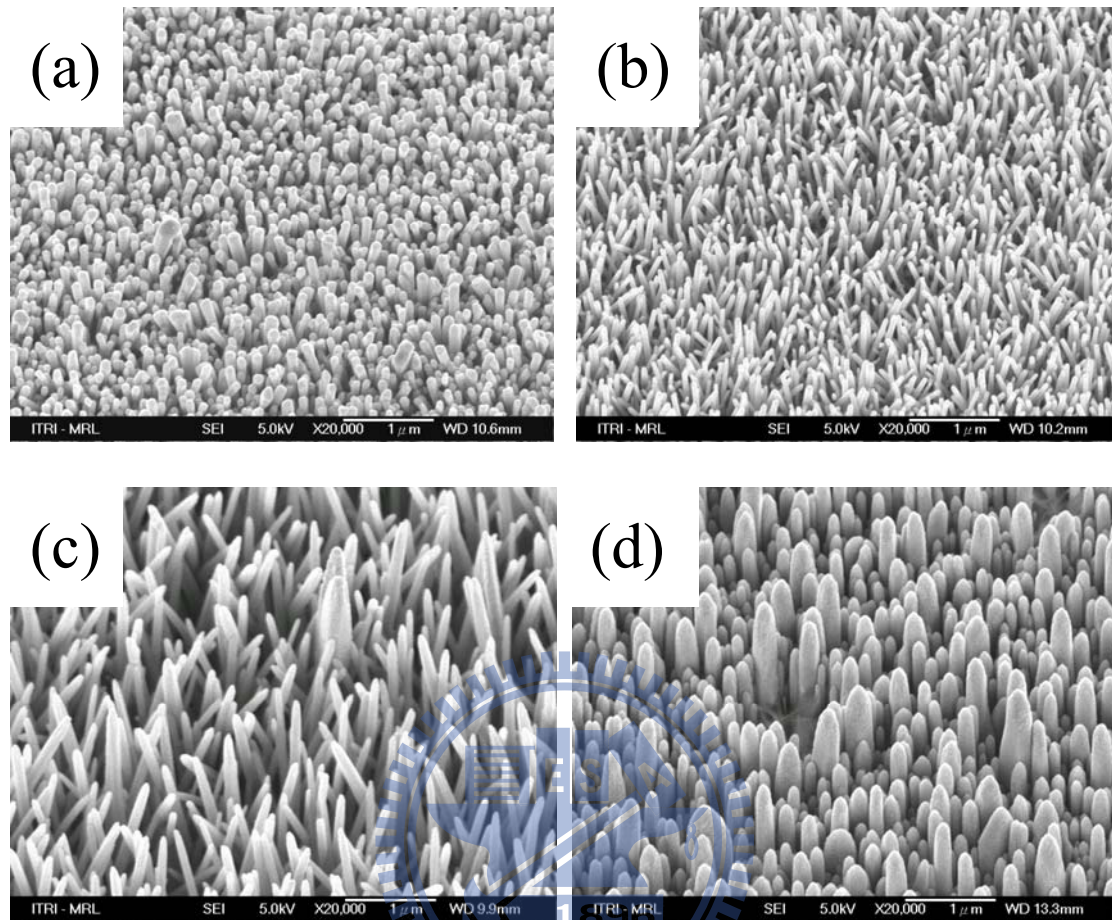


Figure 4-19. The SEM images of the ZnO nanowires and nanorods with different growth conditions (a) FTO substrate, without PEI, grown 2.5 hrs, (b) FTO substrate, with PEI, grown 2.5 hrs, (c) FTO substrate, with PEI, grown 7.5 hrs, (d) AZO substrate, with PEI and grown 7.5 hrs.

fluctuation of diameter for ZnO nanowire is huge while using AZO substrates, which could be related to the uniformity of AZO under layers. The detail growth mechanism will be studied elsewhere in the further investigation. We focus on the growth of ZnO nanowires on FTO substrates in this present section.

4.2.2 Branched ZnO Nanowires

Beyond the ZnO nanowires, we also try to fabricate branched ZnO nanowires from solvothermal method. First, the arrays of ZnO nanowires were synthesized on seeded fluorine doped tin oxide (FTO) substrates by immersing the seeded substrates in aqueous solutions containing 0.08 M zinc nitrate hydrate, 0.08 M HTMA, and 12 mM PEI at 95 °C for 10 hours. Second, the ZnO nanowires substrate obtained from the first step were re-coated with seed layers of ZnO nanoparticles by dip-coating in a 0.005 M Zn(OAc)₂ in ethanol. Then the branched nanowires were grown by immersing the seeded ZnO nanowires in aqueous solutions containing 0.02 M zinc nitrate hydrate, 0.02 M HMTA and 3 mM PEI at 95 °C for 5 hours. The branched ZnO nanowires were finally rinsed with deionized water and baked in air at 450 °C for 30 minutes to remove any residual organics.

The formation mechanism of the branched ZnO nanowires is illustrated in Fig. 4-20(a) and its corresponding FESEM images Fig. 4-20(b)-(d). Figure 4-20(b) shows the bare ZnO nanowires with slight vertical off-alignment were grown perpendicularly on the FTO substrate using a solvothermal method. Through the pre-coating process on the ZnO nanowires, little crystalline nanoparticles with diameter 10-20 nm were formed on the backbone nanowires, as shown in Fig. 4-20(c). After the second growth step, radial secondary ZnO branches emanated from the seeds, as shown in Fig. 4-20(d). Figure 4-21 presents the large-scale and magnified FESEM micrographs of branched ZnO arrays. The branched ZnO nanostructures were fabricated over the entire substrate with a density of backbone nanowire about 7×10^8 cm⁻². The backbone nanowires have length and diameter in the range of 7-8 μm and 150–250 nm, respectively, whereas the secondary branches have length and diameter ranging from 100-300nm and 20-50nm, respectively. The branched ZnO nanowires

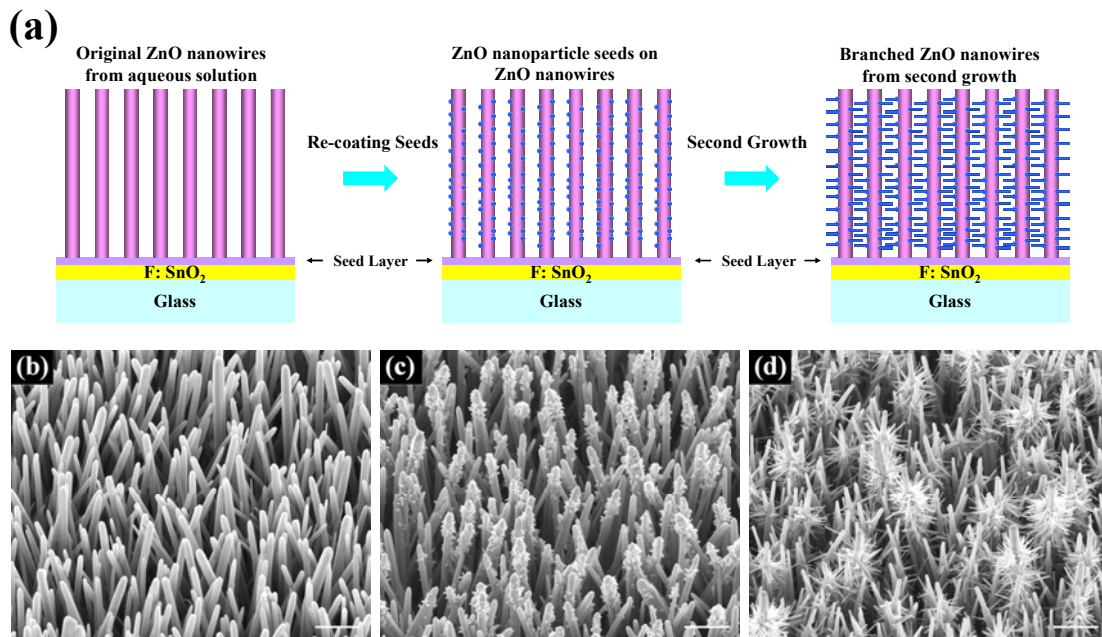


Figure 4-20. (a) The schematic growth procedure from the original ZnO nanowires to the branched ZnO nanowires. (b) Before and (c) After re-coating a seed layer of the original ZnO nanowires obtained from a solvothermal method. (d) The branched ZnO nanowires after second growth. Scale bar, 1 μm .

can be fabricated by the infiltration of moderate concentrated $\text{Zn}(\text{OAc})_2$ solution into interstitial voids between backbone ZnO nanowires. However, the secondary branches were not produced on the surface of each ZnO backbone. The lack of uniformity of secondary branches can be interpreted as the results of rough dip-coating processes that cause non-uniform infiltration and finally lead to randomly disturbed seed layers upon the backbone ZnO nanowires. Moreover, in some conditions, the seed layers hardly infiltrate into the deep side-wall of original ZnO nanowires during the immersion but left as coverage upon the ZnO nanowires, as shown in Fig. 4-21. Those failed conditions would mostly occur when using more concentrated $\text{Zn}(\text{OAc})_2$ solution and also when the substrates were heated during dip-coating. The fast crystallization would lead the aggregation of ZnO seed layers

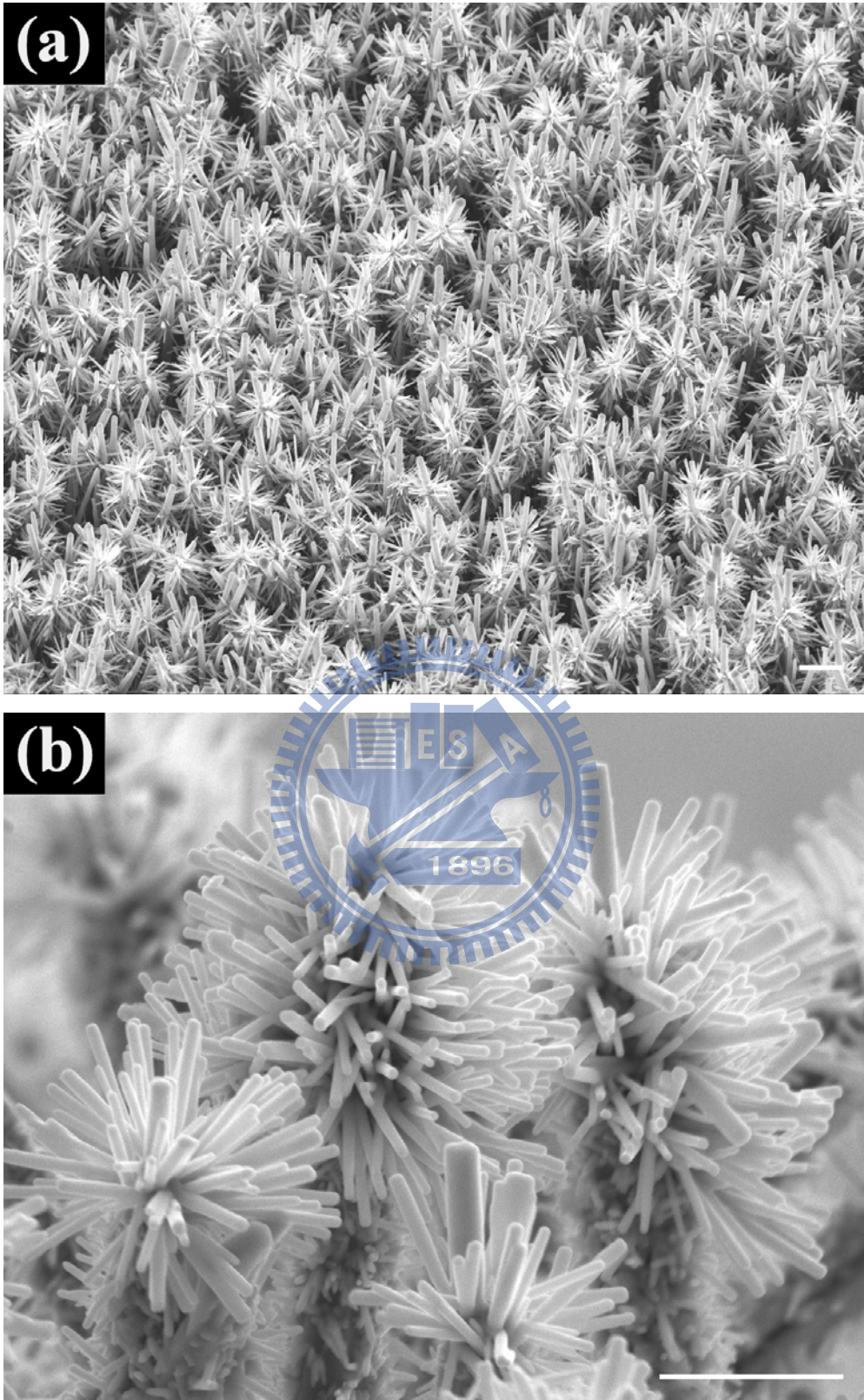


Figure 4-21. (a) Low- and (b) High-magnification FESEM images of the branched ZnO nanowires after second growth. Scale bar, 1 μm .

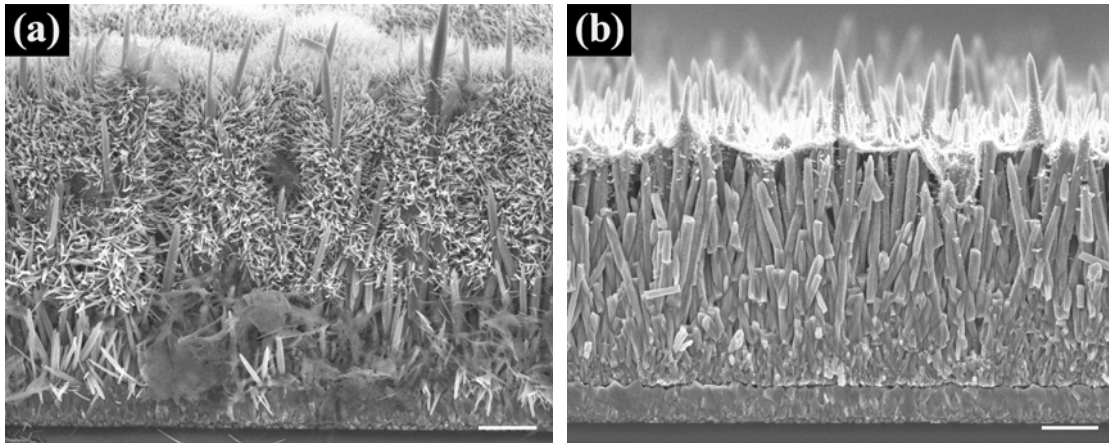


Figure 4-22. The cross section FESEM images of (a) successful branched ZnO nanowires and (b) failed branched ZnO nanowires. ZnO nanowires were all synthesized on seeded fluorine doped tin oxide substrates. Scale bar, 1 μm .

and consequently blocked the infiltration of subsequent aqueous solutions.

Further structural characterizations of the branched ZnO nanowires were performed with TEM. Unlike the other reports of comblike ZnO nanostructures which demonstrated the monolithically single-crystalline relationship between the branches and backbone nanowires [24, 25], in the present mechanism, the secondary ZnO branches were fabricated merely on the ZnO seeds regardless of the coordinate crystal relationship. Figure 4-23(a) displays the secondary ZnO branches which were grown on the side walls of nanowires backbone with different radial angles. The evidence confirmed the secondary ZnO branches were not the derivatives of ZnO nanowires but definitely originated from the small crystallite ZnO seeds via our pre-coating process. The magnified intersection area of ZnO branch and nanowire was shown in Fig. 4-23(b). Figure 4-23(c) and (d) show the corresponding nano-beam diffraction (NBD) of the secondary ZnO branch and select-area electron diffraction (SAED) of the ZnO nanowire backbone, respectively. The diffraction patterns confirmed the each ZnO nanostructure was preferentially oriented in the *c*-axis

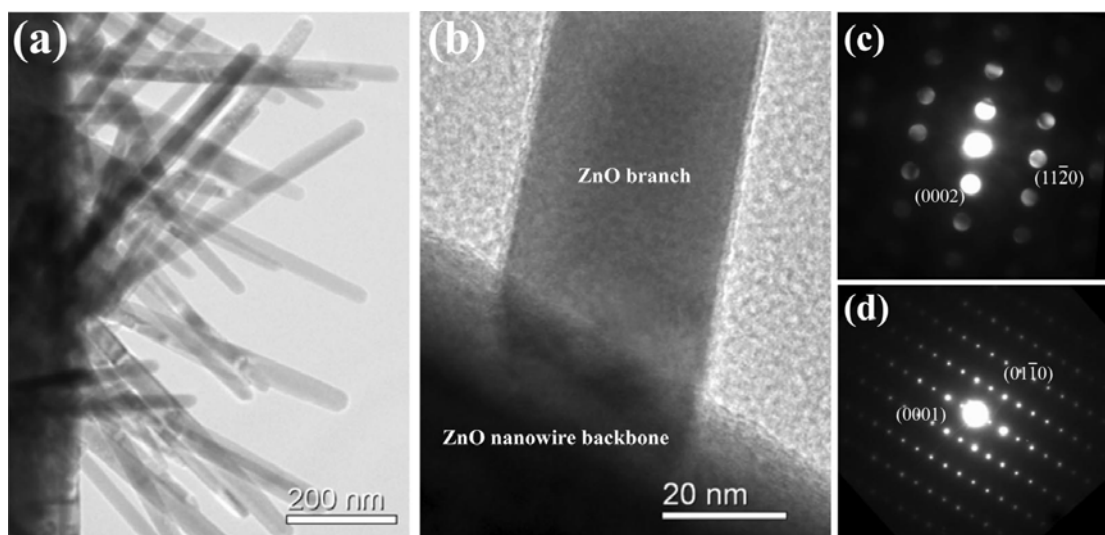


Figure 4-23. (a) TEM image of a single branched ZnO nanowire. (b) The magnified intersection area of ZnO branch and nanowire. (c and d) The corresponding nano-beam diffraction (NBD) and select-area electron diffraction (SAED) for the secondary ZnO branch and the ZnO nanowire backbone, respectively.

direction with the single-crystal wurtzite structure even though the two components of ZnO nanostructures were not fabricated simultaneously.

Figure 4-24(a) shows the θ - 2θ X-ray diffraction patterns of ZnO nanostructures, which corresponds to the presence of hexagonal wurtzite crystallites with cell constants of $a = 3.251 \text{ \AA}$ and $c = 5.208 \text{ \AA}$. The strong $\{0001\}$ diffraction family of ZnO indicates that the nanowires are moderately oriented in the c -axis direction. No excess peaks were detected, which indicates that all the precursors have been completely decomposed. Figure 4-24(b) shows a Raman spectrum of the branched ZnO nanowires which was taken with an accumulation time of 120 s from a $5 \mu\text{m}^2$ spot size excited by a frequency-doubled Yb:YAG laser ($\lambda = 515 \text{ nm}$). As we can see, the remarkable $E_2(\text{low})$ and $E_2(\text{high})$ mode of ZnO are located at 98 cm^{-1} and 438 cm^{-1} , respectively. The peak at 332 cm^{-1} can be assigned to the second order Raman scattering arising from zone-boundary phonons $2-E_2(\text{M})$ of ZnO. The weak and

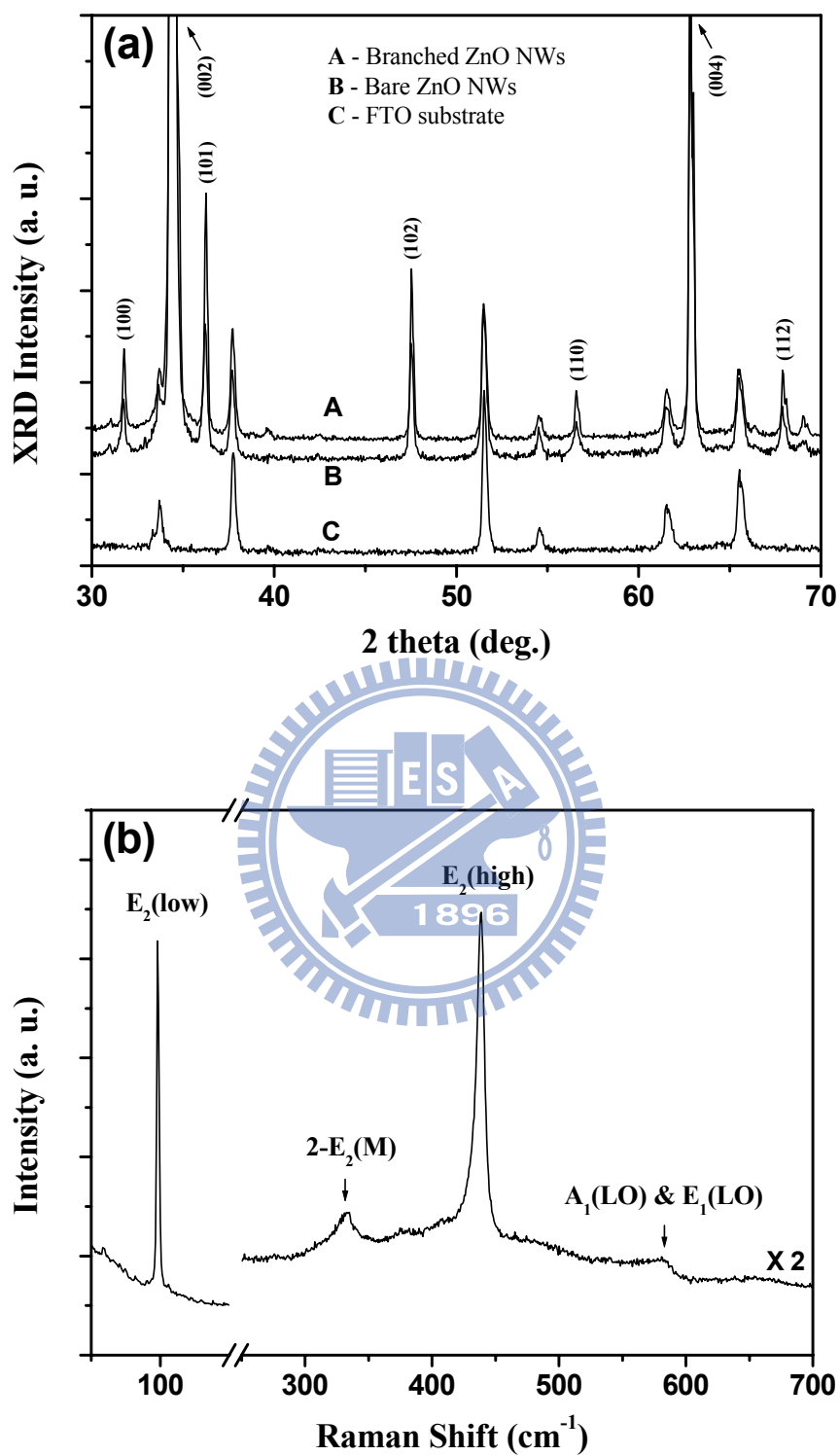


Figure 4-24. (a) θ - 2θ XRD profiles of A: The branched ZnO nanowires, B: The bare ZnO nanowires on the FTO substrate, and C: FTO substrate only. (b) Raman spectra of the branched ZnO nanowires, using a frequency-doubled Yb:YAG laser ($\lambda = 515$ nm).

almost invisible signal around 581 cm^{-1} is contributed to the superimposition of $A_1(\text{LO})$ and $E_1(\text{LO})$. No substrate signals appeared because of the penetration limitation of 515-nm laser light. The good crystalline quality of ZnO nanostructures confirmed above ensure that the photoelectrode can offer good electronic conductivity and avoid the electron trapping within the structural defects.

4.3 Summary

In summary, vertically well-aligned ZnO nanorods were synthesized without employing any metal catalysts on glass, Si (111), 6H-SiC (0001) and sapphire (0001), but were pre-coated with *c*-oriented ZnO buffer layers. The in-plane alignments of ZnO nanorods depend on the crystallographic alignment of pre-coated ZnO buffer layer. Similarly, the photoluminescence of ZnO nanorods are basically related to the type of the substrates used.

High-density, vertically oriented arrays of ZnO nanowires were also successfully epitaxially grown on the GaN(0001)-buffered sapphire substrate. We demonstrated that the arrays of ZnO nanowires are well aligned along the *c*-axis and suffer a small biaxial compressive stress of 121.9 MPa. The resonant Raman spectra show good crystal quality and reveal phonon modes that are affected by the size confinement of the ZnO nanowire. The exciton-related recombinations near the band edge dominate the UV emissions at room temperature as well as at low temperature.

Furthermore, a low-temperature synthesis for further application requirements, the solvothermal method was utilized to fabricate the ZnO nanowires and branched nanowires on FTO substrates. The concept of these one-dimensional branched nanostructures could simultaneously afford a direct conduction pathway and achieve higher surface area to significantly enhance the application potentials.

References and Notes

- [1] Nahhas, A.; Kim, H. K.; Blachere, J. *Appl. Phys. Lett.* **2001**, 78, 1511.
- [2] Li, D.; Leung, Y. H.; Djurišić, A. B.; Liu, Z. T.; Xie, M. H.; Shi, S. L.; Xu S. J.; Chan, W. K. *Appl. Phys. Lett.* **2004**, 85, 1601.
- [3] Tseng, Y. K.; Chia, C. T.; Tsay, C. Y.; Lin, L. J.; Cheng, H. M.; Kwo, C. Y.; Chen, I. C. *J. Electrochem. Soc.* **2005**, 152, G95.
- [4] Park, W. I.; Kim, D. H.; Jung, S-W.; Yi, G -C. *Appl. Phys. Lett.* **2002**, 80, 4232.
- [5] Potin V.; Ruterana P.; Nouet G.; Pond R. C.; Morkoç H. *Phys. Rev. B* **2000**, 61, 5587.
- [6] McMurdie, H.; Morris, M.; Evans, E.; Paretzkin, B.; Wong-Ng, W.; Ettliger, L.; Hubbard, C. *Powder Diffr.* **1986**, 1, 76.
- [7] Vispute, R. D.; Talyansky, V.; Choopun, S.; Sharma, R. P.; Venkatesan, T.; He, M.; Tang, X.; Halpern, J. B.; Spencer, M. G.; Li, Y. X.; Salamanca-Riba, L. G.; Iliadis, A. A.; Jones, K. A. *Appl. Phys. Lett.* **1998**, 73, 348.
- [8] Puchert, M. K.; Timbrell, P. Y.; Lamb, R. N. *J. Vac. Sci. Technol. A* **1996**, 14, 2220.
- [9] Zhang, Y.; Jia, H.; Wang, R.; Chen, C.; Luo, X.; Yu, D.; Lee C. *Appl. Phys. Lett.* **2003**, 83, 4631.
- [10] Damen, T. C.; Porto, S. P. S.; Tell, B. *Phys. Rev.* **1966**, 142, 570.
- [11] Scott, J. F. *Phys. Rev. B* **1970**, 2, 1209.
- [12] Zhang, X. T.; Liu, Y. C.; Zhi, Z. Z.; Zhang, J. Y.; Lu, Y. M.; Shen, D. Z.; Xu, W.; Zhong, G. Z.; Fan, X. W.; Kong, X. G. *J. Phys. D* **2001**, 34, 3430.
- [13] Ursaki, V. V.; Tiginyanu, I. M.; Zalamai, V. V.; Masalov, V. M.; Samarov, E. N.; Emelchenko, G. A.; Briones, F. *J. Appl. Phys.* **2004**, 96, 1001.
- [14] Ng, H. T.; Chen, B.; Li, J.; Han, J.; Meyyappan, M.; Wu, J.; Li, S. X.; Haller, E. E. *Appl. Phys. Lett.* **2003**, 82, 2023.

- [15] Rajalakshmi, M.; Aror, A. K.; Bendre, B. S.; Mahamuni, S. *J. Appl. Phys.* **2000**, 87, 2445.
- [16] Reynolds, D. C.; Litton, C. W.; Collins, T. C. *Phys. Rev.* **1965**, 140, A1726.
- [17] Chen, Y. F.; Bagnall, D. M.; Koh, K. O.; Park, K. T.; Hiraga, K.; Zhu, Z.; Yao, T. *J. Appl. Phys.* **1998**, 84, 3912.
- [18] Chichibu, S. F.; Sota, T.; Cantwell, G.; Eason, D. B.; Litton, C. W. *J. Appl. Phys.* **2003**, 93, 756.
- [19] Jung, S. W.; Park, W. I.; Cheong, H. D.; Yi, G.-C.; Jang, H. M. *Appl. Phys. Lett.* **2002**, 80, 1924.
- [20] Park, W. I.; Jun, Y. H.; Jung, S. W.; Yi, G. C. *Appl. Phys. Lett.* **2003**, 82, 964.
- [21] Hsu, H. C.; Tseng, Y. K.; Cheng, H. M.; Kuo, J. H.; Hsieh W. F. *J. Cryst. Growth* **2004**, 261, 520.
- [22] Schmidt, T.; Lischka, K.; Zulehner, W. *Phys. Rev. B* **1992**, 45, 8989.
- [23] Law, M.; Greene, L. E.; Johnson, J. C.; Saykally, R.; Yang, P. *Nat. Mater.* **2005**, 4, 455.
- [24] Yan, H.; He, R.; Johnson, J.; Law, M.; Saykally, R.; Yang, P. *J. Am. Chem. Soc.* **125**, **2003**, 4728.
- [25] Wang, Z. L.; Kong, X.Y.; Zuo, J.M. *Phys. Rev. Lett.* **2003**, 91, 185502-1.

Chapter 5 Growth and Structural Properties for 0-D ZnO Nanostructures

5.1 Secondary ZnO Nanoparticles

In this section, we show the growth of high-quality ZnO NPs via a simple sol-gel method. The secondary ZnO NPs are formed by the aggregation of primary single crystallites. The primary crystallites have an interesting self-organized behavior, and then compose the texture-like polycrystalline secondary ZnO NPs. In addition, it is also found that the enhancement of resonant Raman scattering (RRS) of the ZnO NPs, and the coupling between the lowest electronic excited state and longitudinal optical (LO) phonon modes, diminishes when compared with post-annealed ZnO NPs.

5.1.1 Fabrication and Structural Properties of ZnO Nanoparticles

Secondary ZnO nanoparticles were synthesized via sol-gel method as a detailed mention in chapter 3.3. The SEM photographs shown in Fig. 5-1 are the products synthesized in various aging time using 10ml of primary supernatant. ZnO was agglomerated from the beginning as white seeds shown in Fig. 5-1(a). The zinc complexes links as networks initially [see Fig. 5-1(b)] and condensed isotropic to finally form hierarchical packing of colloidal particles as Fig. 5-1(c). The unidirectional aggregate phenomenon and formation mechanism were presented by Serna et al. in other metal oxide colloidal systems [1]. The monodispersed spherical ZnO colloids with an average particle size of ca. 185nm were obtained after at least one hour aging. Careful analysis of the micrographs determines that the spheres formed are monodispersive within 5 to 10%. The EDS spectra of the products with different aging time in Fig. 5-2 reveal that they contain Zn, O and C. The carbon

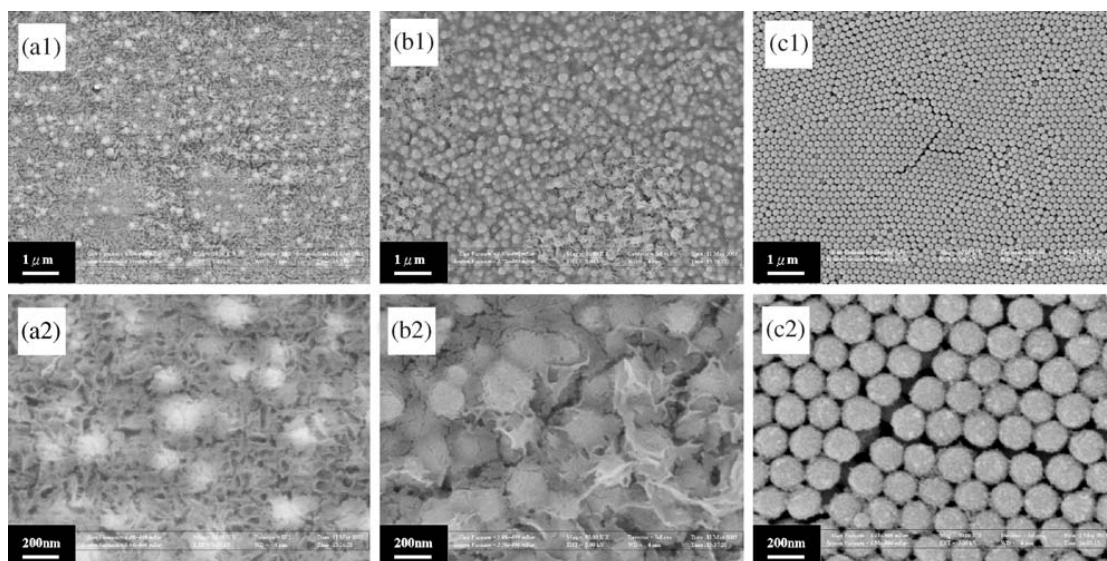


Figure 5-1. Large and local scale of scanning electron micrographs of various aging time products synthesized using 10ml of primary supernatant. The aging times are (a) 15mins. (b) 30mins. (c) 60mins., respectively.

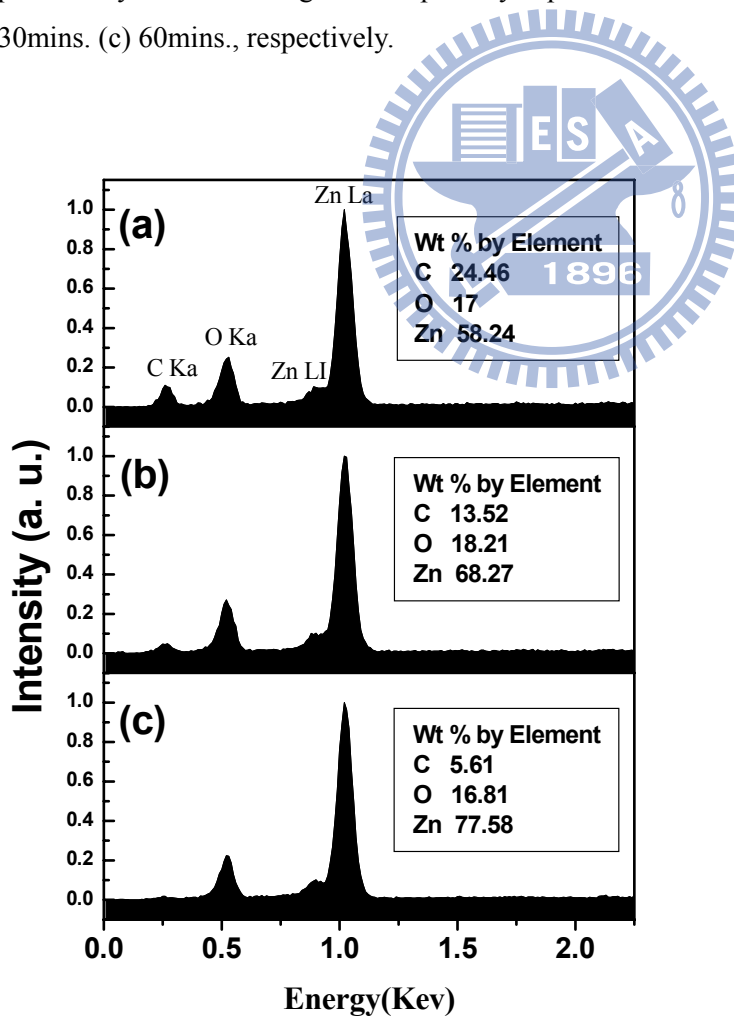


Figure 5-2. Composition variation analysis by energy dispersive x-ray spectra (EDS) of different aging time products as (a) 15 mins. (b) 30 mins. (c) 60 mins.

proportion decreases as the aging time increases. This means that it is necessary for the products to have enough aging time to remove ethanoate ion.

Shown in parts a–d of Fig. 5-3 are typical TEM micrographs of the ZnO NPs. The mean-particle size is estimated to be ca. 185 nm and the shape is essentially spherical. Hierarchical packing of the secondary ZnO NPs are formed in the condensation reactions of the sol-gel process, and the spherical shape of the ZnO NPs is recognized with agglomeration of many primary single crystallites (also called subcrystals) ranging from 6 to 12nm. In particular, it should be noted here that when we carry out the selected area electron diffraction (SAED) for several secondary ZnO NPs, the pattern reveals the poly-crystal wurtzite structure of the ZnO, as indicated in the inset of Figure 5-3(a). On the contrary, the pattern reveals the single crystal like diffraction, as shown in the inset of Figure 5-3(b), when we restrict the SAED area within only one ZnO NPs. Obviously, the secondary ZnO NPs are polycrystals consisting of much smaller subcrystals of the same crystal orientation. More evidence can be demonstrated in the high-resolution TEM (HRTEM) image and its corresponding fast Fourier transform image in Figure 5-3(c). In most cases, the Van der Waals interactions between the surface molecules of the nanocrystallites form the driving force for selfassembly, and then colloidal nanocrystals can be assembled to form solids. If the size distribution of the nanocrystals is sufficiently small, ordered arrays (also called superlattices), quantum dot solids, or artificial solids are formed by self-assembly [2, 3]. Accordingly, the growth of the secondary ZnO NPs mentioned above must proceed in basically the same fashion, and the individual subcrystals of a particle are the subunits of a secondary ZnO NP, with some discontinuity between the subunits. Similar self-assembly structures also were reported in the α -Fe₂O₃ particles by Sugimoto et al. [4, 5]. The cause of the discontinuity on the internal structure has

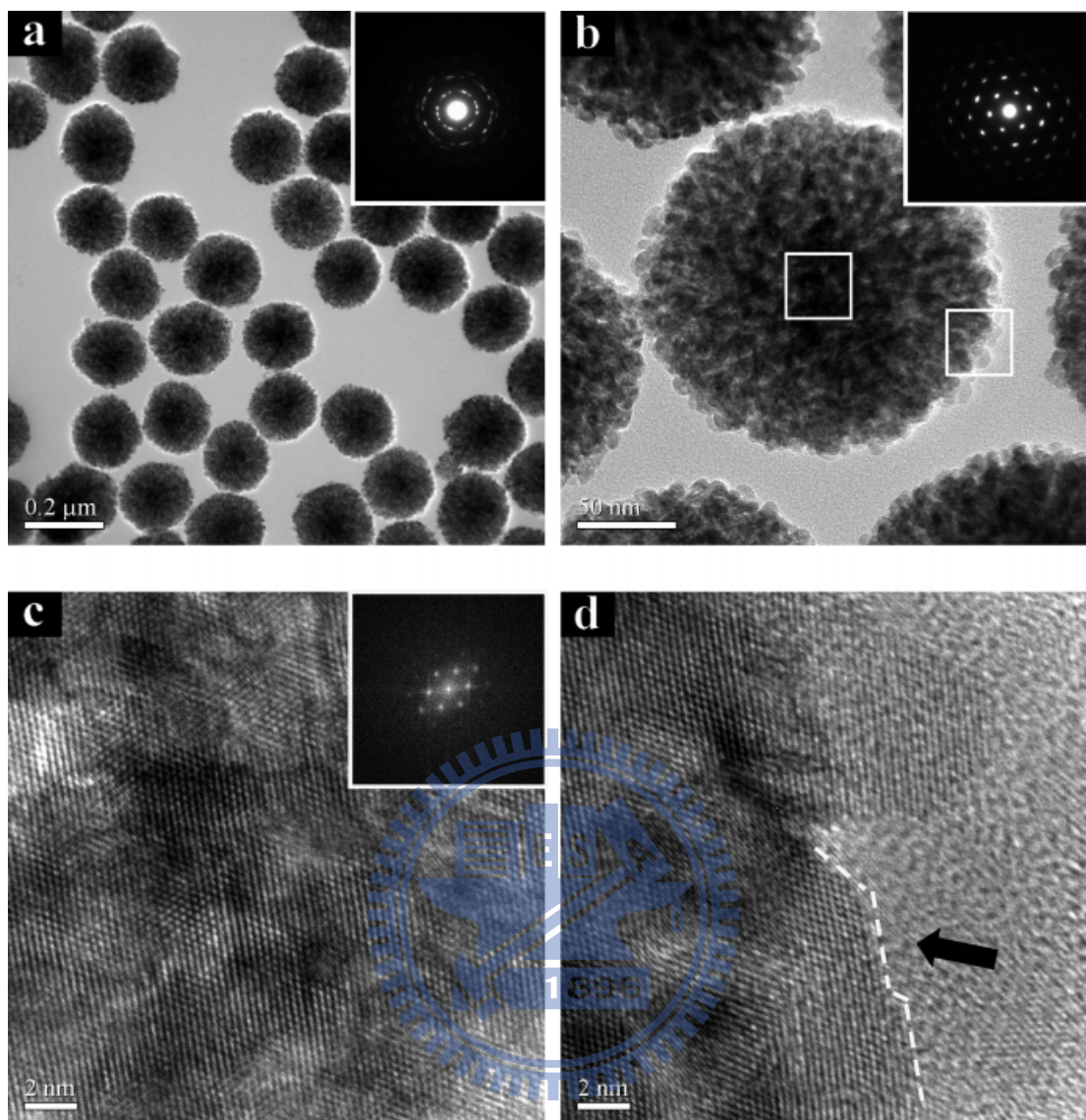


Figure 5-3. TEM images of secondary ZnO NPs recognized of crystalline subcrystals. (a) A typical low-magnification TEM image and SAED pattern of several uniform ZnO NPs. (b) High-magnification TEM image of one individual ZnO NP and its corresponding single-crystal like SAED spots. (c) and (d) High-resolution TEM images of central area and boundary part of one individual ZnO NP, respectively.

been explained in terms of blocked fusion among the surface grains by the strong adsorption of ions used in the reaction process [6-8]. However, there is no existence of other available ions during the whole process in this present work. Presumably due to the block of DEG, the solvent may behave as a microemulsion system causing the

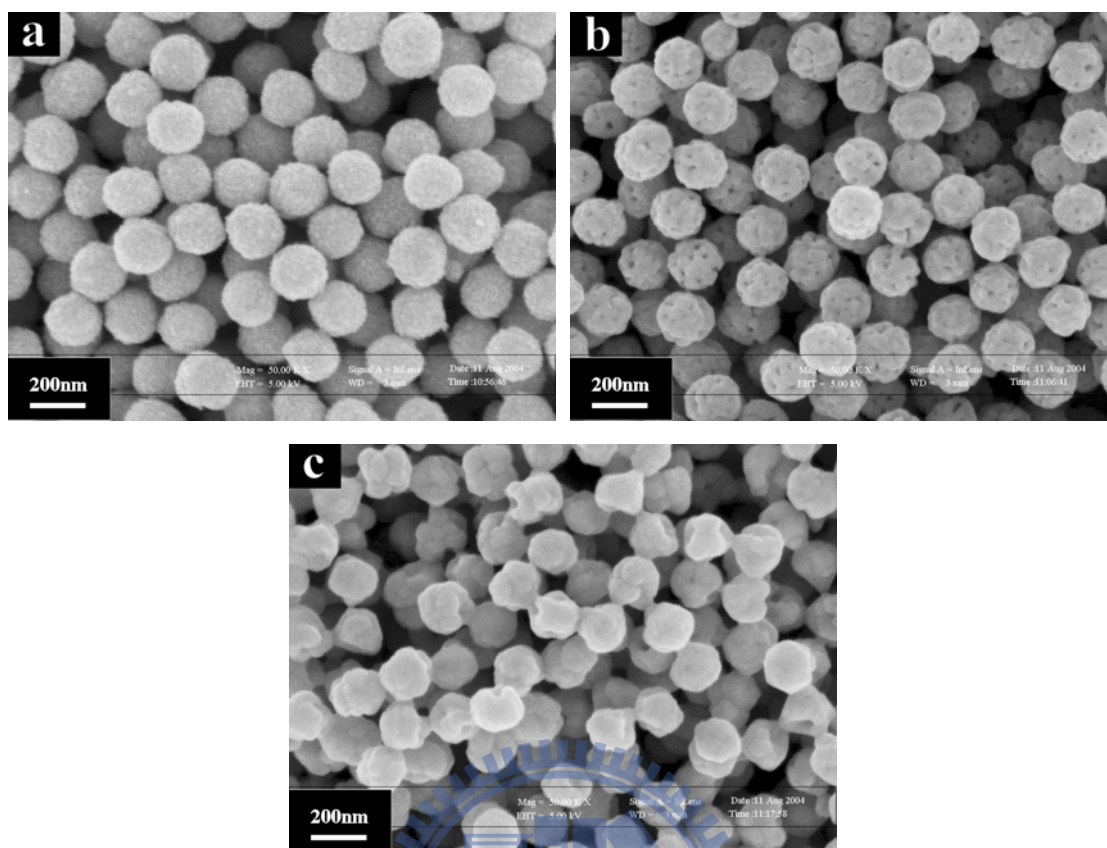


Figure 5-4. SEM micrographs of (a) as-grown, (b) 350°C annealing for 1hour, and (c) 500°C annealing for 1hour secondary ZnO NPs, respectively.

individual ZnO subcrystals that grew up separately and finally assembled to form secondary NPs under the driven force of Van der Waals interaction. The subcrystals are perfect crystalline and exhibiting facets; the evidence was depicted in the HRTEM image from the edge of ZnO NPs as shown in Figure 5-3(d). Consequently, the subcrystals self-assembled slowly via sintering, and belong to the same definite orientation with the adjacent ones.

Figure 5-4 displays the SEM images of as-grown ZnO NPs and the samples after post-annealing at 350°C and 500°C in air ambient for one hour, respectively. The evolutions of morphology in ZnO NPs show the subcrystals significantly fused with the neighbor crystals during the heating process. The grain growth also is investigated

from the XRD profiles (not shown here), as the crystalline sizes were estimated to be approximately 9nm, 14nm, and 20nm for as-grown, 350°C-annealed and 500°C-annealed samples, respectively, by using the Scherrer formula.

5.1.2 Raman Scattering of ZnO Nanoparticles

The UV Raman scattering was performed at room temperature to investigate the vibrational properties of the secondary ZnO NPs before and after being heat-treated. Since the wurtzite structure of ZnO belongs to the space group $C_{6v}^4 (P6_3mc)$, one primitive cell includes two formula units, with all of the atoms occupying $2b$ sites of symmetry C_{3v} . Figure 5-5 shows a normal Raman spectra by a frequency-doubled Yb:YAG laser ($\lambda = 515$ nm). As we can see, the remarkable feature at 520 cm^{-1} is due to the TO phonon mode from the Si substrate. The peak at 331 cm^{-1} can be assigned to the second order Raman scattering arising from zone-boundary phonons $2-E_2(M)$ of ZnO, while the peak at 437 cm^{-1} corresponds to $E_2(\text{high})$. Another broadened peak around 580 cm^{-1} is contributed to the superimposition of $A_1(\text{LO})$ and $E_1(\text{LO})$. We found there is no significant change of Raman spectra for the 350°C-annealed and 500°C-annealed samples. After thermal annealing over 350°C, the intense $E_2(\text{high})$ peak means good crystallinity, and the full width at half-maximum (FWHM) decreases (from 14 to 11 cm^{-1}) as the crystal size increases which is consistent with the XRD results. Whereas, the observance of $A_1(\text{LO})$ and $E_1(\text{LO})$ modes are associated with existence of some nonstoichiometric defects, such as oxygen vacancy, interstitial zinc, or their complexes [9-11] in the secondary ZnO NPs after heating treatment.

In previous resonant Raman scattering (RRS) experiments, in principle the electron phonon interaction could be straightly probed. A He-Cd laser ($\lambda = 325$ nm)

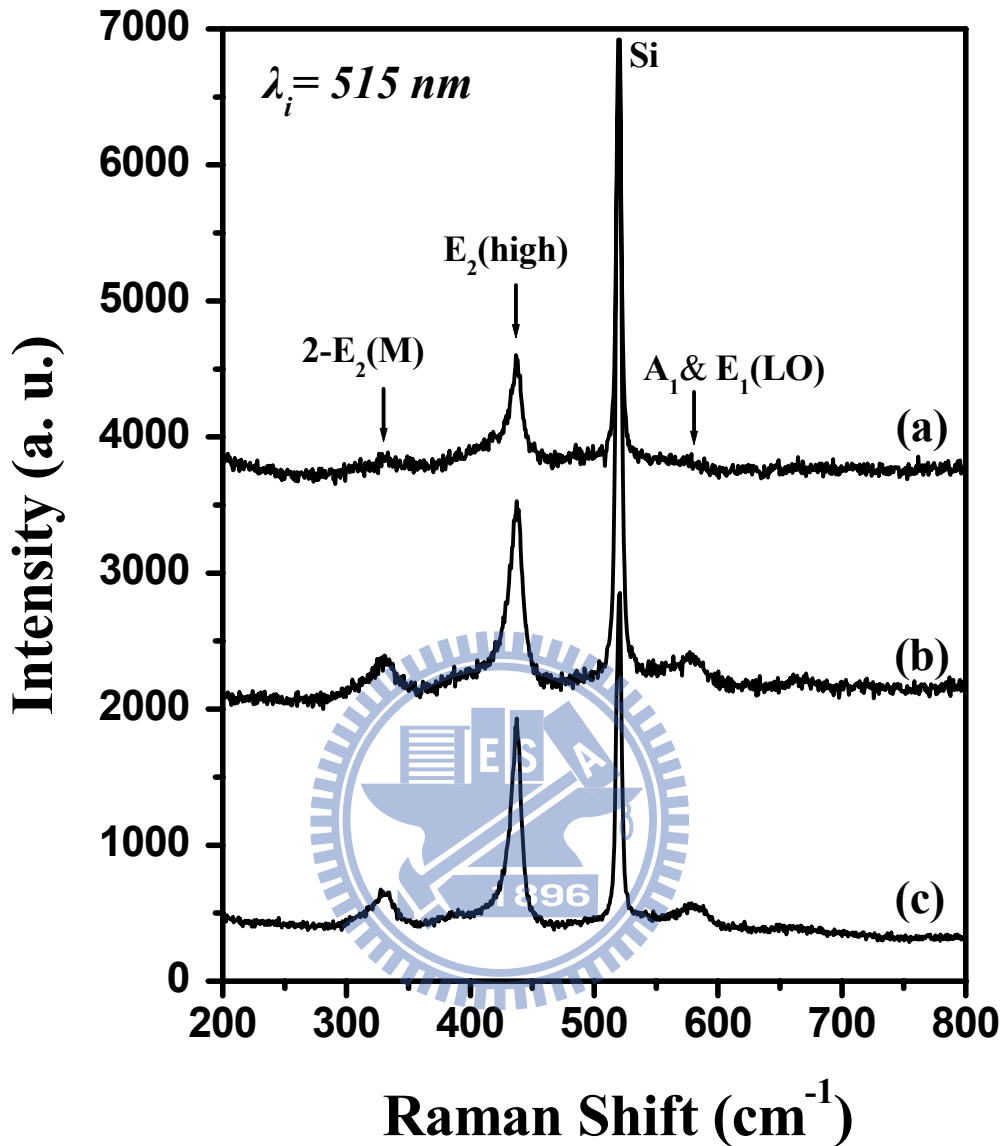


Figure 5-5. Normal Raman spectra of (a) as-grown, (b) 350°C annealing for 1 hour, and (c) 500°C annealing for 1 hour secondary ZnO NPs, using a frequency-doubled Yb:YAG laser ($\lambda_i = 515$ nm).

was used as the excitation source for RRS. The exciting photon energy is resonant with the electronic interband transition energy of the wurtzite ZnO. The polar symmetry makes the $A_1(\text{LO})$ and $E_1(\text{LO})$ modes the dominant modes, and it may exhibit different frequencies from the TO modes. An intense multi-phonon scattering

of the secondary ZnO NPs before and after heat treatment was observed in the resonant Raman spectrum of Figure 5-6, where four major bands were observed to mainly result from the polar symmetry modes $A_1(\text{LO})$ and $E_1(\text{LO})$ and their overtones. The first order Raman mode is a superposition of the LO phonon mode in which Zn atoms and O atoms have the same vibration direction, respectively, to the neighbor lattices of the wurtzite ZnO [12]. The weak peak, which is contributed to the $E_2(\text{high})$ mode around 437 cm^{-1} , is almost imperceptible as a result of other stronger RRS peaks. Multiphonon scattering processes also have been previously reported for single crystalline bulk ZnO [13], and recently for ZnO films [14], ZnO-opal structures [15] and ZnO nanowires [16, 17] but rarely mentioned for ZnO NPs. From the RRS spectra, it is remarkable that the intensities of the first order Raman mode and its overtones are enhanced in the as-grown ZnO NPs compared with the post-annealed samples. The reason can be explained using the total Raman cross section for an n -phonon process written as [18, 19]

$$\sigma_n = \int \sigma_n^R(\omega) f(R) dR \quad , \quad (1)$$

$$\sigma_n^R(\omega) = \mu^4 \left| \sum_{m=0}^{\infty} \frac{\langle n|m\rangle \langle m|0\rangle}{E_0 + n\hbar\omega_{LO} - \hbar\omega + i\hbar\Gamma} \right|^2 \times \exp\left(-\frac{i\hbar\omega_{LO}}{k_B T}\right) \quad , \quad (2)$$

where μ is the electronic dipole transition moment, E_0 is the size-dependent energy of the electronic transition, $\hbar\omega$ and $\hbar\omega_{LO}$ are the energies of the incident photon and the LO phonon, respectively, m denotes the intermediate vibrational level in the excited state, and Γ is the homogeneous linewidth, k_B is Boltzmann's constant, T is the temperature, and the bracket indicates the overlap integral between

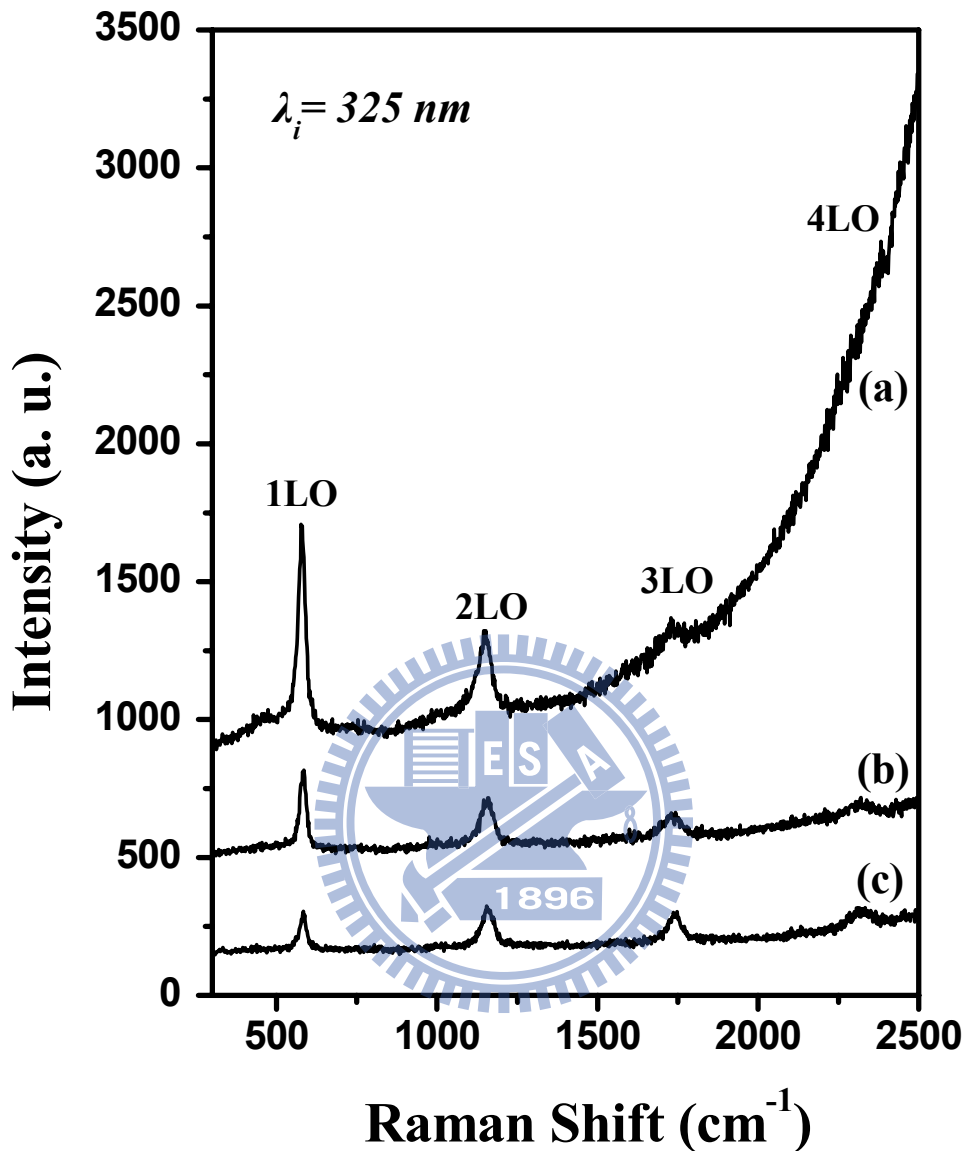


Figure 5-6. Resonant Raman scatterings (RRS) of (a) as-grown, (b) 350°C annealing for 1hour, and (c) 500°C annealing for 1hour secondary ZnO NPs, using a He–Cd laser ($\lambda = 325 \text{ nm}$).

the ground and excited states wave functions. Consequently, RRS intensity can be enhanced as a result of the energy of the incoming or the scattered photons, to match real electronic states in the material and cause the denominator in the Raman scattering cross section to tend to zero. Similar results have been previously reported

for CdS and ZnO, using various laser wavelengths [20]. In our case, the band gap of as-grown ZnO NPs would tend to approach the excitation laser energy because of the quantum-confined effect as the subcrystal size is relative to the exciton radius. The quantum-confined evidence can be seen as the intensive tail of the blue-shift photoluminescence (PL) signal of the as-grown sample and also discovered in RRS spectra rather than normal RS spectra, as a result of the redshift, broadening, and the asymmetry of the first order optical phonon mode of the smaller ZnO NPs. It is well known that phonon eigenstates in an ideal crystal are plane waves due to the infinite correlation length; therefore the $K = 0$ momentum selection rule of the first order Raman spectrum can be satisfied. When the crystalline is reduced to nanometer scale, the momentum selection rule will be relaxed. This allows the phonon with wave vector $|k| = |k'| \pm 2\pi/L$ to participate in the first-order Raman scattering, where k' is the wave vector of the incident light and L is the size of the crystal. The phonon scattering will not be limited to the center of the Brillouin zone, and the phonon dispersion near the zone center must also be considered so that the shift, broadening, and the asymmetry of the first order optical phonon can be observed. In recently reported studies, Alim et al. [21, 22] have shown that the large redshifts in the resonant Raman spectra from 20nm ZnO NPs are most likely due to the local heating by UV laser excitation. In our study, since the as-grown secondary ZnO NPs contain more air gaps than the annealed ones, the smaller thermal conductivity may become one of the other possibilities which results in higher temperatures and larger phonon redshift. The detailed numerical analysis of ZnO NPs of this experiment is distinctively listed at Table 5-1 for clarity.

Furthermore, the ratio between second- and first-order Raman scattering cross sections was found to increase remarkably from 0.38 to 2.05 with an increase of the

TABLE 5-1. Wave number, broadening and the ratio of n-LO phonons found in RRS spectra. The assignments of bulk ZnO are also listed as a reference.

	as-grown ^a	350 °C ^a	500 °C ^a	bulk ^b
grain size (nm)	9	14	20	>1000
1LO (cm ⁻¹) (fwhm)	578 (27.2)	582 (24.2)	584 (23.9)	585 (N/A)
2LO (cm ⁻¹) (fwhm)	1149 (54.7)	1154 (49.3)	1158 (47.3)	1165 (N/A)
I_{2LO}/I_{1LO}	0.38	0.59	1.07	2.05

^a this work

^b From ref 13, (used the same He-Cd laser, $\lambda = 325$ nm, as the excitation source for RRS)

ZnO crystallite size from nanoparticle to the bulk. Within the Franck-Condon approximation, [23, 24] the coupling strength of the exciton transitions to the LO phonon may be expressed in terms of Huang-Rhys parameter S . The cross section of RRS was a function of particle size, temperature, and excitation wavelength. Scamarico et al. [25] suggested that keeping constant the resonance condition is mandatory for a meaningful comparison of spectra associated with nanocrystals having different sizes and hence different electron transitions, due to the strong energy dependence of the Raman scattering cross section. In this study, we have carefully used the same experimental conditions, such as laser wavelength, power, spot size, and so on for each sample. We reported here with an emphasis on the tendency of the increasing electron-phonon interaction with increasing nanocrystal size. It is generally accepted that the electron phonon coupling is determined by two mechanisms: the deformation potential and the Fröhlich potential. Following Loudon [26] and Kaminow [27], the TO Raman scattering cross section is mainly determined

by the deformation potential that involves the short-range interaction between the lattice displacement and the electrons. On the other hand, the LO Raman scattering cross section includes contributions from both the Fröhlich potential that involves the long-range interaction generated by the macroscopic electric field associated with the LO phonons, and the deformation potential. We found that the intensity of TO phonon in ZnO NPs is almost insensitive, while that of LO phonon is greatly enhanced under the resonant conditions. Therefore, we believe that the electron-LO-phonon coupling as decreasing the nanocrystal size is mainly associated with the Fröhlich interaction. Although the complex origin is not well understood, the result in this study is extremely consistent with recently reports in other low-dimensional ZnO nano-systems, such as the ZnO nanowires [28] and ZnO based quantum wells [29].

5.1.3 Photoluminescence of ZnO Nanoparticles

Figure 5-7 shows the normalized room temperature PL spectra of the as-grown and the heat-treated ZnO NPs, respectively. As we can see, the UV emission peaks, which were attributed to the exciton-related recombination, slightly shift their position from 376 nm to 387 nm after heat treatment. The band gap enlargement happens to the as-grown ZnO sample that results in enhancing the intensity of RRS, as mentioned above. Then, the grain grows after the annealing process, resulting in the optical property returning back to the bulk similarity. Besides, some various impurity exciton complexes also probably cause the shifts of UV emission from ZnO NPs. Fonoberov et al. [30, 31] have theoretically reported two possible sources of UV PL in ZnO QDs, which have been considered as excitons confined in the quantum dot and excitons bound to an ionized impurity located at the quantum-dot surface. Compared with the bulk ZnO, the slightly blue shift of UV photoluminescence in our

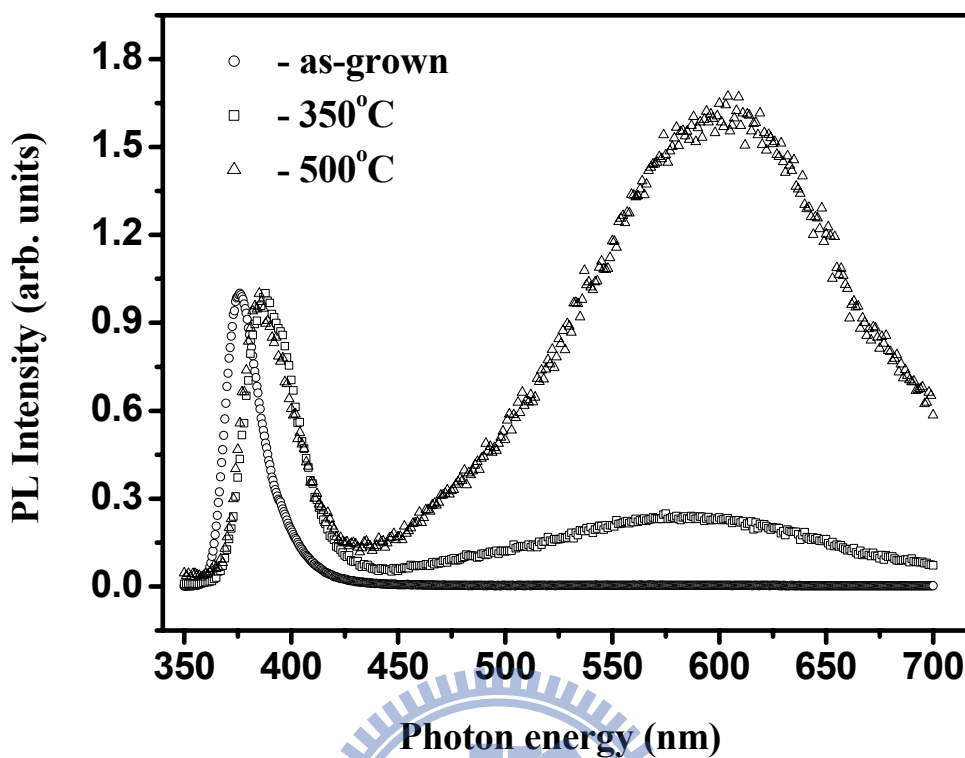


Figure 5-7. Normalized room-temperature PL spectra of the secondary ZnO NPs before and after heat treatment, respectively.

as-grown ZnO NPs was due to the influence of size effect on energy level of confined excitons. Moreover, the UV photoluminescence peaks of post-annealed ZnO samples red-shifted from the general bulk free exciton energy (~ 3.31 eV at 298K) as far as more than one hundred of milli electron volts. Therefore, we argue that the redshifts may be caused by the presence of acceptors bound excitons if there are existing numerous impurities at the surface of ZnO NPs after annealing at the high temperature. So far, the opinions are in agreement with Ref 56, and the more accurate possibility of UV transition indeed needs to be further confirmed. In addition, a broadening visible band, from 500 nm to 700 nm, appears gradually when raising the heating temperature. It is generally agreed that the visible emission is due to

nonstoichiometric composition, and visible PL is most commonly green, though other peaks such as, for example, yellow and orange emissions also can be observed which come from oxygen vacancies (V_o), [32] oxygen interstitials (O_i) [33] and ionic dopants [34]. In our room temperature PL spectra, the broad yellow emission at local maximum position 600 nm was observed; such a deep level involved in the yellow luminescence of ZnO is attributed to oxygen interstitials (O_i). The origin is due to oxygen diffusion of the ZnO NPs after annealing in the atmosphere, and also is consistent with the previous study for ZnO samples sintered in moist air [35]. Furthermore, Greene et al. [36] have provided strong evidence of the disappearance of the yellow emission in oxygen-deficient ZnO nanowires after reducing treatment. Consequently, the yellow emission in our present work is associated with oxygen interstitials, beyond all doubt.

5.2 Size-controlled ZnO Quantum Dots

In this section, we demonstrate that the size-dependent PL and RRS of ZnO QDs which are fabricated by a simple sol-gel method without placing any ligands. The enlargement of free-exciton transition energy is responsible for the blueshift of near-band-edge emission in ZnO QDs at room temperature. Moreover, the size dependence of electron-phonon coupling, which can be addressed principally as a result of the Fröhlich interaction, is confirmed by resonant Raman spectra.

5.2.1 Fabrication and Structural Properties of ZnO Quantum Dots

The ZnO QDs were synthesized via a simple sol-gel method without placing any ligands. The average size can be tailored by the concentration of precursor, zinc acetate dihydrate (99.5% $Zn(OAc)_2$, Riedel-deHaen). A high speed centrifuge was

used to separate the final colloids into the upper suspension and the white bottom layer, which include the monodispersed single crystalline ZnO QDs and the secondary ZnO clusters, respectively. In this present section, we considered only the monodispersed ZnO QDs to avoid the intricately mutual interaction. Additional detail of the synthesis can be found in chapter 3.3.

Figure 5-8 shows a TEM micrograph of the ZnO QDs formed using 0.06M zinc precursor. The ZnO QDs are little aggregated but still appear to be sphere and ellipsoid in shape. The mean-particle size is estimated to be ca. 4.2 nm. Figure 5-9 demonstrates the XRD profiles of the ZnO QDs prepared with various concentrations of Zn(OAc)₂. The diffraction peaks and their relative intensities of spectra all coincide with JCPDS card no. 36-1451, so that the observed patterns can be

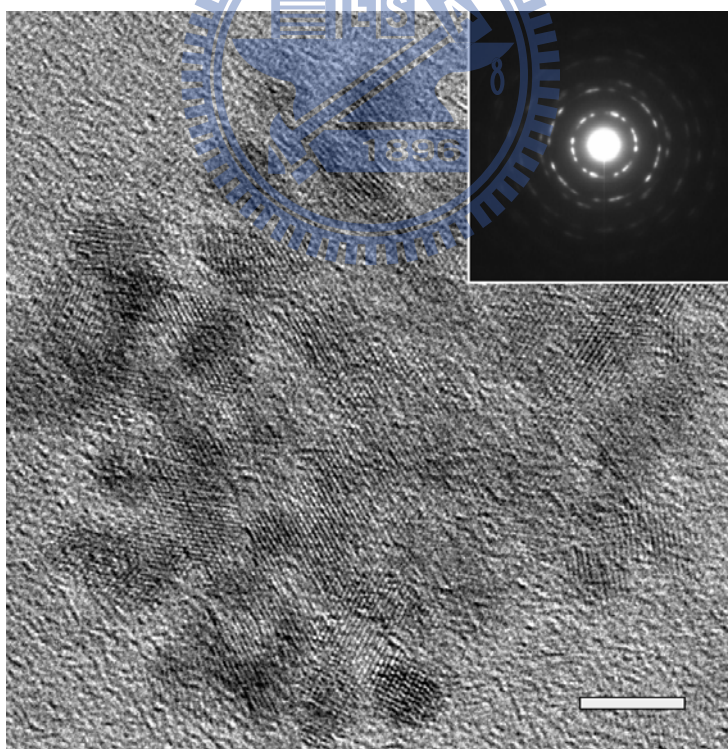


Figure 5-8. TEM image of the ZnO QDs fabricated using 0.06M precursor with the inset of its corresponding selected area electron diffraction (SAED) pattern. The scale bar has a length of 5 nm.

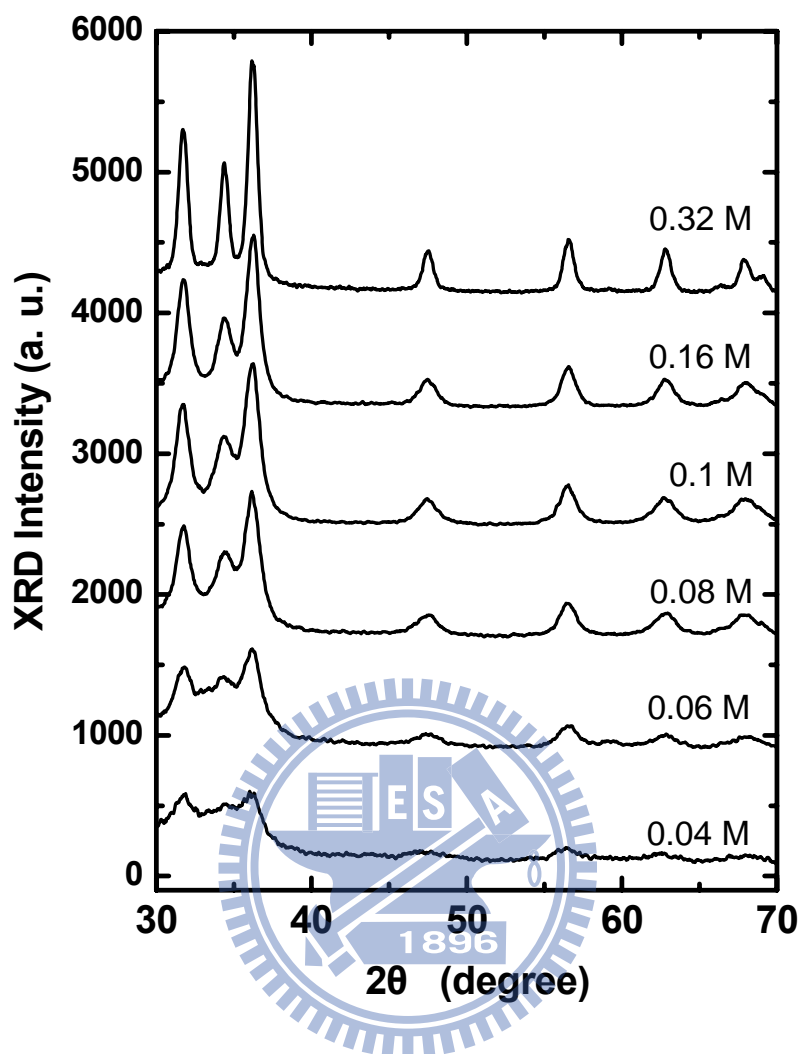


Figure 5-9. XRD profiles of the ZnO QDs prepared with various concentration of $\text{Zn}(\text{OAc})_2$. The crystalline size can be approximately estimated to be 12, 7.4, 6.5, 5.3, 4.2 and 3.5nm, respectively (top to bottom), for concentration 0.32, 0.16, 0.1, 0.08, 0.06 and 0.04 M.

unambiguously attributed to the presence of hexagonal wurtzite crystallites with cell constants of $a = 3.251 \text{ \AA}$ and $c = 5.208 \text{ \AA}$. No excess peaks detected, which indicates that all the precursors have been completely decomposed and no other complex products were formed. It should be noted here that the full width at half maximum (FWHM) of the diffraction peaks increase while decreasing the concentration of zinc precursor duo to the size effect. Furthermore, the crystalline size can be estimated to be 12, 7.4, 6.5, 5.3, 4.2 and 3.5nm, for concentration 0.32, 0.16, 0.1, 0.08, 0.06 and

0.04 $M.$, respectively, by using the Debye-Scherer formula. The statistical result is consistent with the observation from TEM.

5.2.2 Band Gap Variation of ZnO Quantum Dots

Blue-shift of room-temperature ultraviolet (UV) emission was investigated in a series of ZnO QDs with different average sizes, as shown in Fig. 5-10(a). The broad shape of PL peaks is apparently due to the moderate size distribution of ZnO QDs. The nature of the UV-PL from ZnO QDs itself is still a matter of controversy. [30] Aforementioned Demangeot et al., [37] have reported that ligands coordinated at the surface of the nanoparticles may induce some changes in ZnO bonds, leading to some modifications of either their mechanical or dielectric properties. The UV-PL came from surface-bound ionized acceptor-exciton complexes revealed no significant energy shift with varying size of ZnO NPs; furthermore, the weak bound emission vanished at the measured temperature higher than 15K. In contrast, in the present work, the relaxed state near the band edge is attributed to free exciton emission with high electronic density of states because no ligands were added during our synthesis process and the intense UV emission still exhibited even at room temperature. The UV emission shifts to the higher energy from 3.3 to 3.43 eV as the particle size reduces from 12 to 3.5 nm. Moreover, the discernible broad green band (2.1-2.8 eV) was observed only when the size of ZnO QDs is smaller than 4.2 nm as shown in Fig. 5-10(b), the surface-located complex emission reasonably be enhanced while the surface volume of QDs were increased as decreasing the particle size. The relatively weak visible emission indicated that the ZnO QDs contain less intrinsic defects at the surface. Since the exciton Bohr radius, a_B , of bulk ZnO is 2.34 nm, [38] the carrier confinement in these ZnO QDs are in the moderate to strong confinement regimes.

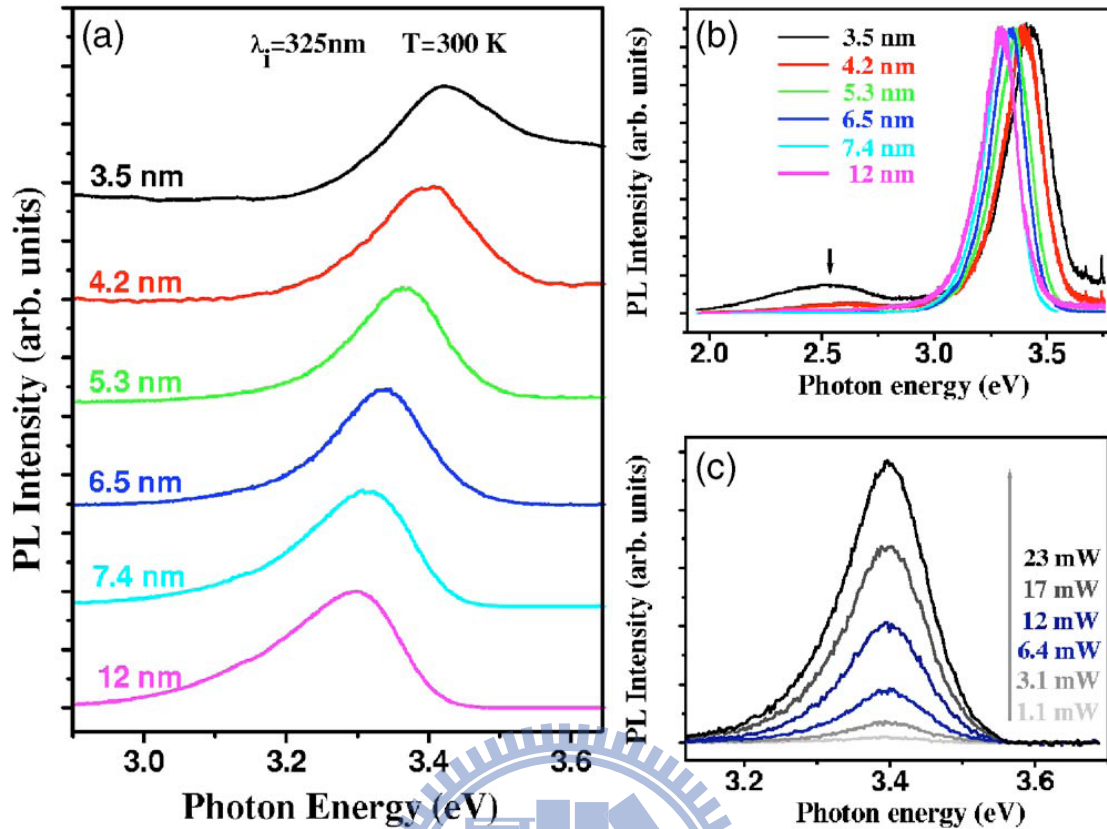


Figure 5-10. Room temperature PL spectra (a) and green emission (b) of ZnO QDs with various sizes; and (c) PL spectra of ZnO QDs (4.2 nm in diameter) as a function of excitation laser intensity (from 1.1mW to 23mW), the exponent γ of power law $I \sim L^\gamma$ lies about 1.3.

The enlarged band gap from 3.41 to 3.60 eV as the ZnO QDs size reduces from 12 to 3.5 nm have been estimated by effective mass model in our previous work [39]. Although the energy differences come from the relaxed state of the exciton and its binding energy but the parallel tendency consists with our assumption of quantum confinement effect. To circumvent other probabilities, we operated the PL measurements at different power. The unchanged energies of the UV emission peaks, as shown in Fig. 5-10(c), exhibit no considerable local heating effect in ZnO QDs, and the obtained exponent value about 1.3 of power law confirmed our assignment that the observed UV emission bands are due to excitonic transition.

The relationship between band gap and size of QD can be obtained using a number of models [40-43]. Using the effective mass model for spherical particles with a Coulomb interaction term [40], the band gap E_g^* [eV] can be approximately written as:

$$E_g^* \cong E_g^{bulk} + \frac{\hbar^2 \pi^2}{2er^2} \left(\frac{1}{m_e} + \frac{1}{m_h} \right) - \frac{1.8e^2}{4\pi\epsilon\epsilon_0 r}, \quad (3)$$

where E_g^{bulk} is the bulk energy gap, r is the particle radius, m_e is the effective mass of the electrons, m_h is the effective mass of the holes, ϵ is the relative permittivity, ϵ_0 is the permittivity of free space, \hbar is Planck's constant divided by 2π , and e is the charge of the electron. The polarization term included in this model is usually negligible.

Figure 5-11 shows both the UV emission peaks, absorption onsets and the dependence of the band gap enlargement on the ZnO QD diameter as calculated from the effective mass model (Eq. 2) with $E_g^{bulk} = 3.35$ eV, $m_e = 0.24 m_0$, $m_h = 0.45 m_0$, and $\epsilon = 3.7$, where m_0 is the free electron mass [44]. Enlargement effects are expected to be predominant when the QD size is less than 6 nm, meanwhile PL data and absorption data of the same tendency indicates effective mass theories accurately, which predict the size dependent energy gap. We note here that the absorption data closely coincides with the curve calculated from the effective mass model. However, the PL data is not fixed since it represents the emission from a relaxed state and the exciton binding energy should be considered. We also observed a size-dependent Stokes shift of the PL maximum relative to the absorption onset as shown in the inset of Fig. 5-11. This Stokes shift increases as the particle size decreases and has been

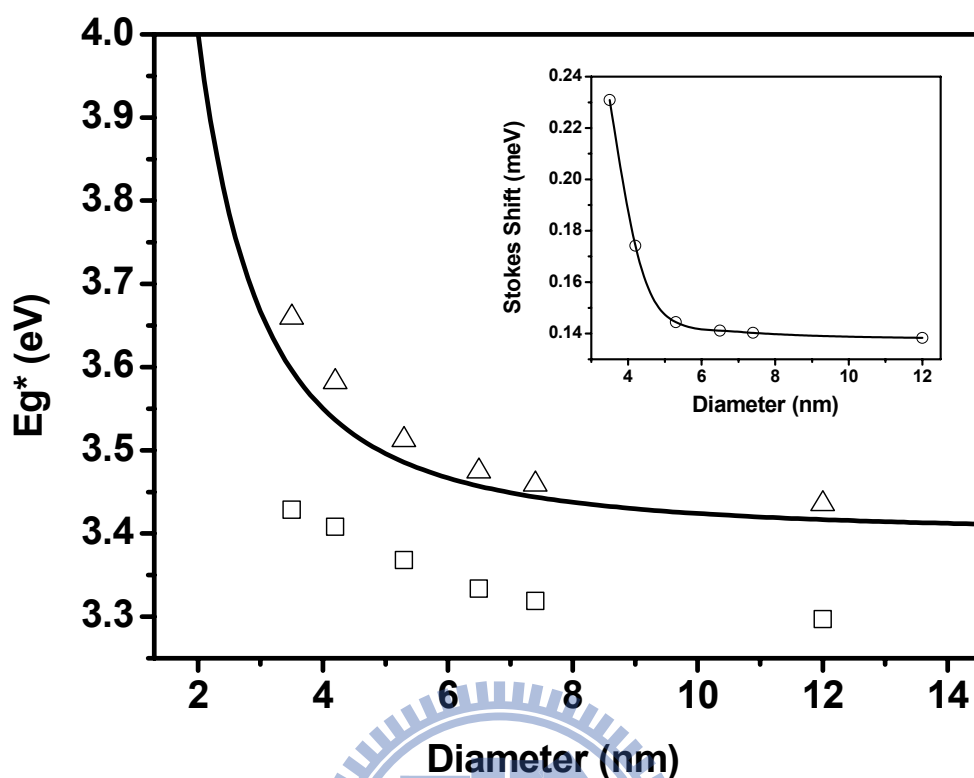


Figure 5-11. The dependence of the band gap enlargement versus the ZnO QDs diameter as calculated from the effective mass model and the corresponding experimental data of PL peak maximum (□) and the absorption onset (Δ) [39]. The inset shows the size-dependent Stokes shift of various QD diameter.

observed in other II–VI and III–V QDs (e.g., InP, CdSe) and extrapolated exponentially or hyperbolically [45]. Such a presentation was previously reported as either size-dependent electron-phonon processes or size-dependent spin-orbit exchange interaction, which may contribute to the Stokes shift. However, the origin of the size-dependent Stokes shift in semiconductor QD systems remains unclear at present [45, 46].

5.2.3 Electron-Phonon Coupling of ZnO Quantum Dots

The electron phonon interaction could be straightly probed by the RRS when the exciting photon energy is resonant with the electronic interband transition energy of the wurtzite ZnO. The polar symmetry makes the $A_1(\text{LO})$ and $E_1(\text{LO})$ modes the dominant ones, while the nonpolar E_2 phonon is not visible. An intense multi-phonon scattering of the ZnO QDs with various size was observed in the resonant Raman spectra of Figure 5-12 with background (luminescence) subtracted, where three major bands were observed to result mainly from the polar symmetry modes $A_1(\text{LO})$ and $E_1(\text{LO})$ and their overtones. Multiphonon scattering processes have been previously reported for 1D, 2D and 3D ZnO systems [13-17], in particular have recently been reported intensely for 0D systems [22, 37].

It is remarkable that the intensities of the first order Raman modes and their overtones are enhanced while the size of ZnO QDs decreases. The reason can be explained using the total Raman cross section for an n-phonon process as a result of the energy of the incoming or the scattered photon matches real electronic states in the material to enhance the Raman scattering cross section. The band gap of the present ZnO QDs certainly tends to approach the excitation laser energy as decreasing its size because of the quantum-confined effect mentioned above. Alim et al. [22] have shown that the large redshifts in the RRS spectra from 20nm ZnO QDs are most likely due to the local heating by UV laser excitation. In the present RRS spectra, the 1LO frequencies were all located at $\sim 575 \text{ cm}^{-1}$ (within $\pm 2 \text{ cm}^{-1}$ fluctuation) for the ZnO QDs of different sizes. The heating effect coming from the inspection of micro-Raman seems to be negligible, because we used the laser power of only 0.8 mW at the spot size about $100 \mu\text{m}^2$.

Beyond the phonon frequency-shift, by observing the size dependence of

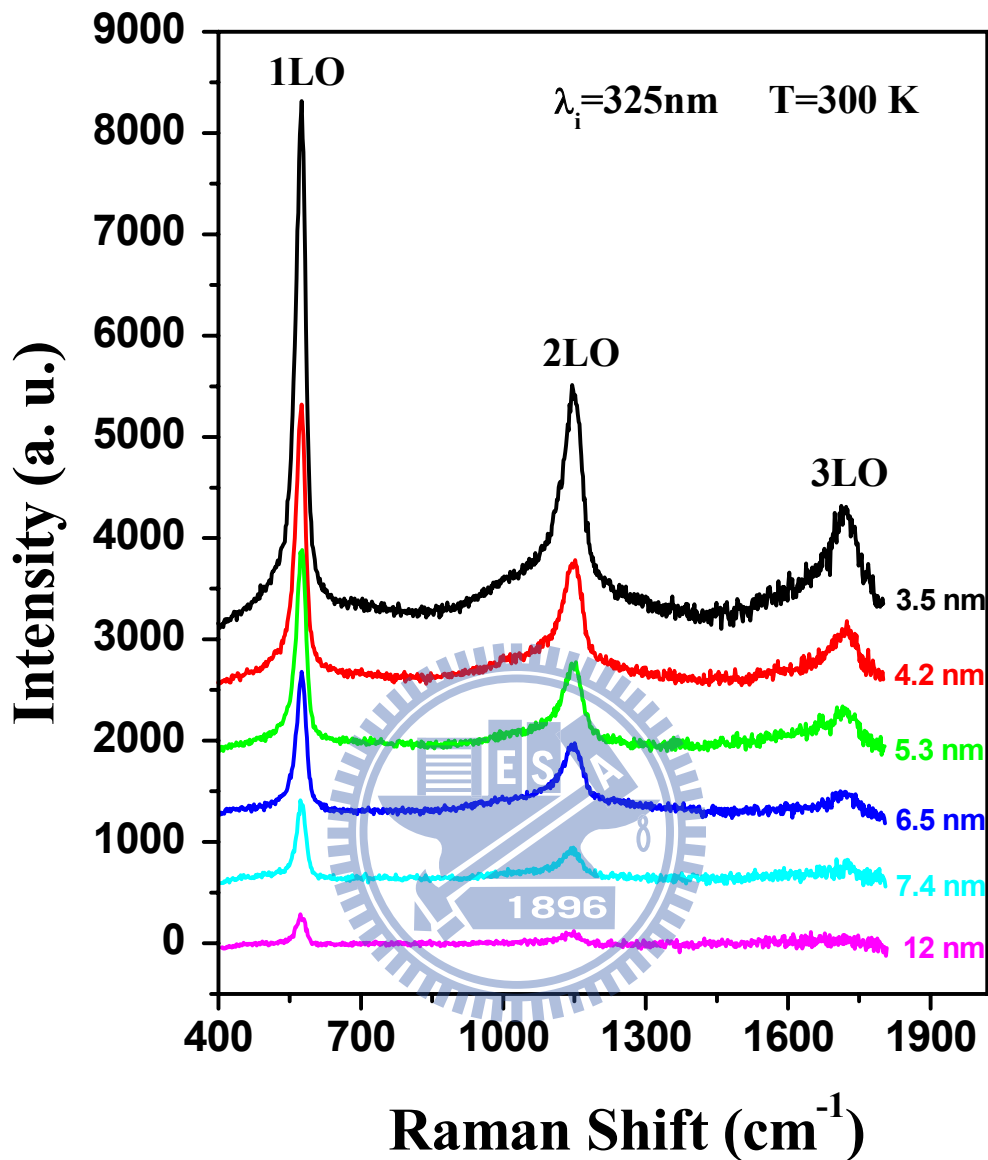


Figure 5-12. Resonant Raman scatterings of ZnO QDs with various particle sizes measured at room temperature using a He–Cd laser ($\lambda = 325$ nm).

intensity ratio between the second- and the first-order LO Raman scattering, one can evaluate the coupling strength of the electron-phonon interaction. Within the Franck-Condon approximation [47], the electronic oscillation strength distribution over n th phonon mode is defined as $I \sim S^n e^{-S} / n!$, in which S is Huang-Rhys

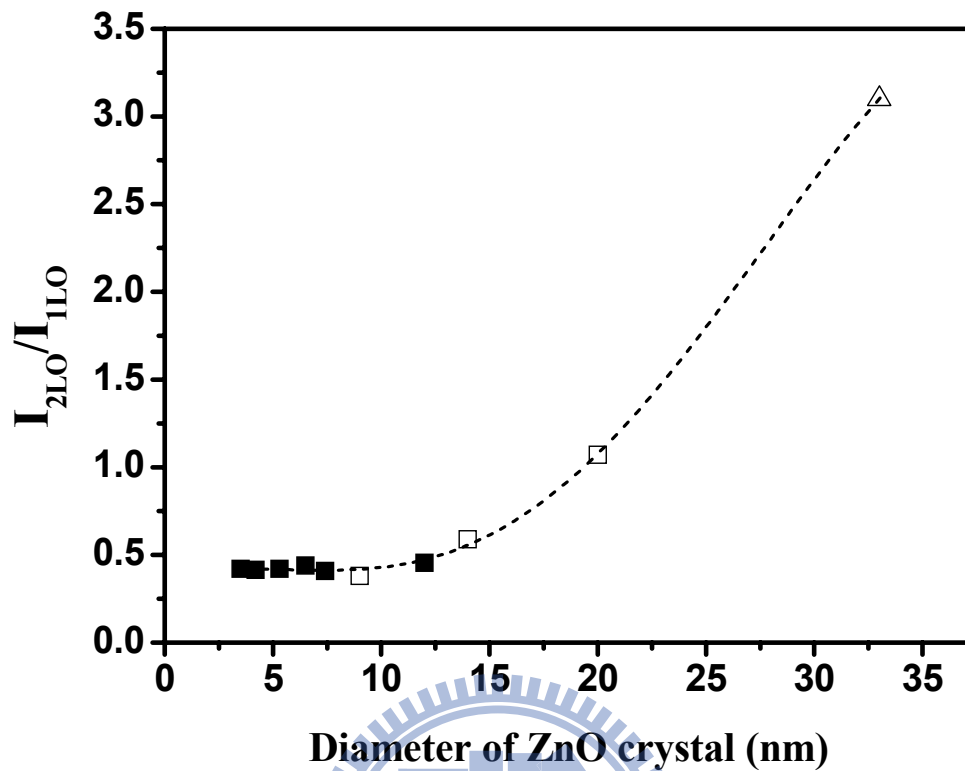


Figure 5-13. Ratio between the second- and the first-order Raman scattering cross section as a function of ZnO diameter. The experimental values of ZnO QDs in this section (squares) compared with ZnO NPs of TABLE 5-1 (empty squares) and nanocrystalline ZnO thin films of Ref. 14 (empty triangle). The dashed line joining the data points is just a guide for the eyes.

parameter, and also can be used to express the coupling strength of the electron to the LO phonon. The ratio between the second- and the first-order Raman scattering cross sections was found to increase remarkably from 0.4 to 3.1 while an increase of the ZnO crystallite size from 3.5 nm to 33 nm, as shown in Fig. 5-13.

The electron phonon coupling is generally determined by two mechanisms: the deformation potential and the Fröhlich potential. On the one hand, following Loudon [26] and Kaminow [27], the transverse optical (TO) Raman scattering cross section is determined by the deformation potential that involves the short-range interaction

between the lattice displacement and the electrons, and on the other, the LO Raman scattering cross section includes contributions from both the deformation potential and Fröhlich potential that involves the long-range interaction generated by the macroscopic electric field associated with the LO phonons. We found that under the resonant conditions the intensity of TO phonon in ZnO QDs is almost insensitive, while that of LO phonon is greatly enhanced. Therefore, we believe that the electron-phonon coupling as decreasing the nanocrystal size is mainly associated with the Fröhlich interaction. Although the complex origin of coupling is not well understood, the result in this study is extremely consistent with reports in other low-dimensional ZnO nano-systems^[28, 29, 48].

5.3 Summary

We have demonstrated the self-assembled secondary ZnO nanoparticles recognized with the agglomeration of crystalline subcrystals ranging from 6 to 12nm synthesized by a sol-gel method. From TEM analyses, the artificial clusters behave like a single-crystal structure, owing to the subcrystals coagulating as the same crystal orientation with adjacent ones via the sintering process. The as-grown sample exhibits phonon redshift in a resonant Raman scattering, compared with the samples after post-annealing at 350°C and 500°C. Moreover, the electron-phonon coupling parameter is unambiguously extracted from resonant Raman scattering, and an interesting phenomenon of increasing electron-LO-phonon coupling is also be discovered when the crystal size of ZnO enlarges after heating treatment. The tendency of the size-dependent electron-phonon coupling in the 0-D ZnO particles is similar to other 1-D and 2-D ZnO systems.

For ZnO QDs, the enlarged free-exciton transition energy is responsible for the

blueshift of near-band-edge PL spectra and gives significant evidence for the quantum confinement effect. Moreover, an increasing electron-phonon coupling was also discovered from RRS analysis while the diameter of ZnO crystal increases. The size dependence of electron-phonon coupling is also principally as a result of the Fröhlich interaction.



References and Notes

- [1] Ocana, M. Clemente, R. Serna, C. J. *Adv. Mater.* **1995**, 7, 212.
- [2] Murray, C. B.; Kagan, C. R.; Bawendi, M. G. *Science* **1995**, 270, 1335.
- [3] Murray, C. B.; Sun, S. H.; Gaschler, W.; Doyle, H.; Betley, T. A.; Kagan, C. R. *IBM J. Res. Dev.* **2001**, 45, 47.
- [4] Park, G.; Shindo, D.; Waseda, Y.; Sugimoto, T. *J. Colloids Interfaces Sci.* **1996**, 177, 198.
- [5] Sugimoto, T.; Wang, Y.; Itoh, H.; Muramatsu, A. *Colloid Surfaces A: Physicochem. Eng. Aspect* **1998**, 134, 265.
- [6] Sugimoto, T.; Sakata, K.; Muramatsu, A. *J. Colloids Interfaces Sci.* **1993**, 159, 372.
- [7] Sugimoto, T.; Khan, M. M.; Muramatsu, A. *Colloid Surfaces A: Physicochem. Eng. Aspect* **1993**, 79, 233.
- [8] Sugimoto, T.; Muramatsu, A.; Sakata, K.; Shindo, D. *J. Colloids Interfaces Sci.* **1993**, 158, 420.
- [9] Exarhos, G. J.; Sharma, S. K. *Thin Solid Films* **1995**, 270, 27.
- [10] Xu, X. L.; Lau, S. P.; Chen, J. S.; Che, G. Y.; Tay, B. K. *J. Cryst. Growth* **2001**, 223, 201.
- [11] Ashkenov, N.; Mbenkum, B. N.; Bundesmann, C.; Riede V.; Lorenz, M.; Spemann, D.; Kaidashev, E. M.; Kasic, A.; Schubert, M.; Grundmann, M.; Wagner, G.; Neumann, H.; Darakchieva, V.; Arwin, H.; Monemar, B. *J. Appl. Phys.* **2003**, 93, 126.
- [12] Damen, T. C.; Porto, S. P. S.; Tell, B. *Phys. Rev.* **1966**, 142, 570.
- [13] Scott, J. F. *Phys. Rev. B* **1970**, 2, 1209.
- [14] Zhang, X. T.; Liu, Y. C.; Zhi, Z. Z.; Zhang, J. Y.; Lu, Y. M.; Shen, D. Z.; Xu, W.;

- Zhong, G. Z.; Fan, X. W.; Kong, X. G. *J. Phys. D* **2001**, 34, 3430.
- [15] Ursaki, V. V.; Tiginyanu, I. M.; Zalamai, V. V.; Masalov, V. M.; Samarov, E. N.; Emelchenko, G. A.; Briones, F. *J. Appl. Phys.* **2004**, 96, 1001.
- [16] Ng, H. T.; Chen, B.; Li, J.; Han, J.; Meyyappan, M.; Wu, J.; Li, S. X.; Haller, E. E. *Appl. Phys. Lett.* **2003**, 82, 2023.
- [17] Cheng, H. M.; Hsu, H. C.; Tseng, Y. K.; Lin, L. J.; Hsieh, W. F. *J. Phys. Chem. B* **2005**, 109, 8749.
- [18] Alivisatos, A. P.; Harris, T. D.; Carroll, P. J.; Steigerwald, M. L.; Brus, L. E. *J. Chem. Phys.* **1989**, 90, 3463.
- [19] Klein, M. C.; Hache, F.; Ricard, D.; Flyzannis, C. *Phys. Rev. B* **1990**, 42, 11123.
- [20] Callender, R. H.; Sussman, S. S.; Selders, M.; Chang, R. K. *Phys. Rev. B* **1973**, 7, 3788.
- [21] Alim, K. A.; Fonoberov, V. A.; Balandin, A. A. *Appl. Phys. Lett.* **2005**, 86, 053103.
- [22] Alim, K. A.; Fonoberov, V. A.; Shamsa, M.; Balandin, A. A. *J. Appl. Phys.* **2005**, 97, 124313.
- [23] Bartolo, B. D.; Powell, R. *Phonons and Resonances in Solids* (Wiley, New York, **1976**), Chap. 10.
- [24] Böer, K. W. *Survey of Semiconductor Physics* (Van Nostrand Reinhold, New York, **1990**), Chap. 20.
- [25] Scamarcio, G.; Spagnolo, V.; Ventruti, G.; Lugara, M.; Righini, G. C. *Phys. Rev. B* **1996**, 53, R10489.
- [26] Loudon, R. *Adv. Phys.* **1964**, 13, 23.
- [27] Kaminow, I. P.; Johnston, W. D. *Phys. Rev.* **1967**, 160, 19.
- [28] Wang, R. P.; Xu, G.; Jin, P. *Phys. Rev. B* **2004**, 69, 113303.

- [29] Makino, T.; Tamura, K.; Chia, C.H.; Segawa, Y.; Kawasaki, M.; Ohtomo, A.; Koinuma, H. *Phys. Rev. B* **2002**, 66, 233305.
- [30] Fonoberov, V. A.; Balandin, A. A. *Appl. Phys. Lett.* **2004**, 85, 5971.
- [31] Fonoberov, V. A.; Balandin, A. A. *J. Phys.: Condens. Matter* **2005**, 17, 1085.
- [32] Vanheusden, K.; Warren, W. L.; Seager, C. H.; Tallant, D. R.; Voigt, J. A.; Gnade, B. E. *J. Appl. Phys.* **1996**, 79, 7983.
- [33] Wu, X. L.; Siu, G. G.; Fu, C. L.; Ong, H. C. *Appl. Phys. Lett.* **2001**, 78, 2285.
- [34] Studenikin, S. A.; Golego, N.; Cocivera, M. *J. Appl. Phys.* **1998**, 84, 2287.
- [35] Liu, M.; Kitai, A. H.; Mascher, P. *J. Lumin.* **1992**, 54, 35.
- [36] Greene, L. E.; Law, M.; Goldberger, J.; Kim, F.; Johnson, J. C.; Zhang, Y.; Saykally, R. J.; Yang, P. *Angew. Chem., Int. Ed.* **2003**, 42, 3031.
- [37] Demangeot, F.; Paillard, V.; Chassaing, P. M.; Pagès, C.; Kahn, M. L.; Maisonnat, A.; Chaudret, B. *Appl. Phys. Lett.* **2006**, 88, 071921.
- [38] Senger, R. T.; Bajaj, K. K. *Phys. Rev. B* **2003**, 68, 045313..
- [39] Lin, K. F.; Cheng, H. M.; Hsu, H. C.; Lin, L. J.; Hsieh, W. F. *Chem. Phys. Lett.* **2005**, 409, 208.
- [40] Brus, L. E. *J. Chem. Phys.* **1984**, 80, 4403.
- [41] Hyberstsen, M. S. *Phys. Rev. Lett.* **1994**, 72, 1514.
- [42] Efros, A. L.; Rosen, M. *Annu. Rev. Mater. Res.* **2000**, 30, 475.
- [43] Andersen, K. E.; Fong, C. Y.; Pickett, W. E. *J. Non. Cryst. Solids* **2002**, 299, 1105.
- [44] Studenikin, S. A.; Golego, N.; Cocivera, M.; *J. Appl. Phys.* **1998**, 84, 2287.
- [45] Fu, H.; Zunger, A. *Phys. Rev. B* **1997**, 56, 1496.
- [46] Nirmal, M.; Norris, D. J.; Kuno, M.; Bawendi, M. G.; Efros, A. L.; Rosen, M. *Phys. Rev. Lett.* **1995**, 75, 3728.

[47] Huang, K.; Rhys, A. *Proc. R. Soc. London A* **1950**, **204**, 406.

[48] Makino, T.; Chia, C. H.; Tuan, N. T.; Sun, H. D.; Segawa, Y.; Kawasaki, M.; Ohtomo, A.; Tamura, K.; Koinuma, H. *Appl. Phys. Lett.* **2000**, **77**, 975.



Chapter 6 Low-Dimensional ZnO Nanostructures for Dye-Sensitized Solar Cells

6.1 Introduction of Dye-Sensitized Solar Cells (DSCs)

6.1.1 The History from Photography [1]

In 1839, Edmund Becquerel, a French experimental physicist of nineteen years old, noticed the generation of an electric current while experimenting with a silver coated platinum electrode placed in the electrolyte [2]. Almost at the same time when Becquerel found the photovoltaic effect, Louis Daguerre made the first “daguerreotype” photographic image onto a mirror-polished surface of silver bearing a coating of silver halide particles, which is now considered as the beginning of photography. The silver halides used in photography have band gaps ranging from 2.7 to 3.2 eV, and are therefore not photoactive for wavelengths longer than 460 nm, lacking the sensitivity to the mid-visible spectral and red light. An improvement was made in 1873 by a German photochemist, Vogel, via the dye sensitization of silver halide emulsions, leading to an extended photoresponse into the red and even infrared regions and the first panchromatic film rendering a realistic black and white picture [3]. In 1887, Moser intuitively observed the first case of dye-sensitized semiconductor electrode when using the dye erythrosin on silver halide electrodes [4]. However, it was not until 1960s that people clearly understood the operating mechanism is the electron injection from a photo-excited state of the dye molecules into the conduction band of the *n*-type semiconductor substrates, following the work of Namba and Hishiki,[5] Tributsch and Gerischer et al. [6-8] on ZnO. Those prototype dye-sensitized cells were characterized with poor dye anchorage (mostly physisorbed) on semiconductor surface and low conversion efficiencies restricted by the limited,

weak light absorption (in the order of 1 to 2%) of the dye monolayer on the planar surface. Thicker dye layers increased the resistance of the system without adding to the current generation [9], which disappointed Gerischer and led him not to “follow the idea of constructing a photocell based on this effect”[10]. Incremental improvements were then achieved both in the chemisorption of sensitizers,[11-13] electrolyte redox chemistry and the judicious selection of photoelectrode materials.[10, 13-19] Most semiconductors such as CdS, CdSe, GaP and Si underwent serious photocorrosion or even normal corrosion in the dark, thus a stable, wide band-gap semiconductor, TiO₂, became the material of choice, following the successful demonstration of direct photolysis of water with TiO₂ [20, 21]. To solve the absorption dilemma, the concept of using dispersed particles to provide a sufficient interface emerged first,[22] then photoelectrodes with high surface roughness were employed to generate multiple reflections at a rough surface, permitting the capture of most of the incident light by a monolayer of a dye with a high molar extinction coefficient [23, 24].

All these improvements finally led to the announcement from O'Regan and Grätzel in 1991 of the sensitized nanocrystalline photovoltaic device with a conversion efficiency at that time of 7.1 -7.9 % under solar illumination and 12% in diffuse daylight [25]. With the discovery of the N3 sensitizer and the later panchromatic “black dye”, the power to electricity conversion efficiency was pushed well over 10% [26, 27]. An interesting modification to this classic system was replacing the electrolyte with a solid hole conductor, yielding an all-solid state dye-sensitized device [28, 29]. Recent achievements of long-time stability under accelerated experiments with non-volatile liquid and quasi-solid molten salt (ionic liquid) electrolyte greatly promoted the practical application of this third generation

photovoltaic technology and put it currently right at the start of commercialization stage [30-33].

6.1.2 Base Principles of DSCs [1]

Conventional silicon and other inorganic semiconductor photovoltaic cells are built on p - n junctions. Figure 6-1(a) depicts the energy band diagram of a p - n junction after thermal equilibration of positive and negative charge carriers. Through the concentration difference between the p and the n type semiconductor, holes move to the n region and electrons to p region. The uncompensated charges induced by the diffusion generate a built-in electric field at the junction and impair further percolation of charge carriers since the orientation of the electric field is opposite to the direction of the carrier diffusion. At equilibrium, no net charge diffusion occurs and a depletion region is formed, which is also referred to as a space charge layer. In the case of illumination as shown in Figure 6-1(b), absorption of photons with an energy higher than a threshold, the band gap, results in generation of excitons which interact via columbic forces. Considering that excitons will recombine after a certain time with emission of photons or phonons (heat), therefore only those created in or close to the space charge layer can be separated by the built-in electric field and contribute to the photocurrent. Since both electrons and holes coexist in the same chemical phase, these cells are called minority carriers devices and their efficiencies are highly dependent on the ability of photogenerated minority carriers (for example, electrons in a p -type material) to be collected out of devices before recombining with the majority carriers (holes, in this case)[34].

On the contrary, with an electron-conducting phase (n -type semiconductor) and a hole conducting phase (redox species or hole conductors) forming a “bulky”

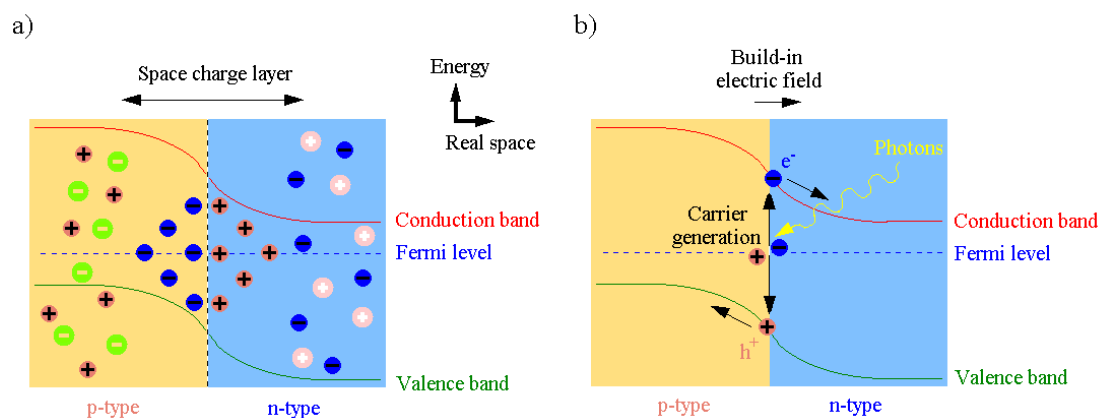


Figure 6-1. (a) Energy band diagram of a conventional p - n junction solar cell in the case of short circuit condition; (b) Charge separation under illuminations. [1]

heterojunction, DSCs are majority carrier devices where electrons and holes are separated in two chemical phases. Upon illumination, the surface anchored dyes are sensitized to the excited state (S^*) by light absorption. This mode of carrier generation is also shared in organic, bulk heterojunction (BHJ) solar cells where a light-absorbing organic polymer works as the sensitizer and a derivatized fullerene as the electron acceptor. These devices are classified by Gregg as “excitonic solar cells”, referring to the generation of a molecular excited-state or Frenkel exciton (see Chapter 2.2.2) as the first step of a photovoltaic event [35, 36]. In most other “excitonic” solar cells, photogenerated excitons have to diffuse a few nm to the interface before dissociating to an electron-hole pair. While in DSCs, the excitons are generated right at the interface and they dissociate readily to create an electron-hole pair, with electrons subsequently injected into the conduction band of the semiconductor while the holes, at least initially, remain on the sensitizers. The dye ground state (S^0) is then regenerated by electron donation from the redox system to the oxidized state of the sensitizer (S^+). The recuperation of redox system is realized by transporting holes to the counter electrode either in a diffusion or hopping

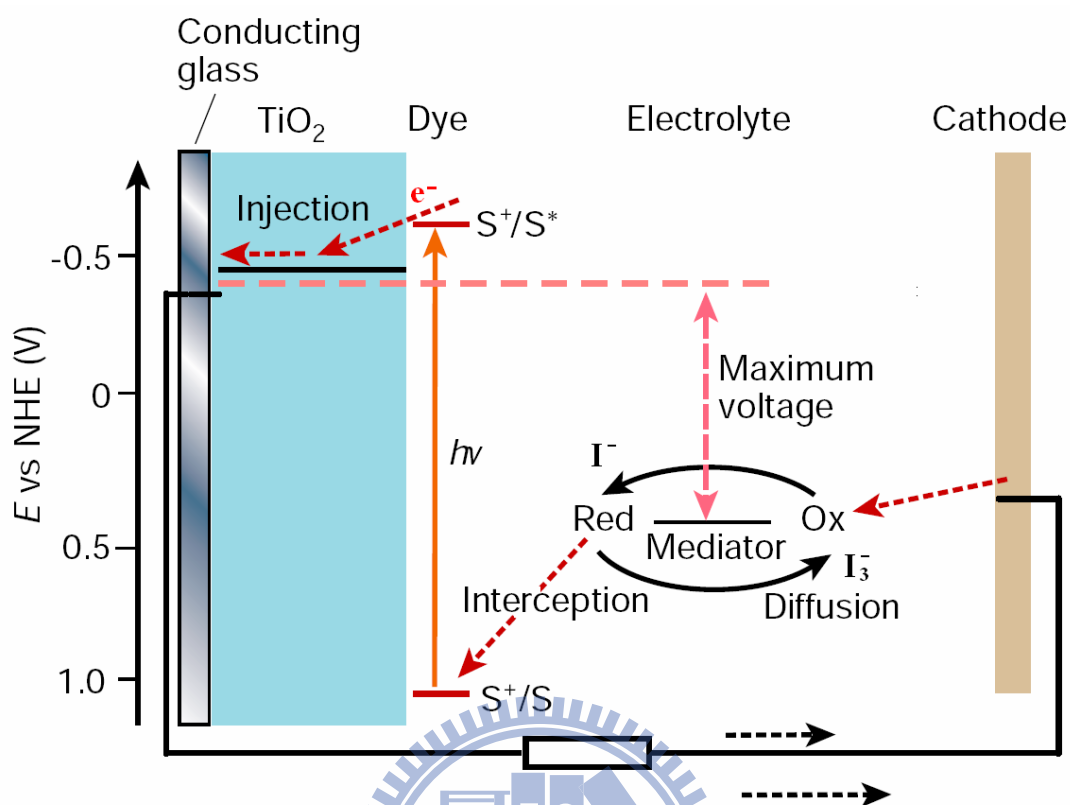


Figure 6-2. Scheme of the operational principle of the DSCs.

mechanism (depending on the transporting mediator). The whole process is finally completed by electron migration via the outer circuit and the device generates electric power from light without penalty of any permanent chemical transformation [37]. These photophysical processes are schematically depicted in Fig. 6-2.

DSCs are photoelectrochemical devices where several electron transfer (ET) processes are in parallel and in competition. Figure 6-3 shows the typical time constants of processes involved in such a DSC device. The initial events of electron injection and dye regeneration leading to photoinduced charge separation occur on a femto- to nanosecond or microsecond time scale, [38] while the redox capture of the electron by the oxidized relay and the electron migration across the nanocrystalline film take place within milliseconds or even seconds. The square root of the product of

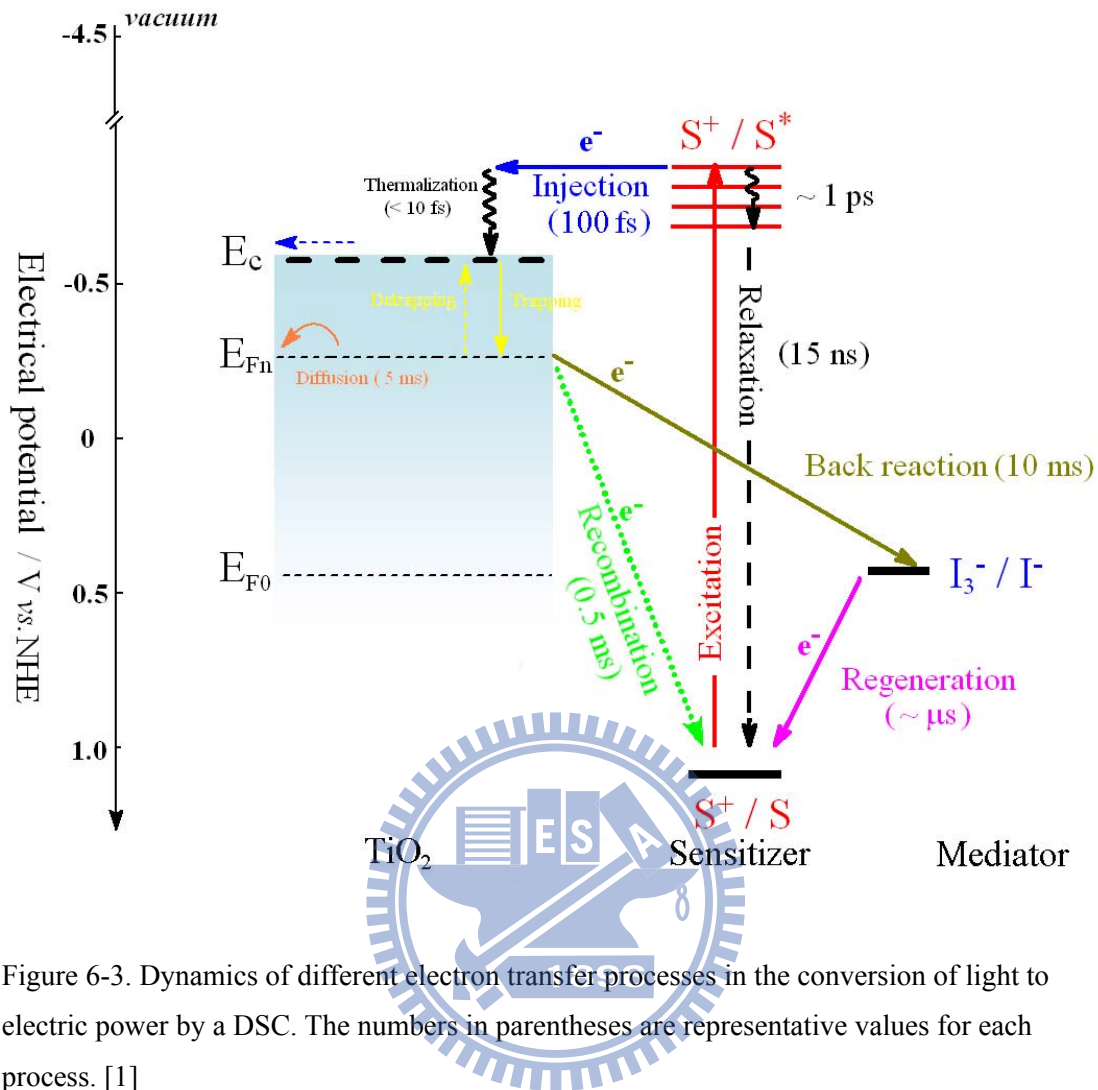


Figure 6-3. Dynamics of different electron transfer processes in the conversion of light to electric power by a DSC. The numbers in parentheses are representative values for each process. [1]

the diffusion coefficient (D_n) and electron lifetime (τ_n) corresponds to the diffusion length (L_n) of the electron ($L_n = \sqrt{D_n \tau_n}$). If the latter is greater than the film thickness, all of the photogenerated carriers will be collected. However, excitons formed further away from the interface decay by relaxation processes (nonradiative or radiative) before reaching the interface and do not contribute to the photocurrent. Furthermore, the recombination or back reaction while electron trapped in the semiconductor diminishes the photocurrent.

Following the above rationales, it is clear that photogeneration, separation and recombination take place nearly exclusively at the high-surface area heterointerface in

nanocrystalline DSCs. Thus the chemical stability and electron transport properties of these interfaces are of critical importance to the conversion efficiency of the device.

6.1.3 ZnO Photoanodes for DSCs

For DSCs, a photoanode composed with the dye-sensitized nanocrystalline semiconductors plays a significant role in converting photons into electricity. Light harvesting, electron injection and collection, and unwanted electron recombination are all correlated with the photoanode. So far, the most impressive DSCs are the ones based on TiO₂ nanocrystalline particle films loaded with a Ruthenium (II) polypyridyl complexes with the structure of RuLL'(NCS)₂ (L, L' stand for polypyridine ligands), such as N3 and N719 dyes [26, 39]. The work was first initiated by Prof. Grätzel, and a remarkable breakthrough in conversion efficiency (7.1-7.9%) was obtained [25]. From now on, the conversion efficiency was continually improved, and a highest overall conversion efficiency of 11.18% has been achieved using the purified N719 photosensitizer adsorbed on TiO₂ nanoporous films in its monoprotonated state [40, 41]. Unfortunately, the record high conversion efficiency of DSCs (11.18%) plateaued in an unchanged level over the following 5 years. Further increase in conversion efficiency is restricted due to large energy loss from serious recombination between electrons and either oxidized dye molecules or electron-accepting species in the electrolyte during the charge-transport process [41-43]. Such a recombination is related to the lack of a depletion layer on TiO₂ nanocrystallite surfaces [44], and becomes relatively serious as the thickness of TiO₂ photoanode film increases. In order to optimize the electron-transfer energetics and kinetics, more basic research is needed to modify the natural components and the structural designs in the DSCs, particularly in the semiconductor photoanode materials that bridge the dyes and the

electron collecting anode. In this regard, the wide-band-gap semiconductor ZnO has attracted much attention as a fascinating alternative to conventional TiO₂ photoanode in DSCs. This is because ZnO and TiO₂ exhibit similar lowest conduction band edges and electron injection process from the excited dyes. Additionally, the lifetime of carriers in ZnO is significantly longer than that in TiO₂ [45]. More importantly, ZnO has a higher electronic mobility which is favorable for electron transport in comparison with TiO₂ [46]. Therefore, it is expected that reduced recombination would be achieved when ZnO is used as photoanode in DSC due to rapid electron transferring and conduction. Currently, increasing interest has been focused on ZnO-based DSCs, and many research groups all over the world have spent much effort on optimizing the components of ZnO-based DSCs, such as the morphology of photoanode, the categories of dye and electrolyte, and the selection of the catalyst on counter electrode. Also, a large amount of studies on the performance parameters of DSCs including open-circuit photovoltage (V_{oc}), short-circuit photocurrent (I_{sc}), and fill factor (FF) have been performed intensively. Based on these extensive investigations, at present, a highest conversion efficiency (η) of 6.58% has been primitively achieved [47]. Many researchers exploring on ZnO-based DSCs expect that there is still huge potential to improve the cell conversion efficiency by further optimization in all aspects, especially the morphology of ZnO nanostructures. Due to the ease of crystallization and anisotropic growth of ZnO material, it embodies a wide variety of nanostructures, such as zero-dimensional (0-D) ZnO nanoparticles, one-dimensional (1-D) nanowires/rods/tubes/fibers, 2-D nanosheets/belts/plates, and 3-D hierarchical architectures. All these nanostructures have been successfully applied in ZnO-based DSCs. These ZnO nanostructures can be fabricated by various techniques, including thermal evaporation, dc plasma reaction, chemical vapor

deposition (CVD), molecular beam epitaxy (MBE), sputtering, template-assisted method and solution-derived synthesis methods, and so forth. Considering that DSCs will hold the balance in the future energy production and take up a considerable market quotient in energy supply, ZnO nanostructured photoanodes should be constructed by some facile, low-cost and scale-up methods. Recently, many researchers have presented reviews on ZnO-based DSCs [48-50].

6.1.4 Research Motivation

ZnO is a versatile semiconductor having recently been reported as an alternative for DSCs because ZnO offers a large direct band gap of 3.37 eV (similar to TiO₂) and very high electron mobility for its relatively small electron effective mass as compared to TiO₂ [51-53]. ZnO also can be tailored to various nanostructures, such as nanorods/nanowires [44, 54-57], nanotubes [58, 59], nanoflowers [60], nanosheets [61-63], tetrapod-like nanopowders [64-66], and polydispersive aggregates [67, 68]. ZnO nano-architectures can significantly enhance DSCs performance through offering either a large surface area for dye adsorption or direct transport pathways for photoexcited electrons.

Utilizing sensitized dye with a high absorption coefficient is another key issue to improve the light harvesting of DSCs. Numerous metal-free organic dyes with high absorption coefficients have recently been reported to act as good sensitizers for TiO₂. Ruthenium complex dyes are not suitable for environmental-friendly photovoltaic devices that limit the potentially wide applications from the low cost and mass production requirements. In particular, indoline dyes have been reported to show the highest power conversion efficiency over 9.0% using volatile electrolytes [69, 70] and efficiency 7.2% using nonvolatile ionic-liquid electrolytes [71] among organic dyes.

The indoline dyes that exhibit remarkable performance as DSCs are relatively inexpensive due to the simple preparation procedures [72, 73]. Recently, an indoline dye (D149) has also been utilized in ZnO nanosheets [62] and tetrapod-like ZnO nanopowders [65], and achieved the DSC performances of 4.2% and 4.9%, respectively. Accordingly, a systematic study of the characterization in indoline-sensitized ZnO DSCs are important for both the further dye molecular engineering and are proposed for photovoltaic application points of view.

6.2 Experimental Procedures

6.2.1 Cell Fabrication

Preparation of DSCs from ZnO Nanowires. The ZnO nanowires on FTO were fabricated from a hydrothermal synthesis as mentioned in Chapter 3.2. The arrays of ZnO nanowires were then rinsed with deionized water and baked in air at 450°C for 30 minutes to remove any residual organics. On the contrary, the VS method seriously degraded the electric conductivity of FTO owing to the relatively raised synthesis temperature (the 700°C for ZnO buffer layers and 550°C for growth of ZnO nanowires). Consequently, the small short-circuit current of DSCs from high resistance of FTO leads poor performances ($\eta < 0.2\%$).

Solar cells were prepared by immersing the ZnO nanowires on conductive glass substrates into a solution of 0.5 mM cis-bis(isothiocyanato)bis(2,2'-bipyridyl-4,4'-dicarboxylato)-ruthenium(II) bis-tetrabutylammonium (N719, Solaronix) in acetonitrile/*tert*-butanol (1:1) for 20 min, and the films were then rinsed with acetonitrile. The sensitized electrodes were sandwiched together with thermally platinized FTO counter electrodes separated by 25- μm -thick hot-melt spacers (Surlyn, Dupont). The internal space of the cell was

filled with an electrolyte solution (0.1M LiI, 0.5M 1,2-dimethyl-3-propylimidazolium iodide, 0.03M I₂, and 0.5M *tert*-butylpyridine in acetonitrile). The area of active electrode was typically 0.28 cm².

Preparation of DSCs from ZnO Secondary Nanoparticle. The ZnO colloidal solution was produced from zinc acetate dihydrate in diethylene glycol, similar to what we presented in Chapter 3.3 and published papers [74, 75]. The as-synthesized solution was placed in a centrifuge operating at 8000 rpm for 30 mins. After centrifugation, the precipitation of ZnO colloids was then redispersed in ethanol via high-speed stirring for 30 mins. The excess DEG solvent was then removed by a second centrifugation. The ZnO paste for screen-printing was prepared typically by mixing resultant ZnO colloids, ethyl cellulose (EC) and terpineol (anhydrous, #86480, Fluka), the detailed procedure is as follows. EC 5–15 mPas and EC 30–70 mPas, (#46070 and #46080, Fluka) were individually dissolved in ethanol to yield 10 wt.% solution. Then 12g EC 5–15 and 12g EC 30–70 were added to a round bottomed rotavap flask containing 12g ZnO colloids and 25g terpineol. The mixture paste was dispersed in an ultrasonic bath and a rotary-evaporator (BUCHI V850) was used to remove the residual ethanol and water in the mixture. The final formulations of the ZnO pastes were made with a three-roll mill (EXAKT E50).

The DSCs were basically sandwiched together with many parts. The photoanodes of self-assembled ZnO nanoparticles were prepared by screen-printing the 0.28 cm² ZnO films with various thicknesses (18, 21, 27 and 32 μm) on fluorine-doped tin oxide (FTO) substrates (Nippon Sheet Glass Co. Ltd., 10 Ω/per square, 3 mm thickness). The photoelectrodes were then gradually heated under an O₂ flow at 350 °C for 30 mins to remove the organic materials in the paste. After cooling to room temperature, the ZnO photoelectrodes were immersed into a solution

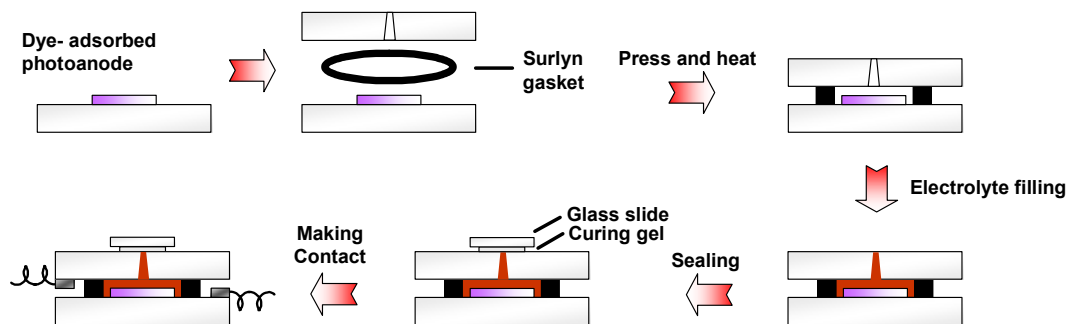


Figure 6-4. Flow chart of device assembly.

made of 0.3 mM D149 or D205 organic sensitizer (Chemicrea Inc.) with 0.6 mM chenodeoxycholic acid (CDCA, Sigma-Aldrich) in acetonitrile/tert-butyl alcohol mixture (v/v = 1 : 1) at 65 °C for 1h. The counter electrodes were also made of NSG FTO glass on which the nanocrystalline Pt catalysts were deposited by decomposing from H_2PtCl_6 at 400 °C for 20 mins. The internal space of the ZnO photoelectrodes and counter electrodes was separated by 60 μm thick hot-melting spacer (Surlyn, DuPont) and filled through a hole with volatile electrolytes, which are composed of 0.5 M 1,2-dimethyl-3-propylimidazolium iodide (PMII), 0.03 M I_2 (Sigma-Aldrich), and 0.5 M tert-butylpyridine (TBP, Sigma-Aldrich) in acetonitrile. Fabrication process was schemed as Fig. 6-4. It is important to note that the LiI should not be added in electrolyte solution to avoid desorption of indoline dyes from ZnO surfaces.

6.2.2 Performance Characterization

6.2.2.1 The Solar Spectrum and Air Mass

The solar spectrum is a mixture of light with different wavelengths, ranging from ultraviolet, visible and infrared regions of the electromagnetic spectrum. According to

the black-body radiation, the energy density per wavelength $dU(\lambda, T)/d\lambda$ can be expressed as a function of λ by Eq. 6.1.

$$\frac{dU(\lambda, T)}{d\lambda} = \frac{2hc_0 d\Omega}{\lambda^5} \frac{1}{\exp(hc_0/k_B T) - 1} \quad (6.1)$$

where $d\Omega$ is solid angle element, c_0 is the velocity of light in the medium, k_B and h is the Boltzmann constant and Planck constant, respectively. By taking $d^2U(\lambda, T)/d\lambda^2 = 0$, the maximum value of $dU(\lambda, T)/d\lambda$ is at a wavelength

$$\lambda_{\max} = \frac{hc_0}{4.965k_B T} = 0.2497 \frac{\mu\text{meV}}{k_B T} \quad (6.2)$$

The power density at the sun's surface is 62 MW m^{-2} and it reduces to 1353 W m^{-2} at the point just outside the Earth's atmosphere since the solid angle subtended by the sun, Ω_s , is as small as $6.8 \times 10^{-5} \text{ sr}$. On passing through the atmosphere, the spectrum is partially attenuated by the absorption of oxygen, ozone in the ultraviolet region and water vapor, carbon dioxide, methane in the infrared. This attenuation is described by the "Air Mass" factor since the absorption increases with the mass of air through which the radiation passes. For a thickness of l_0 of the atmosphere, the path length l through the atmosphere for radiation at an incident angle α relative to the normal to the earth's surface is given by

$$l = l_0 / \cos \alpha \quad (6.3)$$

The ratio l/l_0 is called the Air Mass factor. The spectrum outside the atmosphere is denoted as AM0 and that on the surface of the earth for perpendicular incidence as

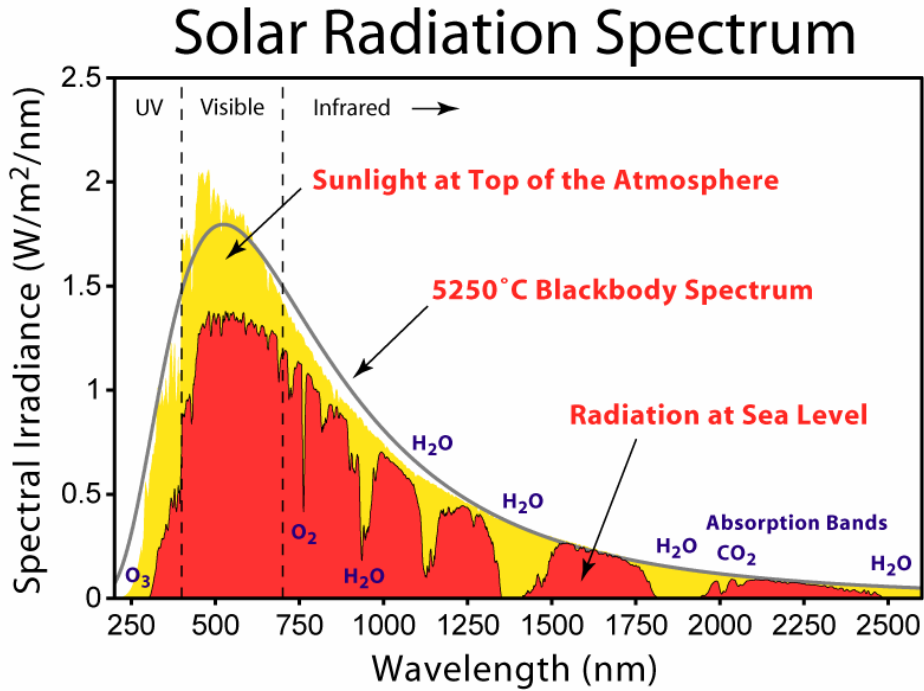


Figure 6-5. Spectra of Black body 5250°C AM0 and AM1.5, respectively. [76]

AM1. The standard spectrum for moderate weather is AM 1.5, which corresponds to a solar incident angle of 48° relative to the surface normal and gives a mean irradiance of 1000 W m^{-2} . Figure 6-5 shows the comparison between the spectrum of a 5250°C black body and those of AM0 and AM1.5. The actual irradiation varies with seasons, climates, day time and the position of the sun. Averaged over the year, the global mean energy current density ranges from less than 100 W m^{-2} at high latitude areas to around 300 W m^{-2} in Saudi Arabia. It is a little more than 100 W m^{-2} in central Europe, where the amount of energy incident to a normal surface in a year is about 1000 kWh m^{-2} and also known as 1000 sun hours per year.

6.2.2.2 Photocurrent-Voltage (J-V) Characterization

Standard current-voltage measurement of a DSC determines the current voltage response of the device, i.e. current-voltage characteristics, in the dark and under

different light intensities. In the dark, the applied voltage (bias) on the device generates a current that flows in the direction opposite to that of the photocurrent. This reverse current is usually called the dark current. For an ideal diode, the dark current I_{dark} relates to voltage with Eq. 6.4.

$$I_{dark} = I_s (e^{qV/k_B T} - 1) \quad (6.4)$$

where I_s is the saturation current of the diode (typically 10^{-7} - 10^{-9} A), V is the voltage applied on the terminals of the cell and q is the elementary charge.

Under illumination, the current-voltage characteristics follow

$$I = I_{ph} - I_s (e^{qV/k_B T} - 1) = I_{ph} - I_s (e^{V/V_T} - 1) \quad (6.5)$$

where I_{ph} is the photocurrent that depends on irradiation intensity and V_T is often referred to as the thermal voltage that equals $k_B T/q$. For non-ideal devices, an ideality factor, m , is used to describe the weaker dependence of dark current on voltage

$$I = I_{ph} - I_s (e^{V/mV_T} - 1) \quad (6.6)$$

An experimental J-V curve is shown in Figure 6-6, together with the power curve. The following parameter can be derived with the J-V curve.

Open-Circuit Voltage (V_{oc}). The V_{oc} is measured under the condition when there is no external load connected, i.e. the circuit is broken or open. In this condition, there is no external current flow between the two terminals of the device, i.e. $I = 0$ and

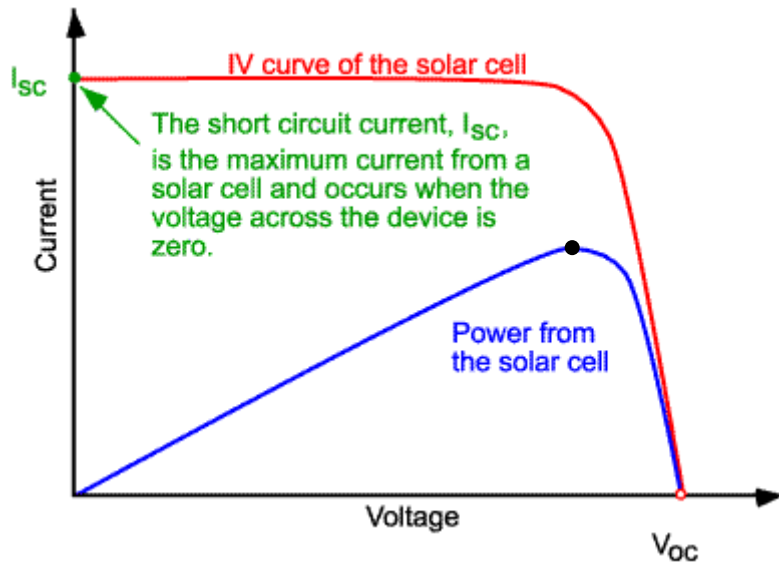
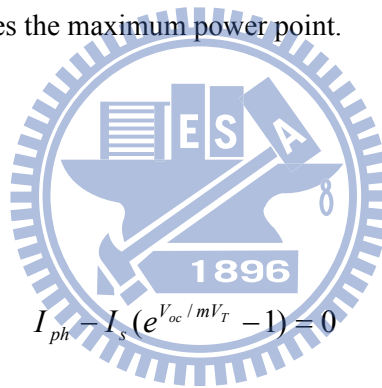


Figure 6-6. A typical J-V curve in the experiment. The blue line shows the power output at different bias. The dot indicates the maximum power point.

$V = V_{oc}$. From Eq. 6.7,



$$I_{ph} - I_s (e^{V_{oc}/mV_T} - 1) = 0 \quad (6.7)$$

$$V_{oc} = mV_T \ln\left(\frac{I_{ph}}{I_s} + 1\right) \cong mV_T \ln\left(\frac{I_{ph}}{I_s}\right) \quad (6.8)$$

V_{oc} increases logarithmically with the photocurrent and light intensity.

Short-Circuit Current (I_{sc}). The I_{sc} is measured at the condition when the applied voltage, V , equals zero. From Eq. 6.9,

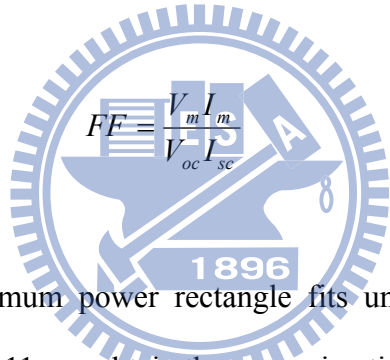
$$I_{sc} = I_{ph} \quad (6.9)$$

I_{sc} increases linearly with the light intensity.

Fill Factor (FF). The power is calculated as the product of $I \times V$ and the maximum power point is labeled with the dot. At this point, the device delivers the highest power output with the voltage, V_m and current, I_m .

$$V_m = V_{oc} - mV_T \ln\left(\frac{V_m}{V_T} + 1\right) \quad (6.10)$$

The fill factor (FF) is defined as the ratio

$$FF = \frac{V_m I_m}{V_{oc} I_{sc}} \quad (6.11)$$


to describe how the maximum power rectangle fits under the I - V characteristics.

Combining Eqs. 6.10 and 6.11, we obtain the approximation for FF in Eq. 6.12.

$$FF = \frac{V_{oc} / mV_T - \ln(V_{oc} / mV_T + 1)}{V_{oc} / mV_T + 1} \quad (6.12)$$

Typical FF of DSC ranges from 0.6 to 0.8 depending on the individual device and usually increases with the decreasing light intensity. It is also influenced by the series resistance (R_s) arising from the internal resistance and resistive contacts of the cell and parallel resistance (R_{sh}) from the leakage of the current. Figure 6.7 illustrates a simplified equivalent circuit for DSC included R_s and R_{sh} . For an efficient solar cell, we need a small R_s but a large R_{sh} since a large R_s and a small R_{sh} decrease the FF

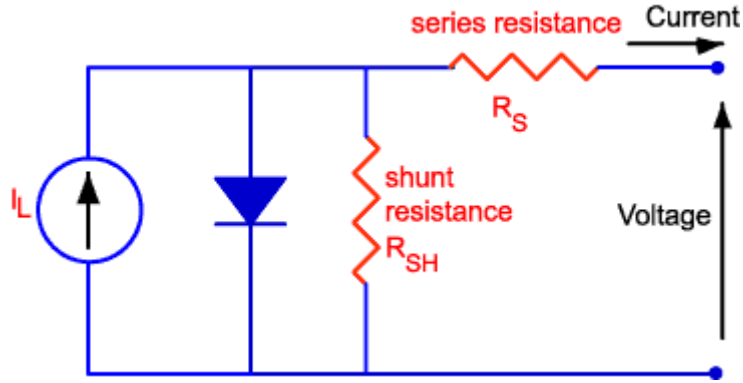


Figure 6-7. A simplified equivalent circuit for DSC. Series (R_s) and shunt resistances (R_{sh}) are taken into account.

dramatically. When are taken into account, a more precise diode equation is given by eq. 6.13.

$$I = I_{ph} - I_s (e^{(V+IR_s)/mV_T} - 1) - (V+IR_s)/R_{sh} \quad (6.13)$$

Solar-to-Electric-Power Conversion Efficiency (η). The efficiency η of the device is the parameter that is associated with the performance of the device. It is defined as the ratio of the maximum power (P_{max}) to the incident sunlight power (P_s).

$$\eta = \frac{V_m I_m}{P_s} = \frac{V_{oc} I_{sc} FF}{P_s} \quad (6.14)$$

P_s is an important experimental parameter and in order to compare different results, standard test condition is always used for all the devices in this work including AM 1.5 spectrum illumination with an incident power density of 100 mW cm^{-2} .

6.2.2.3 Incident Photon-to-Current Conversion Efficiency (IPCE)

The incident photon-to-current conversion efficiency (IPCE) is defined as the number of light-generated electrons in the external circuit divided by the number of incident photons at a certain wavelength.

$$IPCE = \frac{N_{electron}}{N_{photon}} = \frac{qN_{electron} / s}{qN_{photon} / s} = \frac{I_{ph} (amp)}{qN_{photon} / s} \quad (6.15)$$

The incident power

$$P_{in} (Watt) = P_{in} \left(\frac{Joule}{s} \right) = \frac{N_{photon}}{s} h\nu = \frac{N_{photon}}{s} \frac{hc_0}{\lambda} \quad (6.16)$$

With Eq. 6.16, Eq. 6.15 can be rewritten as

$$IPCE = \frac{I_{ph}}{qP_{in} \lambda / hc_0} = \frac{I_{ph} hc_0}{P_{in} q \lambda} = \frac{I_{ph}}{P_{in}} \times \frac{1240}{\lambda(nm)} \times 100\% \quad (6.17)$$

6.2.2.4 Electrochemical Impedance Spectroscopy (EIS)

The principle of using EIS to study response of the device resembles that of the phototransient experiment except that an electrical signal is used as the probe. In EIS experiments, the device is first poised by an external potential bias and then subjected to a harmonically modulated low-amplitude voltage, $\Delta U = U_{amp} e^{i\omega t}$, as a small perturbation. An increase of ΔU on the device will cause a current flow of $\Delta i = i^{amp} e^{i(\omega t - \theta)}$ by a delay of phase angle θ . The impedance of the device is thus given by

$$Z_{EIS} = \left| \frac{\Delta U}{\Delta I} \right| = \left| \frac{U_{amp}}{i_{amp}} \right| e^{i\theta} \quad (6.18)$$

The interpretation of the EIS spectrum of a DSC has been thoroughly discussed recently [77-88]. Generally, a transmission line model is used to describe the system, as is shown in Figure 6.8. Here, the whole mesoscopic TiO₂ film is treated as an interconnected network. Under a forward bias, electrons are injected from FTO substrate into the TiO₂ and the film is charged by electron propagation through individual particles with a resistance of r_{trans} . Some of the injected electrons recombine with the oxidized species in the electrolyte, characterized by a charge transfer resistance of r_{ct} and a capacitance of c_{ch} , and the rest of the electrons are then recaptured by the FTO current collector during the opposite phase of the sinusoidal voltage modulation. The two channels for electron transportation through TiO₂ and that of the I₃⁻ through the electrolyte are coupled in series. Taking d as the thickness of the mesoscopic TiO₂ film, the electron transport resistance is $R_t = r_t \times d$, the interfacial charge recombination resistance is $R_{ct} = r_{ct}/d$ and the chemical capacitance of the film is $C_{ch} = c_{ch} \times d$, where the lower case letters represent resistances and capacitance that are normalized to the film thickness [84]. $R_{FTO/EL}$ and $C_{FTO/EL}$ stand for the charge transfer resistance and the corresponding double layer capacitance at exposed FTO/electrolyte interface and change with surface conditions (blocking layer and cleanliness). Due to the irreversibility of I/I₃⁻ couple on FTO, $R_{FTO/EL}$ is usually very large. The diffusion of I₃⁻ within a thin layer cell is described by a Nernst diffusion impedance Z_d . Regeneration of I₃⁻ at the counter electrode is characterized by R_{CE} and C_{CE} , which are the charge transfer resistance and double layer capacitance at the platinized FTO, respectively.

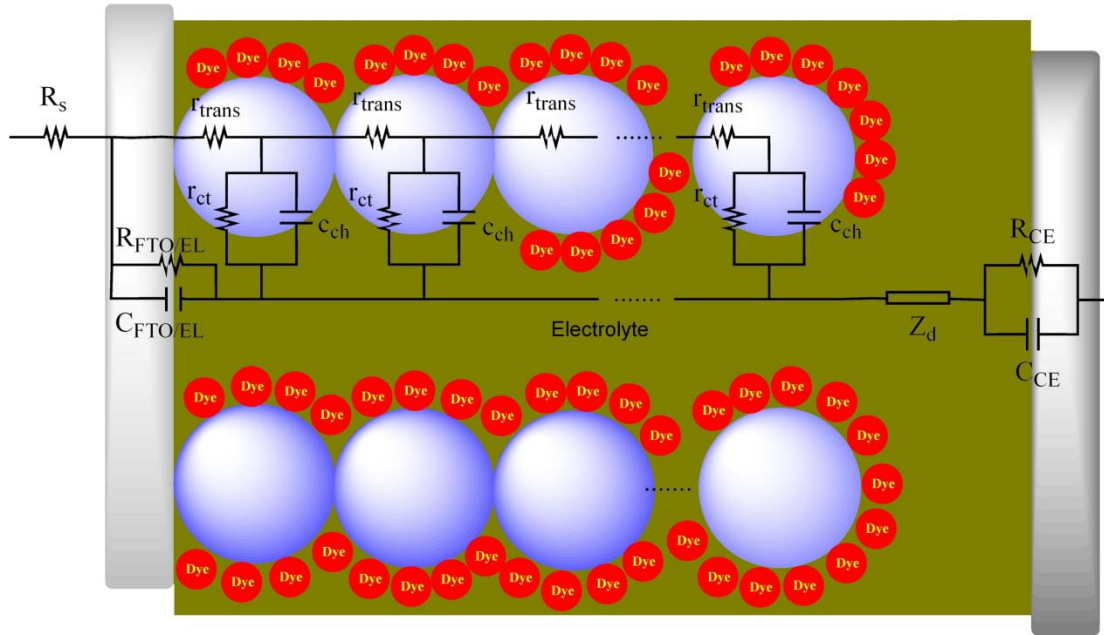


Figure 6.8. Equivalent circuit model for DSCs using TiO_2 photoanode. [1]

The impedance of TiO_2 from equivalent circuit as depicted in Fig. 6.8 can be written as [85]

$$Z_{\text{TiO}_2} = \frac{R_{\text{trans}}}{\sqrt{\left(\frac{R_{\text{trans}}}{R_{\text{ct}}}\right)\left(1 + \frac{i\omega}{\omega_k}\right)}} \coth\left[\sqrt{\left(\frac{R_{\text{trans}}}{R_{\text{ct}}}\right)\left(1 + \frac{i\omega}{\omega_k}\right)}\right] \quad (6.18)$$

Where $\omega_k = 1/\tau_n$, ω_k and τ_n are defined as the recombination rate constant and lifetime of an electron in TiO_2 , respectively. The impedance of the electron transfer at the Pt counter electrode can be described approximately by the following simple RC circuit.

$$Z_{\text{pt}} = \frac{1}{\frac{1}{R_{\text{CE}}} + i\omega C_{\text{CE}}} \quad (6.19)$$

The finite Warburg impedance describes the diffusion of triiodide ions in the electrolyte [75, 76].

$$Z_d = \frac{R_D}{\sqrt{\frac{i\omega}{D_1/\delta^2}}} \tanh\left[\sqrt{\frac{i\omega}{D_1/\delta^2}}\right] \quad (6.20)$$

$$R_D = \frac{k_B T}{m^2 q^2 A_V C^* D_1 \delta} \quad (6.21)$$

$$\omega_{\max} \approx 2.5 \frac{D_1}{\delta^2} \quad (6.22)$$

where D_1 and δ represent the diffusion coefficient of I_3^- and the thickness of the liquid film, respectively. The number of electrons transferred in each reaction, m , is 2 in this case. A_V and C^* are Avogadro's constant and the concentration of I_3^- in the bulk, respectively.

The total impedance of the DSC, Z_{total} , is given as the summation of the impedance of diffusion and recombination in the TiO_2 electrode, Z_{TiO_2} , Z_{pt} , Z_d and R_s which is a series resistance for the transport resistance of FTO and all resistances out of the cell.

$$Z_{total} = Z_{TiO_2} + Z_{Pt} + Z_d + R_s \quad (6.23)$$

Typical EIS spectra are shown in Figure 6.9 and the measured data are presented in squares. The upper curve displays real part (Z') versus the imaginary part (Z'') of

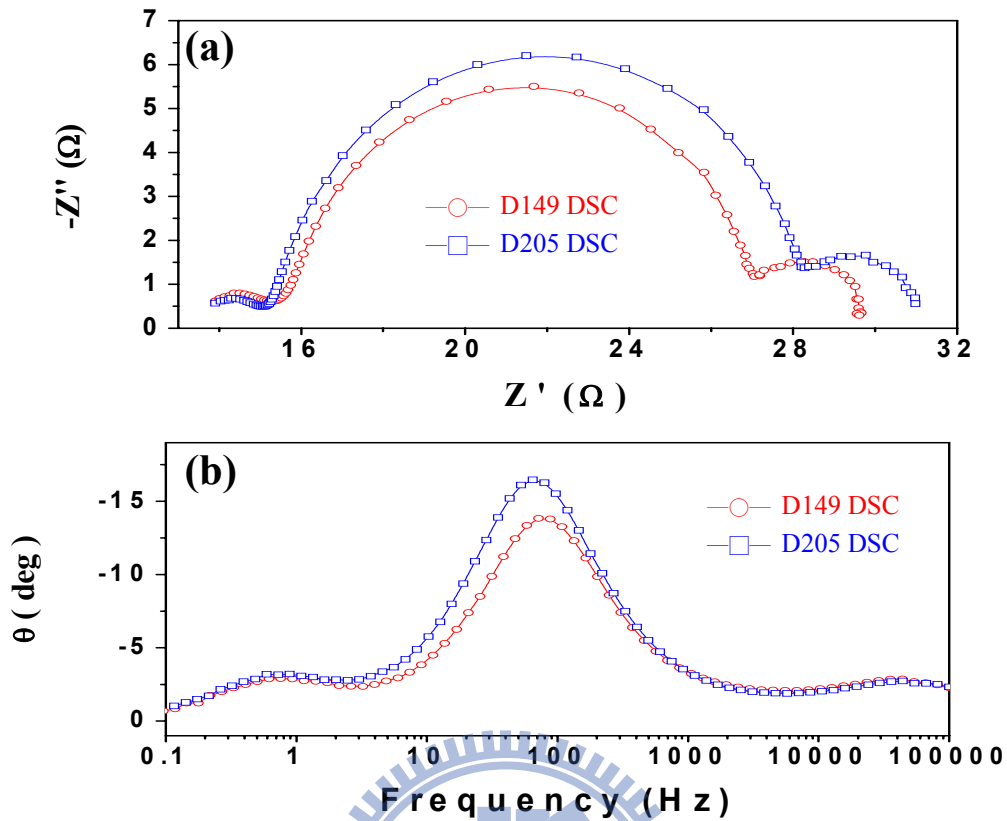


Figure 6.9. Typical curves of impedance spectra for a DSC. (a) Nyquist plots and (b) Bode phase plots. Experimental data are plotted in black squares and the fitting is in solid lines.

the impedance, usually known as the Nyquist plot. The lower curve is the Bode plot where the phase angle θ is plotted against frequency. It is apparent that the Nyquist plot consists of three semicircles. The small semicircle occurring at highest frequencies represents redox charge transfer at the platinum counter electrode, the larger one at intermediate frequencies stands for the electron transport in the TiO_2 layer, the electron transfer at the oxide/electrolyte interface and the third one at lower frequencies is attributed to ion diffusion within the electrolyte. Accordingly, there are three peaks in the Bode plot (Fig. 6-9 bottom), corresponding to the RC time constants shown in the Bode plot. Based on the equivalent circuit in Fig. 6.8, fairly satisfactory fittings can be obtained as the solid lines shown in Fig. 6.9.

The data fitting gives key parameters of the device. The diffusion coefficient D_n

is then calculated by $D_n = d^2 / (R_{trans}C_{ch})$ while the electron lifetime τ_n is obtained by $\tau_n = R_{ct}C_{ch}$. The electron diffusion length L_n thus can be delivered as

$$L_n = \sqrt{D_n \tau_n} = d \sqrt{\frac{R_{ct}}{R_{trans}}} \quad (6.24)$$

6.2.3 Characteristic Instruments

Photocurrent–Voltage (J-V) and Electrochemical Impedance Spectroscopy (EIS). Efficiencies for solar energy conversion and electrochemical impedance spectroscopy (EIS) measurements, a white light source (Yamashita Denso, YSS-100A) was used to give an irradiance of 100 mWcm^{-2} (the equivalent of one sun at AM 1.5) on the surface of the solar cells, and the data were collected by an electrochemical analyzer (Autolab, PGSTAT30). The light power was calibrated with a set of neutral density filters and detected by a silicon photodiode (BS-520, Bunko Keiki).

Incident Monochromatic Photon to Current Conversion Efficiency (IPCE). The action spectra of the incident monochromatic photon to current conversion efficiency (IPCE) for solar cells were measured as a function of wavelength from 400 to 900 nm using a specially designed IPCE system (C-995, PV-measurement Inc.) for DSCs.

Optical Absorbance. The optical absorbance of photoanodes was carried out with a Hitachi U-2800 UV-VIS spectrophotometer. Dye loading was determined by detaching the dye from the ZnO photoelectrode surface with 0.1 M NaOH solution and measuring the optical absorbance.

Photoluminescence (PL) and Time-Resolved Photoluminescence (TRPL). The steady-state and time-resolved photoluminescence (PL) spectroscopy were

monitored using a Jobin-Yvon Triax-320 monochromator with a charge-coupled device and a time-correlated single photon counting (TCSPC) system (PicoHarp 300, PicoQuant), respectively. The pumping apparatus was employed by a frequency-doubled mode-locked Ti:sapphire laser (Mai Tai, Spectra-Physics) to generate output pulses at 400 nm with duration ~100 femtosecond and a repetition rate of 80 MHz.

6.3 ZnO Nanostructures for DSCs

6.3.1 Branched ZnO Nanowires for DSCs

The formation mechanism of the branched ZnO nanowires has been mentioned in Chapter 4. Figure 6-10 shows the compared photocurrent–voltage (J-V) characteristics for solar cells, constructed using the bare ZnO nanowires and the branched ZnO nanowires, with AM 1.5 illumination at 100 mW/cm² from a xenon lamp. The short-circuit current density (J_{sc}) and the overall light conversion efficiency of the branched ZnO nanowire DSCs were 4.27 mA/cm² and 1.51 %, respectively, which are almost twice higher than that of the bare ZnO nanowires. One factor for the increment in short-circuit current density would be the enhanced photon absorption associated with the presence of enlargement of internal surface area resulting in sufficient dye-loading. Although the length and density of ZnO structures exhibit the disadvantage compared with previous study [44], the overall efficiency can achieve almost the same value via utilizing the extra secondary nanobranches. The values of fill factor (FF) for ZnO DSCs are general lower than those using TiO₂ nanoparticles (0.6–0.7). This is attributed to recombination between photoexcited carriers in the photoanodes and tri-iodide ions in the electrolyte. Slightly different value in the bare ZnO nanowire and branched ZnO nanowire DSCs revealed almost the same

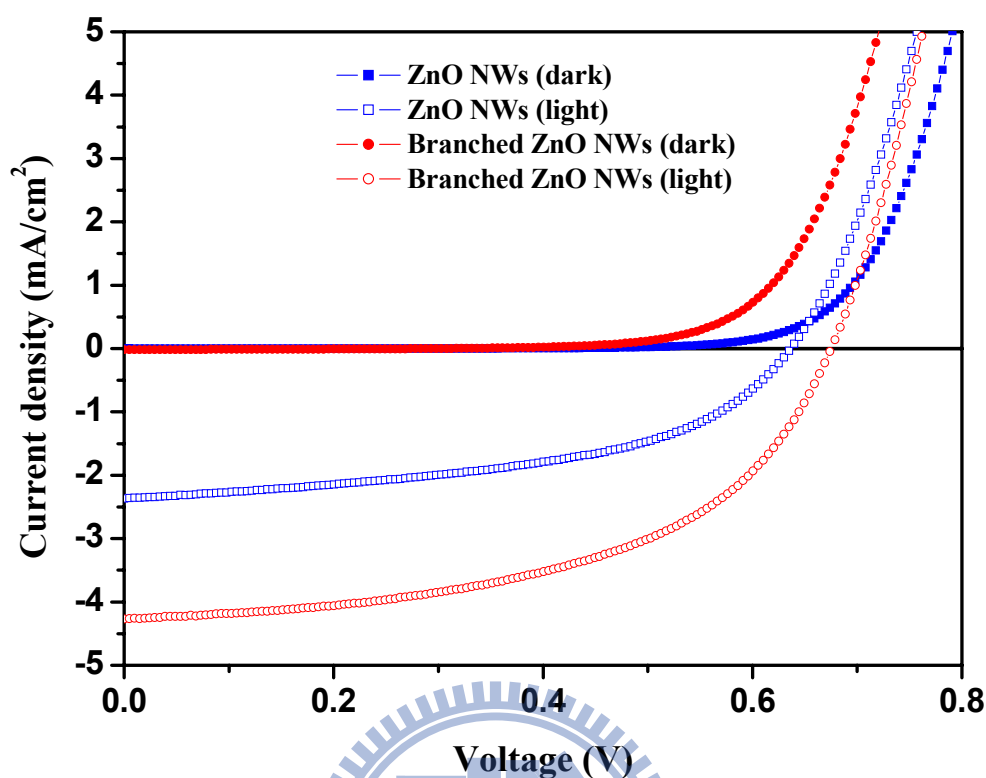


Figure 6.10. Current density against voltage (J-V) characteristics of the bare ZnO nanowires and the branched ZnO nanowire DSCs.

interfacial recombination, which was evidenced by the equivalent value of the shunt resistance $R_{sh}=(dV/dI)_{V=0}$ from the J-V curves under illumination. The series resistance $R_s=(dV/dI)_{I=0}$ for branched ZnO nanowire DSCs ($25.64 \Omega\text{cm}^2$) was significantly lower than the bare ZnO nanowire ones ($46.13 \Omega\text{cm}^2$).

Recently, electrochemical impedance spectroscopy (EIS) measurement has been widely performed to investigate electronic and ionic processes in DSCs [86-94]. The Nyquist plots of the impedance data for bare and branched ZnO nanowire DSCs were performed by applying a 10 mV ac signal over the frequency range of 10^{-2} – 10^5 Hz under illumination at the applied bias of V_{oc} , as shown in Fig. 6-11. r_w is the transport resistance of the electrons in the ZnO electrode; r_k is the charge-transfer resistance of

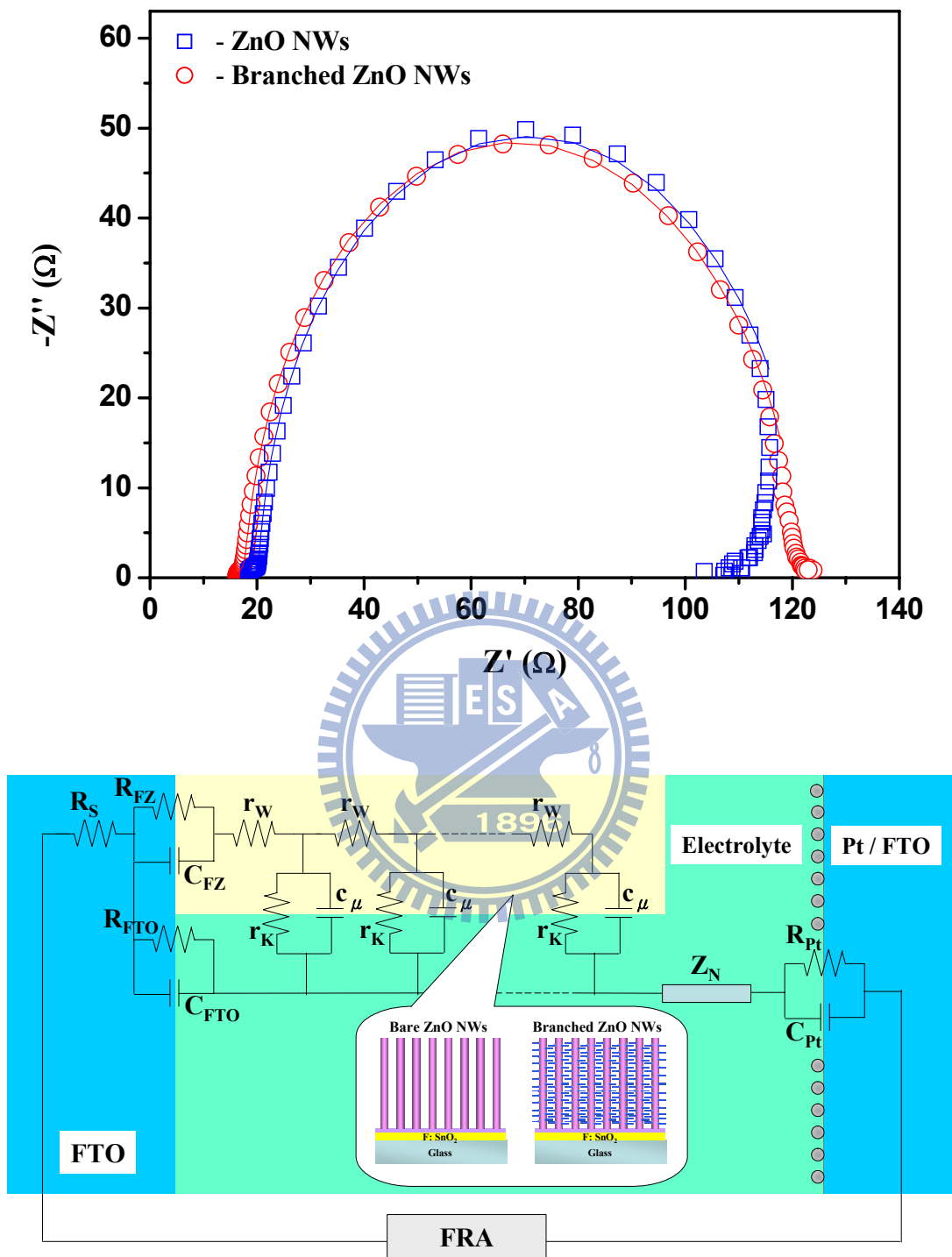


Figure 6.11. Nyquist plots of the bare ZnO nanowires and the branched ZnO nanowire DSCs. The solid lines in are the fitting results based on the equivalent circuit model (modified from ref 87) as shown in the inset.

the charge recombination between electrons in the ZnO electrode and I_3^- in the electrolyte; The thickness L_F of all anodes are about $8\mu\text{m}$; $C_\mu = (c_\mu L_F)$ is the chemical capacitance of the ZnO electrode; R_s is a series resistance for the transport resistance of FTO and all resistances out of the cell; Z_N is the impedance of diffusion of I_3^- in the electrolyte; R_{Pt} and C_{Pt} are the charge-transfer resistance and the interfacial capacitance at the counter electrode (platinized FTO glass) /electrolyte interface, respectively; R_{FTO} and C_{FTO} are the charge-transfer resistance and the interfacial capacitance at the exposed FTO/electrolyte interface, respectively; R_{FZ} and C_{FZ} are the resistance and the capacitance at the FTO/ZnO contact, respectively. Some interior parameters of the devices with thickness of L_F can be derived by well fitting the impedance data of the Nyquist plots to expressions based on the modified equivalent circuit of nanowire DSCs suggested by Wu et al [92, 93].

In fact, the concrete equivalent circuit might be more complex in the operation of the DSC devices. Mora-Seró et al. have recently reported a negative capacitance for different types of solar cells, that is, an inductive behavior which comes from the conductivity modulation of the electrolyte by injected electrons from the photoelectrode when providing high forward bias with low frequency [91]. Hence, the impedance data obtained at different applied potentials cannot be fitted with a single equivalent circuit. An essential component such as an inductive response was suggested to be considered in series with a recombination resistance. In order to avoid the unnecessary interference from the inductive behavior, we presently ignored the low frequency part of impedance data. The fitted results were listed in Table 6-1 which include the first-order reaction rate constant for the loss of electrons (k_{eff}), the electron lifetime ($\tau = 1/k_{eff}$), the electron transport resistance ($R_w = r_w L_F$), and the charge transfer resistance related to recombination of an electron at the

TABLE 6-1. Performances and electron transport properties of the bare ZnO nanowire and the branched ZnO nanowire DSCs determined by photocurrent density-voltage (J-V) characteristics and electrochemical impedance spectroscopy (EIS) analysis.

ZnO DSCs	J_{sc} (mA/cm ²)	V_{oc} (V)	FF	η (%)	k_{eff} (s ⁻¹)	τ_{eff} (s)	R_k (Ω)	R_w (Ω)	D_{eff} (cm ² /s)
Bare Nanowires	2.37	0.636	0.498	0.75	38.31	0.026	92.12	3.63	6.23×10^{-4}
Branched Nanowires	4.27	0.675	0.522	1.51	26.31	0.038	86.85	3.36	4.35×10^{-4}

ZnO/electrolyte interface ($R_k = r_k/L_F$). We found R_k and R_w are quite similar for both DSCs in this present work, which indicated the same interfacial recombination and equal crystallinity for either bare ZnO nanowires or branched ZnO nanostructures. On the contrary, k_{eff} in the branched ZnO nanowire DSCs was smaller than the bare nanowire ones to cause the smaller effective diffusion length [88] ($D_{eff} = (R_k/R_w)L_F^2 k_{eff}$) in branched ZnO nanowire DSCs. Since k_{eff} is related to reaction rate, the electron lifetime ($\tau_{eff} = 1/k_{eff}$) could be prolonged by the additional transport distance between branches and conductive electrode (backbone nanowires).

In general, the current density for DSCs is determined by the initial number of photogenerated carriers, the electron injection efficiency from dye molecules to semiconductor, and the recombination rate between the injected electrons and oxidized dye or redox species in the electrolyte. Base on the assumption of the same injection efficiency and recombination rate for the given ZnO DSCs systems, it is reasonable that the initial number of photogenerated carriers may be significantly affected by the variation in the light-harvesting capability of different-structured photoanodes. Figure 6-12 displays the wavelength distribution of incident monochromatic photon to current conversion efficiency (IPCE). The photocurrent peaks occurring at approximately 400 nm were due to direct light harvesting by ZnO

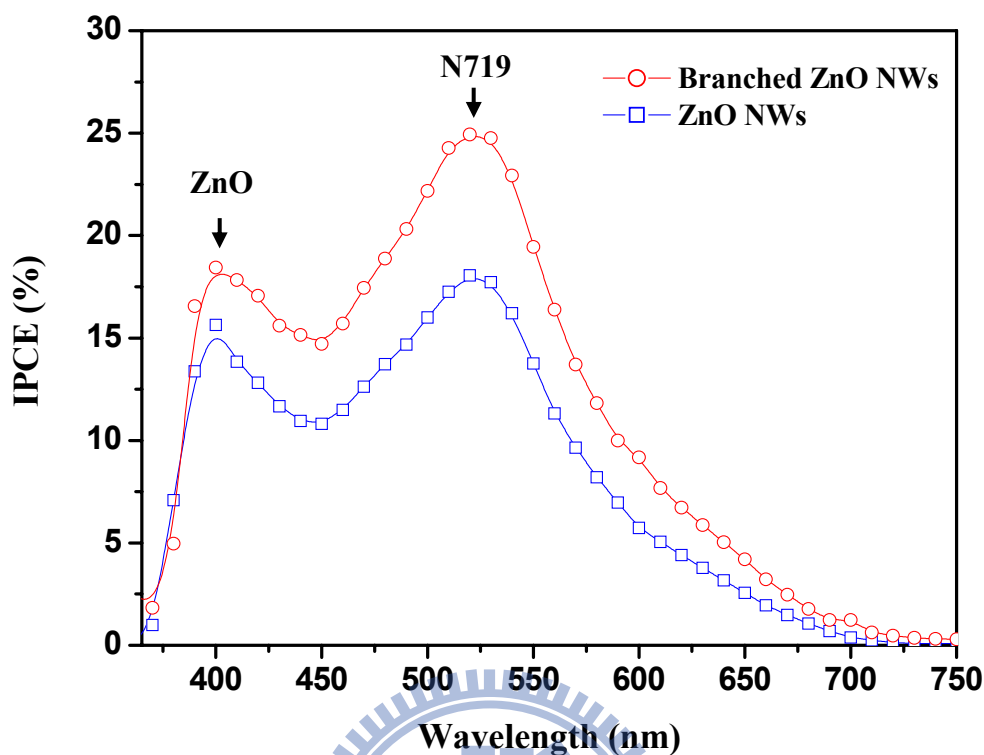


Figure 6.12. The incident monochromatic photon to current conversion efficiency (IPCE) of the bare ZnO nanowire and the branched ZnO nanowire DSCs.

semiconductor, in which the photogenerated electrons diffused through ZnO and the holes in the valence band were replenished directly by charge transfer from the I_3^-/I^- electrolyte [95]. The maxima of IPCE at approximately 525 nm are contributed by the dye absorption, corresponding to the visible $t_2 \rightarrow \pi^*$ metal-to-ligand charge transfer (MLCT). The IPCE obtained for the branched ZnO nanowire DSCs was almost 1.5 times that of the bare ZnO nanowire. The improvement in the IPCE suggested that the high energy conversion efficiency results predominantly from sufficient dye-loading by branched ZnO nanowires, which enlarged internal surface area within the photoelectrode. The dye loading of the photoelectrodes was measured to determine the surface concentration of dye molecules adsorbed on different ZnO

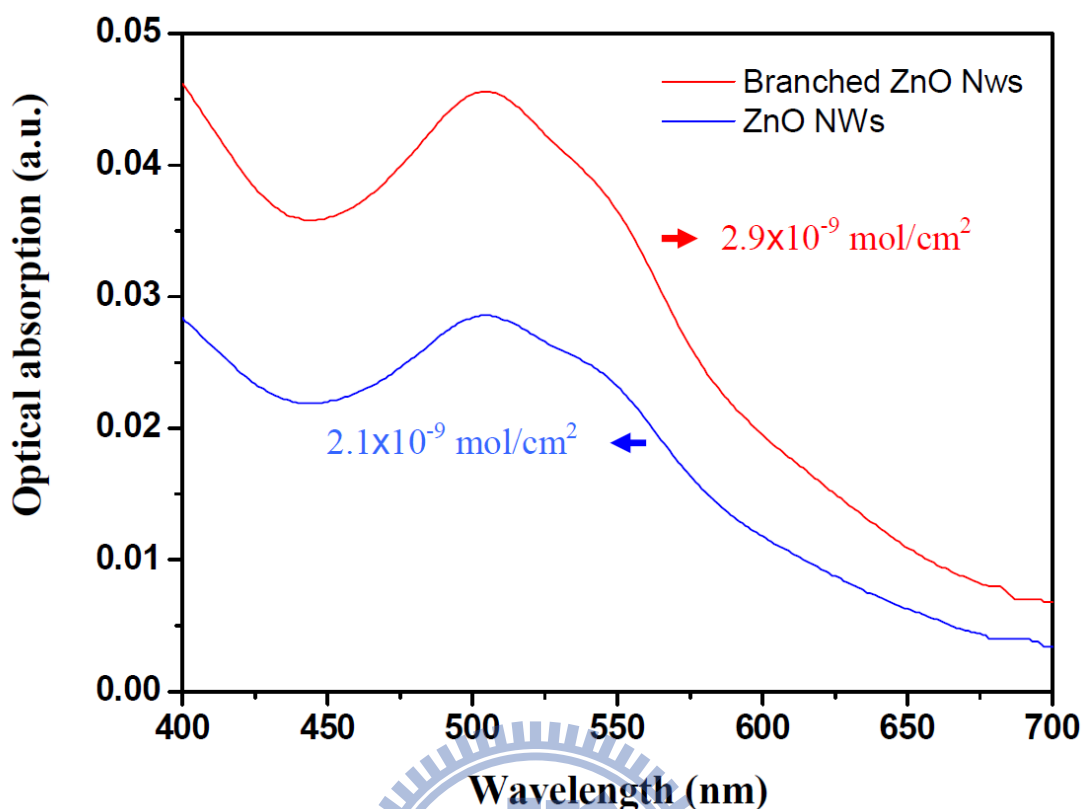


Figure 6-13. Optical absorption of dye detached from the bare ZnO nanowire and the branched ZnO nanowire substrates, and dissolved in 0.1M NaOH solution.

nanostructures, as shown in Fig. 6-13. The concentration of dye in the branched ZnO nanowire electrode was found to be $2.9 \times 10^{-9} \text{ mol/cm}^2$ as measured from dye-desorption experiments, which is almost 40% higher than the obtained value of $2.1 \times 10^{-9} \text{ mol/cm}^2$ for the bare ZnO nanowire electrode. It is important to note that the dye loading of the branched ZnO nanowires was not twice as higher as the value of the bare ZnO nanowires, even though the current density and energy conversion efficiency of the branched ZnO nanowire DSCs are twice higher than the bare ZnO nanowire ones. The different could be ascribed to the insufficient internal surface of the bare ZnO nanowires and the excess dye which resulted in the formation of Zn^{2+} /dye complexes instead of the effective chemical bonding between ZnO and dye

moleculars [96]. The shorter immersion time for deficient chemical-stability ZnO electrode as compared with TiO₂ electrode have recently been reported in detail by Chou et al. [97]. Therefore, the excess immersion time for the insufficient internal surface of bare ZnO nanowires could not achieve more dye loading but seriously deteriorate the performance of DSCs.

The concept of the branched nanostructures is anticipated to be applicable to other semiconductor photoelectrodes in organic–inorganic nanocomposite solar cells, and branched heterojunction nanostructures for the future applications. Although the secondary branches had non-uniform distribution, the branches emanated from partial ZnO nanowires due to the simple dip-coating process, they still can offer greater effective surface area for dye adsorption than the bare nanowires. For optimization of the filling factor of the ZnO nanostructures, the dc or radio-frequency (RF) magnetron sputtering and atomic layer deposition (ALD) might be a great benefit to the pre-coating processes. Further improvement of energy conversion efficiency could be implemented through adjusting denser and longer branches to fill the interstitial voids between backbone nanowires, which will substantially improve the light harvesting and the current density.

6.3.2 Hierarchical ZnO Nanoparticles for DSCs

Hierarchically-packed ZnO nanoparticles were formed in the condensation reactions of the sol-gel process that be mentioned in Chapter 5. The spherical shape of the secondary ZnO nanoparticles, with the diameter in the range of 160-580 nm, is recognized with agglomeration of many primary single crystallites ranging from 6 to 12 nm, as shown in Fig. 6-14. The similar ZnO architectures have been elucidated as the random lasers in which the cavities were formed by multiple scattering between

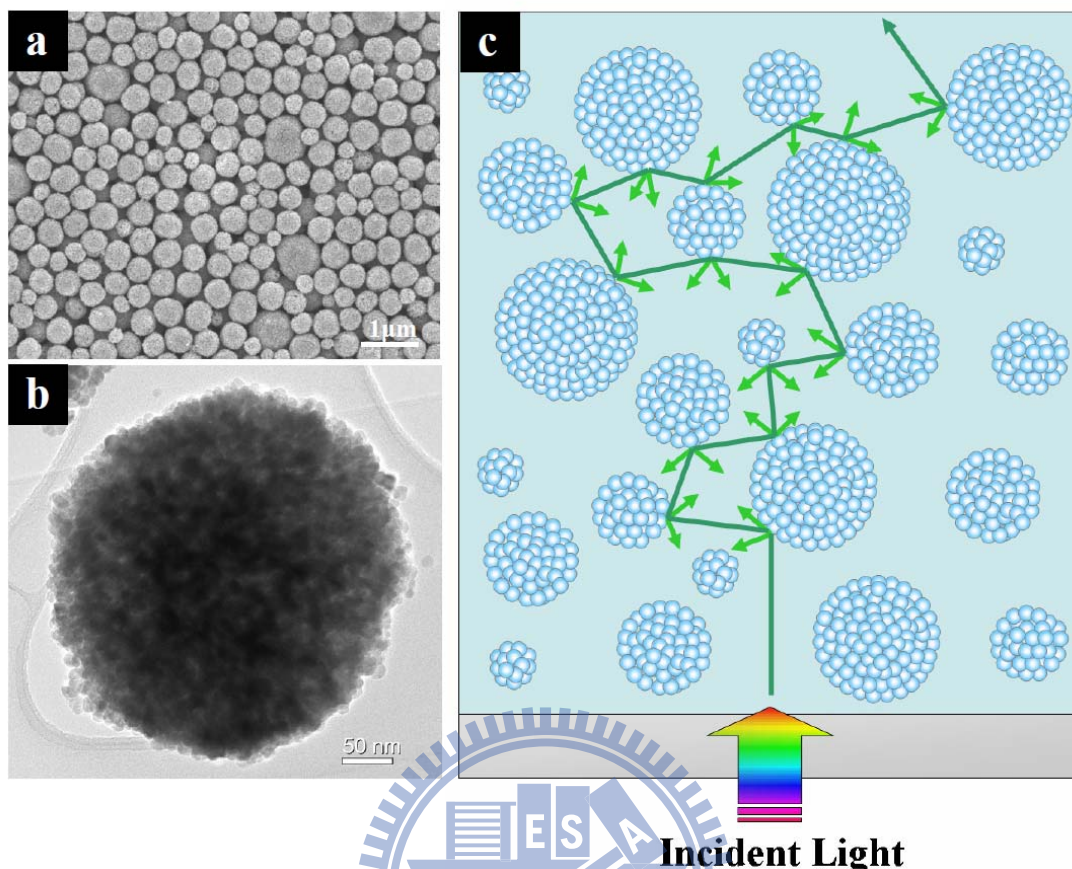


Figure 6-14. (a and b) The FESEM and TEM images for the self-assembled ZnO secondary nanoparticles, respectively. (c) The schematic multiple scattering of light within the hierarchical ZnO photoelectrode composed by self-assembled ZnO secondary nanoparticles.

ZnO primary particles [98]. The laser action emerges from efficient amplification along the closed loop light-scattering paths within a secondary ZnO nanoparticle. Recently, Cao et al. have demonstrated that the aggregation of ZnO nanocrystallites perform an effective scheme to generate light scattering within the photoelectrode film of DSCs without using any other scattering layers [67, 68]. In addition, dye-molecule adsorption could retain sufficiently due to enough internal surface area provided by the primary nanocrystallites. The maximum energy conversion efficiency of 5.4% has been achieved with utilization of ruthenium complex *cis*-[RuL₂(NCS)₂] (L=4,4'-dicarboxy-2,2'-bipyridine), N3 dye. Herein, the

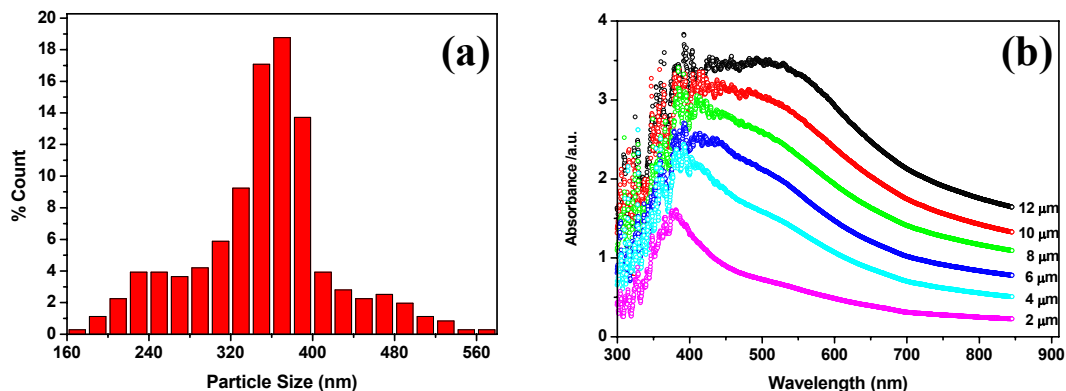


Figure 6-15. (a) Diameter distribution for the ZnO secondary nanoparticles. (b) The corresponding optical absorption spectra of ZnO photoelectrodes with various film thicknesses, from 2 μm to 12 μm .

broad size-distribution of secondary nanoparticles with mean radius of 360 nm, as shown in Fig. 6-15(a), is controlled to provide the wide range absorption of visible sun light within the preferable packing of the ZnO photoelectrode. The hierarchical ZnO photoelectrode provides the multiple scattering of light and therefore the light-traveling distance can be significantly prolonged. Figure 6-15(b) also shows the corresponding optical absorption spectra of ZnO photoelectrodes with various film thicknesses. The absorption peak at 375 nm, which could be particularly identified from 2 μm film, mainly resulted from the intrinsic exciton absorption of ZnO. However, the absorption at wavelengths around 400-650 nm is enhanced dramatically with increasing the thickness of the ZnO photoelectrodes from 2 μm to 12 μm . The ZnO films with thicknesses above 10 μm provide light localization through significant light scattering from the highly disordered structure. The results manifest the light-scattering capability of the films with different thicknesses and the formation of optical confinement through the aggregated ZnO films that could provide more photon absorption in the visible region by the dye molecules.

The molecular structures of the indoline-based organic dyes employed in this

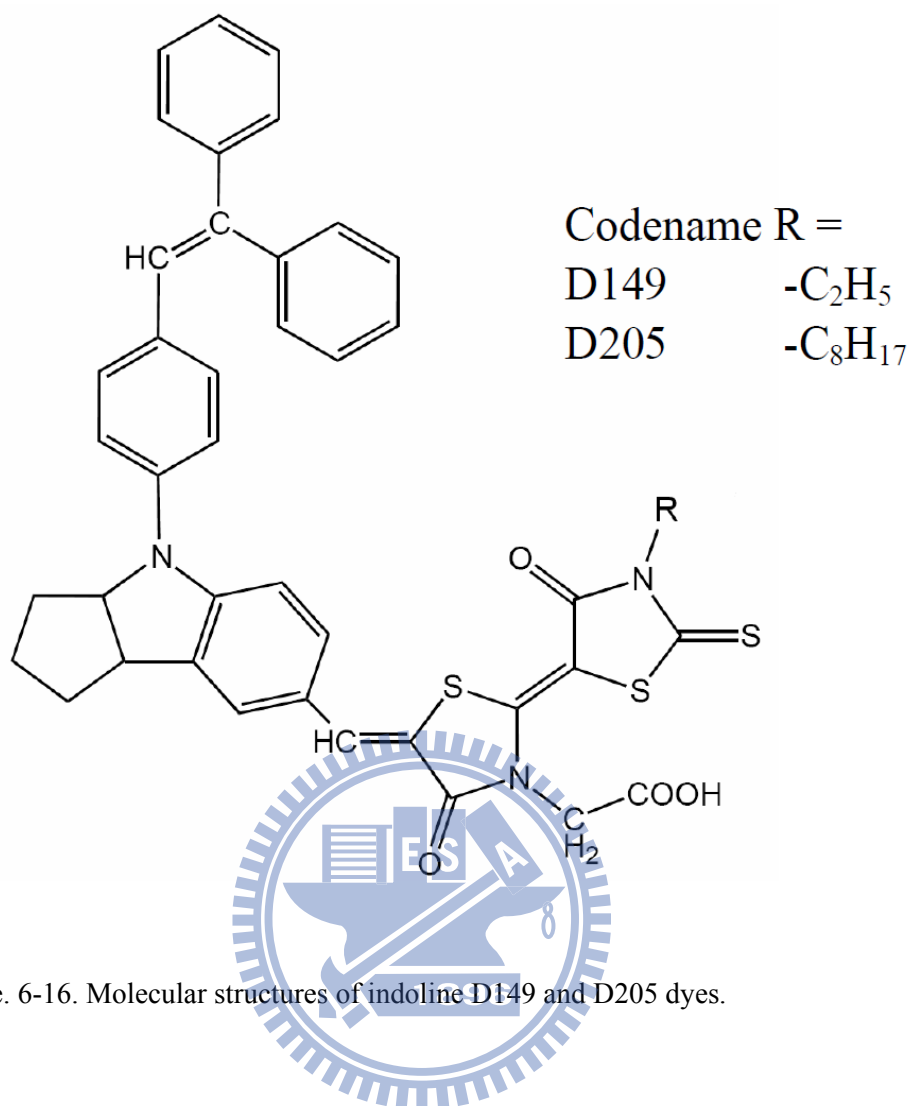


Figure. 6-16. Molecular structures of indoline D149 and D205 dyes.

section are depicted in Fig 6-16. The double rhodanic acid was used as an anchor moiety for both D149 and D205 sensitizers. The D205 is designed by introducing an octyl substitute onto the terminal rhodanine ring to replace the ethyl group of D149. The detail molecular structures of the indoline-based organic dyes employed in this study have been depicted in previous reports [70, 71]. Figure 6-17(a) shows the light absorption spectra and PL spectra of D149 and D205 in acetonitrile as the concentration of 0.015 mM, respectively. The solutions were filled within cuvette cells to avoid thickness and geometry effects. The absorption spectra of D149 and D205 in solution consist of two branches. The 388 nm peak is ascribed to a mixture of intramolecular charge-transfer (ICT) and the π - π^* excitation from the HOMO to the

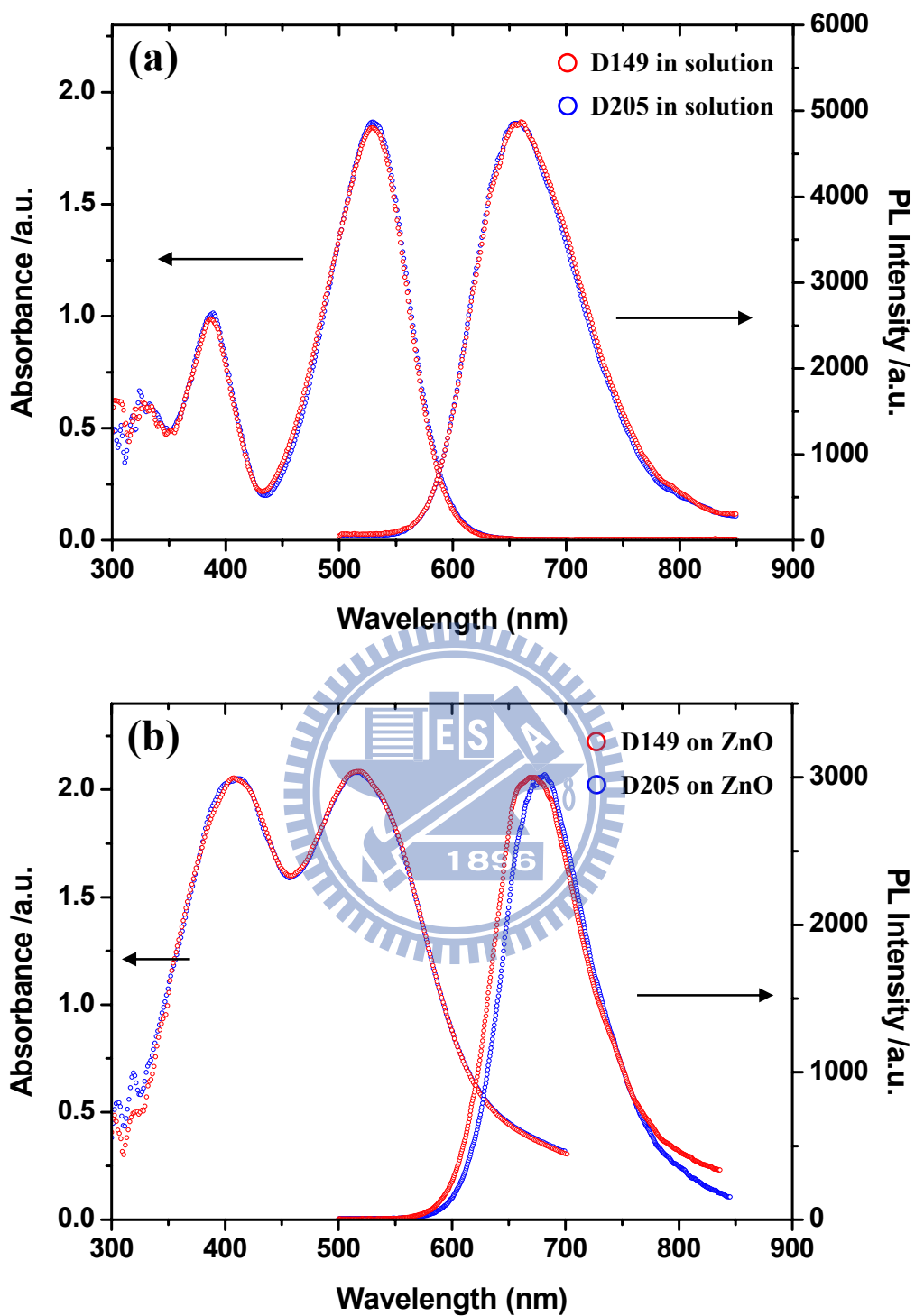


Figure 6-17. Absorption and photoluminescence spectra of : (a) D149 and D205 dyes in tert-butyl alcohol/acetonitrile (1/1) solution and (b) D149 and D205 dyes anchored on the 4 μ m-thick ZnO photoelectrodes.

LUMO+1, on the other hand, the main absorption peak, located at 530 nm, is ascribed to an ICT transition from the HOMO to the LUMO [99, 100]. Both the absorption spectra are almost identical, revealing that the D205 dye has almost the same molecular coefficient value of $68700 \text{ M}^{-1} \text{ cm}^{-1}$ as D149 [73]. The PL spectra of D149 and D205 in solution are also identical with broad peaks at around 660 nm which could attribute to radiative relaxation. The transition predominantly results from the absorption maximum since the wavelength of excitation at 400 nm. Figure 6-17(b) shows the light absorption and PL spectra of D149 and D205 on $4\mu\text{m}$ -thick ZnO photoelectrodes, respectively. The dye-sensitized ZnO films were prepared as the standard procedure as mentioned in experimental section but covered with pure acetonitrile without the additive redox couple. The absorption spectra of D149 and D205 on ZnO photoelectrodes have broadened peaks and blue-shifted main absorption peaks centered around 516 nm that indicates these indoline dyes have a moderate interaction between dye molecules on the ZnO surface. The red-shift absorption peaks at low wavelength for indoline dyes on ZnO could be related to the influence of thickness effect on the photoelectrode. The blue shift of the main absorption peak from 530 nm (indoline dyes in the solution) to 516 nm (indoline dyes on ZnO films) could be addressed as a hypsochromic shift due to plane-to-plane arrangement (H-aggregation). The observation is similar to the previous reports concerning about the indoline dye on TiO_2 [98]. The origin is mainly attributed to the formation of a bidentate complex between the carboxylate and the polar ZnO surface [102]. While the yield of the fluorescence decreases substantially for D149 and D205 on ZnO with respect to D149 and D205 in solution, suggesting the occurrence of PL quenching. Furthermore, the PL spectra consistently move toward a lower energy with respect to those of indoline dye in solution. The observed redshift in PL spectra

indicates the interface between adsorbed dye molecules and ZnO is strongly bonded that provides effective electron transfer between dye molecules and ZnO. Meanwhile, the polar ZnO surface enhances the delocalization of the π -electrons and lowers the band gap energy of indoline dye. With the 20 nm (from 660 nm to 680 nm) redshift for D205 and 10 nm (from 660 nm to 670 nm) for D149, we presumably ascribe a remarkable bonding force while D205 anchor onto ZnO surface. However, further investigations on the interactions of dye aggregation are needed for better understanding the dynamics of DSCs.

To investigate the interfacial electron-transfer between indoline dye and ZnO, the TCSPC studies were employed to provide further information of the electron injection dynamics. Time-dependent fluorescence was collected at the confirmed emission maximum for each specimen from Fig. 6-17. Figure 6-18(a) shows the emission decay recorded with indoline dyes. A biexponential decay kinetics was found to be satisfactory in determination of emission lifetimes. Normally, the PL decay has a fast decay to begin with followed by a slow decay. The fast decay normally results from nonradiative energy transfer or charge transfer with shorter decay time τ_{NR} , while the slow decay attributes to radiative recombination with longer decay time τ_R . The lifetimes and corresponding amplitudes are listed in Table 6-2. The radiative decay times for pure D149 and D205 in solution are 0.86 and 0.96 ns, respectively. It is apparent that increasing the alkyl chain length results in slower fluorescence decay, indicative of the slower radiative recombination. The reduction in the radiative decay times to 0.73 and 0.7 ns for D149 and D205 on ZnO suggests PL quenching as mentioned previously from the decreasing fluorescence yields that appears more dramatically for D205 dye.

Besides, it should be noted that the dynamics of excited state decay is strongly

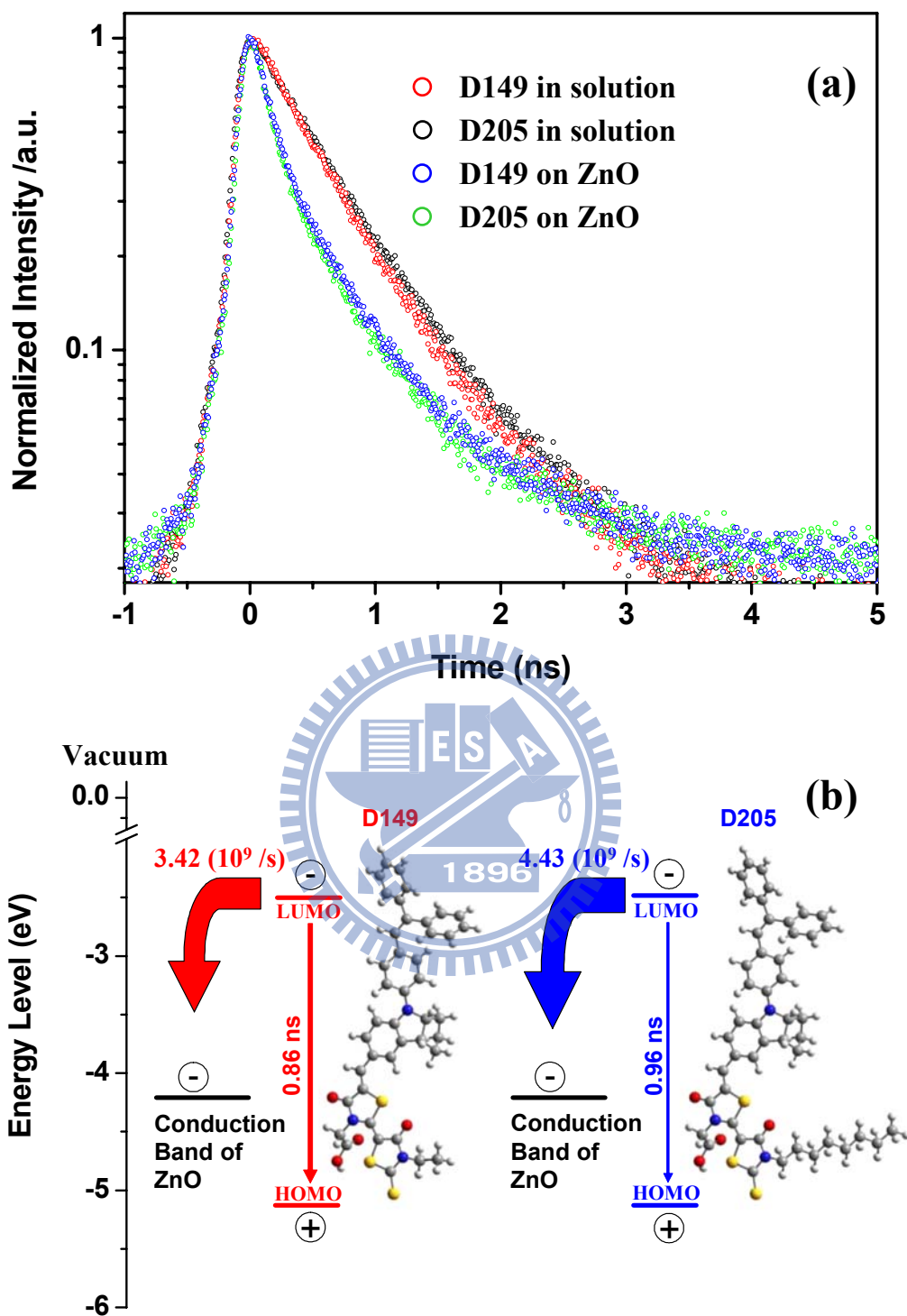


Figure 6-18. (a) Photoluminescence decay of D149 and D205 dyes in tert-butyl alcohol/acetonitrile (1/1) solution and on ZnO photoelectrodes, respectively. (b) Schematic representation of the charge transfer of photo-excited indoline dyes anchored onto ZnO surfaces. The energy levels of D149 and D205 are sourced from [100]. The vacuum level is defined at 0 eV.

TABLE 6-2. Kinetic Parameters of the Indoline Dye Emission Decay Analysis^a

Indoline dye		a_{NR}	τ_{NR} (ns)	a_R	τ_R (ns)	K_{et} ($10^9/s$)
D149	In solution	2641	0.47	1218	0.86	--
D205	In solution	2823	0.55	953	0.96	--
D149	On ZnO	2298	0.18	1524	0.73	3.42
D205	On ZnO	1845	0.16	1192	0.70	4.43

^a Time coefficients, including lifetime and corresponding amplitude, can be obtained from fitting the biphasic decay. The charge-transfer rate constant was estimated from the formula (6-25).

enhanced for the indoline dyes anchor onto ZnO surfaces; indicative of a faster interfacial electron transfer behaves as a new relaxation process. The nonradiative decay takes 0.47 and 0.55 ns for D149 and D205 in solution, respectively. However, the nonradiative decay times have dramatically decreased to 0.18 and 0.16 ns for D149 and D205 anchored on ZnO. As a dilute system (indoline dyes in acetonitrile solution) with the concentration of 0.015 mM, the probabilities of intermolecular charge-transfer and intermolecular energy-transfer are presumably negligible. The nonradiative decay of dyes in solution with $\tau_{NR(Dye)}$ is mainly attributed to intramolecular energy transfer, the observed decrease in nonradiative time $\tau_{NR(Dye+ZnO)}$ for dyes on ZnO is contributed by the additional pathway of charge transfer between the excited-state dye and ZnO surface. Therefore, the charge-transfer rate can be evaluated from the nonradiative part by the expression:

$$K_{et} = \frac{1}{\tau_{NR(Dye+ZnO)}} - \frac{1}{\tau_{NR(Dye)}} \quad (6.25)$$

Here we assume that $\tau_{NR(Dye+ZnO)}$ counts for both energy transfer and charge transfer

but $\tau_{NR(Dye)}$ for energy transfer only. The electron-transfer rates of 3.42×10^9 and $4.43 \times 10^9 \text{ s}^{-1}$ for D149 and D205 on ZnO surfaces are obtained, respectively. We thus conclude that the D205 exhibits efficient electron injection dynamics for ZnO nanoparticles with respect to D149 as a result of faster interfacial electron transfer and retardant fluorescence decay. The simplified diagram describing the mechanism of charge transfer between the indoline dyes and ZnO interfaces is also presented schematically as Fig. 6-18(b).

In order to improve the DSC performance, optimization of the thickness of the ZnO photoelectrode is necessary because the photovoltaic characteristics exhibit significant variation depending on the thickness. Figure 6-19 displays the incident monochromatic photon to current conversion efficiency (IPCE) spectra of DSCs constructed using two indoline dyes with different ZnO photoelectrode thicknesses. Because of the UV cut-off effect caused by the thick glass substrate the spectra at wavelengths shorter than 400 nm are deteriorated. The photocurrent peak at approximately 367 nm is due to direct light harvesting by ZnO semiconductor which remain almost unchanged while increasing the photoelectrode thickness from 18 μm to 32 μm because of short penetration depth for UV light. However, with increase in thickness of ZnO photoelectrode, the maximal IPCE increase from 71% to 74% and 77% to 79% at 550 nm for D149- and D205-sensitized ZnO DSCs, respectively. Moreover, the values of IPCE increase significantly in the longer wavelength region (580-700 nm) with thicker photoelectrode films but saturated at the thickness above 30 μm because of the limitation of electron diffusion length. The numerous cracks in thick photoelectrode films ($>32 \mu\text{m}$) were also observed due to unpracticed-printing technique. The optimal IPCE obtained for the D205-sensitized ZnO DSCs are higher than the D149-sensitized DSCs in the visible-wavelength (400-700 nm) region.

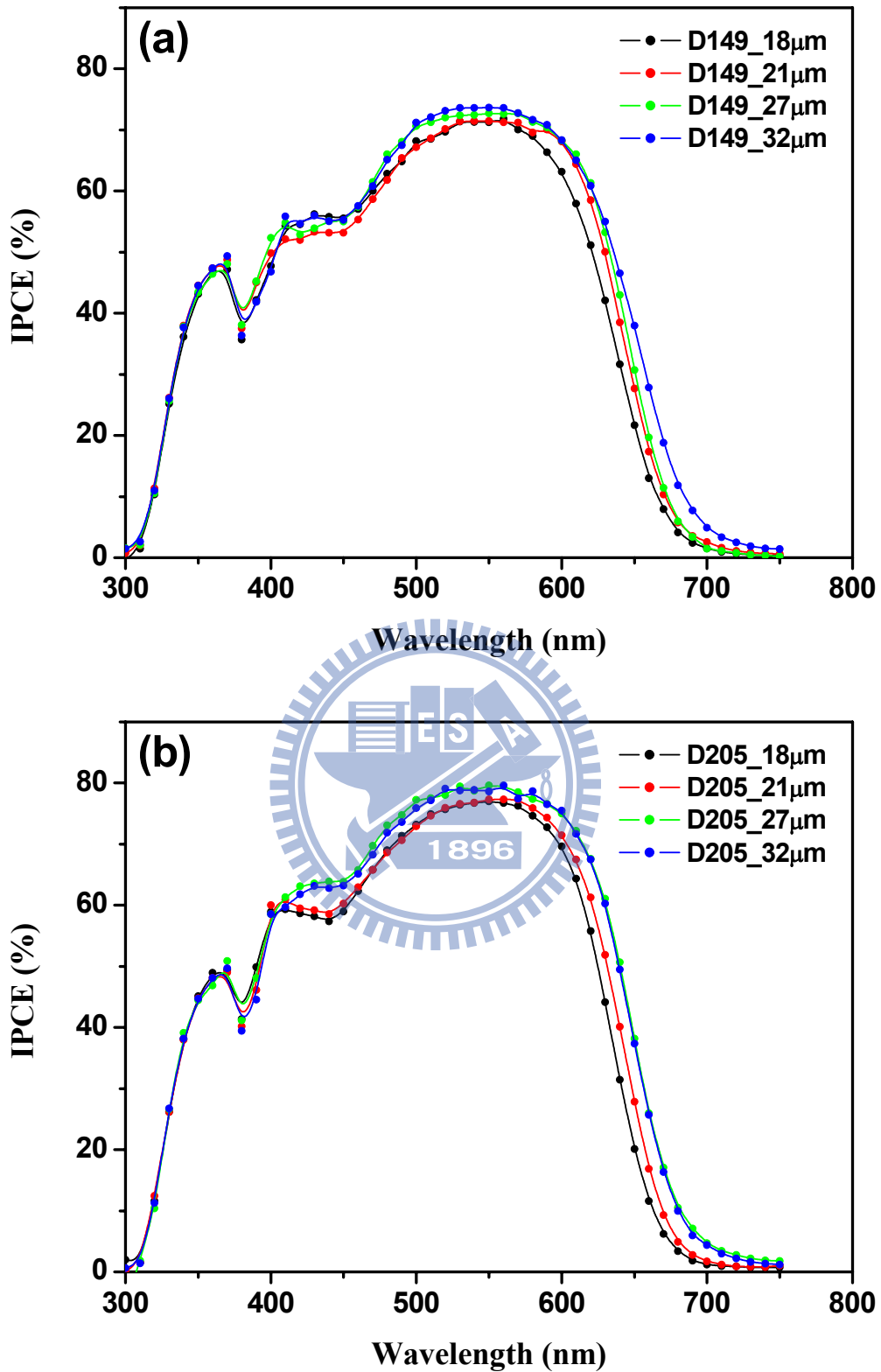


Figure 6-19. Photocurrent action spectra of ZnO DSCs constructed using (a) D149 and (b) D205, with different photoelectrode thicknesses.

Figure 6-20 also shows the variations in the photovoltaic characteristics of DSCs depending on the thickness of the indoline dye-sensitized hierarchical ZnO photoelectrode. The open-circuit photovoltage (V_{oc}) decreased linearly with the increase in ZnO film thickness (Fig. 3a). Increasing the thickness leads to increasing the non-excited area meanwhile lowers V_{oc} further after averaging the electron density in the non-excited area. On the contrary, the short-circuit photocurrent density (J_{sc}) for DSCs using both indoline dyes increases monotonically with increasing in ZnO film thickness (Fig. 6-20 (b)), as a result of enlarged dye loading. In addition, V_{oc} and J_{sc} for D205-sensitized ZnO DSCs are higher than D149-sensitized ones. This observation can be ascribed to the effective suppression of electron recombination between I_3^- and electrons injected in the photoelectrodes by extending the alkyl chain on the terminal rhodanine moiety from ethyl to octyl [103]. The further examination will be described via the electron transport analysis afterward. The fill factor (FF) for D205-sensitized ZnO DSCs is slightly lower than that of D149-sensitized ZnO DSCs that is rationalized in terms of the series resistance of the DSC, the higher J_{sc} values end up the lower FF values. Although V_{oc} decreases with the ZnO film thickness, this loss of V_{oc} is compensated by a gain in J_{sc} ; and consequently the maximal energy conversion efficiencies (η) of 4.95% and 5.34% were achieved for D149- and D205-sensitized ZnO DSCs, respectively, with 27 μ m-thick ZnO photoelectrode film under AM 1.5 solar radiation. It is important to recognize that the influence of thickness on the photocurrent of DSCs utilized secondary ZnO nanoparticles is relatively small in comparison with utilizing tetrapod-like ZnO nanoparticles in our previous report [62]. The possible explanation for this could be ascribed to the sufficient light-harvesting capability of these hierarchical ZnO architectures even with quite thin photoelectrodes.

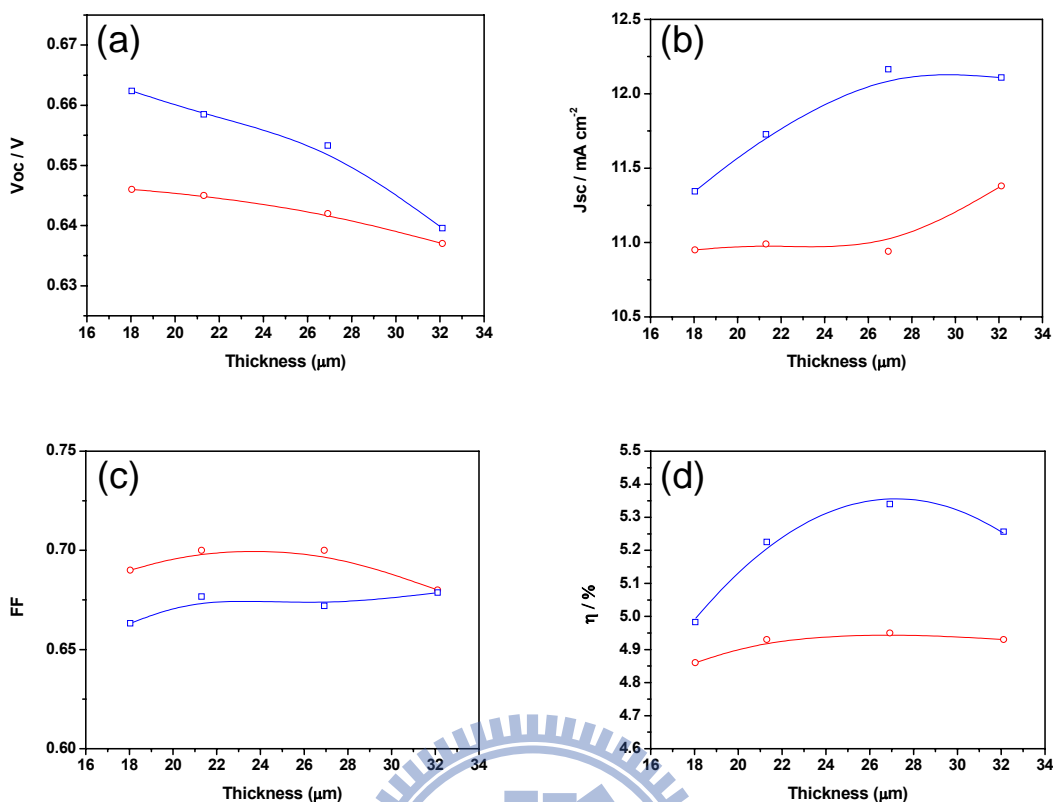


Figure 6-20. Relationship between photovoltaic characteristics and photoelectrode thickness of ZnO DSCs. Red circles and blue squares represent D149- and D205-sensitized DSCs, respectively. (a) Open-circuit photovoltage, V_{oc} ; (b) Short-circuit photocurrent density, J_{sc} ; (c) Fill factor, FF ; and (d) Photopower energy conversion efficiency, η . The solid lines are plotted to guide the eyes.

Figure 6-21(a) shows the detail comparison of photocurrent–voltage (J-V) characteristics for solar cells constructed using 27 μm -thick ZnO photoelectrode films and these two indoline dyes under AM 1.5 full sunlight illumination (100mW cm^{-2}) and in the dark. For D205 uptake, the J-V plot reveals $V_{oc} = 0.653\text{ V}$, $J_{sc} = 12.17\text{ mA cm}^{-2}$, $FF = 0.67$, and $\eta = 5.34\%$. For comparison, the J-V plot of D149 uptake reveals $V_{oc} = 0.641\text{ V}$, $J_{sc} = 10.94\text{ mA cm}^{-2}$, $FF = 0.71$, and $\eta = 4.95\%$. The resultant improvement in J_{sc} responds to the corresponding higher IPCE for the D205-sensitized ZnO DSCs as compared with the D149-sensitized ZnO ones. The

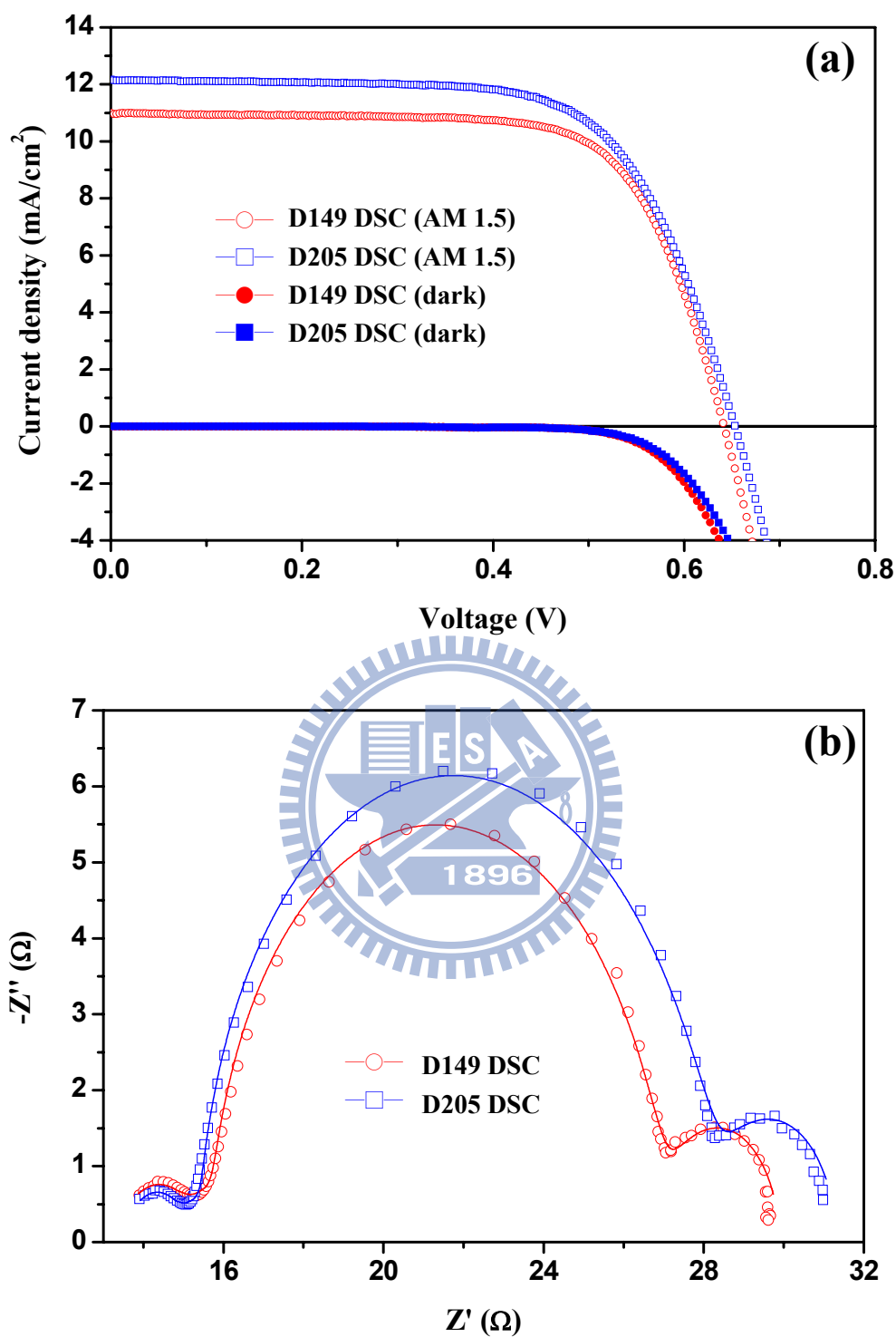


Figure 6-21. Photovoltaic characteristics of DSCs with 27 μm -thick ZnO photoelectrodes and two different indoline dyes: (a) J-V curves for D149- and D205-sensitized DSCs with AM 1.5 illumination and in the dark, respectively. (b) Nyquist plots of D149- and D205-sensitized DSCs performed under illumination at the applied bias of V_{oc} . The solid lines are the fitting results.

curves of dark current also indicate that D205-sensitized ZnO DSCs have a slightly more negative onset potential for the reduction of I_3^- than D149-sensitized ZnO DSCs. The lower dark current could also be rationalized in terms of a negative shift in the conduction band edge of ZnO caused by the adsorption of D205 dye. Both V_{oc} and J_{sc} for D205-sensitized ZnO DSCs are higher than D149-sensitized ones. The superior performance for D205 dye uptake can be ascribed to the effective suppression of electron recombination between I_3^- and efficient electrons injection into the photoelectrodes by extending the alkyl chain on the terminal rhodanine moiety from ethyl to octyl [103]. Principally, the dyes with the hydrophobic alkyl chains would not only form a blocking layer over the sensitizer dye layer to protect the dye layer against water ingress from the electrolyte but rearrange the dye orientating more perpendicular to the ZnO surface. The effects of different dyes on the electron transport of the interfaces in the DSCs can be further investigated with aid of the electrochemical impedance spectroscopy (EIS). Adequate physical models and equivalent circuits have been proposed and widely applied to analyze the electron transport in photoelectrode and recombination between the photoelectrode and electrolyte interface in DSCs [86-94]. The Nyquist plots of the impedance data for D149-, and D205-sensitized ZnO DSCs were performed by applying a 10 mV ac signal over the frequency range of 10^{-2} – 10^5 Hz under illumination at the applied bias of V_{oc} . The Nyquist plots in Fig. 6-21(b) show the radius of the middle semicircle, which belongs to D205-sensitized ZnO DSCs, is larger than that of D149-sensitized ZnO DSCs, indicating that the electron recombination resistance is enlarged from D149 to D205. Some interior parameters of the devices can be further derived by well fitting the impedance data of the Nyquist plots to the expressions based on the equivalent circuit of DSCs as shown in Fig. 6-22, similar as Fig. 6-11. $r_w = (R_w/L_F)$ is

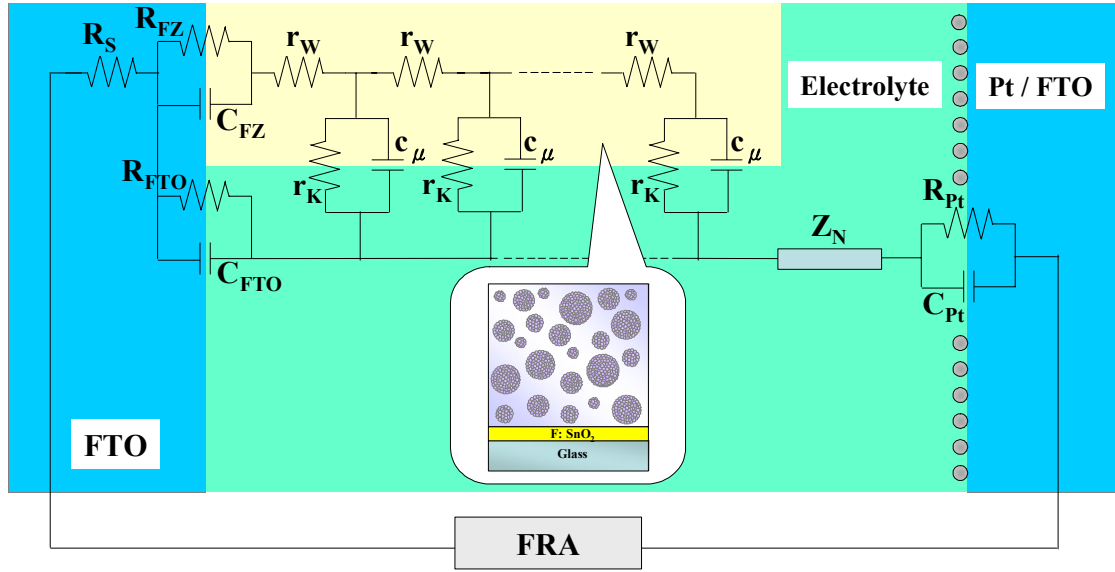


Figure 6-22. The equivalent circuit model of ZnO DSCs composed with hierarchical nanoparticles.

the transport resistance of the electrons in the ZnO electrode; $r_k = (R_k L_F)$ is the charge-transfer resistance of the charge recombination between electrons in the ZnO electrode and I_3^- in the electrolyte. The thickness L_F of all anodes are about $27\mu\text{m}$; $C_\mu = (c_\mu L_F)$ is the chemical capacitance of the ZnO electrode; R_s is a series resistance for the transport resistance of FTO and all resistances out of the cell; Z_N is the impedance of diffusion of I_3^- in the electrolyte; R_{Pt} and C_{Pt} are the charge-transfer resistance and the interfacial capacitance at the counter electrode (platinized FTO glass) /electrolyte interface, respectively; R_{FTO} and C_{FTO} are the charge-transfer resistance and the interfacial capacitance at the exposed FTO/electrolyte interface, respectively; R_{FZ} and C_{FZ} are the resistance and the capacitance at the FTO/ZnO contact, respectively. The fitted results are also listed in Table 6-3 which include the first-order reaction rate for the loss of electrons (k_{eff}), the electron lifetime ($\tau = 1/k_{eff}$), the electron transport resistance (R_w), and the charge transfer resistance related to recombination of electron at the ZnO/electrolyte interface (R_k). The electron-loss rate k_{eff} in the D205-sensitized

TABLE 6-3. Performances and electron transport properties of the D149- and D205-sensitized DSCs (27 μ m-thick ZnO photoelectrode) determined by J-V characteristics and EIS analysis.

ZnO DSCs	J_{sc} (mA/cm ²)	V_{oc} (V)	FF	η (%)	k_{eff} (s ⁻¹)	τ_{eff} (ms)	R_k (Ω)	R_w (Ω)	D_{eff} (cm ² /s)
D149	10.94	0.641	0.71	4.95	57.85	17.29	12.55	2.47	2.14×10^{-3}
D205	12.17	0.653	0.67	5.34	47.12	21.22	14.43	1.98	2.51×10^{-3}

ZnO DSCs is smaller than the D149-sensitized ones, which causes the prolonged electron lifetime in the D205-sensitized ZnO DSCs. The increase in electron lifetime supports more effective suppression of the back reaction of the injected electrons with the I₃⁻ in the electrolyte. This evidence can also be confirmed with the larger R_k value for D205-sensitized ZnO DSCs that indicates the less interfacial recombination occurring between the ZnO and electrolyte interface. Moreover, the effective electron diffusion coefficient ($D_{eff} = (R_k/R_w)L_F^2 k_{eff}$) is also enhanced with utilization of D205 sensitizer. In general, the current density for DSCs is determined by the initial number of photogenerated carriers, the electron injection efficiency from dye molecules to semiconductor, and the recombination rate between the injected electrons and oxidized dye or redox species in the electrolyte. Based on the assumption of the same injection efficiency and dye loading for the given ZnO DSCs systems, it is reasonable that the photocurrent density may be straightly affected by the variation in the electron recombination rate. The amphiphilic nature of D205 may assist the formation of a self-assembled dye monolayer that prevents the recapture of the photoinjected electrons by the triiodide ions within electrolyte, consequently resulting in a higher V_{oc} and J_{sc} [72].

The compared ZnO DSCs composed of only primary nanocrystallites without any aggregation were also demonstrated as the contrast. Figure 6-23 shows the cell behaviors of D205-sensitized DSCs composed with 23 μm -thick primary nanoparticles (via girding the secondary ZnO nanoparticles) with 4 μm -thick commercial ZnO particles (Merck Ltd.) as a scattering layer on the top. For the grinded particles, the J-V curve reveals $V_{oc} = 618$ mV, $J_{sc} = 10.22$ mA cm^{-2} , $FF = 0.66$, and $\eta = 4.16$ %, for which the performance is poorer than the hierarchical ZnO photoelectrode. The IPCE spectrum also shows remarkable deterioration in the visible-wavelength (400-700 nm) region for the D205-sensitized DSC composed with grinded nanoparticles because insufficient light-traveling distance. The insufficient light-harvesting for non-aggregated ZnO photoelectrode also leads to increasing the non-excited area, which lowers V_{oc} further after averaging the electron density. From Cao's report [67, 68] the optical-absorption spectra of the ZnO films consisting of aggregates will be affected by different sizes and size distributions. Normally, the scattering efficiency will shift to long wavelength while the secondary particle size is increasing. However, Cao et al. specially indicate that polydisperse aggregates with a large average size or broad size distribution could result in an obvious enhancement in the optical absorption and light-harvesting efficiency of photoelectrode films due to Mie scattering. Moreover, the photoelectrode composed with broad size distributed secondary ZnO particle will superior for obtaining compact films from screen-printing process.

Comparative experiments reported on metal-free indoline dyes emphasize the importance of improving the photovoltaic performance by suitable molecular engineering. The unambiguously enhancement of photopower-conversion efficiency was examined by extending the length of alkyl chain on the indoline sensitizer with

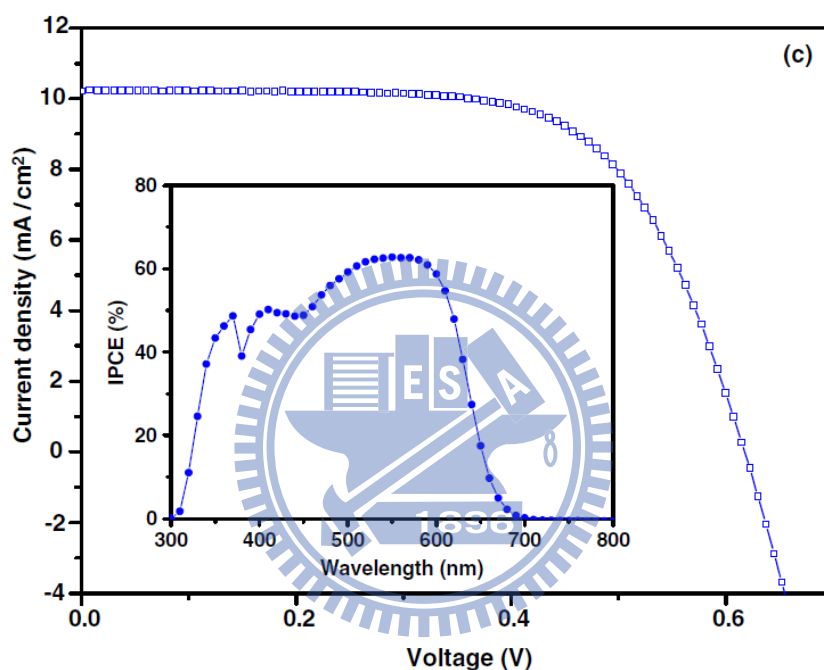
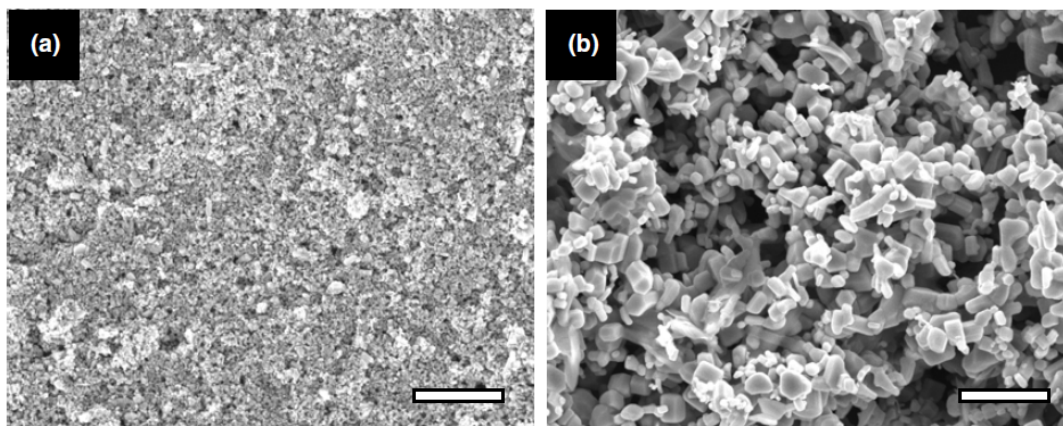


Figure 6-23. (a) FESEM image of non-aggregated primary ZnO nanocrystallites (size 8~10 nm) from grinding the original ZnO secondary nanoparticles; scale bar, 1 μm . (b) Commercial ZnO particles (Merck Ltd.; broad size distribution, 100~600 nm) as a scattering layer on the top; scale bar, 1 μm . (c) J-V curve and IPCE spectrum (Inset) of D205-sensitized DSCs composed with 23 μm -thick grinded nanoparticles and 4 μm -thick commercial ZnO particles as a scattering layer on the top.

the hierarchical photoelectrode composed by aggregated ZnO secondary nanoparticles. Although the efficiency of ZnO DSCs cannot compete with TiO_2 systems, presently, we hope these investigations could shed light on the development of organic

sensitizers and can be used in the ZnO nanostructure optimization for the proposed solar cell applications.

6.4 Summary

For 1-D ZnO nanostructures, the branched ZnO nanowires have been fabricated on FTO substrates using a solvothermal method for DSCs. The short-circuit current density and the overall light conversion efficiency of the branched ZnO nanowire DSCs were almost twice higher than the bare ZnO nanowire ones. The improvement can be explained association with the enlargement of internal surface area within the photoelectrode without increasing interparticle hops. In addition, the sufficient dye-loading in branched ZnO nanowire DSCs was further evidenced from the lower series resistance $R_s=(dV/dI)_{I=0}$ and dye-desorption measurement. The branched ZnO nanowires significantly enhanced IPCE spectra as compared with the bare ZnO nanowires. Therefore, the concept of these one-dimensional branched nanostructures could simultaneously afford a direct conduction pathway and achieve higher dye adsorption to significantly enhance the overall energy conversion efficiency of the DSCs.

Furthermore, self-assembled ZnO secondary 0-D nanoparticles have been demonstrated as an effective photoelectrode within DSCs which retain the desired specific surface area for dye-molecule adsorption and the sufficient light-harvesting from prolonged light traveling. D149 and D205 indoline dyes were used as the effective sensitizers for DSCs composed of hierarchical ZnO photoelectrodes. The higher charge-transfer rate and retardant fluorescence decay reveal that D205 has better electron injection dynamics for ZnO nanoparticles as compared to D149. The optimal energy conversion efficiencies of 4.95% and 5.34% were achieved for D149

and D205 on 27 μm -thick ZnO photoelectrode films under AM 1.5 solar radiation. The significantly enhanced performance for D205-sensitized ZnO DSCs is ascribed to the effective suppression of electron recombination as well as enhancing interfacial electron transfer rate by extending the alkyl chain on the terminal rhodanine moiety from ethyl to octyl. The results of the comparison of the electron transport property were further confirmed, presenting a prolonged electron lifetime in the D205-sensitized ZnO DSCs. Thus, the hybrid system of hierarchical ZnO architecture and metal-free indolne sensitizer may represent an alternative candidate with regard to high-performance DSCs.



References and Notes

- [1] Zhipan Zhang, “Enhancing the Open-Circuit Voltage of Dye-Sensitized Solar Cells: Coadsorbents and Alternative Redox Couples”, Ph.D. thesis, [École Polytechnique Fédérale de Lausanne](#), 2008.
- [2] Becquerel, A. E. *C. R. Acad. Sci. Paris* **1839**, *9*, 561.
- [3] West, W. *Photogr. Sci. Eng.* **1974**, *18*, 35.
- [4] J. Moser, *Monatsch. Chem.* **1887**, *8*, 373.
- [5] Namba, S.; Hishiki, Y. *J. Phys. Chem.* **1965**, *69*, 774.
- [6] Nelson, R. C. *J. Phys. Chem.* **1965**, *69*, 714.
- [7] Bourdon J., *J. Phys. Chem.* **1965**, *69*, 705.
- [8] Gerischer, H.; Tributsch, H. *Ber. Bunsenges. Phys. Chem.* **1968**, *72*, 437.
- [9] Gerischer, H.; Tributsch, H. *Ber. Bunsenges. Phys. Chem.* **1969**, *73*, 251.
- [10] Gerischer, H. *Electroanal. Chem. Interfac. Electrochem.* **1975**, *58*, 263.
- [11] Tsubomura, H.; Matsumura, M.; Noyamaura, Y.; Amamiya, T. *Nature* **1976**, *261*, 402.
- [12] Clark, W. D. K.; Sutin, N. *J. Am. Chem. Soc.* **1977**, *99*, 4676.
- [13] Anderson, S.; Constable, E. C.; Dare-Edwards, M. P.; Goodenough, J. B.; Hamnett, A.; Seddon, K. R.; Wright, R. D. *Nature*, **1979**, *280*, 571.
- [14] Gerischer, H. *Photochem. Photobiol.* **1972**, *16*, 243.
- [15] Memming, R. *Photochem. Photobiol.* **1972**, *16*, 325.
- [16] Fujishima, A.; Watanabe, T.; Tatsuoki, O.; Honda, K. *Chem. Lett.* **1975**, *4*, 13.
- [17] Jayadevaiah, T. S. *Appl. Phys. Lett.*, **1974**, *25*, 399.
- [18] Hamnett, A.; Dare-Edwards, M. P.; Wright, R. D.; Seddon, K. R.; Goodenough, J. B. *J. Phys. Chem.*, **1979**, *83*, 3280.
- [19] Dare-Edwards, M. P.; Goodenough, J. B.; Hamnett, A.; Seddon, K. R.; Wright, R.

- D. Faraday Discuss. Chem. Soc.*, **1980**, 70, 285.
- [20] Fujishima, A.; Honda, K. *Bull. Chem. Soc. Jap.*, **1971**, 44, 1148.
- [21] Fujishima, A.; Honda, K. *Nature*, **1972**, 238, 37.
- [22] Duonghong, D.; Serpone, N.; Grätzel, M. *Helv. Chim. Acta*, **1984**, 67, 1012.
- [23] DeSilvestro, J.; Grätzel, M.; Kavan, L.; Moser, J.; Augustynski, J. *J. Am. Chem. Soc.*, **1985**, 107, 2988.
- [24] Vlachopoulos, N.; Liska, P.; Augustynski, J.; Grätzel, M. *J. Am. Chem. Soc.*, **1988**, 110, 1216.
- [25] O'Regan B.; Grätzel, M. *Nature*, **1991**, 353, 737.
- [26] Nazeeruddin, M. K.; Kay, A.; Rodicio, I.; Humphry-Baker, R.; Müller, E.; Liska, P.; Vlachopoulos N.; Grätzel, M. *J. Am. Chem. Soc.* **1993**, 115, 6382.
- [27] Nazeeruddin, M. K.; Pechy, P.; Grätzel, M. *Chem. Commun.*, **1997**, 1075.
- [28] Bach, U.; Lupo, D.; Comte, P.; Moser, J. E.; Weissortel, F.; Salbeck, J.; Spreitzer, H.; Grätzel, M. *Nature*, **1998**, 395, 583.
- [29] Grätzel, M. *MRS Bull.* **2005**, 30, 23.
- [30] Wang, P.; Zakeeruddin, S. M.; Moser, J. E.; Nazeeruddin, M. K.; Sekiguchi, T.; Grätzel, M. *Nat. Mater.*, **2003**, 2, 402.
- [31] Wang, P.; Klein, C.; Humphry-Baker, R.; Zakeeruddin, S. M.; Grätzel, M. *J. Am. Chem. Soc.* **2005**, 127, 808.
- [32] Kuang, D. B.; Wang, P.; Ito, S.; Zakeeruddin, S. M.; Grätzel, M. *J. Am. Chem. Soc.* **2006**, 128, 7732.
- [33] Kuang, D.; Klein, C.; Ito, S.; Moser, J. E.; Humphry-Baker, R.; Evans, N.; Durrant, J. R.; Grätzel, M.; Zakeeruddin, S. M.; Grätzel, M. *Adv. Mater.*, **2007**, 19, 1133.
- [34] Gregg, B. A.; Hanna, M. C. *J. Appl. Phys.*, **2003**, 93, 3605.

- [35] Gregg, B. A. *J. Phys. Chem. B*, **2003**, *107*, 4688.
- [36] Peter L. M. *J. Phys. Chem. C*, **2007**, *111*, 6601.
- [37] Grätzel, M. *Chem. Lett.* **2005**, *34*, 8
- [38] Bach, U.; Tachibana, Y.; Moser, J.-E.; Haque, S. A.; Durrant, J. R.; Grätzel, M.; Klug, D. R. *J. Am. Chem. Soc.* **1999**, *121* (32), 7445.
- [39] Barbé, C. J.; Arendse, F.; Comte, P.; Jirousek, M.; Lenzmann, F.; Shklover, V.; Grätzel, M. *J. Am. Ceram. Soc.* **1997**, *80*, 3157.
- [40] Nazeeruddin, M. K.; Angelis, F. D.; Fantacci, S.; Selloni, A.; Viscardi, G.; Liska, P.; Ito, S.; Takeru, B.; Grätzel, M. *J. Am. Chem. Soc.* **2005**, *127*, 16835.
- [41] Grätzel, M. *Inorg. Chem.* **2005**, *44*, 6841.
- [42] Grätzel, M. *J. Photochem. Photobiol., A*, **2004**, *164*, 3.
- [43] Nissfolk, J.; Fredin, K.; Hagfeldt, A.; Boschloo, G. *J. Phys. Chem. B*, **2006**, *110*, 17715.
- [44] Law, M.; Greene, L. E.; Johnson, J. C.; Saykally, R.; Yang, P. *Nat. Mater.* **2005**, *4*, 455.
- [45] Quintana, M.; Edvinsson, T.; Hagfeldt, A.; Boschloo, G. *J. Phys. Chem. C*, **2007**, *111*, 1035.
- [46] Kaidashev, E. M.; Lorenz, M.; von Wenckstern, H.; Rahm, A.; Semmelhack, H. C.; Han, K. H.; Benndorf, G.; Bundesmann, C.; Hochmuth, H.; Grundmann, M. *Appl. Phys. Lett.* **2003**, *82*, 3901.
- [47] Saito, M.; Fujihara, S. *Energy Environ. Sci.*, **2008**, *1*, 280.
- [48] Zhang, Q.; Dandeneau, C. S.; Zhou, X.; Cao, G. *Adv. Mater.* **2009**, *21*, 1.
- [49] Gonzalez-Valls, I.; Lira-Cantu, M. *Energy Environ. Sci.* **2009**, *2*, 19.
- [50] Xu, F.; Sun, L. *Energy Environ. Sci.* **2011**, *4*, 818.
- [51] Oskam, G.; Hu, Z. S.; Penn, R. L.; Pesika, N.; Searson, P. C. *Phys. Rev. E* **2002**,

66, 011403.

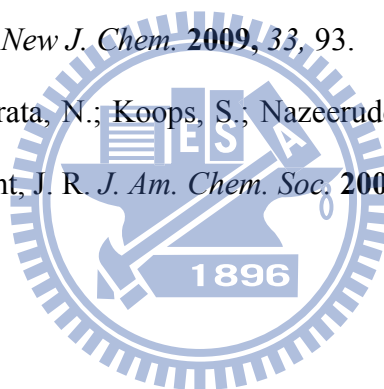
- [52] Özgür, Ü.; Alivov, Y. I.; Liu, C.; Teke, A.; Reshchikov, M. A.; Doğan, S.; Avrutin, V.; Cho, S. J.; Morkoç, H. *J. Appl. Phys.* **2005**, *98*, 041301.
- [53] Pearton, S. J.; Norton, D. P.; Ip, K.; Heo, Y. W.; Steiner, T. *Prog. Mater. Sci.* **2005**, *50*, 293.
- [54] Baxter, J. B.; Aydil, E. S. *Appl. Phys. Lett.* **2005**, *86*, 053114.
- [55] Pasquier, A. D.; Chen, H.; Lu, Y. *Appl. Phys. Lett.* **2006**, *89*, 253513.
- [56] Yang, Z.; Xu, T.; ITO, Y.; Welp, U.; Kwok, W. K. *J. Phys. Chem. C* **2009**, *113*, 20521.
- [57] Gonzalez-Valls, I.; Lira-Cantu, M. *Energy Environ. Sci.* **2010**, *3*, 789.
- [58] Martinson, A. B. F.; Elam, J. W.; Hupp, J. T.; Pellin, M. J. *Nano Lett.* **2007**, *7*, 2183.
- [59] Martinson, A. B. F.; Góes, M. S.; Fabregat-Santiago, F.; Bisquert, J.; Pellin M. J.; Hupp, J. T. *J. Phys. Chem. A* **2009**, *113*, 4015.
- [60] Jiang, C. Y.; Sun, X. W.; Lo, G. Q.; Kwong, D. L.; Wang, J. X. *Appl. Phys. Lett.* *90*, **2007**, 263501.
- [61] Hosono, E.; Fujihara, S.; Honma, I.; Zhou, H. *Adv. Mater.*, **2005**, *17*, 2091.
- [62] Lai, Y.H.; Lin, C. Y.; Chen, H. W.; Chen, J. G.; Kung, C. W.; Vittal, R.; Ho, K.C. *J. Mater. Chem.* **2010**, *20*, 9379.
- [63] Xu, F.; Dai, M.; Lu, Y.; Sun, L. *J. Phys. Chem. C* **2010**, *114*, 2776.
- [64] Hsu, Y. F.; Xi, Y. Y.; Yip, C. T.; Djurišić A. B.; Chan, W. C. *J. Appl. Phys.* **2008**, *103*, 083114.
- [65] Chiu, W. H.; Lee, C. H.; Cheng, H. M.; Lin, H. F.; Liao, S. C.; Wu, J. M.; Hsieh, W. F. *Energy Environ. Sci.* **2009**, *2*, 694.
- [66] Chen, W.; Zhang, H.; Hsing, I. M.; Yang, S. *Electrochem. Commun.* **2009**, *11*,

1057.

- [67] Chou, T. P.; Zhang, Q.; Fryxell, G. E.; Cao, G. *Adv. Mater.* **2007**, *19*, 2588.
- [68] Zhang, Q.; Chou, T. P.; Russo, B.; Jenekhe, S. A.; Cao, G. *Angew. Chem., Int. Ed.* **2008**, *47*, 2402.
- [69] Ito, S.; Zakeeruddin, S. M.; Humphry-Baker, R.; Liska, P.; Charvet, R.; Comte, P.; Nazeeruddin, M. K.; Péchy, P.; Takata, M.; Miura, H.; Uchida, S. Grätzel, M. *Adv. Mater.* **2006**, *18*, 1202.
- [70] Ito, S.; Miura, H.; Uchida, S.; Takata, M.; Sumioka, K.; Liska, P.; Comte, P.; Péchy, P.; Grätzel, M. *Chem. Commun.* **2008**, 5194.
- [71] Kuang, D.; Uchida, S.; Humphry-Baker, R.; Zakeeruddin, S. M.; Grätzel, M. *Angew. Chem. Int. Ed.* **2008**, *47*, 1923.
- [72] Horiuchi, T.; Miura, H.; Uchida, S. *Chem. Commun.* **2003**, 3036.
- [73] Horiuchi, T.; Miura, H.; Sumioka, K.; Uchida, S. *J. Am. Chem. Soc.* **2004**, *126*, 12218.
- [74] Cheng, H. M., Hsu, H. C., Chen, S. L., Wu, W. T., Kao, C. C., Lin, L. J. Hsieh, W. *F. J. Cryst. Growth* **2005**, *277*, 192.
- [75] Cheng, H. M., Lin, K. F., Hsu, H. C., Lin, C. J., Lin, L. J. and Hsieh W. F. *J. Phys. Chem. B*, 2005, *109*, 18385.
- [76] http://en.wikipedia.org/wiki/Image:Solar_Spectrum.png
- [77] Bisquert, J. *Phys. Chem. Chem. Phys.* **2003**, *5*, 5360.
- [78] Kern, R.; Sastrawan, R.; Ferber, J.; Stangl, R.; Luther, J. *Electrochim. Acta* **2002**, *47*, 4213.
- [79] Hauch, A.; Georg, A. *Electrochim. Acta* **2001**, *46*, 3457.
- [80] Zaban, A.; Meier, A.; Gregg, B. A. *J. Phys. Chem. B* **1997**, *101*, 7985.
- [81] Schwarzburg, K.; Willig, F. *J. Phys. Chem. B* **2003**, *107*, 3552.

- [82] Bisquert, J. *J. Phys. Chem. B* **2002**, *106*, 325.
- [83] Fabregat-Santiago, F.; Garcia-Canadas, J.; Palomares, E.; Clifford, J. N.; Haque, S. A.; Durrant, J. R.; Garcia-Belmonte, G.; Bisquert, J. *J. Appl. Phys.* **2004**, *96*, 6903.
- [84] Pitarch, A.; Garcia-Belmonte, G.; Mora-Sero, I.; Bisquert, J. *Phys. Chem. Chem. Phys.* **2004**, *6*, 2983.
- [85] Fabregat-Santiago, F.; Bisquert, J.; Garcia-Belmonte, G.; Boschloo, G.; Hagfeldt, A. *Sol. Energ. Mat. Sol. C.* **2005**, *87*, 117.
- [86] Wang, Q.; Moser, J.; Grätzel, M. *J. Phys. Chem. B* **2005**, *109*, 14945.
- [87] Wang, Q.; Ito, S.; Grätzel, M.; Fabregat-Santiago, F.; Mora-Seró, I.; Bisquert, J.; Bessho, T.; Imai, H. *J. Phys. Chem. B* **2006**, *110*, 25210.
- [88] Adachi, M.; Sakamoto, M.; Jiu, J.; Ogata, Y.; Isoda, S. *J. Phys. Chem. B* **2006**, *110*, 13872.
- [89] Bisquert, J.; Garcia-Belmonte, G.; Fabregat-Santiago, F.; Compte, A. *Elec. Commun.* **1999**, *1*, 429.
- [90] Bisquert, J. *Phys. Chem. Chem. Phys.* **2003**, *2*, 4185.
- [91] Mora-Seró, I.; Bisquert, J.; Fabregat-Santiago, F.; Garcia-Belmonte, G.; Zoppi, G.; Durose, K.; Proskuryakov, Y.; Oja, I.; Belaidi, A.; Dittrich, T.; Tena-Zaera, R.; Katty, A.; Lévy-Clément, C.; Barrioz, V.; Irvine, S. J. C. *Nano Lett.* **2006**, *6*, 640.
- [92] Wu, J. J.; Wang, D. K. P. *Adv. Mater.* **2007**, *19*, 2015.
- [93] Wu, J. J.; Chen, G. R.; Yang, H. H.; Ku, C. H.; Lai, J. Y. *Appl. Phys. Lett.* **2007**, *90*, 213109.
- [94] Lin, C. J.; Yu, W. Y.; Chien, S. H. *Appl. Phys. Lett.* **2007**, *91*, 233120.
- [95] Pasquier, A. D.; Chen, H.; Lu, Y. *Appl. Phys. Lett.* **2006**, *89*, 253513.
- [96] Horiuchi, H.; Katoh, R.; Hara, K.; Yanagida, M.; Murata, S.; Arakawa, H.;

- Tachiya, M. *J. Phys. Chem. B* **2003**, *107*, 2570.
- [97] Chou, T. P.; Zhang, Q.; Cao, G. *J. Phys. Chem. C* **2007**, *111*, 18804.
- [98] Cao, H.; Zhao, Y. G.; Ho, S. T.; Seelig, E. W.; Wang, Q. H.; Chang, R. P. H. *Phys. Rev. Lett.* **1999**, *82*, 2278.
- [99] Xu, J.; Zhang, H.; Liang, G. J.; Wang, L. X.; Xu, W. L.; Gui, W. G.; Li, Z. C. *J. Serb. Chem. Soc.* **2010**, *75*, 259.
- [100] Ham, H. W.; Kim, Y. S. *Thin Solid Films* **2010**, *518*, 6558.
- [101] Jose, R.; Kumar, A.; Thavasi, V.; Ramakrishna, S. *Nanotechnology* **2008**, *19*, 424004.
- [102] Dentani, T.; Kubota, Y.; Funabiki, K.; Jin, J.; Yoshida, T.; Minoura, H.; Miura, H.; Matsui, M. *New J. Chem.* **2009**, *33*, 93.
- [103] Kroeze, J. E.; Hirata, N.; Koops, S.; Nazeeruddin, M. K.; Schmidt-Mende, L.; Grätzel, M.; Durrant, J. R. *J. Am. Chem. Soc.* **2006**, *128*, 16376.



Chapter 7 Conclusions

7.1 Conclusions

Vertically well-aligned ZnO nanorods were synthesized without employing any metal catalysts on glass, Si (111), 6H-SiC (0001) and sapphire (0001), but were pre-coated with *c*-oriented ZnO buffer layers. The in-plane alignments of ZnO nanorods depend on the crystallographic alignment of pre-coed ZnO buffer layer. Similarly, the photoluminescence of ZnO nanorods are basically related to the type of the substrates used. In addition, high-density, vertically oriented arrays of ZnO nanowires were also successfully epitaxial grown on the GaN(0001)-buffered sapphire substrate. We demonstrated that the arrays of ZnO nanowires are well aligned along the *c*-axis and suffer a small biaxial compressive stress of 121.9 MPa. The resonant Raman spectra (RRS) show good crystal quality and reveal phonon modes that are affected by the size confinement of the ZnO nanowire. The exciton-related recombinations near the band edge dominate the UV emissions at room temperature as well as at low temperature.

The self-assembled secondary ZnO nanoparticles recognized with the agglomeration of crystalline subcrystals ranging from 6 to 12nm synthesized by a sol-gel method have also been demonstrated. The artificial clusters behave like a single-crystal structure, owing to the subcrystals coagulating as the same crystal orientation with adjacent ones via the sintering process. The as-grown sample exhibits phonon redshift in a resonant Raman scattering, compared with the samples after post-annealing at 350°C and 500°C. Moreover, the electron-phonon coupling parameter is unambiguously extracted from resonant Raman scattering, and an interesting phenomenon of increasing electron-LO-phonon coupling is also be

discovered when the crystal size of ZnO enlarges after heating treatment. For ZnO quantum dots, the enlarged free-exciton transition energy is responsible for the blueshift of near-band-edge PL spectra and gives significant evidence for the quantum confinement effect. Moreover, an increasing electron-phonon coupling was also discovered from RRS analysis while the diameter of ZnO crystal increases. The size dependence of electron-phonon coupling is also principally as a result of the Fröhlich interaction.

For further dye-sensitized solar cell (DSC) applications, the solvothermal method was utilized to fabricate the ZnO nanowires and branched nanowires on FTO substrates. The short-circuit current density and the overall light conversion efficiency of the branched ZnO nanowire DSCs were almost twice higher than the bare ZnO nanowire ones. The improvement can be explained association with the enlargement of internal surface area within the photoelectrode without increasing interparticle hops. In addition, the branched ZnO nanowires significantly enhanced the dye-adsorption and IPCE as compared with the bare ZnO nanowires. Therefore, the concept of these one-dimensional branched nanostructures could simultaneously afford a direct conduction pathway and achieve higher dye adsorption to significantly enhance the overall energy conversion efficiency of the DSCs.

Furthermore, self-assembled ZnO secondary nanoparticles have been demonstrated as an effective photoelectrode within DSCs which retain the desired specific surface area for dye-molecule adsorption and the sufficient light-harvesting from prolonged light traveling. D149 and D205 indoline dyes were used as the effective sensitizers for DSCs composed of hierarchical ZnO photoelectrodes. The higher charge-transfer rate and retardant fluorescence decay reveal that D205 has better electron injection dynamics for ZnO nanoparticles as compared to D149. The

optimal energy conversion efficiencies of 4.95% and 5.34% were achieved for D149 and D205 on 27 μm -thick ZnO photoelectrode films under AM 1.5 solar radiation. The significantly enhanced performance for D205-sensitized ZnO DSCs is ascribed to the effective suppression of electron recombination as well as enhancing interfacial electron transfer rate by extending the alkyl chain on the terminal rhodanine moiety from ethyl to octyl. The results of the comparison of the electron transport property were further confirmed, presenting a prolonged electron lifetime in the D205-sensitized ZnO DSCs. Thus, the hybrid system of hierarchical ZnO architecture and metal-free indolne sensitizer may represent an alternative candidate with regard to high-performance metal-free organic DSCs.

7.2 Prospective

Coupling between electronic and vibrational excitations plays an important role in semiconductor materials because of its significant influence on the optoelectronic properties of semiconductors, e.g., the transport processes, the energy relaxation rates of excited carriers, and linear or nonlinear optical absorption. Beyond size control, recently, our laboratory also found the strength of exciton-LO-phonon coupling can be reduced in $\text{Zn}_{1-x}\text{Mg}_x\text{O}$ powders ($0 \leq x \leq 0.05$) [1]. The increase of the exciton binding energy results from decrease of the exciton Bohr radius that is responsible for reducing the coupling strength of exciton-LO-phonon as increasing Mg content. This investigation could shed a light on the development of further ZnO nanostructures (ex: ZnO/ZnMgO MQWs) for advanced photonic devices with Bose–Einstein condensation for the realization of room-temperature polariton lasers. Beside resonance Raman scattering, femtosecond pump-probe methods appears to be one of the most direct, generally applicable methods to probe electron-phonon coupling in

semiconductor nanostructures. As a controversial topic for electron-phonon coupling, it should be important to circumvent the confounding factor that has not been considered in most of previous experiments and obtain more reliable results for my further works. An interpretation with the aid of numerical simulations and multiple experimental observables will also be considered.

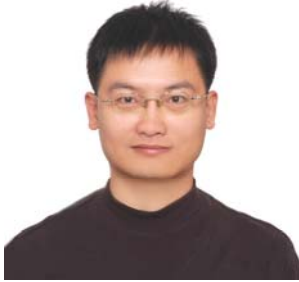
In order to increase the power conversion efficiency, high density, long branched treelike multigeneration hierarchical crystalline ZnO nanoforest photoanodes via a simple selective hierarchical growth sequence and could significantly improve the DSC power conversion efficiency (2.63 %) [2]. However, the performance is still quite inadequate in practice. From Yang's and Gao's reports, the surface of ZnO nanostructures were successfully modified with ultrathin TiO₂ layer by means of atomic layer deposition (ALD) and achieved DSC efficiencies of 2.27% for core-shell ZnO/TiO₂ nanowires [3] and 6.3% for ZnO nanocrystallite aggregates. The utility of TiO₂ ultrathin layer indeed overcome the limitation of the neutrally chemical unstability for ZnO and temporarily avoid the unsuitable dye designed primarily for TiO₂. Furthermore, the concepts of multiexcitations [5] and hot-electron transfer [6] with appropriate chemical treatment of the ZnO surface for quantum dot-sensitized solar cell systems will also be attempted. The pico-second time-resolved photoluminescence (TRPL) and time-resolved second harmonic generation (TR-SHG) could be built up as well to further realize the transient transfer mechanisms.

References and Notes

- [1] Pan, C. J.; Lin, K. F.; Hsu, W. T.; Hsieh, W. F. *J. Appl. Phys.* **2007**, 102, 123504.
- [2] Ko, S. H.; Lee, D.; Kang, H. W.; Nam, K. H.; Yeo, J. Y.; Hong, S. J.; Grigoropoulos, C. P.; Sung, H. J. *Nano Lett.* **2011**, 11, 666.
- [3] Law, M.; Greene, L. E.; Redenovic, A.; Kuykendall, T.; Liphardt, J.; Yang, P. *J. Phys. Chem. B* **2006**, 110, 22652.
- [4] Park, K.; Zhang, Q.; Garcia, B. B.; Zhou, G. X.; Jeong, Y. H.; Cao, G. *Adv. Mater.* **2010**, 22, 2329.
- [5] Klimov, V. I. *J. Phys. Chem. B* **2006**, 110, 16827.
- [6] Tisdale, W. A.; Williams, K. J.; Timp, B. A.; Norris, D. J.; Aydil, E. S.; Zhu, X. Y. *Science* **2010**, 328, 1543.



個人簡歷



姓名：鄭信民 (Hsin-Ming Cheng)

生日：1975 / 12 / 17

籍貫：台灣省屏東縣

戶籍：苗栗縣頭份鎮

學經歷：

清華大學 物理所 學士 (1994/09~1998/06)

清華大學 物理所 碩士 (1998/09~2000/06)

工研院 材化所 研究員 (2001/01~2011/05)

交通大學光電工程研究所博士班進修 (2005/09~2011/05)

中央研究院應用科學中心 (2011/06~)

專長：

微結構分析、表面分析、固態物理、光電半導體

擔任工業技術研究院 材化所 微結構與特性分析實驗室部門

XRD、Raman、SEM、SPM 等設備負責人。

曾執行計畫：

奈米結構氧化鋅場發射與氣體、光感測器應用；氧化鋅染料敏化太陽電池；能源材料瞬時光譜分析；鋰電池電極材料研發相關計畫。

獲獎紀錄：

2004 工研院材化所前瞻研究獎

2006 交通大學光電系博士研究最優秀獎

2006 工研院材化所年度論文獎

2007 工研院年度論文獎

著作目錄

A. Book Chapter

“Optical properties of Zinc Oxide Quantum Dots”, W.F. Hsieh, H. C. Hsu, W. J. Liao, **H. M. Cheng**, K. F. Lin, W. T. Hsu and C. J. Pan, Chapter 13, in Ali Serpenguzel and Andrew W. Poon, Eds, *Optical Processes in Microparticles and Nanostructures: A Festschrift Dedicated to Richard Kounai Chang on His Retirement from Yale University*, Chapter 13, World Scientific (2010).

B. Journal Publications (Impact Factor and times cited are based on Web of Science 2011/5/11)

1. Wei-Hao Chiu, Kun-Mu Lee, **Hsin-Ming Cheng**, Chia-Hua Lee, Meng-Chin Tsui, Hsiu-Fen Lin, Shih-Chieh Liao and Wen-Feng Hsieh, “Tetrapod-like ZnO as framework for ionic-liquid-based dye-sensitized solar cells”, *Submit* (2011).
2. **Hsin-Ming Cheng**, and Wen-Feng Hsieh, “Electron Transfer Properties of Organic Dye-Sensitized Solar Cells Based on Indoline Sensitizers with ZnO Nanoparticles”, *Nanotechnology* 21[48], 285202 (2010). (Cited : 0; SCI IF: 3.137)
3. Shu-Hui Wang, **Hsin-Ming Cheng**, Ren-Jye Wu, and Wen-Hsuan Chao, “Structural and Thermoelectric Properties of HfNiSn Half-Heusler Thin Films”, *Thin Solid Films*, 518, 5901 (2010). (Cited : 0; SCI IF: 1.884)
4. **Hsin-Ming Cheng** and Wen-Feng Hsieh, “High-Efficiency Metal-Free Organic-Dye-Sensitized Solar Cells with Hierarchical ZnO Photoelectrode”, *Energy Environ. Sci.*, 3[4], 442 (2010). (Cited : 4; SCI IF: 8.5)
5. **Hsin-Ming Cheng**, Wei-Hao Chiu, Chia-Hua Lee, Song-Yeu Tsai, and Wen-Feng Hsieh, “Branched ZnO Nanowires for Enhancing Energy Conversion Efficiency of Dye-Sensitized Solar Cells” *Mater. Res. Soc. Symp. Proc.* Vol. 1121-N14-01 (2009). (Cited : 0; SCI IF: 0)
6. Wei-Hao Chiu, Chia-Hua Lee, **Hsin-Ming Cheng**, Hsiu-Fen Lin, Shih-Chieh Liao, Jenn-Ming Wu, and Wen-Feng Hsieh, “Efficient electron transport in tetrapod-like ZnO metal-free dye-sensitized solar cells”, *Energy Environ. Sci.*, 2[6], 694-698 (2009). (Cited : 14; SCI IF: 8.5)
7. **Hsin-Ming Cheng**, Wei-Hao Chiu, Chia-Hua Lee, Song-Yeu Tsai, and Wen-Feng Hsieh, “Formation of Branched ZnO Nanowires from Solvothermal Method and Dye-Sensitized Solar Cells Applications”, *J. Phys. Chem. C*, 112[42], 16359 (2008). (Cited : 36; SCI IF: 3.396)
8. S. C. Ray, Y. Low, H. M. Tsai, C. W. Pao, J. W. Chiou, S. C. Yang, F. Z. Chien, and W. F. Pong, M.-H. Tsai, K. F. Lin, **H. M. Cheng**, and W. F. Hsieh, J. F. Lee, “Size dependence of the electronic structures and electron-phonon coupling in ZnO quantum dots”, *Appl. Phys. Lett.* 91[26], 262101 (2007). (Cited : 4; SCI IF:3.596)
9. Song Yang, Hsu-Cheng Hsu, Wei-Ren Liu, **Hsin-Ming Cheng**, and Wen-Feng Hsieh, “Correlation between photoluminescence and varied growth pressure of well-aligned ZnO nanorods on fused silica substrate”, *Optical Materials* 30 502–507 (2007). (Cited : 0; SCI IF:1.519)

10. Ching-Ju Pan, Hsu-Cheng Hsu, **Hsin-Ming Cheng**, Chun-Yi Wu, and Wen-Feng Hsieh, “Structural and optical properties of ZnMgO nanostructures formed by Mg in-diffused ZnO nanowires”, *Journal of Solid State Chemistry* 180, 1188-1192 (2007). (Cited : 16; SCI IF:2.149)
11. C.-T. Tzeng, K.-D. Tsuei, **H.-M. Cheng**, and R.-Y. Chu, “Covalent bonding and hole-electron Coulomb interaction U in C60 on Be(0001) surfaces”, *J. Phys.: Condens. Matter* 19, 176009 (2007). (Cited : 1; SCI IF:1.886)
12. Hsu-Cheng Hsu, Chun-Yi Wu, **Hsin-Ming Cheng**, and Wen-Feng Hsieh, “Bandgap engineering and stimulated emission of ZnMgO nanowires”, *Appl. Phys. Lett.* 89[1], 013101 (2006). (Cited : 28; SCI IF:3.977)
13. Kuo-Feng Lin, **Hsin-Ming Cheng**, Hsu-Cheng Hsu, and Wen-Feng Hsieh, “Bandgap engineering and spatial confinement of optical phonon in ZnO”, *Appl. Phys. Lett.* 88[26], 263117 (2006). (Cited : 26; SCI IF:3.977)
14. **Hsin-Ming Cheng**, Kuo-Feng Lin, Hsu-Cheng Hsu, and Wen-Feng Hsieh, “Size dependence of photoluminescence and resonant Raman scattering from ZnO quantum dots”, *Appl. Phys. Lett.* 88[26], 261909 (2006). (Cited : 47; SCI IF:3.977)
15. Hsu-Cheng Hsu, **Hsin-Ming Cheng**, Chun-Yi Wu, Hung-Shang Huang, Yi-Chin Lee, and Wen-Feng Hsieh, “Luminescence of selective area growth of epitaxial ZnO nanowires and random-growth oriented nanobelts”, *Nanotechnology* 17[5], 1404-1407 (2006). (Cited : 9; SCI IF:3.037)
16. Chun-Yi Wu, Hsu-Cheng Hsu, **Hsin-Ming Cheng**, Song Yang, and Wen-Feng Hsieh, “Structural and optical properties of ZnO nanosaws”, *J. Cryst. Growth*, 287, 189-193 (2006). (Cited : 2; SCI IF:1.809)
17. Hung-Shang Huang, **Hsin-Ming Cheng**, and Li-Jiaun Lin, “Coating tips used in electrical scanning probe microscopy with W and AuPd”, *Appl. Surf. Sci.* 252, 2085-2091 (2005). (Cited : 2; SCI IF:1.263)
18. **Hsin-Ming Cheng**, Hsu-Cheng Hsu, Song Yang, Chun-Yi Wu, Yi-Chin Lee, Li-Jiaun Lin, and Wen-Feng Hsieh, “The substrate effect on in-plane orientation of vertically well-aligned ZnO nanorods grown on ZnO buffer layer”, *Nanotechnology* 16[12], 2882-2886 (2005). (Cited : 18; SCI IF:2.993)
19. **Hsin-Ming Cheng**, Kuo-Feng Lin, Hsu-Cheng Hsu, Chih-Jen Lin, Li-Jiaun Lin, Wen-Feng Hsieh, “Enhanced Resonant Raman scattering and electron-phonon coupling from self-assembled secondary ZnO nanoparticles”, *J. Phys. Chem. B*, 109[39], 18385 (2005). (Cited : 31; SCI IF:4.033)
20. Kuo-Feng Lin, **Hsin-Ming Cheng**, Hsu-Cheng Hsu, Li-Jiaun Lin, and Wen-Feng Hsieh, “Band Gap Variation of Size-Controlled ZnO quantum dots synthesized by sol-gel method”, *Chem. Phys. Lett.* 409, 208 (2005). (Cited : 71; SCI IF:2.438)
21. **Hsin-Ming Cheng**, Hsu-Cheng Hsu, Yung-Kuan Tseng, Li-Jiaun Lin, Wen-Feng Hsieh, “Raman scattering and efficient UV photoluminescence from well-aligned ZnO nanowires

- epitaxially grown on GaN buffer layer”, *J. Phys. Chem. B*, 109[18], 8749 (2005). (Cited : 53; SCI IF:4.033)
22. C.P. Chen, M. Hong, J. Kwo, **H.M. Cheng**, Y.L. Huang, S.Y. Lin, J. Chi, H.Y. Lee, Y.F. Hsieh and J.P. Mannaerts, “Thin single-crystal Sc_2O_3 films epitaxially grown on Si (111)-structure and electrical properties” *J. Cryst. Growth*, 278, 638 (2005). (Cited : 9; SCI IF:1.681)
 23. **Hsin-Ming Cheng**, Hsu-Cheng Hsu, Shioh-Lian Chen, Wen-Ti Wu, Chih-Chun Kao, Li-Jiaun Lin, Wen-Feng Hsieh, “Efficient UV photoluminescence from monodispersed secondary ZnO colloidal spheres synthesized by sol–gel method”, *J. Cryst. Growth*, 277, 192 (2005). (Cited : 28; SCI IF:1.681)
 24. Y. K. Tseng, C. T. Chia, C. Y. Tsay, L. J. Lin, **H. M. Cheng**, C. Y. Kwo, I. C. Chen, “Growth of Epitaxial Needle-like ZnO Nanowires on GaN Films”, *J. Electrochem. Soc.* 152, G95, (2005). (Cited : 22; SCI IF:2.19)
 25. Hsu-Cheng Hsu, Yung-Kuan Tseng, **Hsin-Ming Cheng**, Jia-How Kuo, and Wen-Feng Hsieh, “Selective growth of ZnO nanorods on pre-coated ZnO buffer layer” , *J. Cryst. Growth*, 261, 520 (2004). (Cited : 24; SCI IF:1.414)
 26. Y. K. Tseng, C. J. Huang, **H. M. Cheng**, I. N. Lin, K. S. Liu, I. C. Chen, “Characterization and field emission properties of needle-like zinc oxide nanowires grown vertically on conductive zinc oxide films”, *Adv. Funct. Mater.*, 13[10], 811 (2003). [Cover Highlight] (Cited : 226; SCI IF:4.798)
- C. International Conferences
1. **Hsin-Ming Cheng** and Wen-Feng Hsieh, “High-Efficiency Dye-Sensitized Solar Cells Based on Metal-Free Indoline Sensitizers with Hierarchical ZnO Nanoparticles” MRS Fall Meeting, poster paper Y6.1 (11/2010).
 2. Shu Hui Wang, Wen-Hsuan Chao and **Hsin-Ming Cheng**, “High-Throughput Screening for Combinatorial Thin Film Library of $\text{La}_x\text{Fe}_{4-x}\text{Sb}_{12}$ Skutterudites” MRS Fall Meeting, poster paper Z5.8 (12/2009).
 3. Wei-Hao Chiu, Kun-Mu Lee, **Hsin-Ming Cheng**, and Wen-Feng Hsieh ‘Performances of tetrapod-like ZnO dye-sensitized solar cells with ionic liquid electrolyte”, 2009 International Symposium on Dye-Sensitized Solar Cells, Taipei Taiwan, (10/22,23/2009)
 4. Chia-Hua Lee, Wei-Hao Chiu, **Hsin-Ming Cheng**, and Hsiu-Fen Lin, “Tetrapod-shaped ZnO nanostructure film as photoelectrode in dye-sensitized solar cells” 3rd international conference on the industrialization of dsc (DSC-IC 09), poster paper PMV029, Nara Japan (4/23/2009).
 5. Wei-Hao Chiu, Chia-Hua Lee, **Hsin-Ming Cheng**, Hsiu-Fen Lin, and Wen-Feng Hsieh, “Excellent electron diffusion property in tetrapod-like ZnO metal-free dye sensitized solar cell” 3rd international conference on the industrialization of dsc (DSC-IC 09), poster paper THV006, Nara Japan (4/23/2009).
 6. **Hsin-Ming Cheng**, Wei-Hao Chiu, Chia-Hua Lee, Song-Yeu Tsai, and Wen-Feng Hsieh,

- “Branched ZnO Nanowires for Enhancing Energy Conversion Efficiency of Dye-Sensitized Solar Cells” International Symposium on Solar Cell Technologies (ISSCT), poster paper Sat-P2-053 (12/2008).
7. **Hsin-Ming Cheng**, Wei-Hao Chiu, Chia-Hua Lee, Song-Yeu Tsai, and Wen-Feng Hsieh, “Branched ZnO Nanowires for Enhancing Energy Conversion Efficiency of Dye-Sensitized Solar Cells” MRS Fall Meeting, poster paper N14.1 (12/2008).
 8. Wen-Feng Hsieh, Kuo-Feng Lin, **Hsin-Ming Cheng** and Hsu-Cheng Hsu, “Bandgap engineering and spatial confinement of optical phonon in ZnO quantum dots” Conference Information: 19th Annual Meeting of the IEEE-Lasers-and-Electro-Optics-Society, OCT 29-NOV 02, 2006 Montreal, CANADA, Pages: 939-940 (10/2006).
 9. Wen-Feng Hsieh, Kuo-Feng Lin, **Hsin-Ming Cheng** and Hsu-Cheng Hsu, “Spatial Confinement of Optical Phonon in ZnO Quantum Dots” MRS Spring meeting, oral paper AM DD1.8 (4/2006).
 10. Song Yang, Hsu-Cheng Hsu, Wei-Ren Liu, **Hsin-Ming Cheng**, and Wen-Feng Hsieh “Well-aligned ZnO Nanorods with Variable Diameter on Fused Silica Substrate” MRS Spring meeting, poster paper P13.34 (4/2006).
 11. Hsu-Cheng Hsu, Chun-Yi Wu, Yi-Chin Lee, Wen-Feng Hsieh, **Hsin-Ming Cheng**, “Luminescence of Selective Area Growth of Epitaxial ZnO Nanowires and Nanobelts” International Conference on Materials for Advanced Technologies (ICMAT 2005 & IUMRS-ICAM 2005), oral paper Symposium-N-8-OR25 (7/2005).
 12. **Hsin-Ming Cheng**, Hsu-Cheng Hsu, Song Yang, Yi-Chin Lee, Wen-Feng Hsieh, “Substrate Effect on In-plane Orientation of Vertically Well-aligned ZnO Nanorods” International Conference on Materials for Advanced Technologies (ICMAT 2005 & IUMRS-ICAM 2005), oral paper Symposium-N-9-OR26 (7/2005).
 13. Chun-Yi Wu, Hsu-Cheng Hsu, **Hsin-Ming Cheng**, Song Yang, Wen-Feng Hsieh, “Structure and Optical Properties of ZnO Saw-like Nanostructures” International Conference on Materials for Advanced Technologies (ICMAT 2005 & IUMRS-ICAM 2005), poster paper Symposium-N-4-PO42 (7/2005).
 14. Wen-Feng Hsieh, **Hsin-Ming Cheng**, Kuo-Feng Lin and Hsu-Cheng Hsu, “Size dependence of band gap variation and electron-phonon coupling in ZnO Quantum Dots” International Conference on Quantum Electronics and the Pacific Rim Conference on Lasers and Electro-Optics (IQEC/CLEO-PR, Tokyo, JAPAN), oral paper CTuN4-2, p269-271 (7/2005).
 15. Wen-Feng Hsieh, Hsu-Cheng Hsu, **Hsin-Ming Cheng** and Kuo-Feng Lin, “Enhancement of resonant Raman scattering from ZnO Quantum Dots” Conference on Lasers and Electro-Optics; Quantum Electronics and Laser Science Conference (CLEO/QELS), post paper JWB30 (5/2005).
 16. C. L. Hsu, S. J. Chang, Y. K. Tseng, C. J. Huang, **H. M. Cheng** and I. C. Chen, “Vertical ZnO nanowires grown by self-catalyzed vapor-liquid-solid process.” The international Conference on One-Dimensional Nanomaterials, post paper SOR107 pp.88 (1/2005).
 17. Huang Hun-Shen and **Hsin Ming Cheng**, “Tip Coating Conductive Metals for use in Scanning

Probe Microscopy”, The IUMRS International Conference in Asia (IUMRS-ICA), pp.105 (11/2004).

18. C.P. Chen, M. Hong, J. Kwo, **H.-M. Cheng**, Y. L. Hwang, S. Y. Lin, J. Chi, H.-Y. Lee, and J. P. Mannaerts, “Epitaxial Growth and Structure of Thin Single Crystal Sc₂O₃ Films on Si (111).” International MBE conference. (8/2004).
19. K.-D. Tsuei, and C.-T. Tzeng, **H.-M. Cheng**, and R.-Y. Chu, "Covalent bonding and hole-electron interaction U in C60 on Be(0001) surfaces", APS March Meeting, Session H17.007 (3/2004).

D. Domestic Magazines

1. 謝登存、**鄭信民**，“臨場光譜在鋰電池界面反應之研究”，工業材料雜誌第 252 期 (2007).
2. 溫景發，田大昌，羅聖全，黃宏勝，**鄭信民**，胡堂祥，何家充，“有機薄膜電晶體微結構分析技術開發”，電子與材料第 27 期 (2005).
3. 陳一誠，曾永寬，**鄭信民**，許正良，郭忠義，“氧化鋅奈米線材技術平台與其應用”，工業材料雜誌第 213 期 (2004).
4. **鄭信民**，林麗娟，“多功能薄膜 X 光繞射儀”，化工資訊與商情 第八期 (2004).
5. 黃宏勝，**鄭信民**，“場發射掃描式電子顯微鏡及附加配件在材料分析之應用”，化工資訊與商情 第八期 (2004).
6. **鄭信民**，林麗娟，“場發射掃描式電子顯微鏡分析技術應用簡介”，工業材料雜誌第 201 期 (2003).
7. **鄭信民**，林麗娟，“X 光繞射應用簡介”，工業材料雜誌第 181 期 (2002).

E. Domestic Conferences

1. Wen-Feng Hsieh, Wan-Jiun Liao, Chin-Chia Kuo, **Hsin-Ming Cheng**, Wei-Hao Chiu and Chen-Shiung Chang “Invariable Exciton States upon Increasing Pumping in ZnO Quantum Dots” , 28th Symposium on Spectroscopic Technologies and Surface Sciences Conference Agenda, (7/2010).
2. Wei-Hao Chiu (邱偉豪), **Hsin-Ming Cheng (鄭信民)**, Kun-Mu Lee(李坤穆), Chia-Hua Lee(李佳樺), Meng-Chin Tsui(崔孟晉), Hsiu-Fen Lin (林秀芬), Shih-Chieh Liao (廖世傑), Wen-Feng Hsieh(謝文峰), “Hierarchical Frameworks Film Assembled by Terapod-like ZnO Nanoparticles for Dye-sensitized Solar Cells Applications”, in Conference of Year 2010 Annual Meeting of Chinese Physical Society, National Cheng Kung University, TAIWAN, oral paper pp. 39(B9-1), (2/2010).
3. **鄭信民**、邱偉豪、謝文峰, "High-Efficiency ZnO Nanoparticle Based Dye-Sensitized Solar Cells with Metal-Free Indoline Sensitizers" 2009 材料年會, National Dong Hwa University, Hualien (2009/11/26,27)
4. **鄭信民**、邱偉豪、李佳樺、蔡松雨、謝文峰, “Branched ZnO Nanowires for Enhancing Energy Conversion Efficiency of Dye-Sensitized Solar Cells” , 2008 年材料科學學會年會, Taipei,

- Taiwan, post paper P07-008, (11/2008) (佳作).
5. 謝登存、張國馨、**鄭信民**，“商用高功率鋰電池失效模式分析”，2007年材料科學學會年會，Hsin-Chu, Taiwan, post paper P01-067 p-34, (11/2007).
 6. 羅聖全、陳淑貞、陳世明、**鄭信民**、林麗娟、劉文亮、黃宏勝、Satoshi Ak, Hirokazu H.,”利用 XRD、SEM 與 TEM 研究 PEO/clay 奈米複合材料之微結構特性”，「台俄軟質材料物理與應用研討會」，pp.43-46,(11/2007)
 7. Wei-Tse Hsu, Kuo-Feng Lin, **Hsin-Ming Cheng**, and Wen-Feng Hsieh, “Size-dependence of band gap engineering and electron-phonon coupling in ZnO quantum dots”, in Conference of Year 2007 Annual Meeting of Chinese Physical Society, TAIWAN, post paper PA-12, (1/2007).
 8. Ching-Ju Pan, Hsu-Cheng Hsu, **Hsin-Ming Cheng**, Chun-Yi Wu and Wen-Feng Hsieh “Stimulated emission of ZnMgO sponges formed by simple diffusion MgO capped ZnO nanowires” 2005 台灣光電科技研討會暨國科會光電學門研究成果發表會，Tainan, Taiwan, oral paper A-FR-II 4-6 p-51, (12/2005).
 9. 溫景發、田大昌、羅聖全、**鄭信民**、吳仁傑，“LCD-DBEF 之奈米結構及成分分析”，2005年材料科學學會年會，Taipei, Taiwan, post paper 4-3-P-007 p-376, (11/2005).
 10. **鄭信民**、林國峰、徐旭政、謝文峰、林智仁、林麗娟、洪健龍，“Enhancement of resonant Raman scattering and electron-phonon coupling from self-assembled secondary ZnO”，2005年材料科學學會年會，Taipei, Taiwan, post paper 4-3-P-030 p-388, 壁報論文佳作獎 (11/2005).
 11. Chun-Yi Wu, Hsu-Cheng Hsu, **Hsin-Ming Cheng**, Song Yang, and Wen-Feng Hsieh “Structural and optical properties of ZnO saw-like nanostructures”, Taiwan Nano Tech 2005, Taipei, Taiwan, post paper D20 p.491-494, (9/2005).
 12. Hsu-Cheng Hsu, **Hsin-Ming Cheng**, Chun-Yi Wu, Hung-Shang Huang, Yi-Chin Lee, and Wen-Feng Hsieh “Structure and luminescence properties of epitaxial ZnO nanowires and nanobelts”, Taiwan Nano Tech 2005, Taipei, Taiwan, post paper D21 p.495-498, (9/2005).
 13. Kuo-feng Lin, **Hsin-Ming Cheng**, Hsu-Cheng Hsu, Li-Jiaun Lin and Wen-Feng Hsieh “Band Gap Variation of Size-Controlled ZnO quantum dots synthesized by sol-gel method”, Taiwan Nano Tech 2005, Taipei, Taiwan, post paper D22 p.499-502, (9/2005).
 14. Song Yang, Hsu-Cheng Hsu, Wei-Ren Liu, **Hsin-Ming Cheng** and Wen-Feng Hsieh “Fabrication of well-aligned ZnO nanorods on fused silica substrates”, Taiwan Nano Tech 2005, Taipei, Taiwan, post paper D23 p.503-506, (9/2005).
 15. **Hsin-Ming Cheng**, Kuo-feng Lin, Hsu-Cheng Hsu, Wen-Feng Hsieh, Chih-Jen Lin, Li-Jiaun Lin and Jain-Long Horng, “Enhancement of resonant Raman scattering and electron-phonon coupling from self-assembled secondary ZnO”，Taiwan Nano Tech 2005, Taipei, Taiwan, post paper D25 p.511-514, (9/2005).
 16. Hsu-Cheng Hsu, Chun-Yi Wu, **Hsin-Ming Cheng**, Song Yang, and Wen-Feng Hsieh, “Random lasing in 1D disorder-oriented ZnO nanosaws” in Conference of Year 2005 Annual Meeting of Chinese Physical Society, Kaohsiung, TAIWAN, oral paper BA-5, (2/2005).
 17. **Hsin-Ming Cheng**, Hsu-Cheng Hsu, and Wen-Feng Hsieh, “Optical properties of arrays of

well-aligned ZnO nanowires epitaxially grown on GaN(0001) buffer layer”, in Conference of Year 2005 Annual Meeting of Chinese Physical Society, Kaohsiung, TAIWAN, post paper PK-20, (2/2005). (best post paper award)

18. Kuo-Feng Lin, Hsu-Cheng Hsu, **Hsin-Ming Cheng**, and Wen-Feng Hsieh “Influence of crystal size on the photoluminescence of ZnO quantum dots grown by sol-gel technique” in Proceedings of Optics and Photonics Taiwan'04, Chunli, TAIWAN, (12/2004).
19. Chun-Yi Wu, Hsu-Cheng Hsu, **Hsin-Ming Cheng**, Song Yang, and Wen-Feng Hsieh, “Self-formed laser cavity in ZnO nanosaws” in Proceedings of Optics and Photonics Taiwan'04, Chunli, TAIWAN, (12/2004).
20. Ming-Rung Tsai, Kuo-Feng Lin, Hsu-Cheng Hsu, **Hsin-Ming Cheng**, and Wen-Feng Hsieh, “以溶膠凝膠法製備 $Mg_xZn_{1-x}O$ 粉末之發光特性研究” in Proceedings of Optics and Photonics Taiwan'04, Chunli, TAIWAN, (12/2004).
21. K.-D. Tsuei, and C.-T. Tzeng, **H.-M. Cheng**, and R.-Y. Chu, "Covalent bonding and hole-electron interaction U in C60 on Be(0001) surfaces", 物理年會 TC-4, p108 (2/2004).
22. **鄭信民**, 曾永寬, 郭忠義, 陳一誠 “兩階段注入氧氣法成長氧化鋅奈米線及其應用”, 奈米國家型科技計畫商機探討暨成果發表會, post paper P-8-1 pp.293 3rd post award, (9/2003).
23. 曾永寬, **鄭信民**, 郭忠義, 陳一誠 “低溫成長氧化鋅奈米線” 第六屆 奈米工程暨微系統技術研討會 (11/2002).

